UNIVERSITAT POLITÈCNICA
DE CATALUNYA
BARCELONATECH

Raman dressed Bose-Einstein condensates with tunable interactions: topological gauge theories and supersolids

Craig S. Chisholm

Raman Dressed Bose-Einstein Condensates with Tunable Interactions: Topological Gauge Theories and Supersolids

Craig S. Chisholm

A thesis submitted in fulfilment of the requirements for the degree of Doctor of Philosophy in Photonics

Thesis supervisor: Prof. Dr. Leticia Tarruell

UNIVERSITAT POLITÈCNICA DE CATALUNYA
BARCELONATECH

ICFO - Insitut de Ciències Fotòniques
UPC - Universitat Politècnica de Catalunya

May, 2023

Thesis committee:

Prof. Sandro Stringari	Dipartimento di Fisica, Università di Trento
Prof. Dr. Markus K. Oberthaler	Kirchoff-Insitute for Physics, Heidelberg University
Prof. Dr. Morgan W. Mitchell	ICFO - The Institute of Photonic Sciences

Substitute examiners:

Prof. Dr. Verònica Ahufinger	Department of Physics, Universitat Autònoma de Barcelona
Prof. Dr. Adrian Bachtold	ICFO - The Institute of Photonic Sciences

Abstract

The exquisite control available in atomic ultracold quantum gases experiments makes them an ideal candidate for quantum simulation of diverse topics ranging from high energy physics and analogue quantum gravity to strongly correlated condensed matter systems and exotic states of matter. This thesis describes the use of Raman coupling to engineer novel chiral interactions and a double well dispersion relation in potassium Bose-Einstein condensates and exploits them to realise a topological gauge theory and an exotic state of matter known as a supersolid, respectively.

A common feature of many topics of interest for quantum simulation is the ability to describe them from the perspective of a gauge theory. Raman coupling has been used to produce artificial gauge fields for more than a decade but usually the gauge fields lack the symmetry constraints necessary to constitute a gauge theory. A well known gauge theory which is used to describe fractional quantum Hall states is the Chern-Simons theory. The Chern-Simons theory is a topological gauge theory so does not have gauge field dynamics in the absence of matter. We have used optical dressing to create chiral interactions in a Bose-Einstein condensate of potassium atoms and encode the dynamics of a one-dimensional reduction of the Chern-Simons theory known as the chiral BF theory into the dynamics of the matter. We have observed chiral solitons and a density-dependent electric field. Our experimental results represent the first successful quantum simulation of a topological gauge theory in the continuum.

Supersolids were predicted theoretically more than fifty years ago and have been realised in Bose-Einstein condensates in recent years. In a second series of experiments, we have taken advantage of the unique interaction properties of potassium to engineer a supersolid in a Raman coupled Bose-Einstein condensate with greater stability and contrast than what can be achieved with other alkali atoms. Using matterwave optics techniques, we have been able to image the characteristic density modulations of a supersolid in a Raman coupled Bose-Einstein condensate for the first time. We explore a previously inaccessible parameter regime and demonstrate that the fringe spacing depends on the optical intensity, in contrast to a shallow optical lattice where the fringe spacing is given by the lattice wavevector.

Our method of engineering chiral interactions broadens the field of quantum simulation of gauge theories to include topological gauge theories in the continuum and is a step towards simulating the Chern-Simons theory in two dimensions. Our application of matterwave optics to the supersolid phase in a Raman coupled Bose-Einstein condensate introduces a new tool for probing low energy Goldstone modes and phase coherence properties.

Resumen

El exquisito control disponible en los experimentos con gases cuánticos ultrafríos los convierte en un candidato ideal para la simulación cuántica de áreas de la física que van desde la física de altas energías y modelos análogos de gravedad cuántica hasta los sistemas de materia condensada fuertemente correlacionados y los estados exóticos de la materia. Esta tesis describe el uso del acoplamiento Raman para diseñar nuevas interacciones quirales y una relación de dispersión con dos mínimos en condensados de Bose-Einstein de potasio, y los explota para realizar una teoría gauge topológica y un estado exótico de la materia conocido como supersólido, respectivamente.

Una característica común de muchos temas de interés para la simulación cuántica es la posibilidad de describirlos desde la perspectiva de una teoría gauge. El acoplamiento Raman se ha utilizado para producir campos gauge artificiales durante más de una década, pero normalmente los campos gauge carecen de las restricciones de simetría necesarias para constituir una teoría gauge. Una teoría gauge bien conocida, utilizada para describir estados Hall cuánticos fraccionarios es la teoría de Chern-Simons. La teoría de Chern-Simons es una teoría gauge topológica, en la cual el campo de gauge no tiene dinámica en ausencia de materia. Hemos utilizado acoplamiento óptico para diseñar interacciones quirales en un condensado de Bose-Einstein de átomos de potasio y codificar la dinámica de una reducción unidimensional de la teoría de Chern-Simons conocida como teoría BF quiral en la dinámica de la materia. Hemos observado solitones quirales y un campo eléctrico dependiente de la densidad. Nuestros resultados experimentales corresponden a la primera simulación cuántica exitosa de una teoría de gauge topológica en el continuo.

Los supersólidos se predijeron teóricamente hace más de cincuenta años y se han hecho realidad en los últimos años utilizando condensados de Bose-Einstein. En una segunda serie de experimentos, hemos aprovechado las propiedades de interacción únicas del potasio para crear un supersólido en un condensado de Bose-Einstein acoplado por transiciones Raman con mayor estabilidad y contraste que lo que es posible con otros átomos alcalinos. Utilizando técnicas de óptica de ondas de materia, hemos podido obtener por primera vez imágenes de las modulaciones de densidad características de un supersólido en un condensado de Bose-Einstein con acoplamiento Raman. Exploramos un régimen de parámetros previamente inaccesible y demostramos que el periodo de las franjas depende de la intensidad óptica, en contraste con una red óptica poco profunda en la cual el periodo de las franjas viene dado por el vector de onda de la red óptica.

Nuestro método para generar interacciones quirales efectivas amplía el campo de la simulación cuántica de teorías gauge para incluir teorías gauge topológicas en el continuo y supone un paso hacia la simulación de la teoría de Chern-Simons en dos dimensiones. Nuestra aplicación de la óptica de ondas de materia a la fase supersólida en un condensado de Bose-Einstein con acoplamiento Raman introduce una nueva herramienta para sondear los modos de Goldstone de baja energía y las propiedades de coherencia de fase del supersólido.

Resum

El control exquisit disponible en els experiments de gasos quàntics ultrafreds els converteix en un candidat ideal per la simulació quàntica de temes diversos que van des de la física d'altes energies i models anàlegs de gravetat quàntica fins a sistemes de matèria condensada fortament correlacionats i estats exòtics de la matèria. En aquesta tesi s'hi descriu l'ús d'acoblament Raman per dissenyar noves interaccions quirals i una relació de dispersió amb dos mínims amb condensats de Bose-Einstein de potassi, i s'exploten per realitzar una teoria gauge topològica i un estat exòtic de la matèria conegut com supersòlid, respectivament.

Una característica comuna de molts temes d'interès per la simulació quàntica és la possibilitat de descriure'ls des de la perspectiva d'una teoria gauge. L'acoblament Raman s'ha utilitzat per produir camps gauge artificials durant més d'una dècada, però normalment als camps gauge els manquen restriccions de simetria necessàries per construir una teoria gauge. Una teoria gauge ben coneguda que s'utilitza per descriure estats quàntics de Hall fraccionat és la teoria de Chern-Simons. La teoria de Chern-Simons és una teoria gauge topològica, de manera que no té dinàmica de camp gauge en absència de matèria. Aquí utilitzem acoblament òptic per dissenyar interaccions quirals en un condensat de Bose-Enstein d'àtoms de potassi i codificar la dinàmica d'una reducció unidimensional de la teoria de Chern-Simons coneguda com teoria BF quiral en la dinàmica de la matèria. Hem observat solitons quirals i un camp elèctric dependent de la densitat. Els nostres resultats experimentals representen la primera simulació quàntica amb èxit d'una teoria gauge topològica en el continu.

Els supersòlids van ser predits teòricament fa més de cinquanta anys i s'han fet realitat en els condensats de Bose-Einstein en els últims anys. En una segona sèrie d'experiments, hem aprofitat les propietats d'interacció úniques del potassi per crear un supersòlid en un condensat de Bose-Einstein amb acoblament Raman amb major estabilitat i contrast del que es pot aconseguir amb altres àtoms alcalins. Fent servir tècniques d'òptica d'ones de matèria hem obtingut per primera vegada imatges de les modulacions de densitat característiques d'un supersòlid en un condensat de Bose-Einstein amb acoblament Raman. Explorem un règim de paràmetres prèviament inaccessible i demostrem que el període de les franges depèn de la intensitat òptica, a diferencia d'una xarxa òptica poc profunda en la qual el període de les franges ve donat pel vector d'ona de la xarxa òptica.

El nostre mètode d'enginyeria d'interaccions quirals amplia el camp de la simulació quàntica de teories gauge incloent teories gauge topològiques en el continu i suposa un

pas endavant cap a la simulació de la teoria de Chern-Simons en dues dimensions. La nostra aplicació de la òptica d'ones de la matèria a la fase supersòlida en un condensat de Bose-Einstein amb acoblament Raman introdueix una nova eina per detectar els modes de Goldstone de baixa energia i les propietats de coherència de fase.

List of Publications

The work in this thesis has contributed to the following publications:

- J. Sanz, A. Frölian, C. S. Chisholm, C. R. Cabrera, and L. Tarruell, "*Interaction Control and Bright Solitons in Coherently Coupled Bose-Einstein Condensates.*" Physical Review Letters **128**, 013201 (2022).
- A. Frölian*, C. S. Chisholm*, E. Neri, C. R. Cabrera, R. Ramos, A. Celi, and L. Tarruell "*Realizing a 1D topological gauge theory in an optically dressed BEC.*" Nature **608**, 293 (2022).
- C. S. Chisholm, A. Frölian, E. Neri, R. Ramos, L. Tarruell, and A. Celi, "*Encoding a one-dimensional topological gauge theory in a Raman-coupled Bose-Einstein condensate.*" Physical Review Research **4**, 043088 (2022).

ORCID ID: 0000-0002-5599-0158

*These authors contributed equally: Anika Frölian, Craig S. Chisholm.

Acknowledgements

This thesis summarises the work accomplished during my time as a PhD student in the ultracold quantum gases group led by Prof. Dr. Leticia Tarruell at ICFO. Quantum gases experiments consist of several elements which have to work in unison to achieve a goal. Likewise, running a quantum gas experiment is a highly collaborative process requiring a whole team of people. Just like the mechanical and electrical elements of the machine itself, I could not have achieved the results presented in this thesis working entirely on my own and I therefore have a number of people to thank.

First of all, thanks go to Leticia for giving a chance to some guy from the other side of the world who wanted to do all of the applications and interviews online (long before that was a normal thing to do). Leticia has been a crucial source of guidance and advice while also giving me space to explore ideas and make mistakes on my own.

During my time in the group, I have had the pleasure of working directly along side and learning from a number people in the potassium lab. Dr. Cesar Cabrera helped me to learn how to operate the machine, made phone calls to arrange viewings for flats when I couldn't speak much Spanish, taught me some Spanish words which can't be found in conventional classes, and showed me the "second best" kebab shop in Barcelona (he never told me what the best one was). Dr. Julio Sanz also helped me with learning how to operate the machine, explained the correct way to eat *pan con tomate*, provided insights into Catalan culture, and was always ready to debate ideas until we got right to the bottom of a problem.

Dr. Anika Frölian is one of the people I have spent the most time working with. Anika and I have had moments feeling incredibly stupid but many more moments of learning and success. Outside of the lab, we have attempted to learn Spanish and spent a few great Sundays hiking around Catalunya. Dr. Ramón Ramos joined the group as a postdoc while Anika and I were in the middle of a crisis trying to recover the BEC and provided an unmatched calmness and optimism. I'm not sure if I spent more time in the lab with Ramón or with Anika but I do know that Ramón and I have realigned the MOT more times than I want to count. In spite of any issues we have had to solve, Ramón has always managed to stay focused on solutions which has helped to drive me to the end of this thesis.

Dr. Elettra Neri joined the group as a postdoc shortly after Ramón and brought with her a great deal of knowledge about physics and several strong opinions about food. Elettra managed to not physically attack me no matter how many sacrilegious things I said about or did to Italian cuisine and taught me several words in Italian which I'm sure Cesar would be proud of. Ana Pérez joined us as a Master's student

and it has been extremely satisfying to watch her confidence and skills grow so much in such a short time. I had the pleasure of supervising Sofie Castro Holbæk during a Summer project but her rate of picking up new things was so high that my supervision was almost unnecessary.

I would also like to express gratitude to the members of the strontium lab: Jonatan Höschele, Dr. Vasiliy Makhalov, Sandra Buob, and Dr. Toni Rubio for sharing of tools and ideas. A special mention to Toni for helping with setting up monitoring of environmental variables in the lab. Thanks also to Dr. Alessio Celi and Dr. Josep Cabedo for direct and substantial theory support, to Luca Cavicchioli and Martina D'Andrea for enjoyable Sunday lunches at the beach, and to all other former and current members of the group who I have benefited from in one way or another.

I am grateful to the quantum optics theory group led by Prof. Dr. Maciej Lewenstein for allowing me to use some of their computing resources for my numerical simulations. Thanks in particular to Dr. Valentin Kasper for helping me with setting up virtual machines.

Life at ICFO is made easier by a large network of support personnel. I would be surprised to hear of anyone who has worked at ICFO and hasn't been helped immensely by Anne Gstöttner and Ingrid Solsona Baya with all manners of bureaucracy. Magda Lara and Santi Martín keep the purchasing unit running like a well oiled machine. Xavi Menino and his team in the mechanical workshop always manage to produce pieces which function far better than the designs we give them. Likewise for José Carlos Cifuentes and his team in the electronics workshop, I especially want to mention Xavi Padilla for his talent for taking my hand drawn circuits and producing fully functioning and professional looking systems. The labs at ICFO would probably cease functioning without Carlos Dengra and his team. The IT department also plays an important role in keeping ICFO running, Oriol Bardes and Dr. Juli Céspedes i Capdevila deserve special mentions for borderline unreasonably prompt responses to emails about IT issues.

I have several people to thank back home in New Zealand as well. Thanks to Brad Ion, Callum Riddle, Phillip de Vos, Larissa Ou, Michael Cawte, and Tash de Jongh for keeping in contact with me after I moved so far away. Thanks to Prof. Blair Blakie for explaining Bessel transforms to me. Thanks to Prof. Niels Kjærgaard and Dr. Amita Deb for introducing me to the world of ultracold atoms many years ago. Thanks to my parents for supporting me in my decision to move away from home to study physics at university and then move even further away for a PhD in Barcelona.

Thanks to Leticia and Ramón for proofreading this thesis and assistance with translating the abstract to Spanish, to Toni for translating the abstract to Catalan, and Dr. Sarah Hirthe for proofreading the introduction. And finally, my sincerest thanks to Jelena Rakonjac for all that you do for me.

During my PhD I have received funding from the European Union's Horizon 2020 research and innovation programme under the Marie Skłodowska-Curie grant agreement No. 713729 (ICFOstepstone 2), the Deutsche Forschungsgemeinschaft Research Unit FOR2414, Project No. 277974659, and the European Union's European Research Council grant agreement No. 101003295 (SuperComp).

Contents

Chapter 1

Introduction

In 1982, Nobel laureate Richard Feynman proposed that in order to simulate the physical world, which is quantum mechanical, a probabilistic computer would be required in order to avoid resource requirements which grow exponentially with system size [1]. Furthermore, it was pointed out that the probabilistic computer must be governed by quantum mechanical probabilities in order to simulate a quantum system. In the last thirty years, a large number of research articles have been written on the subject of quantum computing and today limited quantum computers exist which are subject to constraints related to the number of qubits available and the noise which they are subjected to [2, 3].

A direct analogy may be drawn between the state of quantum computers today and the development of classical computers. Perhaps the first "computer" ever constructed was an analog device consisting of bronze gears created by the ancient Greeks for the purpose of modelling the motion of the sun and moon in order to predict solar eclipses [4]. Similar devices, such as Lord Kelvin's wheel based integrator used to predict tides [5], have been constructed in the more than two thousand years since. These devices, known as analog computers, represent one continuous quantity with another and are purpose built for a specific task. The earliest example of a digital computer is the abacus [3], which was built for computing sums of integers. The first all purpose digital computer was proposed by Charles Babbage around 1837 and was the inspiration for the first algorithm created by Ada Lovelace [3, 6].

The first working general purpose digital computer was the Electronic Numerical Integrator and Computer, constructed in 1945 [5]. In spite of the existence of general-purpose digital computers, analog computers were still widely used with a striking example being The Bay Model, a scale model of the San Francisco bay including tides which was used to predict (and prevent) the consequences of a proposed project to build two dams within the bay [7]. While analog computers were largely replaced by general purpose digital computers with the advent of the transistor in the 1960s, they were still used for decades after and today applications for analog computers are foreseen in the field of artificial intelligence [8].

The field of quantum simulation can be seen as the quantum version of analog

computers. In quantum simulation, a highly controllable quantum system may be used to engineer a Hamiltonian which mimics another quantum system which may be less easily controllable or where observables may be inaccessible [9–11]. A fully fledged quantum computer is still considered a long term goal and in the short term quantum simulation is an important tool for advancing the understanding of fundamental and complex quantum systems.

There are many different platforms being actively developed for quantum simulation, and each platform is complementary to all others. A model which is inaccessible in one platform may be straightforward to implement in another and where two platforms can access the same model, they can be used to validate each other once the physics is out of reach of classical computing methods [10]. A nonexhaustive list of current platforms for quantum simulation includes photonic circuits [12], polar molecules [13, 14], quantum dots [15], Rydberg atom arrays [16–19], superconducting qubits [20], trapped ions [21], and ultracold quantum gases [22–24]. This thesis focuses on ultracold quantum gases, specifically Bose-Einstein condensates, as a platform for quantum simulation.

1.1 Quantum Simulation with Bose-Einstein Condensates

Bose-Einstein condensates (BECs) were first produced in atomic gases of alkali atoms in 1995 [25–27]. The experimental realisation of atomic BECs opened up the possibility of experimentally accessible many body quantum systems with previously unprecedented control of both the strength and sign of interactions between particles [28–31] as well as the temperature and number of atoms in the BEC [32] and the potential energy landscape of the atoms [33–39]. A BEC is a macroscopic matterwave which can serve as a platform for the investigation of many body physics [32] and the high level of control which can be achieved in experimental platforms makes BECs an ideal candidate for quantum simulation [1].

An important research direction in quantum simulation across many platforms is the simulation of gauge theories [19, 40–48]. This is because dynamical gauge theories play a fundamental role in our understanding of interactions between elementary particles which are mediated by gauge bosons [49–51] and gauge theories can be applied to construct powerful effective descriptions of the low energy properties of condensed matter systems in the presence of strong correlations [52, 53]. Early experiments involving quantum simulation in BECs involved artificial rotation of atomic clouds to study superfluid properties, such as vortex formation [54–57], which was previously only accessible in superfluid helium where the vortex core size was too small to be observed optically but has been detected by trapping ions or electrons in the vortex cores [58, 59]. Additionally, rotating BECs were used to simulate charged particles in a uniform magnetic field [60, 61] and the link to superconductivity was discussed [56]. The realisation of multicomponent BECs consisting of mixtures of internal spin states of atoms [62] and later the coupling of internal spin states using laser light [63, 64]

enabled the simulation of charged particles in uniform vector potentials [65], magnetic fields [66], and electric fields [67] without the need for rotating traps.

A crucial difference between the first experiments using BECs to simulate charged particles in electromagnetic fields and real charged particles was the fact that since atoms are electrically neutral, they did not have any influence on the synthetic gauge fields which influenced their dynamics. In nature, gauge fields influence the motion of particles but the configuration of particles also influences the state of the gauge field, creating a feedback loop.

Recently, density-dependent gauge fields where the matter constrains the gauge field as well as the gauge field influencing the matter have been realised in BECs in optical lattices where the interatomic interactions and the lattice have been modulated simultaneously [68, 69]. Density-dependent gauge fields have also been realised in superconducting qubits [70], ultracold gases of fermionic atoms in optical lattices [45], and experiments with atoms in high-lying Rydberg states where interactions are governed by long range van der Waals forces [71]. These experiments simulating density-dependent gauge fields, though groundbreaking, lacked certain symmetry constraints which are required for the quantum simulation of gauge theories.

Another important area of research in the field of quantum simulation with BECs, and ultracold quantum gases in general, is the use of optical lattices to simulate solid systems and light in nonlinear materials [22, 72]. A textbook example of condensed matter physics simulated with a BEC in an optical lattice is the superfluid to Mott insulator transition [73] where the system transitions from a superfluid state with all particles delocalised across the lattice to a state where particles are pinned to lattice sites with no phase coherence across the lattice. Mott insulator states have also been realised in fermionic systems [74, 75] and ultracold atoms in optical lattices can also be used to demonstrate the emergence of different physics appearing in different geometries [76].

An artificial gauge field generated by optically coupling internal states of atoms in a one-dimensional optical lattice can be formulated as a two-dimensional lattice with a "synthetic" dimension consisting of the discrete internal states of the atoms [77]. The flux piercing the synthetic two-dimensional lattice is controlled by the optical coupling and can be tuned to produce both bulk dynamics and chiral skipping orbits corresponding to the edge states of quantum Hall systems [78–80].

Other aspects of quantum simulation with ultracold atoms include but are not limited to the study of low dimensional systems [81–86], out of equilibrium dynamics [87–94], the study of inflationary cosmology [95, 96], and the realisation of exotic states of matter such as self-bound quantum liquid droplets [97–101], and supersolids, which combine the properties of solids and superfluids without the introduction of an optical lattice [102–104]. Supersolidity has been explored in BECs coupled to optical cavities [105, 106], BECs with dipolar interactions [107–110], and BECs with optically coupled internal states [111, 112].

The focus of this thesis is the use of optical coherent coupling as a platform for the quantum simulation of a so-called topological gauge theory known as the chiral BF theory [113–116] and for the realisation of a supersolid [102–104, 117].

1.2 Gauge Theories

When two different quantum states have the same properties, there is a symmetry between those two states. When two different labels are given to the same state then there is a gauge symmetry between the two labels. There is a distinction between gauge symmetry and symmetry in that a gauge symmetry describes changes in labels applied to a state and can never be broken because it is not a symmetry in the conventional sense [52].

Gauge transformations are mathematical mappings between two labels of the same state. All of the physical states and operators of a system described by a gauge theory must be gauge invariant, meaning that a gauge transformation does not change physical observables [52]. Gauge invariance which applies at every point in space and time is sometimes referred to as a local symmetry constraint. Local symmetry constraints exclude almost all possible configurations in Hilbert space and can be used to simplify redundant equations of motion by imposing a choice of gauge.

The most well known example of a gauge theory is quantum electrodynamics, also known as Maxwell theory, which describes the coupling of charged particles to electromagnetic gauge fields. Maxwell theory is an example of a dynamical gauge theory, meaning that the electromagnetic gauge fields are matter-dependent but have propagating degrees of freedom, electromagnetic waves, even in the absence of matter. Another class of gauge theory, which frequently emerges in condensed matter systems, is a topological gauge theory. Topological gauge fields do not have propagating degrees of freedom in the absence of matter and instead gain their dynamics from coupling to matter through a local conservation law [118].

An example of a topological gauge theory which arises as an effective theory in condensed matter systems is the Chern-Simons theory. One of the many applications of Chern-Simons theory is the effective description of fractional quantum Hall states [52]. In a fractional quantum Hall state, a strongly correlated gas of electrons is confined to a two-dimensional plane in the presence of a magnetic field perpendicular to the plane [52]. Following Wilczek's formulation of flux attachment [119–121], the strongly correlated electrons and the magnetic field are replaced by a gas of weakly interacting composite particles consisting of integer numbers of magnetic flux quanta attached to massive particles. The Chern-Simons theory describes the coupling of the particles and the magnetic flux which is attached to them.

1.2.1 Quantum Simulation of Gauge Theories

The simulation of the real time dynamics of many gauge theories is out of reach for classical computing methods and is a prime example of the type of problem Richard Feynman envisioned solving using quantum simulation [1]. Some ambitious goals in the field of quantum simulation of gauge theories include accessing both equilibrium and out of equilibrium properties of the phase diagram of quantum electrodynamics [122] and quark-gluon plasma [123]. Additionally, engineering gauge theories emerging in condensed matter physics in highly controllable quantum systems can provide access

to exotic excitations without the need for strongly correlated systems [124].

A common type of gauge theory employed in quantum simulation with ultracold gases is a lattice gauge theory. Lattice gauge theories were introduced by Wilson to regularise the ultraviolet divergences in quantum electrodynamics by replacing continuous space(time) with a lattice of discrete points which cuts off ultraviolet divergences at wavevectors greater than the reciprocal lattice wavevector [125].

Several experimental works on the quantum simulation of lattice gauge theories have examined the Schwinger model, which is a discretised version of quantum electrodynamics in one dimension. The Schwinger model has been implemented in a number of quantum simulation platforms including trapped ion arrays [40, 42, 126], Rydberg atom arrays [19, 127] and ultracold atoms in optical lattices [47, 128, 129]. Other works have demonstrated the engineering of gauge symmetries and present pathways to quantum simulation of lattice gauge theories once independent sites can be linked and sources of decoherence can be overcome. These experiments constitute building blocks for quantum simulation in higher dimensions and of more complex gauge theories [44–46, 130]. Progress has also been made towards the quantum simulation of gauge theories describing anyons (exotic particles which have neither bosonic nor fermionic exchange statistics) [68, 69, 71] although these experiments did not enforce the local conservation laws required to implement local gauge invariance.

Although synthetic gauge fields for ultracold atoms were introduced in the continuum, the quantum simulation of gauge theories in the continuum has received little attention in comparison to lattice gauge theories. A seminal proposal by Edmonds *et al.* [131], which will be discussed in Ch. 4, has proposed the use of optical coupling of a BEC with properly chosen interactions to realise a one-dimensional reduction of the Chern-Simons theory known as the chiral BF theory. We have expanded upon the proposal of Edmonds *et al.* [131] and shown that the key ingredient is creating interactions between atoms which can be tuned depending on the momentum of the atoms [118, 132]. An interesting fact about the experimental realisation of the tunable interactions required to simulate the chiral BF theory is that the same tunable interactions can be used to study a supersolid state by simply changing the optical coupling regime.

1.3 Supersolids

A supersolid is a remarkable phase of matter which combines the opposing concepts of a conventional solid such as crystalline order (spontaneously broken translational symmetry) and deformation under shear forces with those of a superfluid such as flow without dissipation [117]. The archetypal example of a superfluid is liquid ^{4}He at very low temperature [133, 134]. A superfluid carries no entropy and flows without dissipation [117]. The zero entropy condition means that any finite temperature superfluid system always has a superfluid and a normal fluid component since a finite temperature system necessarily has entropy which must be carried by the normal component [117]. The existence of the two components gives rise to "second sound" in the fluid with heat transfer conducted by wave-like motion in the normal fluid component [135].

In three-dimensional systems, superfluidity is accompanied by Bose-Einstein condensation [117] but there is no unique relationship between a BEC and a superfluid [32]. In two dimensions, an interacting Bose gas of infinite extent can exhibit superfluidity described by the Berezinskii-Kosterlitz-Thouless theory but BEC is not possible [136] and in an ideal gas, a BEC is not a superfluid [32]. A superfluid requires off-diagonal long range order, meaning that all particles are indistinguishable and can trade place with each other. The indistinguishability of particles in a superfluid means that each particle can be seen as being completely delocalised throughout the entire system [117].

Supersolids were predicted independently in three proposals made in 1969 and 1970 [102–104]. The formation of a supersolid requires both the spontaneous long range order of a solid and the delocalisation of particles associated with a superfluid. These two requirements must be fulfilled in a homogeneous manner, not as the coexistence of solidity and superfluidity in different parts of the system [117]. An important feature of a supersolid is that the translational symmetry must be broken spontaneously. Superfluid ^{4}He adsorbed on a layer of graphite [137] and a gaseous BEC in an optical lattice formed by interfering laser beams [33–36] both exhibit long range order but it is externally imposed and these systems cannot be considered to be supersolids [117].

Superfluid helium has a roton-maxon spectrum, meaning that there is a local minimum in the dispersion relation at nonzero momentum [138]. Supersolidity is predicted to occur when the roton becomes soft [139–141]. That is, when the energy of the roton minimum is below a critical value. In spite of pessimistic estimates on the feasibility of detecting supersolidity in samples of solid helium [142], the theoretical proposals sparked many experimental efforts [117] which were buoyed by more promising theoretical estimates of the superfluid fraction in a sample of solid ^{4}He in 1976 and 1977 [143, 144]. In 2004 Kim and Chan reported a reduction in the rotational inertia of a torsional oscillator filled with solid ^{4}He which was initially interpreted as evidence of supersolidity [145, 146] but later found to be the result of bulk solid properties of ^{4}He [147]. In spite of continuing experimental interest, no conclusive evidence of supersolidity in helium samples has been reported to date [148].

Due to the highly controllable nature of ultracold quantum gases, BECs started to garner theoretical interest as a platform for supersolidity. The diluteness of typical atomic BECs and their characteristic short range contact interactions seem to rule out spontaneous long range density modulations [149]. However, theoretical proposals in 2003 suggested that the long range interactions in BECs composed of atoms with strong magnetic dipole moments could be used to create a roton-maxon spectrum similar to that of superfluid helium [150, 151]. Roton-maxon spectra were also predicted and measured for BECs under the influence of Raman coupling [63, 152–154] and for BECs coupled to optical cavities [155, 156]. Indeed, BECs have proven to be a powerful platform for the observation of supersolidity, with supersolid features reported in experiments with BECs in optical cavities [105], in the presence of synthetic spin-orbit coupling [111, 112, 157], and with dipolar interactions [107–110].

Spontaneous symmetry breaking occurs when the Hamiltonian of a system is invariant under a certain symmetry operation but the groundstate of the system is not [158, 159]. Continuous symmetry breaking gives rise to Goldstone [160] and

Higgs [161] modes, which are gapless and massive excitations, respectively. A key feature of supersolids is the existence of two Goldstone modes arising from the spontaneous breaking of two continuous symmetries which correspond to a solid-like phonon and a softer collective excitation [162]. The two modes are related to the solid and superfluid properties of breaking of translational invariance and gauge invariance and correspond to two distinct speeds of sound. In the case of the supersolid, one of the collective Goldstone excitations manifests as a zero energy translation of density modulations [106, 158, 159, 163]. Additionally, the Higgs mode corresponds to oscillations of the density modulation contrast [106, 164].

In comparison to dipolar systems, the fringe spacing of the density modulation in a supersolid under the influence of Raman coupling is generally much smaller. The small fringe spacing is usually below the optical diffraction limit [111, 112] which makes direct observation of the Goldstone and Higgs modes challenging. We have employed matterwave optics techniques to magnify the fringe spacing of a Raman coupled supersolid and image the stripes. The ability to image the density modulation of the supersolid paves the way towards direct observation of the Goldstone and Higgs modes.

1.4 Thesis Outline

In this thesis, I will describe the use of atomic Bose-Einstein condensates (BECs) of ^{39}K and ^{41}K where two internal spin states with tunable interactions are coherently coupled using an optical field. In particular, I will focus on the situation where the coherent coupling of the BEC links the spin composition to the momentum of the atoms [63, 65, 67, 165]. The coupling of spin to momentum provides a tool for tuning interactions in an unconventional manner. In a regime where the optical coupling is the dominant energy scale, we realise the quantum simulation of the chiral BF theory, which is a topological gauge theory in the continuum. For weak optical coupling we realise a supersolid state known as the stripe phase [67, 111, 112, 154, 157, 166–168] and image the characteristic density modulations for the first time by means of matterwave optics.

In Ch. 2, I will give a basic introduction to BECs in atomic gases including both experimental techniques and theoretical descriptions. In Ch. 3, I will introduce coherent coupling as a means of interaction control in BECs. In Ch. 4, I will show how the dynamics of a topological gauge field can be encoded in the dynamics of matter to obtain a Hamiltonian which is amenable to quantum simulation. In Ch. 5, I will present experimental and numerical results of the quantum simulation of a topological gauge theory known as the chiral BF theory. In Ch. 6, I will present a theoretical framework and numerical simulations for supersolid states which will be explored experimentally in Ch. 7. Finally, in Ch. 8, I will provide some concluding remarks and outline potential future research directions.

Chapter 2

Background

The results presented in this thesis are built upon tuning the interactions in Bose-Einstein condensates with optical fields. In this chapter, I will introduce the theory of Bose-Einstein condensation in atomic gases and I will cover the experimental route to produce a BEC and the experimental techniques used to probe it. The construction of the experimental apparatus has been carried out by a number of people and has been presented in the PhD theses of Dr. Cesar Cabrera [169] and Dr. Julio Sanz [170].

2.1 Bose-Einstein Condensates

In this thesis, I will focus only on Bose-Einstein condensates (BECs) in atomic gases, although BEC has been demonstrated in other systems including molecules of fermionic atoms [171–173], magnon [174] and exciton-polariton [175] quasiparticles, and photons in optical cavities [176]. Since the first demonstration of BEC in atomic vapours of ^{87}Rb [25], ^{23}Na [26], and ^{7}Li [27] in 1995, the list of atomic species in which BEC has been produced has grown to include ^{1}H, ^{4}He* (in a metastable electronic excited state), ^{39}K, ^{41}K, ^{52}Cr, ^{84}Sr, ^{85}Rb, ^{86}Sr, ^{88}Sr, ^{133}Cs, ^{151}Eu, ^{160}Dy, ^{162}Dy, ^{164}Dy, ^{166}Er, ^{168}Er, ^{169}Tm, ^{170}Yb, ^{174}Yb, and ^{176}Yb [98, 177–186].

The apparatus used for experiments in this thesis was constructed to cool the three naturally occurring isotopes of potassium: ^{39}K, ^{40}K, and ^{41}K [169, 170]. Potassium is an alkali atom belonging to the first group of the periodic table and possessing one valence electron. The ground state electronic configuration is $[\mathrm{Ar}]4^2\mathrm{S}_{1/2}$. The isotopes ^{39}K and ^{41}K both have half-odd integer nuclear spin, $I = 3/2$ [187], owing to the odd number of nucleons which makes the total angular momentum, F, integer valued [188] and these two isotopes are bosonic.

In potassium BECs, like other alkali atoms, the dominant interaction is a two-body contact interaction, characterised by the coupling constant $g_s = 4\pi\hbar^2 a_s/m$ where $\hbar$ is the reduced Planck constant, a_s is the s-wave scattering length, and m is the mass of the atom. The s-wave scattering length is usually specified in units of the Bohr radius, a_0, and depends on the atomic species and internal state. The value of a_s can be tuned by adjusting the bias magnetic field in the proximity of a Feshbach resonance [28–31].

The Hamiltonian of the BEC in second quantised form is [177, 189]

$$\hat{H} = \int \mathrm{d}^3\mathbf{r}\hat{\phi}^\dagger(\mathbf{r}) \left[-\frac{\hbar^2}{2m}\nabla^2 + V(\mathbf{r}) + \frac{g_s}{2}\hat{\phi}^\dagger(\mathbf{r})\hat{\phi}(\mathbf{r}) \right] \hat{\phi}(\mathbf{r}) \tag{2.1}$$

where $\hat{\phi}^\dagger(\mathbf{r})$ and $\hat{\phi}(\mathbf{r})$ are the bosonic creation and annihilation field operators for a particle at position $\mathbf{r} = x\mathbf{e}_1 + y\mathbf{e}_2 + z\mathbf{e}_3$ and $V(\mathbf{r})$ is a conservative trapping potential. Here, $\mathbf{e}_1$, $\mathbf{e}_2$, and $\mathbf{e}_3$ are the unit vectors pointing along the x-, y-, and z-axes, respectively. From the Hamiltonian, we construct the action

$$\hat{S} = \int \hat{\mathcal{L}}\mathrm{d}^3\mathbf{r}\mathrm{d}t = \int \left[\int i\hbar\hat{\phi}^\dagger\partial_t\hat{\phi}\mathrm{d}^3\mathbf{r} - \hat{H} \right] \mathrm{d}t \tag{2.2}$$

where $\hat{\mathcal{L}}$ is the Lagrangian density. The Euler-Lagrange equation of motion for the field operators can be constructed according to Noether's theorem [190]

$$\frac{\delta\hat{\mathcal{L}}}{\delta\hat{\phi}^\dagger} = \frac{\partial}{\partial x}\frac{\delta\hat{\mathcal{L}}}{\delta\partial_x\hat{\phi}^\dagger} + \frac{\partial}{\partial y}\frac{\delta\hat{\mathcal{L}}}{\delta\partial_y\hat{\phi}^\dagger} + \frac{\partial}{\partial z}\frac{\delta\hat{\mathcal{L}}}{\delta\partial_z\hat{\phi}^\dagger} + \frac{\partial}{\partial t}\frac{\delta\hat{\mathcal{L}}}{\delta\partial_t\hat{\phi}^\dagger} \tag{2.3}$$

where $\delta/\delta\cdot$ is a functional derivative.

The field operators can be decomposed in the form $\hat{\phi} = \phi + \delta\hat{\phi}$ where $\phi(\mathbf{r}, t)$ is a mean-field wavefunction representing the macroscopically occupied state of the BEC and $\delta\hat{\phi}$ represents quantum fluctuations [177, 189]. For atomic densities relevant in experiments presented in this thesis, correlations between atoms are weak and the quantum fluctuations can generally be neglected. The Euler-Lagrange equation gives an equation of motion for the mean-field wavefunction known as the Gross-Pitaevskii equation (GPE)

$$i\hbar\frac{\partial}{\partial t}\phi(\mathbf{r}, t) = \left[-\frac{\hbar^2}{2m}\nabla^2 + V(\mathbf{r}) + g_s|\phi(\mathbf{r}, t)|^2 \right] \phi(\mathbf{r}, t). \tag{2.4}$$

The normalisation condition is $\int |\phi|^2\mathrm{d}^3\mathbf{r} = N$, where N is the number of particles.

The nonlinearity stemming from the contact interactions in the GPE means that the wave function, $\phi(\mathbf{r}, t)$, does not have analytic solutions in general and must be determined numerically. We can write the groundstate condensate wavefunction in polar form, $\phi(\mathbf{r}, t) = \sqrt{n(\mathbf{r})}\exp(-i\mu t/\hbar)$ where $n(\mathbf{r})$ is the mean-field density, which is real and positive, and μ is the chemical potential of the BEC, which is also a Lagrange multiplier ensuring the normalisation condition in the Euler-Lagrange equation [177]. Substituting the polar form expression into Eq. 2.4, we have an eigenvalue problem

$$\mu\sqrt{n(\mathbf{r})} = \left[-\frac{\hbar^2}{2m}\nabla^2 + V(\mathbf{r}) + g_s n(\mathbf{r}) \right] \sqrt{n(\mathbf{r})}. \tag{2.5}$$

For large N, the dominant energy scales are the trapping potential and the interactions. In this case, we can neglect the kinetic energy term which is also known as the quantum pressure and find

$$n(\mathbf{r}) = \max\left[\frac{\mu - V(\mathbf{r})}{g_s}, 0 \right] \tag{2.6}$$

which is the Thomas-Fermi approximation [177, 189]. If $V(\mathbf{r})$ is a box with volume V, then the density is simply $n(\mathbf{r}) = N/V \equiv \bar{n}$ and the chemical potential is $\mu = g_s N$.

A more common scenario in experiments is a trapping potential approximated by a three-dimensional anisotropic harmonic oscillator, $V(\mathbf{r}) = m\left(\omega_x^2 x^2 + \omega_y^2 y^2 + \omega_z^2 z^2\right)/2$. In this case, the density is

$$n(\mathbf{r}) = \frac{\mu}{g_s}\max\left[1 - \left(\frac{x}{\sigma_{T,x}}\right)^2 - \left(\frac{y}{\sigma_{T,y}}\right)^2 - \left(\frac{z}{\sigma_{T,z}}\right)^2, 0\right] \tag{2.7}$$

where $\sigma_{T,j} = \sqrt{2\mu/(m\omega_j^2)}$ for $j = x, y, z$. The chemical potential is

$$\mu = \left(\frac{15 g_s m^{3/2} \bar{\omega}^3 N}{16\sqrt{2}\pi}\right)^{2/5} \tag{2.8}$$

where $\bar{\omega} = (\omega_x \omega_y \omega_z)^{1/3}$ is the geometric mean trapping frequency. The Thomas-Fermi density profile in a harmonic oscillator potential has mean density $n_{\text{mean}} = 3N/(4\pi\sigma_{T,x}\sigma_{T,y}\sigma_{T,z})$ and peak density $n_{\text{peak}} = 5n_{\text{mean}}/2$.

Another situation where we can find an analytic expression for the groundstate wavefunction is in a (quasi)one-dimensional geometry. If $\omega_y, \omega_z \gg \omega_x$ such that transverse motion is frozen out, we can assume a Gaussian transverse density profile such that [191, 192] $\phi(\mathbf{r}, t) = \varphi\left[y, z; w_y(x), w_z(x)\right] f(x, t)$ where

$$\varphi\left[y, z; w_y(x), w_z(x)\right] = \frac{1}{\sqrt{\pi w_y(x) w_z(x)}} \exp\left[-\frac{y^2}{2w_y(x)^2} - \frac{z^2}{2w_z(x)^2}\right]. \tag{2.9}$$

Note that $\int |f(x,t)|^2 \mathrm{d}x = N$ because $\int |\varphi\left[y, z; w_y(x), w_z(x)\right]|^2 \mathrm{d}y\mathrm{d}z = 1$. In the weakly interacting limit, we have $a_s |f(x,t)|^2 \ll 1 \forall x$ and the transverse widths correspond to the harmonic oscillator lengths $w_j(x) = \sqrt{\hbar/(m\omega_j)}$ for $j = y, z$ [191, 192].

Integrating out the transverse degrees of freedom in Eq. 2.4 gives

$$i\hbar\frac{\partial}{\partial t} f(x,t) = \left[-\frac{\hbar^2}{2m}\frac{\partial^2}{\partial x^2} + \frac{1}{2}m\omega_x^2 x^2 + 2\hbar\sqrt{\omega_y\omega_z}a_s N|f(x,t)|^2\right] f(x,t). \tag{2.10}$$

In the limit $\omega_x/\sqrt{\omega_y\omega_z} \to 0$, Eq. 2.10 can be solved analytically. For $a_s/a_0 < 0$ we have

$$f(x,t) = \frac{1}{\sqrt{2\sigma_s}}\mathrm{sech}\left(\frac{x}{\sigma_s}\right)\exp\left(-i\mu t/\hbar\right) \tag{2.11}$$

where $\sigma_s = -\hbar/(\sqrt{\omega_y\omega_z}a_s N m)$ and $\mu = -\omega_y\omega_z N^2 a_s^2 m/2$. This solution is referred to as a bright soliton [193, 194] which is a dispersionless matter wave packet where the attractive interactions between particles are compensated by the repulsive quantum pressure (the kinetic energy). The size of the bright soliton decreases for increasing atom number and above a critical atom number, the soliton becomes unstable and collapses under the mean-field attraction [195].

Bright solitons can also be prepared with repulsive interactions in the presence of a periodic potential by preparing a BEC at the edge of the Brillouin zone. At the edge of the Brillouin zone, the lowest energy band has negative effective mass which makes

the quantum pressure attractive so that it can compensate the repulsive interactions and form a dispersionless matterwave packet. Since the edge of the Brillouin zone corresponds to the minimum energy gap between the lowest energy band and first excited band, these solitons are referred to as gap bright solitons [196].

Another type of solution to Eq. 2.10 is a dark soliton, where the dispersionless wave packet is an absence of matter in a finite density background [197–200]. A dark soliton requires $a_s/a_0 > 0$ and the density dip is accompanied by a π phase jump in the condensate wave function. Both bright and dark solitons are unstable in two and three dimensions so in experimental realisations, the interaction energy must remain below $\hbar\omega_r$ where $\omega_r \equiv \omega_y \sim \omega_z$ [195, 201, 202].

2.1.1 Mixtures of Bose-Einstein condensates

Extending the second quantised Hamiltonian in Eq. 2.1 to a mixture of two or more BECs is straightforward. For concreteness, we consider a homonuclear mixture of atoms in different Zeeman sublevels (see Sec. 2.2). We consider a BEC in the presence of a magnetic bias field such that the atoms can occupy two internal states and collisions which change the occupancy of those two states are energetically forbidden. We label the states $|\uparrow\rangle$ and $|\downarrow\rangle$ and the energy difference between the states is $\hbar\omega_0$. We chose $|\downarrow\rangle$ to be the lower energy state and set its energy to zero. We consider state-dependent trapping potentials, $V_\uparrow(\mathbf{r})$ and $V_\downarrow(\mathbf{r})$, such that the second quantised Hamiltonian is [177]

$$\hat{H} = \sum_{\sigma=\uparrow,\downarrow} \int \mathrm{d}^3\mathbf{r}\hat{\phi}^\dagger_\sigma(\mathbf{r}) \left[-\frac{\hbar^2}{2m}\nabla^2 + V_\sigma(\mathbf{r})\right] \hat{\phi}_\sigma(\mathbf{r}) + \hbar\omega_0 \int \mathrm{d}^3\mathbf{r}\hat{\phi}^\dagger_\uparrow(\mathbf{r})\hat{\phi}_\uparrow(\mathbf{r}) + \frac{1}{2}\sum_{\sigma_1,\sigma_2=\uparrow,\downarrow} g_{\sigma_1\sigma_2} \int \mathrm{d}^3\mathbf{r}\hat{\phi}^\dagger_{\sigma_1}(\mathbf{r})\hat{\phi}^\dagger_{\sigma_2}(\mathbf{r})\hat{\phi}_{\sigma_1}(\mathbf{r})\hat{\phi}_{\sigma_2}(\mathbf{r}) \quad (2.12)$$

where $\hat{\phi}^\dagger_\sigma(\mathbf{r})$ ($\hat{\phi}_\sigma(\mathbf{r})$) is the creation (annihilation) field operator for a particle in state $|\sigma\rangle$ for $\sigma = \uparrow, \downarrow$. We have defined the intrastate coupling constants, $g_{\uparrow\uparrow}$ and $g_{\downarrow\downarrow}$, which characterise collisions between two particles in the same state and the interstate coupling constant, $g_{\uparrow\downarrow} = g_{\downarrow\uparrow}$ which characterises collisions between two atoms in different states. The interstate and intrastate s-wave scattering lengths are given by $a_{\sigma_1\sigma_2} = mg_{\sigma_1\sigma_2}/(4\pi\hbar^2)$ for $\sigma_1, \sigma_2 = \uparrow, \downarrow$.

Extending Eq. 2.12 to more than two states is straightforward, in this thesis I will present results only for BECs with two spin components. The generalisation of the Euler-Lagrange equation to a set of Euler-Lagrange equations for the two-component system is

$$\frac{\delta\hat{\mathcal{L}}}{\delta\hat{\phi}^\dagger_\sigma} = \frac{\partial}{\partial x}\frac{\delta\hat{\mathcal{L}}}{\delta\partial_x\hat{\phi}^\dagger_\sigma} + \frac{\partial}{\partial y}\frac{\delta\hat{\mathcal{L}}}{\delta\partial_y\hat{\phi}^\dagger_\sigma} + \frac{\partial}{\partial z}\frac{\delta\hat{\mathcal{L}}}{\delta\partial_z\hat{\phi}^\dagger_\sigma} + \frac{\partial}{\partial t}\frac{\delta\hat{\mathcal{L}}}{\delta\partial_t\hat{\phi}^\dagger_\sigma} \quad (2.13)$$

for $\sigma = \uparrow, \downarrow$. The mean-field coupled GPEs are

$$i\hbar\frac{\partial}{\partial t}\phi_\uparrow = \left[-\frac{\hbar^2}{2m}\nabla^2 + V_\uparrow(\mathbf{r}) + \hbar\omega_0 + g_{\uparrow\uparrow}|\phi_\uparrow|^2 + g_{\uparrow\downarrow}|\phi_\downarrow|^2\right]\phi_\uparrow$$

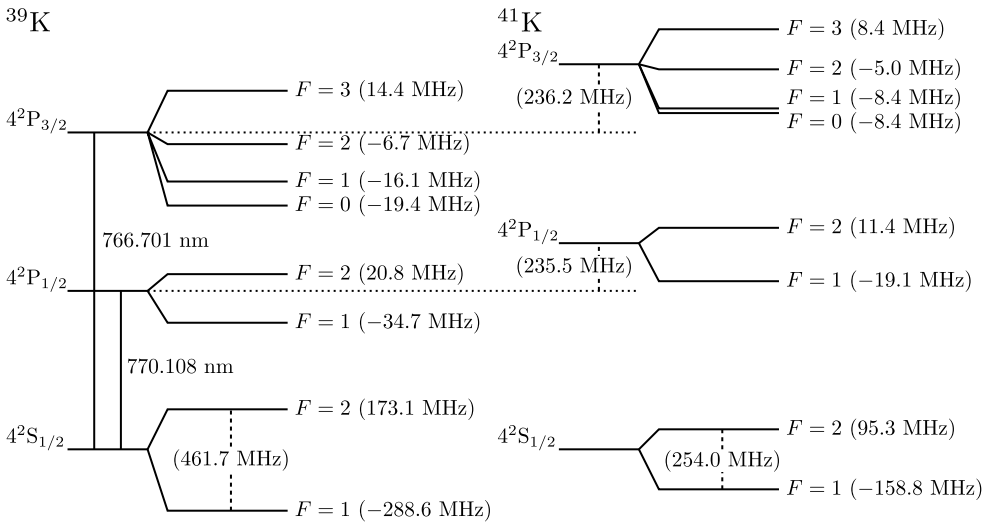

Figure 2.1: Energy level diagram of ^{39}K and ^{41}K with hyperfine structure. Level spacings are not to scale. This figure is based on Figure 2 from Ref. [187].

and

$$i\hbar\frac{\partial}{\partial t}\phi_\downarrow = \left[-\frac{\hbar^2}{2m}\nabla^2 + V_\downarrow(\mathbf{r}) + g_{\downarrow\downarrow}|\phi_\downarrow|^2 + g_{\uparrow\downarrow}|\phi_\uparrow|^2\right]\phi_\downarrow. \tag{2.14}$$

Under the assumption that state changing collisions are forbidden, the number of atoms in each state, $N_\sigma = \int |\phi_\sigma|^2 \mathrm{d}^3\mathbf{r}$, and the total number of particles, $N = N_\uparrow + N_\downarrow$, are conserved independently. This means that the two states have independent chemical potentials and we need both intrastate coupling constants to be positive for the mixture to be stable against mean-field collapse [177]. For a uniform state-independent trapping potential, $V_\uparrow = V_\downarrow$, the two density profiles overlap for $g_{\uparrow\downarrow} < \sqrt{g_{\uparrow\uparrow}g_{\downarrow\downarrow}}$ and phase separate otherwise [177, 203]. For $g_{\uparrow\downarrow} < -\sqrt{g_{\uparrow\uparrow}g_{\downarrow\downarrow}}$ the system is unstable against collapse in the mean-field limit [177]. The stability requirement $-\sqrt{g_{\uparrow\uparrow}g_{\downarrow\downarrow}} < g_{\uparrow\downarrow} < \sqrt{g_{\uparrow\uparrow}g_{\downarrow\downarrow}}$, is slightly modified in the presence of a trap [203, 204] but is a sufficient guideline for our purposes. For $g_{\uparrow\downarrow} < -\sqrt{g_{\uparrow\uparrow}g_{\downarrow\downarrow}}$, the mixture may be stabilised against collapse by beyond mean-field corrections and form a self-bound liquid droplet [99, 100, 205].

2.2 Energy levels of Potassium

As previously mentioned, all experiments in this thesis are performed with the naturally occurring bosonic isotopes of potassium, ^{39}K and ^{41}K. Both isotopes have nuclear spin $I = 3/2$ so they have the same level structure with energy level differences due to isotope shift [188]. Figure 2.1 shows the hyperfine structure for both isotopes in the groundstate $4^2\mathrm{S}_{1/2}$ manifold as well as the first two electronic excited state manifolds, $4^2\mathrm{P}_{1/2}$ and $4^2\mathrm{P}_{3/2}$, which correspond to the optical D1 and D2 transitions, respectively.

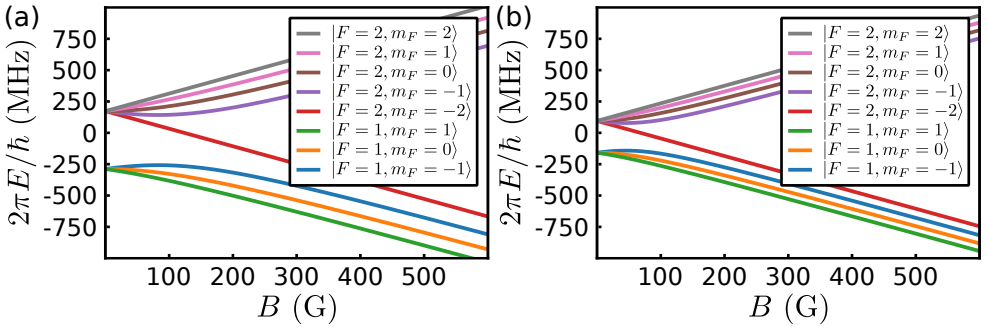

Figure 2.2: Energy levels in the groundstate manifold of (a) ^{39}K and (b) ^{41}K.

In the presence of a weak external magnetic field, the total angular momentum, F, and its projection onto the quantisation axis, m_F, represent eigenstates of the atomic Hamiltonian and are therefore good quantum numbers [206]. For magnetic fields where the Zeeman splitting of sublevels is greater than the hyperfine shift, F and m_F are not good quantum numbers because the nuclear spin is polarised by the magnetic field and states should instead be written in the $|I, J, m_I, m_J\rangle$ basis [188, 207].

When the total electronic angular momentum, J, is equal to 1/2, as is the case in the groundstate manifold of alkali atoms, the energies of the Zeeman sublevels can be determined using the Breit-Rabi formula [206, 208]

$$E(B) = -\frac{A_{\rm hf}}{4} + g_I \mu_B m_F B \pm \frac{A_{\rm hf}\,(I+1/2)}{2}\left(1 + \frac{4m_F\zeta}{2I+1} + \zeta^2\right)^{1/2} \tag{2.15}$$

where $\zeta = (g_J - g_I)\mu_B B/\left[A_{\rm hf}\,(I+1/2)\right]$, $A_{\rm hf}$ is the magnetic dipole constant, g_I and g_J are the Landé g-factors corresponding to the nuclear angular momentum and the total electronic angular momentum, μ_B is the Bohr magneton, and B is the magnitude of the external magnetic field. The value of m_F corresponds to low field where it is a good quantum number but the formula is valid when m_F is no longer a good quantum number.

If $J \neq 1/2$, the energy levels should be determined by diagonalising the Hamiltonian [206]

$$H_{\rm hf} = \frac{A_{\rm hf}}{\hbar^2}\mathbf{I}\cdot\mathbf{J} + \frac{B_{\rm hf}}{\hbar^2}\frac{3\,(\mathbf{I}\cdot\mathbf{J})^2 + 3\mathbf{I}\cdot\mathbf{J}/2 - \mathbf{I}^2\mathbf{J}^2}{2I\,(2I-1)\,J\,(2J-1)} \tag{2.16}$$

where $B_{\rm hf}$ is the electric quadrupole constant. Values of $A_{\rm hf}$ for the manifolds $4^2{\rm S}_{1/2}$, $4^2{\rm P}_{1/2}$, and $4^2{\rm P}_{3/2}$ as well as the value of $B_{\rm hf}$ for the manifold $4^2{\rm P}_{3/2}$ and the value of g_I for the $4^2{\rm S}_{1/2}$ manifold for both ^{39}K and ^{41}K are given in Tab. 2.1. The total electronic g-factor in the $4^2{\rm S}_{1/2}$ manifold is $g_J = 2.00229421(24)$ [187]. Figure 2.2 shows the energies of the Zeeman sublevels in the groundstate manifold in (a) ^{39}K and (b) ^{41}K. We can see that although F and m_F are not good quantum numbers for fields $B \gtrsim 200$ G, the energies of the states never cross and we can unambiguously label the

states as $|F, m_F\rangle$ using the low field quantum numbers[1], which I will do throughout this thesis.

Table 2.1: Magnetic dipole, $A_{\rm hf}$, and electric quadrupole, $B_{\rm hf}$, constants and nuclear g-factor for ^{39}K and ^{41}K. Values are taken from Ref. [187].

Manifold	Quantity	^{39}K	^{41}K
$4^2S_{1/2}$	$2\pi A_{\rm hf}/\hbar$	230.8598601(3) MHz	127.0069352(6) MHz
$4^2P_{1/2}$	$2\pi A_{\rm hf}/\hbar$	27.775(42) MHz	15.245(42) MHz
$4^2P_{3/2}$	$2\pi A_{\rm hf}/\hbar$	6.093(25) MHz	3.363(25) MHz
$4^2P_{3/2}$	$2\pi B_{\rm hf}/\hbar$	2.786(71) MHz	3.351(71) MHz
$4^2S_{1/2}$	g_I	-0.00014193489(12)	-0.00007790600(8)

2.3 Optical Trapping

The Zeeman sublevels which increase in energy with increasing magnetic field at low field are weak field seeking and can be trapped at the point corresponding to the minimum magnitude of a magnetic field with curvature. The magnetically trappable states in ^{39}K and ^{41}K are $|F=1, m_F=-1\rangle$, $|F=2, m_F=1\rangle$, and $|F=2, m_F=2\rangle$. To be able to trap all states in the groundstate manifold, we can apply optical dipole traps [209]. An atom in state $|g\rangle$ of the groundstate manifold exposed to monochromatic light with frequency, ω_L, intensity, $I(\mathbf{r})$, and polarisation, ϵ_q, experiences a potential due to coupling to excited states, $\{|f\rangle\}$, [209, 210]

$$V(\mathbf{r}) = \frac{-1}{2\hbar\epsilon_0 c}\sum_f |\langle f|e\mathbf{r}\cdot\epsilon_q|g\rangle|^2\left(\frac{1}{\omega_{fg}-\omega_L}+\frac{1}{\omega_{fg}+\omega_L}\right)I(\mathbf{r}) \tag{2.17}$$

where ϵ_0 is the vacuum permittivity, c is the speed of light, e is the electron charge, and $\hbar\omega_{fg}$ is the energy difference between states $|g\rangle$ and $|f\rangle$. Usually, we take $|\omega_L-\omega_{fg}| \ll \omega_{fg}$ so that the terms proportional to $1/(\omega_L+\omega_{fg})$ can be ignored [209]. For alkali atoms it is usually sufficient to consider excited states, $\{|f\rangle\}$, corresponding to only the first two electronic excited state manifolds (the D1 and D2 transitions) [210].

We can use the Wigner-Eckart theorem to write

$$\langle I, J, m_I, m_J|e\mathbf{r}\cdot\epsilon_q|I, J', m_I', m_J'\rangle = \delta_{m_I', m_I} W^{J',J}_{m_J',q,m_J}\langle J||e\mathbf{r}\cdot\epsilon_q||J'\rangle \tag{2.18}$$

where $\delta_{a,b}$ is a Kronecker-delta function, $\langle J||e\mathbf{r}\cdot\epsilon_q||J'\rangle$ is the reduced dipole matrix element, and

$$W^{J',J}_{m_J',q,m_J} = (-1)^{J_f-1+m_j}\sqrt{2J+1}\begin{pmatrix} J' & 1 & J \\ m_J' & q & -m_J\end{pmatrix} \tag{2.19}$$

[1]This is not the case for states in the $4^2P_{3/2}$ manifold.

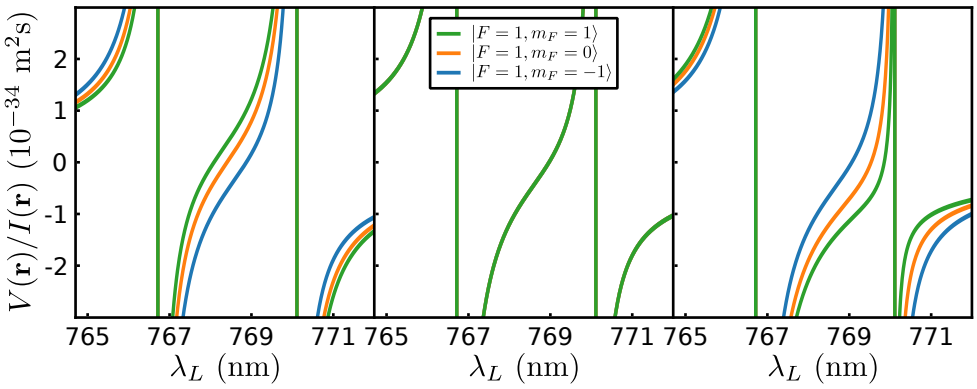

Figure 2.3: Trapping potential, $V(\mathbf{r})$, divided by light intensity, $I(\mathbf{r})$, for the $F = 1$ hyperfine manifold of ^{41}K with $B = 51.766$ G and polarisation $q = -1$ (left), $q = 0$ (middle), and $q = 1$ (right).

is a Clebsch-Gordan coefficient where the factor on the right is a Wigner 3-j symbol. Here, $q = \pm 1$ denotes $\sigma^{\pm}$ circularly polarised light and $q = 0$ denotes π polarised light. Expressing the ground and excited states, $|g\rangle$ and $|f\rangle$, in the $|I, J, m_I, m_J\rangle$ basis as

$$|g\rangle = \sum_{m_I, m_J} \langle I, J, m_I, m_J | g\rangle \, |I, J, m_I, m_J\rangle \tag{2.20}$$

and

$$|f\rangle = \sum_{m'_I, m'_J} \langle I, J', m'_I, m'_J | f\rangle \, |I, J', m'_I, m'_J\rangle \tag{2.21}$$

where the nuclear spin I is fixed for a given atom. We have

$$\langle f|e\mathbf{r}_q|g\rangle = \sum_{m_j, m'_j} \langle I, J', m_I, m'_J | f\rangle \, \langle g | I, J, m_I, m_J\rangle \, W^{J',J}_{m'_J, q, m_J} \, \langle J||e\mathbf{r}\cdot\epsilon_q||J'\rangle \, . \tag{2.22}$$

The reduced dipole matrix element corresponding to the manifold with total electronic orbital angular momentum J' ($J' = 1/2$ for the D1 transition and $J' = 3/2$ for the D2 transition) is related to the radiative decay rate of the manifold, $\Gamma_{J'}$, by [210]

$$\Gamma_{J'} = \frac{\omega^3_{J'} \, |\langle J||e\mathbf{r}\cdot\epsilon_q||J'\rangle|^2}{3\pi\hbar\epsilon_0 c^3} \tag{2.23}$$

where $\omega_{J'}$ is the resonant frequency of the transition, neglecting hyperfine splitting. Values of $\Gamma_{J'}$ and $\omega_{J'}$ for ^{39}K and ^{41}K are given in Tab. 2.2. The trapping potential, $V(\mathbf{r})$, divided by light intensity, $I(\mathbf{r})$, for states in the $F = 1$ hyperfine manifold of ^{41}K with $B = 51.766$ G are shown in Fig. 2.3 for wavelengths $\lambda_L = 2\pi c/\omega_L$ in the vicinity of the optical transitions.

We can see that close to the optical transitions, the optical dipole trapping potential has a complex dependence on wavelength and polarisation. For $|\omega_L - \omega_{fg}|$ much greater than the fine structure splitting, we can simplify Eq. 2.17 to [209]

$$V(\mathbf{r}) = \frac{3\pi c^2}{2\omega_{3/2}} \frac{\Gamma_{3/2}}{\Delta_{3/2}} I(\mathbf{r}) \tag{2.24}$$

Table 2.2: Optical transition properties for ^{39}K and ^{41}K. Values are taken from Ref. [187].

J'	Quantity	^{39}K	^{41}K
1/2	$\omega_{J'}/(2\pi)$	389.286058716(62) THz	389.286294205(62) THz
3/2	$\omega_{J'}/(2\pi)$	391.01617003(12) THz	391.01640621(12) THz
1/2	$\Gamma_{J'}/(2\pi)$	5.956(11) MHz	5.956(11) MHz
3/2	$\Gamma_{J'}/(2\pi)$	6.035(11) MHz	6.035(11) MHz

where $\Delta'_J = \omega_L - \omega'_J$ and we have taken parameters corresponding to the D2 transition because $\Delta_{3/2} \approx \Delta_{1/2}$ and $\Gamma_{3/2} \approx \Gamma_{1/2}$. For negative values of the detuning, $\Delta_{3/2}$, the energy of the atom is lower where the intensity of the light is higher so the atom can be trapped at the maximum intensity of a laser beam. Typically, we use Gaussian laser beams with waist sufficiently large to enable approximating the intensity, $I(\mathbf{r})$, as parabolic which corresponds to a harmonic trapping potential.

Atomic clouds can typically be trapped when the depth of the trap divided by the Boltzmann constant, $\{\max[V(\mathbf{r})] - \min[V(\mathbf{r})]\}/k$, is greater than approximately eight times the temperature of the cloud. Photons can scatter inelastically from the trapped atoms leading to heating and atom loss. In the regime where Eq. 2.24 is valid, the inelastic scattering rate is [209]

$$\Gamma_{\mathrm{sc}}(\mathbf{r}) = \frac{3\pi c^2}{2\hbar\omega_{3/2}} \left(\frac{\Gamma_{3/2}}{\Delta_{3/2}}\right)^2 I(\mathbf{r}). \tag{2.25}$$

Since the inelastic scattering rate scales as $\Delta_{3/2}^{-2}$ while the trapping potential scales as $\Delta_{3/2}^{-1}$, we can choose λ_L such that we can trap atomic clouds with temperatures of a few μK with moderate optical power and without significant inelastic scattering. In our experiments, we use $\lambda_L = 1064$ nm. Generally, the acceleration due to gravity is important and we account for it using the redefinition $V(\mathbf{r}) \to V(\mathbf{r}) + mgz$ where $\mathbf{g} = -g\mathbf{e}_3$ is the acceleration due to gravity. The gravitational sag results in a slight shift of the minimum of the trapping potential and a decrease in trap frequency and trap depth with respect to the z-axis.

2.4 Experimental Platform

The experimental apparatus used in this thesis was constructed as part of the PhD thesis work of Dr. Cesar Cabrera [169] and Dr. Julio Sanz [170]. Figure 2.4(a) shows a sketch of the experimental apparatus. A quartz glass cell, labelled 2D MOT in Fig. 2.4(a), is attached to the stainless steel vacuum chamber with an indium wire sealing the glass to metal transition [170]. A vapour pressure of potassium is established inside the 2D MOT chamber by heating a sample of natural potassium (93.2581(44) %

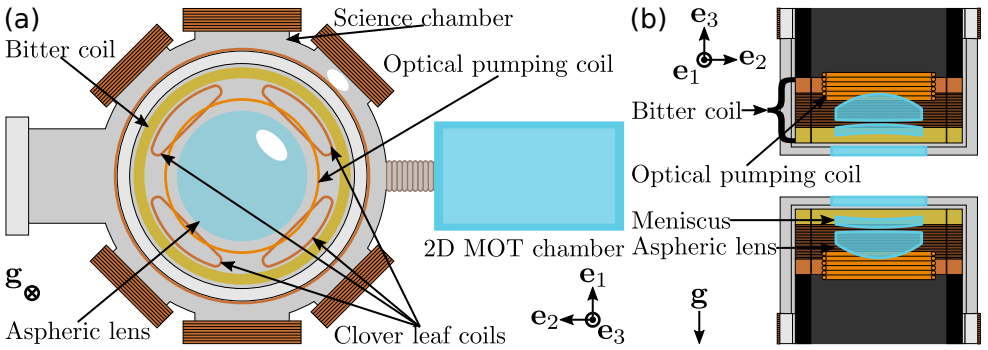

Figure 2.4: (a) Top view sketch of the experimental apparatus (not to scale) showing the locations of the glass cell for the 2D MOT, the top Bitter coil (Feshbach coil), aspheric lens, optical pumping coils, and clover leaf coils. Coils wound around the vacuum viewports allow additional control of the magnetic field. The unit vectors $\mathbf{e}_1$, $\mathbf{e}_2$, and $\mathbf{e}_3$ define the coordinate system used throughout this thesis and the acceleration due to gravity, $\mathbf{g}$, is indicated. (b) Cross section view of the re-entrant view ports showing the meniscus and aspheric lenses, the optical pumping coils, the Bitter coils and the black PVC water distribution blocks[3]. The clover leaf coils have been omitted for clarity. Relative sizes of objects are approximate.

^{39}K, 0.0117(1) % ^{40}K, and 6.7302(44) % ^{41}K) to $\sim$ 70 °C [169]. Thermal atoms are captured from the vapour and cooled in a two-dimensional magneto-optical trap (2D MOT) using a combination of permanent magnets, current carrying coils and red-detuned laser beams [169, 170].

To prevent potassium sticking to the quartz glass, the 2D MOT chamber is enclosed in a secondary frame constructed of aluminium, with glass windows held on by Teflon pieces. The secondary chamber is filled with air and contains heating pads which maintain the glass temperature of $\sim$ 45 °C [170]. The 2D MOT chamber is separated from the stainless steel science chamber by a differential pumping tube which keeps the pressure inside the science cell ($\sim 10^{-11}$ mbar) about four orders of magnitude lower than in the 2D MOT chamber [169]. The pressure inside the science chamber is maintained by two Non-evaporable Getter pumps[2] located between the science chamber and the differential pumping tube and on the opposite side of the science chamber from the 2D MOT. Atoms are transferred from the 2D MOT to the science chamber through a 45° gold plated mirror with a 2 mm hole in the centre under the influence of a blue-detuned push beam [169].

In the science chamber, atoms are captured and cooled in a three-dimensional

[2]NEXTorr D500 and NEXTorr D200 - SAES Getters

[3]Originally, the black PVC distribution blocks were smaller and there was a second set of Bitter coils stacked on the Feshbach coils. The two sets of coils were cooled by the same water but were connected to independent floating power supplies. Voltage differences between the two coils led to electrolysis and the additional Bitter coils were decommissioned. A water leak in the black PVC distribution piece for the top coil prompted us to construct two new Feshbach coils. At the time of writing, the top coil assembly has been replaced as shown in the figure and the bottom coil assembly has not yet been replaced.

magneto-optical trap (3D MOT). The 3D MOT is created by a pair of Bitter-type electromagnets in anti-Helmholtz configuration located inside re-entrant view ports, as shown in Fig. 2.4(b). The electromagnets consist of 24 arcs of metal, the layer closest to the atoms is a brass[4] ring with a thickness of 7 mm, the layer farthest from the atoms is a copper[5] ring with thickness 7 mm and the remaining 22 layers are copper[6] rings of thickness 1 mm. The rings have inner and outer radii of 53 mm and 73 mm and each ring has a slit so that each layer is an open loop. The slits are offset by 45° between layers and current is carried between adjacent layers using copper shims[6] of thickness 0.25 mm.

The layers of the Bitter coils are separated by silicone[7] insulators with water flow channels cut into them. Water from a chiller[8] at 23 °C flows through all layers of the Bitter coils simultaneously, ensuring efficient cooling [169]. Water is delivered through a black PVC distribution piece[3] which is bolted to the brass layer using seven Teflon coated stainless screws and one silicone[9] coated brass screw which carries current from the power supply[10] which returns through the thick copper layer. The screws pass through holes in the copper rings which also serve as entry and exit points for the cooling water.

For the 3D MOT, we supply 13 A to the coils to produce a field gradient of 5.3 G/cm. For both the 2D MOT and the 3D MOT and for both ^{39}K and ^{41}K, we use the D2 transition with the $F = 2 \rightarrow F' = 3$ transition used for cooling and the $F = 1 \rightarrow F' = 2$ transition for repumping [169]. After loading ^{41}K alone or ^{41}K and ^{39}K sequentially in the 3D MOT, the atomic density is increased using a hybrid compressed MOT (CMOT) where ^{41}K is cooled using the $F = 1 \rightarrow F' = 2$ transition on the D1 line while keeping the repumper on the D2 line. During the ^{41}K CMOT, ^{39}K is cooled using a grey molasses technique using the $F = 2 \rightarrow F' = 2$ and $F = 1 \rightarrow F' = 2$ transitions of the D1 line for cooling and repumping, respectively [169].

In potassium, the hyperfine structure of the $5^2P_{3/2}$ manifold shown in Fig. 2.1 has splittings on the order of the natural linewidth of the D2 transition ($\Gamma_{D2}/(2\pi) = 6.035$ MHz [187]) and is therefore not spectroscopically well resolved. This makes sub-Doppler cooling on the D2 line difficult to achieve so we employ grey molasses on the D1 line using a Λ-configuration between the $F = 1$ and $F = 2$ hyperfine manifolds of the ground state and the $F = 2$ hyperfine manifold of the $5^2P_{1/2}$ state for both ^{39}K and ^{41}K [169]. In this case, we perform true molasses cooling at zero magnetic field as opposed to the inefficient molasses in the presence of a weak quadrupole field used for ^{39}K in the previous step.

After the grey molasses, we remove the field gradient and apply a small bias field of 2.5 G using the coils labelled optical pumping in Fig. 2.4 and simultaneously opti-

[4]Broncesval, B-7
[5]Broncesval, B-101
[6]Goodfellow, BS2870 C101
[7]Merefsa, Silicone sheet Thickness 0.3 mm ShA60 ±0.2 mm
[8]Termotek, P306-16968 5 kW
[9]Electrolube, FSC15ML
[10]Delta Elektronika, SM 15-400

cally pump the ^{39}K and ^{41}K atoms into the $|F = 2, m_F = 2\rangle$ state of the groundstate manifold using the $F = 2 \rightarrow F' = 2$ transition of the D1 line after repumping on the $F = 1 \rightarrow F' = 2$ transition of the D1 line. We capture the atoms in a quadrupole magnetic field by supplying 85 A to the Bitter coils corresponding to a gradient of 50 G/cm. We reduce the current in the Bitter coils to create a field gradient of 20 G/cm which causes any atoms remaining in weak field seeking states other than $|F = 2, m_F = 2\rangle$ to fall out of the trap under the influence of gravity. Subsequently, the current is increased to 180 A to produce a field gradient of 105 G/cm [169].

In the magnetic trap we perform forced evaporative cooling by using radio frequency fields to selectively transfer the most energetic atoms to strong field seeking states which are expelled from the trap. The background scattering length of ^{41}K is $\sim 60a_0$ while the background scattering length of ^{39}K is negative. This means that ^{41}K can be cooled efficiently on its own but ^{39}K requires sympathetic cooling by ^{41}K [169]. At the end of the magnetic trap we typically have 4×10^7 atoms (either all ^{41}K or a mixture of ^{39}K and ^{41}K) at a temperature of 30 μK. At much lower temperatures, the atoms will spend a significant fraction of time close to the centre of the quadrupole field resulting in Majorana losses.

To circumvent Majorana losses, we add a Gaussian beam with a wavelength of $\lambda_L = 1064$ nm and $1/\exp(2)$ radius $w_0 \approx 60$ μm propagating in the $\mathbf{e}_1$ direction and positioned below the zero of the quadrupole field. In the presence of the optical dipole trapping beam, the quadrupole trap is decompressed by lowering the current in the Bitter coils to 14 A. An evaporative cooling stage is performed by gradually decreasing the power in the trapping beam. Once the temperature of the atoms is around 4 μK, we add a second laser beam propagating in the $(\mathbf{e}_1 - \mathbf{e}_2)/\sqrt{2}$ direction with a $1/\exp(2)$ radius of $w_1 \approx 100$ μm to form a crossed dipole trap.

Once the atoms have been loaded into the crossed dipole trap, we remove the quadrupole field and put the Bitter coils into Helmholtz configuration using mechanical relays[11] to apply a bias field. We transfer to a desired Zeeman sublevel in the groundstate manifold using radio frequency fields. Sets of peanut shape coils placed inside the top and bottom Bitter coils, labelled clover leaf coils in Fig. 2.4(a), allow us to control magnetic field gradients and curvatures [169]. Coils have also been wound around all of the view port windows of the science chamber for additional control of magnetic fields.

We can prepare a BEC of $\sim 10^5$ atoms with high purity in ^{41}K at almost any bias field up to ~ 500 G in any of the states in the $F = 1$ manifold by evaporative cooling. To prepare a BEC of ^{39}K, we first apply a resonant optical pulse to remove atoms in ^{41}K. Due to the negative background scattering length we have to use the bias magnetic field to condense near a Feshbach resonance[12]. We can prepare BECs of $\sim 10^5$ atoms with high purity in ^{39}K in the states $|F = 1, m_F = -1\rangle$, $|F = 1, m_F = 1\rangle$, and $|F = 1, m_F = 0\rangle$ using broad Feshbach resonances near $B = 40$ G, $B = 397$ G, and $B = 450$ G, respectively.

[11] TE Connectivity, LEV200A4NAF

[12] For this reason, we often refer to the Bitter coils as the Feshbach coils.

2.4.1 Imaging

The two most important probes for collecting information about clouds of ultracold atoms are time of flight and *in situ* images [211]. As their names suggest, time of flight imaging examines the atomic density distribution after suddenly removing the trapping potential and allowing a period of free expansion while *in situ* imaging probes the atomic density distribution in trap.

In time of flight imaging, when interactions can be neglected the atoms expand ballistically from their initial positions in the trap. After a sufficiently long time of flight, the atomic cloud reaches a size much larger than the in trap size and the density distribution corresponds to the in trap velocity distribution. A thermal cloud will expand to become isotropic with a width proportional to the temperature of the atoms and the velocity distribution of a weakly interacting BEC corresponds to the Fourier transform of the in trap density distribution [25, 211]. For a BEC in the Thomas-Fermi regime, the width of the cloud after expansion scales as $\sim (g_s N/m)^{1/5}$ [212].

To image a cloud of atoms, we shine a beam of light on the atoms. For simplicity we assume here that the imaging beam propagates along the z-axis but this is not a requirement and we image along different axes depending on the information we wish to collect. For both time of flight and *in situ* imaging we label the atomic density distribution to be imaged as $n(\mathbf{r})$. When the beam of light passes through the atoms, the three interaction processes are absorption and re-emission of light and shifting the phase of the light [211]. These three effects are used in absorptive, fluorescence and dispersive imaging techniques [211].

Applying a "thin lens" approximation to the atomic cloud, the transmitted light corresponding to an incident electric field, E_0, can be modelled as $E_t = tE_0 \exp(i\Delta\phi)$ where t is the fraction of transmitted light and $\Delta\phi$ is the phase shift of the transmitted light [211]. Both t and $\Delta\phi$ depend on the column density $\tilde{n} = \int n(\mathbf{r})\mathrm{d}z$ and the resonant scattering cross section, σ_0. The transmitted light and phase shift are given by [211]

$$\Delta\phi = -\frac{\tilde{n}\sigma_0}{2}\frac{\Gamma^2/4}{\Gamma^2/4 + (\omega_p - \omega_0)^2} \tag{2.26}$$

and

$$t = \exp(\Delta\phi) \tag{2.27}$$

where Γ is the linewidth of the transition, ω_0 is the resonant frequency of the transition, ω_p is the frequency of the probe light, and we have assumed that the intensity of the probe light is small compared to the saturation intensity of the transition.

For absorption imaging, we typically set $\omega_p = \omega_0$. By collecting the light passing through the atoms with a lens of focal length f_1 placed a distance f_1 from the atoms, we can think of the missing fraction of light absorbed by the atoms (the shadow of the atoms) as a point source which we collimate and can subsequently be focused onto a CCD camera using a second lens with focal length f_2 placed a distance $f_1 + f_2$ from the first lens and a distance f_2 before the camera. As a result, the image on the camera is the intensity of the incident light minus the intensity distribution of

absorbed photons, given by $I_{\mathrm{CCD}}^{(\mathrm{atoms})} \propto t(x,y)^2|E_0(x,y)|^2$ in the limit of small optical density, with a spatial magnification factor of f_2/f_1.

Absorbing a photon causes an atom to recoil with kinetic energy $\hbar^2 \left(\omega_p/c\right)^2/(2m)$ so absorption imaging heats the atomic cloud and is a destructive imaging technique [211]. This means that a single absorption image can be taken of each BEC which we prepare and experiments have to be repeated with a new BEC prepared each time. By taking a second image of the probe beam after the atomic cloud has been destructively probed, we capture the intensity distribution of the probe light on the CCD, $I_{\mathrm{CCD}}^{(\mathrm{bright})} \propto |E_0(x,y)|^2$. We take one extra image without probe light which serves as a measure of the background signal on the CCD, $I_{\mathrm{CCD}}^{(\mathrm{dark})}$. From the three images taken with the CCD, we can extract the column density

$$\tilde{n}(x,y) = -\frac{1}{\sigma_0} \ln\left[\frac{I_{\mathrm{CCD}}^{(\mathrm{atoms})} - I_{\mathrm{CCD}}^{(\mathrm{dark})}}{I_{\mathrm{CCD}}^{(\mathrm{bright})} - I_{\mathrm{CCD}}^{(\mathrm{dark})}}\right]. \tag{2.28}$$

In a typical time of flight measurement, we divide the time after releasing the atoms from the trap into three phases. First, we let the atoms expand without adjusting the magnetic bias field so the cloud becomes dilute before moving away from any Feshbach resonances used for the experiment, this procedure avoids atom loss due to molecule formation while crossing Feshbach resonances. Second, we turn off the current in the Bitter coils and supply a small bias field of of ~ 3 G using the optical pumping coils and a magnetic field gradient along the $\mathbf{e}_3$ direction to separate spin components in a Stern-Gerlach experiment. Finally, we switch off the magnetic field gradient and let the cloud expand for a few milliseconds more while the field stabilises. The atoms are optically pumped to $|2,2\rangle$ and imaged on the $F = 2 \rightarrow F' = 3$ transition of the D2 line.

During time of flight the atoms fall under the influence of gravity so do not stay in focus with respect to a lens placed above or below the science chamber. All time of flight images presented in this thesis are taken with the probe beam propagating through one of the three colinear pairs of view ports in the xy-plane shown in Fig. 2.4(a). The atoms are approximately 15 cm from the view ports so the optics used for imaging are low resolution with magnification factors on the order of unity. We use CCD cameras[13] with physical pixel sizes of 3.75×3.75 μm^2 which we bin 2×2 to create effective pixels with size 7.5×7.5 μm^2. The atom number has been calibrated by measuring the critical temperature for Bose-Einstein condensation [169, 170]. Figure 2.5(a) shows a time of flight image corresponding to a mixture of states $|\downarrow\rangle = |F = 1, m_F = 1\rangle$ and $|\uparrow\rangle = |F = 1, m_F = 0\rangle$ in ^{39}K after being released from a trap at a bias field of 397.01(1) G.

For *in situ* imaging of the atoms, home made objectives have been placed concentric with the Bitter coils in the re-entrant view ports of the science chamber, as shown in Fig. 2.4(b). The home made objectives consist of a meniscus lens[14] which corrects for the spherical aberrations created by the 6 mm thick fused silica glass window of

[13] Point Grey, CMLN-132S2C-CS

[14] Ross Optical Industries, custom BK-7

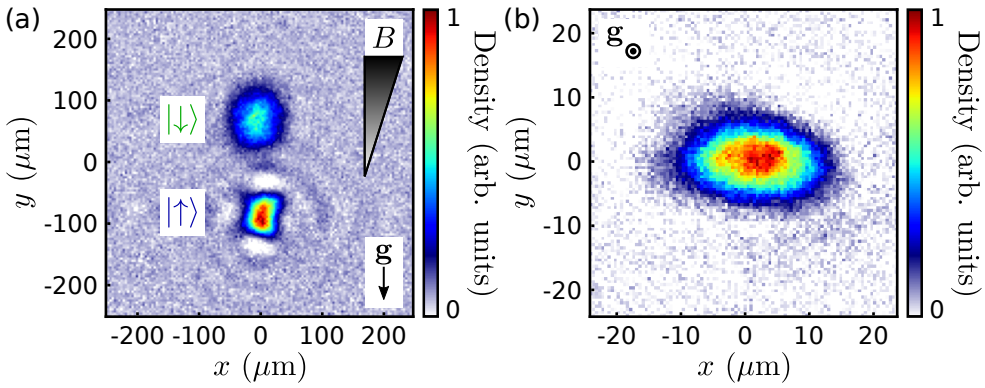

Figure 2.5: (a) Time of flight image of a mixture of ^{39}K BECs in states $|\downarrow\rangle = |F = 1, m_F = 1\rangle$ and $|\uparrow\rangle = |F = 1, m_F = 0\rangle$ with a magnetic field gradient. This image was taken with the probe beam propagating in the $(\mathbf{e}_1 + \mathbf{e}_2)/\sqrt{2}$ direction and the total time of flight was 21 ms. The spatial extent of the $|\downarrow\rangle$ component is much larger than the $|\uparrow\rangle$ component in spite of the fact that there are more atoms in $|\uparrow\rangle$ because $g_{\downarrow\downarrow} \gg g_{\uparrow\uparrow}$ (see Ch. 5). (b) *In situ* image of atoms in state $|\downarrow\rangle$ with a bias field of 397.01(1) G captured using polarisation phase contrast imaging. The acceleration due to gravity, $\mathbf{g}$, is indicated in both images.

the view port and an aspheric lens[15]. The objective has a theoretical diffraction limited resolution of 1.1 μm and a measured resolution of 1.5 μm corresponding to the radius[16] of the Airy disk observed when imaging a pinhole [213, 214].

Absorption imaging a cloud of atoms *in situ* with optical intensities small compared to the saturation intensity is not feasible because the optical depth of the cloud can be so high that all of the light from the probe beam which passes through the cloud is absorbed. Instead, we employ a polarisation phase contrast imaging technique which relies on the vector light shift of the atoms to rotate the polarisation of linearly polarised light by an angle proportional to the column density [170, 215, 216]. The rotation angle is easily measured by placing a thin film polariser[17] in the imaging path and comparing the transmitted light captured by an electron multiplying CCD[18] with and without atoms.

The image of the atoms, which is encoded in the rotation of the polarisation of the probe light, is focused onto the camera with pixel size 16×16 μm^2 using low numerical aperture optics consisting of three achromatic lenses resulting in an effective magnification factor of 33.1(6) [170]. The polarisation phase contrast technique is performed using off-resonant light in a destructive regime and works at intermediate and high magnetic fields where optical transitions are open. In two-component mixtures, the frequency of the probe beam is set such that we obtain the combined column density of both components. The characterisation of the imaging scheme can be found in the

[15] Edmund Optics, 66-336
[16] Distance from central maximum to first minimum of intensity.
[17] QiOptiq, G335-725-000
[18] Andor, iXon Ultra 897

PhD thesis of Dr. Julio Sanz [170]. Figure 2.5(b) shows the *in situ* column density of a ^{39}K BEC in state $|F = 1, m_F = 1\rangle$ with a bias magnetic field of 397.01(1) G.

2.5 Summary

In this chapter, I have presented the theory of single- and two-component BECs in the language of second quantisation and at the mean-field level. I have presented some relevant optical properties of the bosonic isotopes of potassium and presented the experimental platform used in this thesis including the process of making and probing BECs. In the next chapter I will demonstrate the use of coherent coupling as a tool to manipulate interactions in a BEC.

Chapter 3

Coherent Coupling and Interaction Control

In this chapter, I will introduce coherent coupling between two spin components of a BEC with tunable interactions as a method of interaction control. I will first present coherent coupling without momentum dependence and then move to the implementation of Raman coupling to tune interactions using the momentum of the atoms. The engineered momentum-dependent interactions are the key ingredients for the quantum simulation of a topological gauge theory and the realisation of a supersolid discussed in Ch. 5 and Ch. 7, respectively. The results presented in this chapter came as part of experimental collaborations between myself, Dr. Anika Frölian, Dr. Julio Sanz, Dr. Cesar Cabrera, Dr. Elettra Neri, Dr. Ramón Ramos, and Prof. Dr. Leticia Tarruell and have been included in part in the publications "Interaction Control and Bright Solitons in Coherently Coupled Bose-Einstein Condensates" [217] and "Realizing a 1D topological gauge theory in an optically dressed BEC" [132]. Parts of this chapter have also been discussed in the PhD theses of Dr. Julio Sanz [170] and Dr. Anika Frölian [218].

3.1 Coherent Coupling of a Two Level System

We consider a two level system consisting of bare states $|\uparrow\rangle \doteq (1,\,0)^T$ and $|\downarrow\rangle \doteq (0,\,1)^T$ with an energy difference $\hbar\omega_0$ in the presence of an external monochromatic electromagnetic field oscillating at frequency ω. In this thesis, the states will be two adjacent Zeeman sublevels, specifically from the $F = 1$ groundstate manifold and the energy of the electromagnetic field corresponds to radio frequency (RF) waves. In the rotating wave approximation, the system is governed by the Hamiltonian [219]

$$\hat{H}_{0,\mathrm{RF}} \doteq \begin{pmatrix} -\hbar\delta/2 & \hbar\Omega/2 \\ \hbar\Omega/2 & \hbar\delta/2 \end{pmatrix} \tag{3.1}$$

where $\hbar$ is the reduced Planck constant, $\delta = \omega - \omega_0$ is the detuning from atomic resonance, and Ω is the Rabi frequency which characterises the strength of the coupling

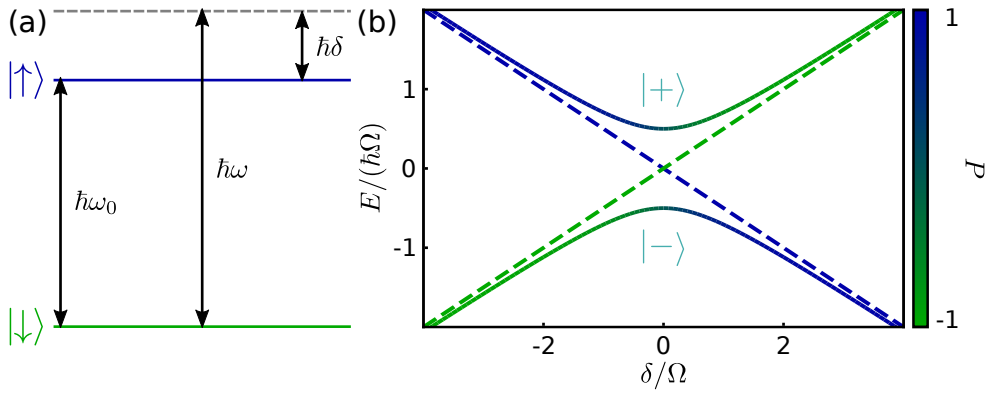

Figure 3.1: (a) Energy level diagram representing two states $|\uparrow\rangle$ and $|\downarrow\rangle$ separated in energy by $\hbar\omega_0$ and coupled by a classical electromagnetic field of frequency ω with corresponding detuning $\delta = \omega - \omega_0$. (b) Energy levels of the dressed states, $|\pm\rangle$, as a function of detuning, δ, normalised by the Rabi frequency, Ω. The colour bar represents the projection of the dressed states onto the bare states. The dashed green (blue) line represents the energy of the state $|\downarrow\rangle$ ($|\uparrow\rangle$) in the rotating frame.

between the atom and the field and is proportional to the field amplitude [188, 220]. Experimentally, the two-level approximation is valid because we always take $\Omega/(2\pi) \sim 10$ kHz and $\delta/(2\pi) < 1$ MHz while we always take magnetic fields $B \gtrsim 50$ G which means that the detuning from other states is always on the order of 10 MHz.

It is convenient to work in the so-called dressed basis which is the eigenbasis of the Hamiltonian in Eq. 3.1. The dressed states are $|-\rangle = \sin\theta\,|\downarrow\rangle - \cos\theta\,|\uparrow\rangle$ and $|+\rangle = \cos\theta\,|\downarrow\rangle + \sin\theta\,|\uparrow\rangle$ where $\cos\theta = \left[\left(1 + \delta/\tilde{\Omega}\right)/2\right]^{\frac{1}{2}}$ and the energies of the two dressed states are given by $\hat{H}_{0,\mathrm{RF}}\,|\pm\rangle = E_\pm\,|\pm\rangle$ with $E_\pm = \pm\hbar\tilde{\Omega}/2$ where $\tilde{\Omega} = \sqrt{\Omega^2 + \delta^2}$. In an ensemble of atoms the polarisation parameter, P, is an observable quantity and can be measured by suddenly turning off the driving field to project the dressed states back onto the bare basis before applying a Stern-Gerlach gradient during time of flight. By measuring the populations $N_\uparrow$ and $N_\downarrow$, we can obtain $P = (N_\uparrow - N_\downarrow)\,/\,(N_\uparrow + N_\downarrow)$. In Fig. 3.1(a), the coupling scheme in the bare basis is represented schematically and the energies and polarisations of the dressed states are given in 3.1(b). For each dressed state, the polarisation is given by $P_\pm = 2|\,\langle\uparrow|\pm\rangle\,|^2 - 1 = \mp\delta/\tilde{\Omega}$ and when we have a mixture of dressed states the total polarisation is given by a weighted sum of the two dressed state polarisations.

3.1.1 Rabi Flopping Dynamics

In the two level system we are considering, the Rabi flopping dynamics can be derived in a straightforward manner. Assume we start with all of the atoms in one of the two bare states, for concreteness we assume $|\downarrow\rangle$. At time $t = 0$, we suddenly turn on the coupling field with Rabi frequency Ω and detuning δ. We represent the initial state in the dressed basis as $|\psi(0)\rangle = |\downarrow\rangle = \cos\theta\,|+\rangle + \sin\theta\,|-\rangle$. The state

evolves according to the Schrödinger equation: $i\hbar\partial_t |\psi(t)\rangle = \hat{H}_{0,\mathrm{RF}} |\psi(t)\rangle$ which means $|\psi(t)\rangle = \cos\theta \exp\left(-i\tilde{\Omega}t/2\right)|+\rangle + \sin\theta \exp\left(i\tilde{\Omega}t/2\right)|-\rangle$. After a certain pulse duration, τ, we can turn off the coupling field and measure the probability of transfer to state $|\uparrow\rangle$ as $P_\uparrow(\tau) = |\langle\uparrow|\psi(\tau)\rangle|^2 = \left(\Omega/\tilde{\Omega}\right)^2 \sin^2\left(\tilde{\Omega}\tau/2\right)$. The transfer probability is periodic in time and it is only possible to achieve full transfer when $\delta = 0$. The first time when full transfer is achieved with $\delta = 0$ is $t_\pi = \pi/\Omega$. A pulse of duration t_π is called a π-pulse. In order to experimentally calibrate the magnetic field one can simply make a pulse of duration $\tau < t_\pi$ and either scan ω at a fixed magnetic field to find the maximum transfer probability or scan the current in the Feshbach coils with fixed ω in order to set the magnetic field corresponding to a desired ω_0. The Rabi frequency is calibrated by fitting the populations in the two bare states as a function of pulse duration with $\delta = 0$.

3.1.2 Magnetic Field Noise

The Rabi flopping dynamics can be used to estimate noise in the magnetic field by fixing Ω, ω, and τ and measuring the fluctuations in the transfer probability across several experimental realisations. This is due to changes in ω_0 which translate into changes in δ. The optimal sensitivity to field noise is found by nominally setting $\delta \neq 0$ and setting $\Omega\tau = n\pi$ where n is an odd-integer. The optimal value of δ depends on n and larger n is better.

Typically, a large component of the magnetic field noise in a laboratory can be expected to come from the 50 Hz main electrical lines which means, for large n, the field deviation can evolve during the Rabi flopping dynamics. Therefore, we would like to have a method for measuring magnetic field noise with high sensitivity and short pulse times. For this purpose we employ Ramsey spectroscopy [221, 222]. In Ramsey spectroscopy, instead of a single pulse of duration τ, two pulses of duration τ are applied with an evolution time, T, in the absence of the electromagnetic field between the pulses. The transfer probability is [221, 222]

$$P_R = 4\frac{\Omega^2}{\tilde{\Omega}^2}\sin^2\left(\frac{\tilde{\Omega}\tau}{2}\right)\left[\cos\left(\frac{\delta T}{2}\right)\cos\left(\frac{\tilde{\Omega}\tau}{2}\right) - \frac{\delta}{\tilde{\Omega}}\sin\left(\frac{\delta T}{2}\right)\sin\left(\frac{\tilde{\Omega}\tau}{2}\right)\right]^2, \quad (3.2)$$

by tuning T and τ the sensitivity to magnetic field fluctuations can be tuned to essentially any value.

To measure the magnetic field noise we first set $\delta = 0$ and measure Ω *via* Rabi flopping. We then validate the results of the Rabi flopping measurements by measuring the transfer probability, P_R, while scanning δ with fixed $\tau \approx t_\pi/2$ and $T \approx t_\pi$. We then set $\delta \neq 0$ and measure P_R over many experimental realisations. The deviations in P_R come from deviations in δ which correspond to deviations in ω_0 since ω is fixed. We use the Breit-Rabi formula [206, 208] to convert to magnetic field fluctuations.

Figure 3.2(a) shows a measurement of P_R as a function of δ using the states $|F = 1, m_F = 1\rangle$ and $|F = 1, m_F = 0\rangle$ of ^{41}K as $|\downarrow\rangle$ and $|\uparrow\rangle$ at a magnetic field of $B = 52.25(1)$ G where $\mathrm{d}\omega_0/\mathrm{d}B/(2\pi) = 390$ Hz/mG and the Rabi frequency was

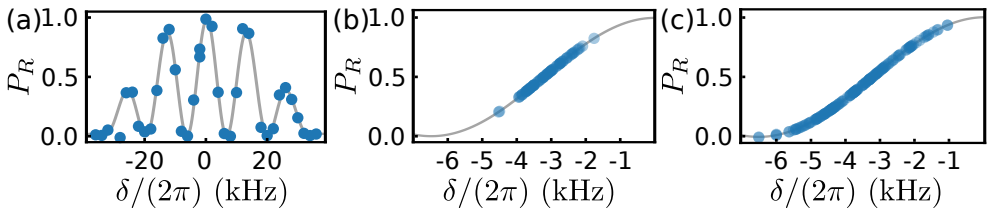

Figure 3.2: (a) Ramsey fringes corresponding to $\Omega = 11.9(1)$ kHz, $\tau = 22.5$ μs, and $T = 50$ μs with the first pulse synchronised to the 50 Hz line. (b) Inferred detuning fluctuations from measured transfer probability with a nominal detuning of -3.2 kHz and the first pulse synchronised to the 50 Hz line. (c) Inferred detuning fluctuations from measured transfer probability with a nominal detuning of -3.2 kHz and the first pulse not synchronised to the 50 Hz line.

determined through Rabi flopping to be $\Omega/(2\pi) = 11.9(1)$ kHz. The RF pulses were generated using an analog frequency generator[1] through an impedance matched high power amplifier[2] [169] with the first pulse synchronised to the zero crossing of the 50 Hz line on the positive slope. The pulse parameters were $\tau = 22.5$ μs and $T = 50$ μs.

To estimate magnetic field noise, we set a nominal value of $\delta/(2\pi) = -3.2$ kHz and run the Ramsey pulse sequence. Figure 3.2(b) shows the detuning inferred from the measured populations in $|\uparrow\rangle$ and $|\downarrow\rangle$ for 80 repetitions with 50 Hz synchronisation and Fig. 3.2(c) shows the inferred detuning for 160 repetitions without synchronisation. From these measurements, we extract the standard deviation of the magnetic field fluctuations as 1.4 mG (2.9 mG) with (without) 50 Hz synchronisation while the peak to peak value is 7.1 mG (13.8 mG). We measure similar values at $B = 198.51(1)$ G and $B = 397.01(1)$ G.

3.1.3 Preparation of Dressed States

Applying pulses of the electromagnetic field creates mixtures of both dressed states. In order to prepare a single dressed state we must connect adiabatically to one of the bare states. This can be achieved by choosing a large initial value of $|\delta|$. For example, as can be seen in Fig. 3.1(b), the $|+\rangle$ ($|-\rangle$) state asymptotically approaches the $|\uparrow\rangle$ ($|\downarrow\rangle$) state in both energy and spin composition for $\delta/\Omega \ll 0$ or the $|\downarrow\rangle$ ($|\uparrow\rangle$) state for $\delta/\Omega \gg 0$. Once the chosen dressed state has been prepared with large $|\delta|$, the detuning can be changed smoothly to any desired value without coupling to the other dressed state provided that the Landau-Zener criterion, $|\mathrm{d}\delta/\mathrm{d}t| < \Omega^2$, is fulfilled [217].

3.2 Properties of Dressed States

To understand interactions between the dressed states in a BEC, we simply add the RF coupling terms to the second quantised Hamiltonian for a two-component

[1] Rhode and Schwarz, SMC100A
[2] Mini-Circuits, ZHL-100W-GAN+

interacting system given in Eq. 2.12

$$\hat{H}_{\mathrm{RF}} = \int \mathrm{d}^3\mathbf{r} \left[\begin{pmatrix} \hat{\phi}_\uparrow^\dagger & \hat{\phi}_\downarrow^\dagger \end{pmatrix} \hat{\mathcal{H}}_{\mathrm{RF}} \begin{pmatrix} \hat{\phi}_\uparrow \\ \hat{\phi}_\downarrow \end{pmatrix} + \frac{1}{2} \sum_{\sigma_1,\sigma_2=\uparrow,\downarrow} g_{\sigma_1\sigma_2} \hat{\phi}_{\sigma_1}^\dagger \hat{\phi}_{\sigma_2}^\dagger \hat{\phi}_{\sigma_1} \hat{\phi}_{\sigma_2} \right] \tag{3.3}$$

where

$$\hat{\mathcal{H}}_{\mathrm{RF}} \doteq \begin{bmatrix} -\frac{\hbar^2}{2m}\nabla^2 + V(\mathrm{r}) - \frac{\hbar\delta}{2} & \frac{\hbar\Omega}{2} \\ \frac{\hbar\Omega}{2} & -\frac{\hbar^2}{2m}\nabla^2 + V(\mathrm{r}) + \frac{\hbar\delta}{2} \end{bmatrix} \tag{3.4}$$

and $V(\mathbf{r})$ is a state-independent trapping potential. Let $\hat{\phi}_\pm^\dagger$ ($\hat{\phi}_\pm$) be the creation (annihilation) field operator for a particle in the dressed state $|\pm\rangle$ i.e. $\left(\hat{\phi}_+, \hat{\phi}_-\right)^T = \hat{U}^\dagger \left(\hat{\phi}_\uparrow, \hat{\phi}_\downarrow\right)^T$ where

$$\hat{U} \doteq \begin{pmatrix} \sin\theta & -\cos\theta \\ \cos\theta & \sin\theta \end{pmatrix} \tag{3.5}$$

is the unitary operator which diagonalises $\hat{H}_{0,\mathrm{RF}}$. Note that $\left[-\hbar\nabla^2/(2m) + V(\mathbf{r})\right]\mathbb{I}$ commutes with $\hat{U}$ and is therefore diagonal in both the bare basis and the dressed basis. Thus, transforming to the dressed basis, we have

$$\hat{H}_{\mathrm{RF}} = \int \mathrm{d}^3\mathbf{r} \begin{pmatrix} \hat{\phi}_+^\dagger & \hat{\phi}_-^\dagger \end{pmatrix} \left\{ \left[-\frac{\hbar^2}{2m}\nabla^2 + V(\mathbf{r}) \right] \mathbb{I} + \frac{\hbar\tilde{\Omega}}{2}\hat{\sigma}_z \right\} \begin{pmatrix} \hat{\phi}_+ \\ \hat{\phi}_- \end{pmatrix} + \hat{H}_{\mathrm{int,RF}} \tag{3.6}$$

where

$$\mathbb{I} \doteq \begin{pmatrix} 1 & 0 \\ 0 & 1 \end{pmatrix} \text{ and } \hat{\sigma}_z \doteq \begin{pmatrix} 1 & 0 \\ 0 & -1 \end{pmatrix}. \tag{3.7}$$

3.2.1 Dressed State Interactions

For the interaction term, we first transform to momentum space and then to the dressed basis [170, 219]

$$\hat{H}_{\mathrm{int}} = \frac{1}{2} \int \frac{\mathrm{d}^3\mathbf{k}_4}{(2\pi)^3} \frac{\mathrm{d}^3\mathbf{k}_3}{(2\pi)^3} \frac{\mathrm{d}^3\mathbf{k}_2}{(2\pi)^3} \frac{\mathrm{d}^3\mathbf{k}_1}{(2\pi)^3} \hat{\mathcal{H}}_{\mathrm{int}} \tag{3.8}$$

where

$$\hat{\mathcal{H}}_{\mathrm{int}} = \sum_{\sigma_1,\sigma_2=\uparrow,\downarrow} g_{\sigma_1\sigma_2} \hat{\Phi}_{\sigma_1}^\dagger(\mathbf{k}_4) \hat{\Phi}_{\sigma_2}^\dagger(\mathbf{k}_3) \hat{\Phi}_{\sigma_1}(\mathbf{k}_2) \hat{\Phi}_{\sigma_2}(\mathbf{k}_1) \delta^{(3)}\left(\mathbf{k}_3 + \mathbf{k}_4 - \mathbf{k}_1 - \mathbf{k}_2\right) \tag{3.9}$$

and $\hat{\Phi}_\sigma(\mathbf{k}) = \int \mathrm{d}^3\mathbf{r} \hat{\phi}_\sigma \exp\left(-i\mathbf{k}\cdot\mathbf{r}\right)$. In the dressed basis

$$\begin{aligned} \hat{\mathcal{H}}_{\mathrm{int,RF}} = & \sum_{n_1',n_2',n_1,n_2=\pm} \hat{\Phi}_{n_1'}^\dagger(\mathbf{k}_4) \hat{\Phi}_{n_2'}^\dagger(\mathbf{k}_3) \hat{\Phi}_{n_1}(\mathbf{k}_2) \hat{\Phi}_{n_2}(\mathbf{k}_1) \\ & \times \sum_{\sigma_1,\sigma_2=\uparrow,\downarrow} g_{\sigma_1\sigma_2} U_{n_1'\sigma_1} U_{\sigma_1 n1}^\dagger U_{n_2'\sigma_2} U_{\sigma_2 n_2}^\dagger \delta^{(3)}\left(\mathbf{k}_3 + \mathbf{k}_4 - \mathbf{k}_1 - \mathbf{k}_2\right). \end{aligned} \tag{3.10}$$

Writing out the interaction Hamiltonian explicitly gives [170, 219]

$$\begin{aligned}\hat{H}_{\text{int,RF}} = \frac{1}{2}\int \mathrm{d}^3\mathbf{r}\left(g_{++}\hat{\phi}_+^\dagger\hat{\phi}_+^\dagger\hat{\phi}_+\hat{\phi}_+ + g_{--}\hat{\phi}_-^\dagger\hat{\phi}_-^\dagger\hat{\phi}_-\hat{\phi}_- + g_{+-}\hat{\phi}_+^\dagger\hat{\phi}_-^\dagger\hat{\phi}_+\hat{\phi}_-\right)\\ + \frac{1}{2}\int \frac{\mathrm{d}^3\mathbf{k}_4}{(2\pi)^3}\frac{\mathrm{d}^3\mathbf{k}_3}{(2\pi)^3}\frac{\mathrm{d}^3\mathbf{k}_2}{(2\pi)^3}\frac{\mathrm{d}^3\mathbf{k}_1}{(2\pi)^3}\delta^{(3)}\left(\mathbf{k}_3+\mathbf{k}_4-\mathbf{k}_1-\mathbf{k}_2\right)\\ \times\Big\{g_\alpha\left[\hat{\Phi}_+^\dagger(\mathbf{k}_4)\hat{\Phi}_+^\dagger(\mathbf{k}_3)\hat{\Phi}_-(\mathbf{k}_2)\hat{\Phi}_-(\mathbf{k}_1)+\hat{\Phi}_-^\dagger(\mathbf{k}_4)\hat{\Phi}_-^\dagger(\mathbf{k}_3)\hat{\Phi}_+(\mathbf{k}_2)\hat{\Phi}_+(\mathbf{k}_1)\right]\\ g_\beta\left[\hat{\Phi}_+^\dagger(\mathbf{k}_4)\hat{\Phi}_+^\dagger(\mathbf{k}_3)\hat{\Phi}_+(\mathbf{k}_2)\hat{\Phi}_-(\mathbf{k}_1)+\hat{\Phi}_-^\dagger(\mathbf{k}_4)\hat{\Phi}_+^\dagger(\mathbf{k}_3)\hat{\Phi}_+(\mathbf{k}_2)\hat{\Phi}_+(\mathbf{k}_1)\right]\\ g_\gamma\left[\hat{\Phi}_+^\dagger(\mathbf{k}_4)\hat{\Phi}_-^\dagger(\mathbf{k}_3)\hat{\Phi}_-(\mathbf{k}_2)\hat{\Phi}_-(\mathbf{k}_1)+\hat{\Phi}_-^\dagger(\mathbf{k}_4)\hat{\Phi}_-^\dagger(\mathbf{k}_3)\hat{\Phi}_-(\mathbf{k}_2)\hat{\Phi}_+(\mathbf{k}_1)\right]\Big\}\end{aligned} \tag{3.11}$$

where the effective interaction constants are

$$\begin{aligned} g_{++} &= g_{\uparrow\uparrow}\sin^4\theta + g_{\downarrow\downarrow}\cos^4\theta + \frac{1}{2}g_{\uparrow\downarrow}\sin^2 2\theta,\\ g_{--} &= g_{\uparrow\uparrow}\cos^4\theta + g_{\downarrow\downarrow}\sin^4\theta + \frac{1}{2}g_{\uparrow\downarrow}\sin^2 2\theta,\\ g_{+-} &= \left(g_{\downarrow\downarrow}+g_{\uparrow\uparrow}\right)\sin^2 2\theta + 2g_{\uparrow\downarrow}\cos^2 2\theta,\\ g_\alpha &= \frac{1}{4}\left(g_{\downarrow\downarrow}+g_{\uparrow\uparrow}-2g_{\uparrow\downarrow}\right)\sin^2 2\theta,\\ g_\beta &= \sin 2\theta\left(g_{\uparrow\uparrow}\sin^2\theta - g_{\downarrow\downarrow}\cos^2\theta + g_{\uparrow\downarrow}\cos 2\theta\right), \text{ and}\\ g_\gamma &= \sin 2\theta\left(g_{\uparrow\uparrow}\cos^2\theta - g_{\downarrow\downarrow}\sin^2\theta - g_{\uparrow\downarrow}\cos 2\theta\right). \end{aligned} \tag{3.12}$$

The first three terms represent elastic collisions between dressed state atoms while the last three terms represent inelastic dressed state changing collisions and have been left in momentum space representation to make momentum conservation explicit.

For $g_{\uparrow\uparrow} = g_{\downarrow\downarrow} = g_{\uparrow\downarrow} \equiv g$, we have $g_{++} = g_{--} = g_{+-} = g$ and $g_\alpha = g_\beta = g_\gamma = 0$ so the dressed states interact in exactly the same way as the bare states. Previous experiments have examined the case where $g_{\uparrow\uparrow} \approx g_{\downarrow\downarrow} \approx g_{\uparrow\downarrow}$ where the inelastic processes remain negligible and the elastic interaction strengths are not strongly modified by changes in δ. In these cases, the modification of the dressed state interactions was observed indirectly through the miscibility of the components [223–225]. It was shown that when $g_{\uparrow\downarrow}/\sqrt{g_{\uparrow\uparrow}g_{\downarrow\downarrow}} < 1 (> 1)$, meaning that the two bare states are miscible (immiscible), we have $g_{+-}/\sqrt{g_{++}g_{--}} > 1 (< 1)$, meaning that the dressed states are immiscible (miscible).

3.2.2 Measurement of Modified Dressed State Interactions

In our experiments, we took $|\uparrow\rangle = |F = 1, m_F = -1\rangle$ and $|\downarrow\rangle = |F = 1, m_F = 0\rangle$ in ^{39}K at $B = 57.280(2)$ G where $a_{\uparrow\uparrow} = 32.5a_0$, $a_{\downarrow\downarrow} = 109a_0$, and $a_{\uparrow\downarrow} = -52.9a_0$ [226]. In this case, the inelastic interaction strengths are in general non-zero. However, since both energy and momentum must be conserved, inelastic processes involving two atoms in state $|-\rangle$ are energetically forbidden if the incoming relative momentum is small, as is the case in a BEC. To measure $a_{--} = mg_{--}/(4\pi\hbar^2)$, we start with a BEC in state $|\uparrow\rangle$ with $9(1) \times 10^4$ atoms in a crossed optical dipole trap (one beam propagating in the vertical, $\mathbf{e}_3$, direction and the other horizontally, along $\mathbf{e}_1$). We

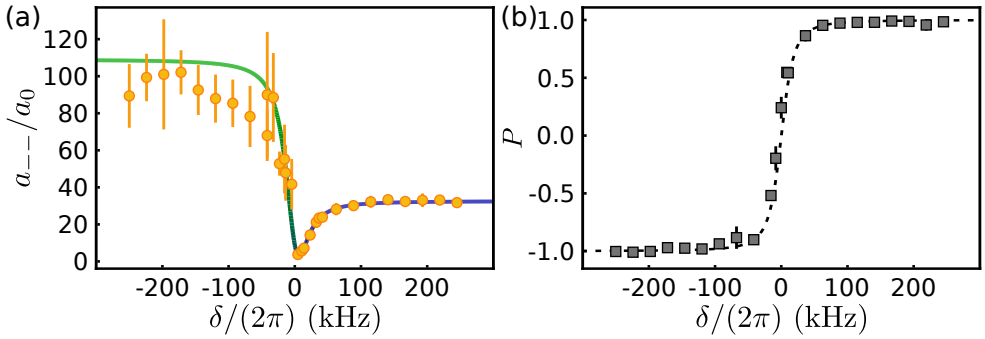

Figure 3.3: (a) Effective interactions of the lower energy dressed state, a_{--}, as a function of the detuning of the RF field determined from measurements of a BEC expanding in an optical waveguide. The coloured line is the theoretical prediction of a_{--}. (b) Bare state polarisation, P, as a function of detuning measured in time of flight. The dashed black line is the theoretical prediction of P. Data points and error bars come from means and standard deviations of five independent measurements.

turn on the coupling with $\Omega/(2\pi) = 20.0(6)$ kHz and $\delta/(2\pi) = 250(2)$ kHz where the uncertainty in detuning comes from the standard deviation of the magnetic field fluctuations measured in Sec. 3.1.2. We ramp the detuning to a chosen final value at a rate of $\mathrm{d}\delta/\mathrm{d}t = -5/6$ kHz ms^{-1} using a direct digital synthesis frequency generator[3]. Once the final detuning is reached, we keep the coupling field on and abruptly turn off the vertical trapping beam to allow the BEC to expand along an optical waveguide with radial trap frequency $\omega_r/(2\pi) = 133(1)$ Hz for 21 ms before taking an *in situ* image of the cloud [170].

To extract the effective scattering length we fit a Thomas-Fermi profile to the expanded BEC and use the relation $a_{--} \propto \sigma_x^5 N$ [212] where σ_x is the Thomas-Fermi radius along the waveguide and N is the atom number extracted from the fit. Extracting the effective scattering length through this scaling relation is advantageous because it allows us to account for atom losses during the experiment which are larger for negative detuning compared to positive detuning due to the high three-body recombination rate in state $|\downarrow\rangle$ [227]. Furthermore, by scaling the data with large positive detuning to yield $a_{\uparrow\uparrow}$, we eliminate systematic uncertainties in the atom number and initial trap frequencies.

Figure 3.3(a) shows the extracted values of a_{--} as a function of δ. The experimental data follows the theoretical predictions very well until $\delta < 0$ where the absolute discrepancies and uncertainties become larger. We have determined through numerical simulations of the dynamics that the absolute discrepancies stem from the breakdown of the Thomas-Fermi approximation as the atom number decreases [170, 217]. The Thomas-Fermi approximation is required for the scaling law to be valid. Additionally, we attribute the larger uncertainties to out of equilibrium initial sizes resulting from the sharp increase of a_{--} as δ becomes more negative and the finite time of the detun-

[3]Analog Devices, AD9958

ing sweep. The polarisation in the bare state basis which was measured in separate Stern-Gerlach experiments in time of flight is shown in Fig. 3.3(b) and shows good agreement with the theoretical prediction.

For the parameters in Fig. 3.3 the effective interactions in state $|-\rangle$ are always repulsive. By adjusting the bias magnetic field the bare state interactions can be adjusted such that $g_{--} < 0$ for a certain range of values of δ which enables the formation of dressed state bright solitons [170, 217]. For small values of Ω, an effective three-body force emerges [228] which has been observed as a repulsive beyond-mean-field interaction [229] and an attractive mean-field interaction [230] in different regimes.

In principle, the state $|+\rangle$ could also be prepared and, from Eq. 3.12, we would expect $g_{++}(\delta) = g_{--}(-\delta)$. However, as can also be seen from Eq. 3.12, two-body inelastic processes involving terms $\hat{\phi}_-^\dagger \hat{\phi}_-^\dagger \hat{\phi}_+ \hat{\phi}_+$ and $\hat{\phi}_-^\dagger \hat{\phi}_+^\dagger \hat{\phi}_+ \hat{\phi}_+$ provide two inelastic decay paths from the $|+\rangle$ state which are energetically allowed. The two processes are I: $|++\rangle \rightarrow |--\rangle$ and II: $|++\rangle \rightarrow (|+-\rangle + |-+\rangle)/\sqrt{2}$ [217]. For a BEC at rest, the inelastic processes lead to the generation of correlated pairs with equal and opposite momenta I: $|\mathbf{p}| = \sqrt{2m\hbar\tilde{\Omega}}$ and II: $|\mathbf{p}| = \sqrt{m\hbar\tilde{\Omega}}$. Depending on the depth of the trap, these atoms either escape from the trap resulting in atom loss from the BEC or remain in the trap resulting in heating. We have observed these inelastic collisions which take place on short time scales and limit the BEC lifetime to just a few milliseconds [170, 217].

3.2.3 State-Dependent Trapping With Coherent Coupling

In cold-atoms experiments, atoms are kept in a trap which gives the atomic cloud a finite extent. We can express an arbitrary state-dependent potential by adding a term $\hat{V} = \int \mathrm{d}^3\mathbf{r} \sum_{\sigma=\uparrow,\downarrow} \hat{\phi}_\sigma^\dagger V_\sigma(\mathbf{r}) \hat{\phi}_\sigma$ to the Hamiltonian. Transforming to the dressed state basis gives

$$\hat{V} = \int \mathrm{d}^3\mathbf{r} \begin{pmatrix} \hat{\phi}_+^\dagger & \hat{\phi}_-^\dagger \end{pmatrix} \begin{bmatrix} V_\uparrow \sin^2\theta + V_\downarrow \cos^2\theta & \sin\theta\cos\theta\,(V_\downarrow - V_\uparrow) \\ \sin\theta\cos\theta\,(V_\downarrow - V_\uparrow) & V_\uparrow \cos^2\theta + V_\downarrow \sin^2\theta \end{bmatrix} \begin{pmatrix} \hat{\phi}_+ \\ \hat{\phi}_- \end{pmatrix} \tag{3.13}$$

For small differences in $V_\uparrow(\mathbf{r})$ and $V_\downarrow(\mathbf{r})$, we can approximate the effect of RF dressing as creating unique potentials for each dressed state which are weighted sums of the original bare state potentials [231, 232]. However, in general, state-dependent potentials result in mixing between the dressed states [165]. For $V_\uparrow(\mathbf{r}) = V_\downarrow(\mathbf{r}) \equiv V(\mathbf{r})$ we recover $\hat{V} = \int \mathrm{d}^3\mathbf{r} \sum_{n=\pm} \hat{\phi}_n^\dagger V(\mathbf{r}) \hat{\phi}_n$ and we see that a state-independent trapping potential does not influence the RF coupling.

3.3 Momentum-Dependent Coherent Coupling of a Two Level System

So far we have seen that interactions in a BEC can be controlled by an external field used to coherently couple two internal states. In this section, we extend the scheme so that interactions can be controlled by the momentum of the BEC. We couple the

two states using two laser beams with wavelength λ_R and frequencies ω and $\omega + \Delta\omega$ ($0 < \Delta\omega/\omega \ll 1$) which intersect at an angle, ϑ. The two laser beams drive Raman coupling *via* an intermediate virtual electronic excited state as depicted in Fig. 3.4(a). The coherent coupling Hamiltonian is modified as [220, 233, 234]

$$\hat{H}_R = \int \mathrm{d}^3\mathbf{r} \begin{pmatrix} \hat{\phi}_\uparrow^\dagger & \hat{\phi}_\downarrow^\dagger \end{pmatrix} \hat{\mathcal{H}}_R \begin{pmatrix} \hat{\phi}_\uparrow \\ \hat{\phi}_\downarrow \end{pmatrix} \tag{3.14}$$

with

$$\hat{\mathcal{H}}_R \doteq \begin{bmatrix} -\frac{\hbar^2}{2m}\nabla^2 - \frac{\hbar\delta_0}{2} & \frac{\hbar\Omega}{2}\exp(2ik_R x) \\ \frac{\hbar\Omega}{2}\exp(-2ik_R x) & -\frac{\hbar^2}{2m}\nabla^2 + \frac{\hbar\delta_0}{2} \end{bmatrix} \tag{3.15}$$

where $\delta_0 = \Delta\omega - \omega_0$ and $k_R = 2\pi \sin(\vartheta/2)/\lambda_R$.

To diagonalise the noninteracting Hamiltonian in Eq. 3.15, we start by applying the unitary transformation defined by [63, 64, 67, 165, 220, 233–235]

$$\hat{U}_R \doteq \begin{bmatrix} \exp(-ik_R x) & 0 \\ 0 & \exp(ik_R x) \end{bmatrix}. \tag{3.16}$$

We have

$$\hat{H}_R = \int \mathrm{d}^3\mathbf{r} \begin{pmatrix} \hat{\phi}_\uparrow^\dagger & \hat{\phi}_\downarrow^\dagger \end{pmatrix} \hat{U}_R^\dagger \hat{U}_R \hat{\mathcal{H}}_R \hat{U}_R^\dagger \hat{U}_R \begin{pmatrix} \hat{\phi}_\uparrow \\ \hat{\phi}_\downarrow \end{pmatrix} \tag{3.17}$$

$$\Rightarrow \hat{H}_R = \int \mathrm{d}^3\mathbf{r} \begin{pmatrix} \hat{\phi}_\uparrow'^\dagger & \hat{\phi}_\downarrow'^\dagger \end{pmatrix} \hat{\mathcal{H}}_R' \begin{pmatrix} \hat{\phi}_\uparrow' \\ \hat{\phi}_\downarrow' \end{pmatrix} \tag{3.18}$$

where $\hat{\phi}_\uparrow' = \exp(-ik_R x)\hat{\phi}_\uparrow$, $\hat{\phi}_\downarrow' = \exp(ik_R x)\hat{\phi}_\downarrow$ and

$$\hat{\mathcal{H}}_R' \doteq \begin{bmatrix} \frac{(-i\hbar\partial_x + \hbar k_R)^2}{2m} - \frac{\hbar^2}{2m}\nabla_\perp^2 - \frac{\hbar\delta_0}{2} & \frac{\hbar\Omega}{2} \\ \frac{\hbar\Omega}{2} & \frac{(-i\hbar\partial_x - \hbar k_R)^2}{2m} - \frac{\hbar^2}{2m}\nabla_\perp^2 + \frac{\hbar\delta_0}{2} \end{bmatrix} \tag{3.19}$$

where $\nabla_\perp^2 = \partial_y^2 + \partial_z^2$. Note that although the unitary transformation appears to have shifted the bare states to be moving with equal and opposite momentum $\pm\hbar k_R \mathbf{e}_1$, the velocity in the laboratory frame has not been changed since the dispersions have been correspondingly modified as $\epsilon_{\uparrow,\downarrow} = \hbar^2(k_x \pm k_R)^2/(2m) \mp \hbar\delta_0/2 + \hbar^2\mathbf{k}_\perp^2/(2m)$ as shown by the dashed lines in Fig. 3.4(b). The velocity along the x-axis in the laboratory frame is [236] $\mathbf{v}_{\uparrow,\downarrow} = \mathbf{e}_1\partial_{k_x}\epsilon_{\uparrow,\downarrow}/\hbar = \mathbf{e}_1\hbar(k_x \pm k_R)/m$ where $\hbar k_x = \hbar\mathbf{k}\cdot\mathbf{e}_1$ is called the quasimomentum along the x-axis in analogy to lattices [237]. The transverse quasimomentum, $\hbar\mathbf{k}_\perp = \hbar k_y\mathbf{e}_2 + \hbar k_z\mathbf{e}_3$, is not impacted by the unitary transformation defined by $\hat{U}_R$.

Notice that since the density and spin density operators, $\hat{n} = \hat{\phi}_\uparrow^\dagger\hat{\phi}_\uparrow + \hat{\phi}_\downarrow^\dagger\hat{\phi}_\downarrow$ and $\hat{s} = \hat{\phi}_\uparrow^\dagger\hat{\phi}_\uparrow - \hat{\phi}_\downarrow^\dagger\hat{\phi}_\downarrow$, commute with $\hat{U}_R$, these physical observables are not modified by the unitary transformation [163]. Also note that the signs in front of k_R are arbitrary and can be exchanged by switching the propagation directions of the two laser beams depicted in Fig. 3.4(a).

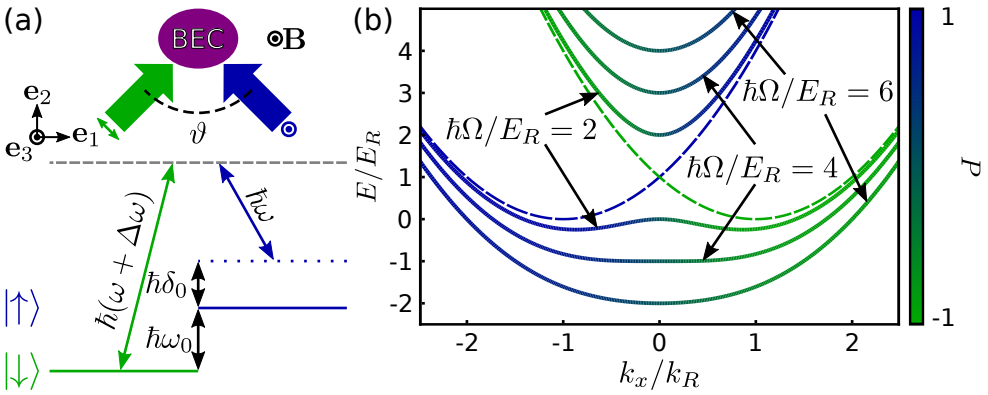

Figure 3.4: (a) Two laser beams intersecting at angle ϑ with frequency difference $\Delta\omega$ couple states $|\downarrow\rangle$ and $|\uparrow\rangle$ in a BEC with two-photon detuning $\delta_0 = \Delta\omega - \omega_0$ and Rabi frequency Ω in the presence of a bias magnetic field $\mathbf{B}$ pointing along the z-axis. (b) The dashed blue (green) line shows the dispersion relation, $\epsilon_\uparrow$ ($\epsilon_\downarrow$), of the bare state $|\uparrow'\rangle$ ($|\downarrow'\rangle$) as a function of the component of the quasimomentum along the x-axis. The coloured lines represent the energies of the upper and lower dressed bands for $\hbar\delta_0/E_R = 0$ at different Raman coupling strengths. The colour scale represents the projections of the dressed states onto the bare spin basis.

To proceed with the diagonalisation, we transform the Hamiltonian to momentum space

$$\hat{H}_{0,R} = \int \frac{\mathrm{d}^3\mathbf{k}}{(2\pi)^3} \begin{bmatrix} \hat{\Phi}'^{\dagger}_{\uparrow}(\mathbf{k}) & \hat{\Phi}'^{\dagger}_{\downarrow}(\mathbf{k}) \end{bmatrix} \hat{\mathcal{H}}'_R(\mathbf{k}) \begin{bmatrix} \hat{\Phi}'_{\uparrow}(\mathbf{k}) \\ \hat{\Phi}'_{\downarrow}(\mathbf{k}) \end{bmatrix} \tag{3.20}$$

where

$$\hat{\mathcal{H}}'_R(\mathbf{k}) \doteq \begin{bmatrix} \frac{\hbar^2}{2m}\left(k_x + k_R\right)^2 + \frac{\hbar^2}{2m}\mathbf{k}_\perp^2 - \frac{\hbar\delta_0}{2} & \frac{\hbar\Omega}{2} \\ \frac{\hbar\Omega}{2} & \frac{\hbar^2}{2m}\left(k_x - k_R\right)^2 + \frac{\hbar^2}{2m}\mathbf{k}_\perp^2 + \frac{\hbar\delta_0}{2} \end{bmatrix} \tag{3.21}$$

We can diagonalise $\hat{\mathcal{H}}'_R(\mathbf{k})$ using the momentum-dependent unitary operator

$$\hat{U}(k_x) \doteq \begin{pmatrix} \sin\left[\theta(k_x)\right] & -\cos\left[\theta(k_x)\right] \\ \cos\left[\theta(k_x)\right] & \sin\left[\theta(k_x)\right] \end{pmatrix} \tag{3.22}$$

where $\cos\left[\theta(k_x)\right] = \left\{\left[1 + \tilde{\delta}(k_x)/\tilde{\Omega}(k_x)\right]/2\right\}^{\frac{1}{2}}$, $\hbar\tilde{\delta}(k_x)/E_R = \hbar\delta_0/E_R - 4k_x/k_R$, and $\tilde{\Omega}(k_x)^2 = \Omega^2 + \tilde{\delta}(k_x)^2$, and we have defined the single photon recoil energy $E_R = \hbar^2 k_R^2/(2m)$.

The dressed states have momentum-dependent representations in the bare spin basis $|+,\mathbf{k}\rangle = \cos\left[\theta(k_x)\right]|\downarrow',\mathbf{k}\rangle + \sin\left[\theta(k_x)\right]|\uparrow',\mathbf{k}\rangle$ and $|-,\mathbf{k}\rangle = \sin\left[\theta(k_x)\right]|\downarrow',\mathbf{k}\rangle - \cos\left[\theta(k_x)\right]|\uparrow',\mathbf{k}\rangle$. The dressed state energies are also momentum-dependent with $\hat{\mathcal{H}}'_R(\mathbf{k})\,|\pm,\mathbf{k}\rangle = \varepsilon_\pm(\mathbf{k})\,|\pm,\mathbf{k}\rangle$ where $\varepsilon_\pm(\mathbf{k}) = \hbar^2\left(k_x^2 + \mathbf{k}_\perp^2 + k_R^2\right)/(2m) \pm \hbar\tilde{\Omega}(k_x)/2$ and rather than dressed states we refer to $|+,\mathbf{k}\rangle$ and $|-,\mathbf{k}\rangle$ as the upper and lower dressed

bands. We have $\langle +, k_x\mathbf{e}_1 + \mathbf{k}_{\perp,1}| -, k_x\mathbf{e}_1 + \mathbf{k}_{\perp,2}\rangle = 0$ for any value of k_x but in general, within a band we have $\langle \pm, k_{x,1}\mathbf{e}_1 + \mathbf{k}_{\perp,1}| \pm, k_{x,2}\mathbf{e}_1 + \mathbf{k}_{\perp,2}\rangle \neq 0$. The exception being $k_{x,1} \to \pm\infty$ and $k_{x,2} \to \mp\infty$.

The energies of the upper and lower dressed bands are shown in Fig. 3.4(b) as functions of k_x for $\hbar\Omega/E_R = 2$, $\hbar\Omega/E_R = 4$, and $\hbar\Omega/E_R = 6$ with $\hbar\delta_0/E_R = 0$. We can see that $\varepsilon_+(\mathbf{k})$ is always greater than the bare state kinetic energies $\epsilon_{\uparrow,\downarrow} = \hbar^2(k_x \pm k_R)^2/(2m)$ while $\varepsilon_-(\mathbf{k})$ is always less. The upper dressed band has a global minimum value with the location given by the recursive relation $k_x/k_R = \tilde{\delta}(k_x)/\tilde{\Omega}(k_x)$. The lower band has three extremal values (two minima with a maximum in between) if $\hbar\Omega/E_R < 4$ and $\hbar|\delta_0|/E_R < 4\left\{1 - [\hbar\Omega/(4E_R)]^{2/3}\right\}^{3/2}$ or a single global minimum otherwise. In both cases, the locations of the extremal values of the lower band are given by $k_x/k_R = -\tilde{\delta}(k_x)/\tilde{\Omega}(k_x)$.

3.3.1 Effective Interactions in a Raman Coupled Bose-Einstein Condensate

The second quantised Hamiltonian for a two-component Raman coupled BEC in the presence of interactions is $\hat{H}_R = \hat{H}_{0,R} + \hat{H}_{\text{int}}$. Let $\hat{\Phi}^\dagger_\pm(\mathbf{k})$ ($\hat{\Phi}_\pm(\mathbf{k})$) be the field operator that creates (annihilates) a particle in state $|\pm, \mathbf{k}\rangle$ with corresponding position space representation $\hat{\phi}_\pm(\mathbf{r}) = \int \frac{\mathrm{d}^3\mathbf{k}}{(2\pi)^3}\hat{\Phi}_\pm(\mathbf{k})\exp(i\mathbf{k}\cdot\mathbf{r})$. The noninteracting part of the second quantised Hamiltonian in the dressed basis is $\hat{H}_{0,R} = \sum_{n=\pm}\int \frac{\mathrm{d}^3\mathbf{k}}{(2\pi)^3}\hat{\Phi}^\dagger_n(\mathbf{k})\varepsilon_n(\mathbf{k})\hat{\Phi}_n(\mathbf{k})$. To understand the interactions of the dressed states, $|\pm, \mathbf{k}\rangle$, we follow the methodology of Williams *et al.* [237]. As we did for the RF dressed states, we can also express the second quantised Hamiltonian for the two-body contact interactions in the dressed basis as $\hat{H}_{\text{int},R} = \frac{1}{2}\int \frac{\mathrm{d}^3\mathbf{k}_4}{(2\pi)^3}\frac{\mathrm{d}^3\mathbf{k}_3}{(2\pi)^3}\frac{\mathrm{d}^3\mathbf{k}_2}{(2\pi)^3}\frac{\mathrm{d}^3\mathbf{k}_1}{(2\pi)^3}\hat{\mathcal{H}}_{\text{int},R}$ with

$$\begin{aligned}\hat{\mathcal{H}}_{\text{int},R} = &\sum_{n_1',n_2',n_1,n_2=\pm}\hat{\Phi}^\dagger_{n_1'}(\mathbf{k}_4)\hat{\Phi}^\dagger_{n_2'}(\mathbf{k}_3)\hat{\Phi}_{n_1}(\mathbf{k}_2)\hat{\Phi}_{n_2}(\mathbf{k}_1)\\ &\times\sum_{\sigma_1,\sigma_2=\uparrow,\downarrow} g_{\sigma_1\sigma_2}U_{n_1'\sigma_1}(k_{x,4})U^\dagger_{\sigma_1 n_1}(k_{x,2})U_{n_2'\sigma_2}(k_{x,3})U^\dagger_{\sigma_2 n_2}(k_{x,1})\\ &\times\delta^{(3)}(\mathbf{k}_3 + \mathbf{k}_4 - \mathbf{k}_1 - \mathbf{k}_2)\end{aligned} \tag{3.23}$$

where $k_{x,j} = \mathbf{k}_j \cdot \mathbf{e}_1$.

It has been shown that inelastic collision processes which cause atoms in the upper dressed band to populate the lower dressed band are significant even when $g_{\uparrow\uparrow} = g_{\downarrow\downarrow} = g_{\uparrow\downarrow}$ [237, 238]. Therefore, we assume that the BEC is prepared in the lower dressed band, which is valid provided that the excitations are small compared to the band separation, $\tilde{\Omega}(k_x)$ [236]. So, we have $\hat{H}_{0,R} = \int \frac{\mathrm{d}^3\mathbf{k}}{(2\pi)^3}\hat{\Phi}^\dagger_-(\mathbf{k})\varepsilon_-(\mathbf{k})\hat{\Phi}_-(\mathbf{k})$ and

$$\hat{\mathcal{H}}_{\text{int},R} = \hat{\Phi}^\dagger_-(\mathbf{k}_4)\hat{\Phi}^\dagger_-(\mathbf{k}_3)\hat{\Phi}_-(\mathbf{k}_2)\hat{\Phi}_-(\mathbf{k}_1)\chi(k_{x,1},k_{x,2},k_{x,3},k_{x,4})\,\delta^{(3)}(\mathbf{k}_3 + \mathbf{k}_4 - \mathbf{k}_1 - \mathbf{k}_2) \tag{3.24}$$

where

$$\chi(k_{x,1},k_{x,2},k_{x,3},k_{x,4}) = \sum_{\sigma_1,\sigma_2} g_{\sigma_1\sigma_2}U_{-\sigma_1}(k_{x,4})U^\dagger_{\sigma_1-}(k_{x,2})U_{-\sigma_2}(k_{x,3})U^\dagger_{\sigma_2-}(k_{x,1}) \tag{3.25}$$

is referred to as the screening function by Williams *et al.* [237]. Letting $C_j = \cos[\theta(k_{x,j})]$ and $S_j = \sin[\theta(k_{x,j})]$, we have

$$\chi(k_{x,1}, k_{x,2}, k_{x,3}, k_{x,4}) = g_{\uparrow\uparrow} C_2 C_4 C_1 C_3 + g_{\downarrow\downarrow} S_2 S_4 S_1 S_3 + g_{\uparrow\downarrow} (C_2 C_4 S_1 S_3 + S_2 S_4 C_1 C_3). \tag{3.26}$$

Note that for $k_{x,1} = k_{x,2} = k_{x,3} = k_{x,4} = 0$ we recover the effective interaction parameter g_{--} of the RF dressed states.

3.3.2 Trapping Potential

As we did in Sec. 3.2.3, we consider the effect of an arbitrary state-dependent trapping potential. We note that $\mathrm{diag}[V_\uparrow(\mathbf{r}), V_\downarrow(\mathbf{r})]$ commutes with $\hat{U}_R$ so in the bare basis, we have $\hat{V} = \int \mathrm{d}^3\mathbf{r} \sum_{\sigma=\uparrow,\downarrow} \hat{\phi}'^\dagger_\sigma V_\sigma(\mathbf{r}) \hat{\phi}'_\sigma$. Transforming to momentum space and the dressed basis, we have

$$\hat{V} = \int \frac{\mathrm{d}^3\mathbf{k}_2}{(2\pi)^3} \frac{\mathrm{d}^3\mathbf{k}_1}{(2\pi)^3} \begin{bmatrix} \hat{\Phi}^\dagger_+(\mathbf{k}_2) & \hat{\Phi}^\dagger_-(\mathbf{k}_2) \end{bmatrix} \hat{\mathcal{V}}(\mathbf{k}_1, \mathbf{k}_2) \begin{bmatrix} \hat{\Phi}_+(\mathbf{k}_1) \\ \hat{\Phi}_-(\mathbf{k}_1) \end{bmatrix} \tag{3.27}$$

where

$$\hat{\mathcal{V}}(\mathbf{k}_1, \mathbf{k}_2) \doteq \begin{pmatrix} \tilde{V}_\uparrow S_1 S_2 + \tilde{V}_\downarrow C_1 C_2 & \tilde{V}_\downarrow S_1 C_2 - \tilde{V}_\uparrow C_1 S_2 \\ \tilde{V}_\downarrow C_1 S_2 - \tilde{V}_\uparrow S_1 C_2 & \tilde{V}_\uparrow C_1 C_2 + \tilde{V}_\downarrow S_1 S_2 \end{pmatrix} \tag{3.28}$$

with $\tilde{V}_\sigma = \int \mathrm{d}^3\mathbf{r} V_\sigma \exp[i(\mathbf{k}_1 - \mathbf{k}_2) \cdot \mathbf{r}]$. Even in the case that $V_\uparrow = V_\downarrow$, the dressed state mixing terms are in general not zero [165, 239]. Typically, the trap mediated promotion of atoms from the lower dressed band to the upper dressed band is negligible and we have $\hat{V} \approx \int \frac{\mathrm{d}^3\mathbf{k}_2}{(2\pi)^3} \frac{\mathrm{d}^3\mathbf{k}_1}{(2\pi)^3} \hat{\Phi}^\dagger_-(\mathbf{k}_2) V_-(\mathbf{k}_1, \mathbf{k}_2) \hat{\Phi}_-(\mathbf{k}_1)$ where $V_-(\mathbf{k}_1, \mathbf{k}_2) = \tilde{V}_\uparrow C_1 C_2 + \tilde{V}_\downarrow S_1 S_2$.

3.4 Experimental implementation of Raman coupling

We implement Raman coupling using light of wavelength $\lambda_R = 768.97$ nm and we set $\vartheta = \pi$ which corresponds to $E_R/(2\pi\hbar) = 8.66$ kHz and $E_R/(2\pi\hbar) = 8.24$ kHz for ^{39}K and ^{41}K, respectively. This wavelength is referred to as the tuneout wavelength [240, 241] and is the wavelength which cancels the scalar light shift discussed in Sec. 2.3 for π-polarised light in potassium [209, 210]. The two Raman beams propagate along the x-axis in the $\pm\mathbf{e}_1$ directions and a bias magnetic field, $\mathbf{B} = B_0\mathbf{e}_3$, sets the quantisation axis and energy splitting between states $|\uparrow\rangle$ and $|\downarrow\rangle$ as well as controlling the bare state interactions *via* Feshbach resonances [226, 242–245].

Since the projection of the total angular momentum along the quantisation axis changes by one when the state is changed from $|\uparrow\rangle$ to $|\downarrow\rangle$, one of the beams must have $\sigma^\pm$ polarisation components [207]. The two beams are set with orthogonal linear polarisations, one beam polarised along the z-axis corresponding to π-polarisation and the other along the y-axis corresponding to equal proportions of σ^+ and σ^- polarisation which cancels the scalar light shift for all states in the $F = 1$ manifold at the tuneout wavelength [209]. Furthermore, the chosen polarisations have a vector product which is orthogonal to the quantisation axis which maximises the Rabi frequency

for a given optical intensity [233]. Using the tuneout wavelength also ensures that the ratio of Rabi frequency to inelastic photon scattering is maximised [207]. Finally, the orthogonal polarisations of the two beams ensure that there can be no interference between the two beams and therefore no optical lattice can be formed, regardless of the value of $\Delta\omega$.

The laser light for Raman coupling is sourced from a commercial external cavity diode laser[4] and amplified by a tapered amplifier[5]. The tapered amplifier is protected from back reflections by an optical isolator[6]. Resonant light from the amplified spontaneous emission spectrum of the tapered amplifier is reduced by passing the light through a series of three interference filters[7]. The light is split into two paths using a polarising beam splitter[8]. To control the value of $\Delta\omega$ the two beams are each passed through an acousto-optic modulator[9] (AOM) where one AOM is driven by a fixed frequency generator[10] and the other is driven by an arbitrary waveform generator[11]. By modifying the frequency difference between the acousto-optic modulators we can directly modify the frequency difference, $\Delta\omega$, between the +1 order diffracted beams. The first version of the Raman coupling optical setup was constructed by Manon Ballu as part of a Master's internship [246].

The frequency shifted beams are coupled to optical fibres[12] to ensure that only the first order diffracted light is present in the experiment. Polarisation is controlled on both sides of the optical fibres using polarising beam splitters[13] for cleaning and $\lambda/2$-plates[14] for setting. At the output of the optical fibres, beam samplers[15] allow a small amount of light to be collected on silicon photodiodes[16] for optical power stabilisation which is achieved by actively modulating the RF power in the acousto-optic modulators using voltage controlled attenuators[17] under the influence of proportional-integral-derivative (PID) controllers. The Raman beams are overlapped with the optical dipole trap beam which forms the optical waveguide using dichroic mirrors[18] and are focused onto the atoms using 300 mm focal length lenses[19] resulting in $1/\exp(2)$ radii of ~ 80 μm which is small enough to achieve the necessary optical intensities with moderate amounts of optical power while being large enough to not break the plane

[4] Toptica, DL-Pro
[5] Eagleyard, EYP-TPA-0765-01500-3006-CMT03-0000
[6] Thorlabs, IOT-5-780-VLP
[7] LaserOptik, IF780/6deg; Semrock, LL01-780-12.5; Semrock, SP01-785RU-2.5
[8] Foctek, PBS0649-650-850nm
[9] Suitable combinations of Intraaction, ATM-601A1, ATM-801A1, ATM-1101A1, and ATM-2001A1, depending on the desired frequency difference.
[10] Rhode and Schwarz, SMC100A
[11] Signadyne, SD AOU-H3444-PXIe-1G
[12] Thorlabs, P3-630PM-FC-10 with Schäfter+Kirchoff, 60FC-4-A6.2S output collimator
[13] QiOptiq, G335525000
[14] Foctek, WPF212H true zero order 768.4 nm
[15] Thorlabs, BSF10
[16] Osram, BPX-65
[17] Mini-Circuits, ZX73-2500-S+
[18] Thorlabs, DMSP1000L and DMLP950L
[19] Thorlabs, LA4579-B-f=300mm

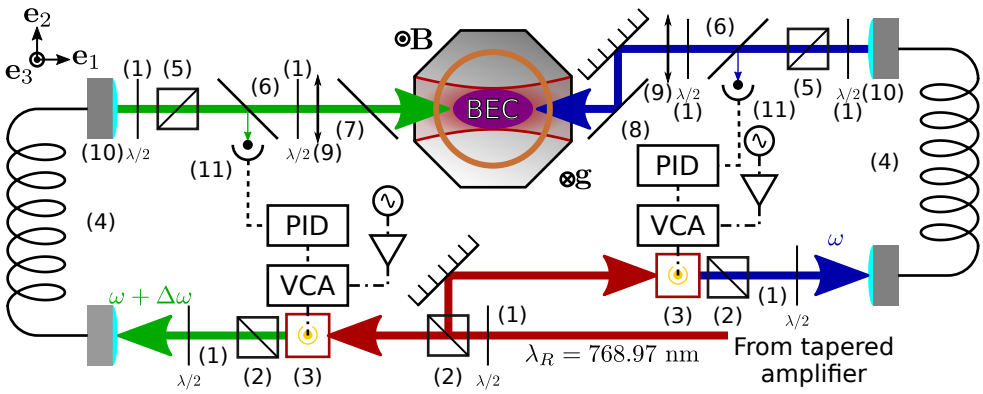

Figure 3.5: A BEC is trapped in an optical waveguide propagating along the x-axis inside a vacuum chamber with a bias magnetic field set along the z-axis by a pair of Bitter coils. The BEC is coupled by a pair of laser beams which are counter propagating along the x-axis and with their frequencies controlled independently by acousto-optic modulators. The optical elements shown are (1) $\lambda/2$-plate, Foctek WPF212H; (2) polarising beam splitter, Foctek PBS0649-650-850nm; (3) acousto-optic modulator, various (see footnote 9); (4) optical fibre, Thorlabs P3-630PM-FC-10; (5) polarising beam splitter, QiOptiq G335525000; (6) beam sampler, Thorlabs BSF10; (7) dichroic mirror, Thorlabs DMSP1000L; (8) dichroic mirror, Thorlabs DMLP950L; (9) 300 mm focal length lens, Thorlabs LA4579-B-f=300mm; (10) output coupler, Schäfter+Kirchoff, 60FC-4-A6.2S; (11) photodiode, Osram BPX-65. Dashed lines represent slowly varying electrical signals and dashed-dotted lines represent radio frequency electrical signals.

wave approximation used in Eq. 3.15. A simplified schematic of the Raman optical setup is shown in Fig. 3.5.

3.4.1 Rabi Flopping Dynamics with Raman Coupling

The Rabi flopping dynamics with Raman coupling are similar to the case of RF coupling discussed in Sec. 3.1.1. The crucial difference is the dependence of both the energy and bare state composition of the dressed states on the quasimomentum. If the initial state is $|\downarrow'\rangle$ and the atoms initially have zero group velocity in the laboratory frame then the quasimomentum is $k_x/k_R = 1$. If at time $t = 0$ we suddenly turn on the Raman beams with Rabi frequency Ω and detuning δ_0 quasimomentum will be conserved [65] so the state expressed in the dressed basis is $|\psi(0), k_x/k_R = 1\rangle = |\downarrow', k_x/k_R = 1\rangle = \cos[\theta(k_R)]\,|+, k_x/k_R = 1\rangle + \sin[\theta(k_R)]\,|-, k_x/k_R = 1\rangle$. As in the RF case, the state evolves according to the Schrödinger equation: $|\psi(t), k_x/k_R = 1\rangle = \cos[\theta(k_R)] \exp\left[-i\tilde{\Omega}(k_R)\right]|+, k_x/k_R = 1\rangle + \sin[\theta(k_R)] \exp\left[i\tilde{\Omega}(k_R)\right]|-, k_x/k_R = 1\rangle$ after a pulse duration τ the projection into state $|\uparrow'\rangle$ can be measured by suddenly turning off the Raman beams as $P_{\uparrow'}(\tau) = \left[\Omega/\tilde{\Omega}(k_R)\right]^2 \sin^2\left[\tilde{\Omega}(k_R)\tau/2\right]$.

So, we see that rather the requiring $\delta_0 = 0$ to achieve full contrast in Rabi oscillations, we require $\tilde{\delta}(k_R) = 0 \Rightarrow \delta_0 = 4E_R/\hbar$. This can be understood in terms of the kinetic energy of the bare state $|\uparrow'\rangle$. The quasimomentum is conserved when

the Raman beams are switched off [65] so the atoms projected into state $|\uparrow'\rangle$ have a velocity in the laboratory frame of $\mathbf{v} = 2\hbar k_R \mathbf{e}_1/m$ corresponding to a kinetic energy of $2\hbar^2 k_R^2/m = 4E_R$ [220]. The conservation of quasimomentum can also be thought of in analogy to band mapping of an optical lattice [35] in which case we would reframe the discussion in terms of mapping the quasimomentum in the Raman dressed band to the free particle momentum. This means that rather than seeing the two spin states separated vertically by the Stern-Gerlach gradient in a time of flight measurement, we see the vertical displacement as well as a horizontal displacement corresponding to the momentum imparted on the atoms which have changed state.

This effect can also be understood without invoking the dressed states. An atom initially in state $|\downarrow'\rangle$ can be promoted to a virtual electronically excited state by absorbing a photon from the beam with frequency $\omega + \Delta\omega$ (shown propagating in the $\mathbf{e}_1$ direction in Fig. 3.5) and gaining momentum $\hbar k_R \mathbf{e}_1$. Since the electronic state is only virtually populated, the atom must either return to the groundstate manifold through spontaneous emission (inelastic photon scattering) or to state $|\uparrow'\rangle$ through stimulated emission into the beam with frequency ω with another momentum gain of $\hbar k_R \mathbf{e}_1$ [247]. The same logic holds for transfer from $|\uparrow'\rangle$ to $|\downarrow'\rangle$ but with the momentum in the opposite direction, in this case the energy difference between the two bare states is reduced by $4E_R$ since the kinetic energy is always added to the final state. Thus, for Rabi flopping dynamics starting with atoms in state $|\uparrow'\rangle$ at rest, the optimal detuning is $\delta_0 = -4E_R/\hbar$ which is also the result $\hbar\tilde{\delta}(-k_R)/E_R = 0$ obtained when doing the calculation with dressed states.

In fact, we do not need to assume that the atoms are initially at rest. To get maximum contrast in Rabi oscillations it is only necessary to have $\hbar\tilde{\delta}(k_x)/E_R = 0$ and the velocity of atoms which project into the initial state will be unchanged by the Rabi flopping while the momentum difference of atoms projected into two different bare states will always be $2\hbar k_R \mathbf{e}_1$. The requirement $\hbar\tilde{\delta}(k_x)/E_R = 0$ can be understood in the absorption and stimulated emission picture in terms of Doppler shifts of the frequencies of the two Raman beams.

The Raman Rabi flopping dynamics starting in state $|\downarrow'\rangle$ and with detuning $\delta_0 = 4E_R/\hbar$ are demonstrated in Fig. 3.6. In this case we use the states $|F = 1, m_F = 0\rangle$ and $|F = 1, m_F = -1\rangle$ of ^{41}K as $|\downarrow'\rangle$ and $|\uparrow'\rangle$, respectively. We apply a bias field of $B = 338.4$ G where we have $\mathrm{d}\omega_0/\mathrm{d}B/(2\pi) \approx 0.1$ Hz/mG and $a_{\downarrow\downarrow} \approx a_{\uparrow\uparrow} \approx a_{\uparrow\downarrow} \approx 61a_0$. Figure 3.6(a) shows absorption images of the atomic clouds in time of flight with Stern-Gerlach separation following Raman pulse times of 15 μs, 30 μs, and 60 μs and Fig. 3.6(b) shows the extracted projection onto state $|\uparrow'\rangle$, $P_{\uparrow'}$, as a function of pulse time, τ. A fit to the data gives $\Omega/(2\pi) = 16.82(5)$ kHz or $\hbar\Omega/E_R = 2.042(6)$.

The Rabi frequency is proportional to the intensity of light at the atoms [207]. To optimise the alignment of the Raman beams on the atoms, we first calibrate the magnetic field using RF pulses and then adjust the alignment of the two beams to minimise the π-pulse time with fixed optical power and $\hbar\tilde{\delta}(k_x)/E_R = 0$. Later, we calibrate the Rabi frequency by measuring the population transfer as a function of pulse time. Once the Rabi frequency is calibrated, we can vary it by setting the optical power in the two laser beams to be equal with a value of P_Ω which gives

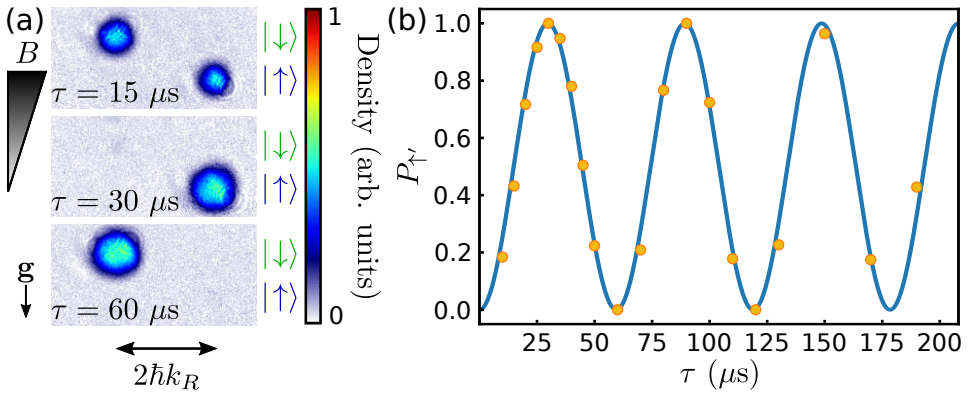

Figure 3.6: (a) Atoms initially at rest in state $|\downarrow'\rangle$ are subjected to a pulse of Raman light with detuning $\delta_0 = 4E_R/\hbar$. A magnetic field gradient is used to create a vertical separation between atoms in states $|\downarrow'\rangle$ and $|\uparrow'\rangle$ in time of flight. The Raman pulse imparts a momentum $2\hbar k_R \mathbf{e}_1$ onto atoms in state $|\uparrow\rangle$ in the laboratory frame, resulting in an additional horizontal displacement. The imaging beam propagates in the $(\mathbf{e}_1 + \mathbf{e}_2)/\sqrt{2}$ direction. (b) Projection onto state $|\uparrow'\rangle$ as a function of pulse time. The blue line is a fit to the data with $\Omega/(2\pi) = 16.82(5)$ kHz. Error bars correspond to the fit uncertainties and are smaller than the data markers.

$\Omega \propto P_\Omega$ [207]. Since the pulses are typically on the order of 10 μs, we are not able to stabilise the optical power using the PID controllers during the calibration and instead the RF power in the AOMs is switched rapidly using RF switches[20]. Power fluctuations result in an upper estimate of the relative uncertainty in Ω of 6 %.

3.4.2 Measurement of the Raman Dressed Dispersion Relations

The dispersion relation of the lower Raman dressed band could be measured, in principle, by tracking the velocity of a BEC as a function of momentum. However, such a measurement would require accurate and precise control of the group momentum of the BEC without restoring forces along the x-axis. Additionally, in the double well regime, the BEC would experience instabilities in the region of $k_x/k_R \approx 0$ due to negative effective mass [236] (see Sec. 5.2.2). While free of negative effect mass effects, the upper dressed band could also not be mapped using this technique since it is not stable against inelastic band changing collisions [237]. A method to precisely map both dressed bands, called spin injection spectroscopy, was developed by Cheuk *et al.* [248].

Spin injection spectroscopy of the Raman dressed bands is illustrated in Fig. 3.7. We consider the existence of two additional auxiliary states $|\text{aux}, \downarrow, \mathbf{k}\rangle$ and $|\text{aux}, \uparrow, \mathbf{k}\rangle$ with $|\text{aux}, \downarrow, \mathbf{k}\rangle$ lower in energy than both of the coupled bare states $|\downarrow', \mathbf{k}\rangle$ and $|\uparrow', \mathbf{k}\rangle$ and $|\text{aux}, \uparrow, \mathbf{k}\rangle$ higher in energy than both bare states. We assume that the

[20] Mini-circuits, ZASWA-2-50DRA+

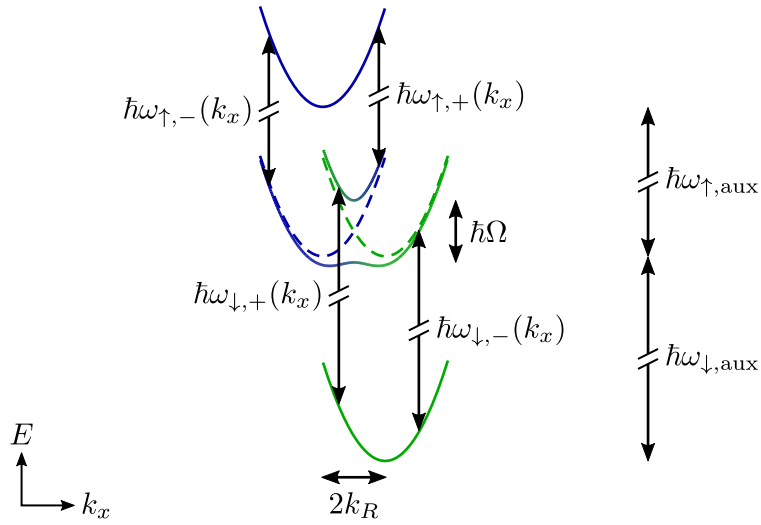

Figure 3.7: Energy level diagram for spin injection spectroscopy of Raman dressed bands. The state $|\mathrm{aux},\uparrow,\mathbf{k}\rangle$ ($|\mathrm{aux},\downarrow,\mathbf{k}\rangle$) with dispersion shown by the solid blue (green) line has an allowed transition to state $|\uparrow',\mathbf{k}\rangle$ ($|\downarrow',\mathbf{k}\rangle$) with momentum-independent transition frequency $\omega_{\uparrow,\mathrm{aux}}$ ($\omega_{\downarrow,\mathrm{aux}}$). The strength of the transitions between state $|\mathrm{aux},\uparrow,\mathbf{k}\rangle$ ($|\mathrm{aux},\downarrow,\mathbf{k}\rangle$) and the dressed bands is dependent on the spin polarisation of the dressed state which is encoded in the colour scale. The transition frequencies have momentum-dependent values $\omega_{\uparrow,\pm}(k_x)$ ($\omega_{\downarrow,\pm}(k_x)$).

$|\mathrm{aux},\downarrow,\mathbf{k}\rangle \leftrightarrow |\downarrow',\mathbf{k}\rangle$ and $|\mathrm{aux},\uparrow,\mathbf{k}\rangle \leftrightarrow |\uparrow',\mathbf{k}\rangle$ transitions are allowed while the $|\mathrm{aux},\downarrow,\mathbf{k}\rangle \leftrightarrow |\uparrow',\mathbf{k}\rangle$ and $|\mathrm{aux},\uparrow,\mathbf{k}\rangle \leftrightarrow |\downarrow',\mathbf{k}\rangle$ transitions are forbidden. In the transformation to quasimomentum, each of the auxiliary states transforms in the same manner as the energetically adjacent coupled state. Thus, the transition frequencies, $\omega_{\downarrow,\mathrm{aux}}$ and $\omega_{\uparrow,\mathrm{aux}}$, between the auxiliary states and the bare states are independent of momentum.

The strength of the transitions between the auxiliary states and the Raman dressed bands are dependent on the projections of the Raman dressed states onto the bare states and are therefore both band- and momentum-dependent. Likewise, the energy differences between the auxiliary states and the Raman dressed bands are momentum-dependent due to the modified dispersion relations of the Raman dressed bands. The momentum-dependent transition frequencies between the auxiliary states and the Raman dressed bands are straight forward to calculate. The resonant frequency for the $|\mathrm{aux},\downarrow,\mathbf{k}\rangle \leftrightarrow |\pm,\mathbf{k}\rangle$ transition is $\omega_{\downarrow,\pm}(k_x) = \omega_{\downarrow,\mathrm{aux}} - \tilde{\delta}(k_x)/2 \pm \tilde{\Omega}(k_x)/2$ and the resonant frequency for the $|\mathrm{aux},\uparrow,\mathbf{k}\rangle \leftrightarrow |\pm,\mathbf{k}\rangle$ transition is $\omega_{\uparrow,\pm}(k_x) = \omega_{\uparrow,\mathrm{aux}} - \tilde{\delta}(k_x)/2 \mp \tilde{\Omega}(k_x)/2$.

In the experiments of Cheuk *et al.*, a degenerate Fermi gas of ^{40}K was studied. Since the Pauli exclusion principle forces the fermionic atoms to occupy a range of momentum states, the dressed bands were mapped by momentum resolved transitions between the auxiliary and dressed states in time of flight [248]. In a BEC, all of the atoms are clustered into a narrow distribution of momenta so only a very small range of the band could be mapped using a BEC at rest. The spin injection technique has also

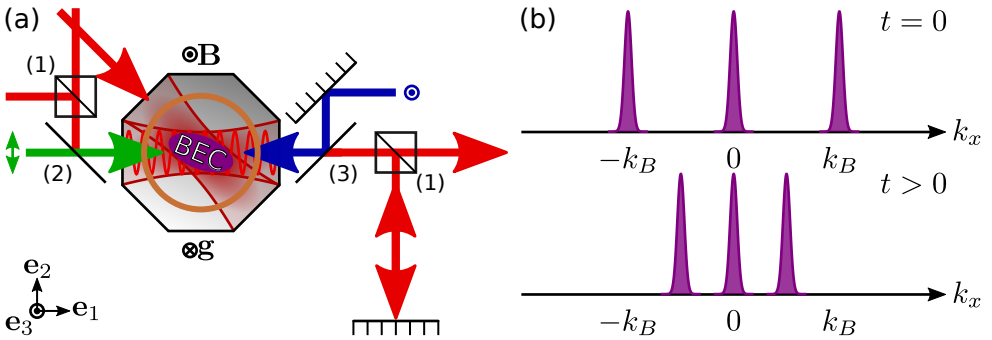

Figure 3.8: (a) Experimental setup for measuring Raman dressed dispersion relations *via* spin injection spectroscopy. A BEC is trapped in two crossed optical beams. An optical lattice is pulsed onto the atoms along the x-axis. After a variable wait time, the Raman beams are suddenly switched on and the energy difference between the Raman dressed bands and the auxiliary state is measured by RF spectroscopy. The optical elements shown are (1) polarising beam splitter, QiOptiq G335525000; (2) dichroic mirror, Thorlabs DMSP1000L; (3) dichroic mirror, Thorlabs DMLP950L. (b) Immediately after flashing the optical lattice, the BEC is split into three momentum components $\pm\hbar k_B \mathbf{e}_1$ and $0\mathbf{e}_1$. By waiting in the trap for a variable time, t, the magnitudes of the non-zero momentum values are reduced.

been applied to two-dimensional Fermi gases [249] fermions in a lattice [250] and later to thermal bosons filling the first Brillouin zone in a lattice [251]. However, the lattice adds further modifications to the dispersion [233]. For the experiments presented in this thesis, we are interested in the Raman dressed dispersions without an additional lattice.

One possibility for mapping the bands with bosons and without a lattice would be to use a gas above the critical temperature for Bose-Einstein condensation such that a thermal distribution of momenta is available. In practice, it is not easy to resolve the momenta in a thermal gas due to the low optical depth compared to a BEC, particularly for large momentum. Our method for mapping the Raman dressed dispersion relations is illustrated in Fig. 3.8. The BEC in a single spin state is trapped in a cross dipole trap formed by two laser beams of wavelength $\lambda_L = 1064$ nm with orthogonal polarisations propagating along the $\mathbf{e}_1$ and $(\mathbf{e}_1 - \mathbf{e}_2)/\sqrt{2}$ directions. The beam waists and powers of the two laser beams are 60 μm and 200 mW and 100 μm and 300 mW, respectively. To impart momentum on the atoms we pulse an optical lattice formed by an additional 1064 nm laser beam which is retroreflected along the x-axis. The two trapping beams and the lattice beam are frequency offset from each other on the order of 10 MHz so the only lattice potential that the atoms respond to is the retroreflected lattice.

When the lattice is pulsed for a short time, atoms are diffracted due to the Kapitza-Dirac effect in the Raman-Nath regime [252–254]. Immediately after the pulse the atoms are split into three laboratory frame momentum components with $k_x = 0$ and $k_x = \pm k_B$ where $k_B = 4\pi/\lambda_L$. Since the lattice is not kept on, the atoms evolve

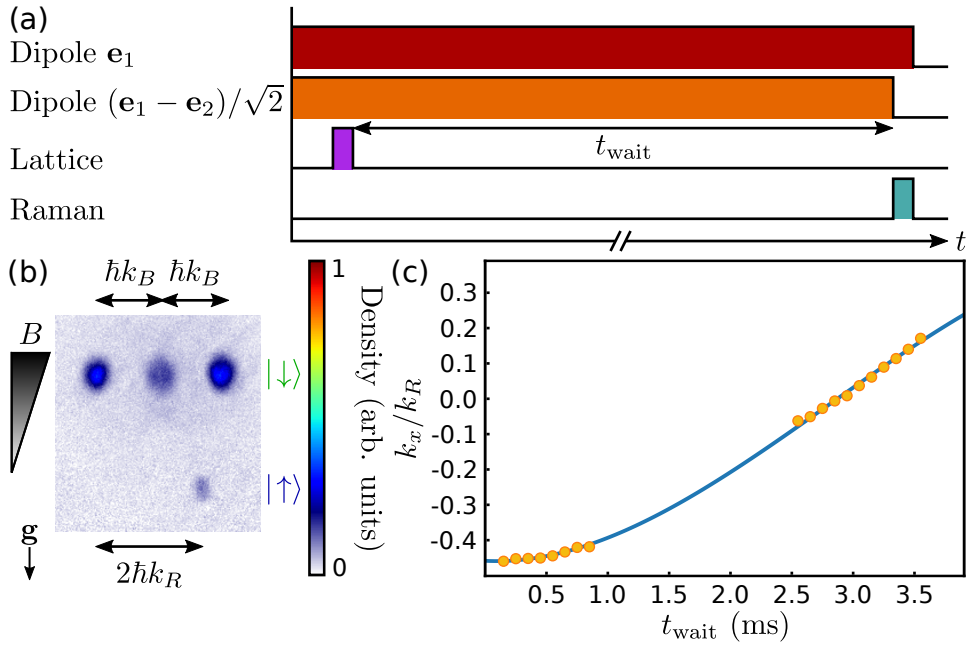

Figure 3.9: (a) Sequence of triggers for momentum calibration. The lattice is pulsed to split the BEC into three momentum components. Then, the BEC is kept in the crossed dipole trap for a variable time, t_{wait}, to reduce the momentum and the Raman beams are pulsed to calibrate the momentum by finding $\hbar\tilde{\delta}(k_x)/E_R = 0$. The relative widths of pulses are not to scale. (b) Time of flight image demonstrating calibration of in trap momentum using Raman Rabi pulses. The transfer from state $|\downarrow\rangle$ to state $|\uparrow\rangle$ is maximised when $\hbar\tilde{\delta}(k_x)/E_R = 0$ which allows the momentum to be determined by scanning δ_0. (c) Extracted momentum versus wait time in trap with cubic fit. Error bars correspond to the fit uncertainties and are smaller than the data markers.

as they normally would in the crossed beam dipole trap and by simply waiting with the trap on, the momentum can be scanned. However, the geometry of the crossed laser beams means that the x-axis is not a principal axis of the trap. This means that while the trap will bring the components towards rest ($k_x = 0$) during the first quarter period, the trap will also tend to mix the momentum into the $\mathbf{e}_2$ direction. Furthermore, the optical lattice is in reality placed at a slight angle with respect to the x-axis to ensure that no lattice is accidentally formed in the beam used for the crossed dipole trap.

To calibrate the momentum of the BEC after flashing the optical lattice, we exploit the Rabi flopping dynamics. To determine the momentum of the component moving to the left after a variable wait time in the crossed trap, we start with the BEC in state $|\downarrow\rangle$ and pulse the Raman beams with Rabi frequency Ω for a pulse time $\tau = \pi/\Omega$. We scan the Raman detuning δ_0 to find the maximum transfer to state $|\uparrow\rangle$ which we know corresponds to $\hbar\tilde{\delta}(k_x)/E_R = 0$. The momentum calibration sequence is sketched in Fig. 3.9(a). We have chosen $|\downarrow\rangle = |F = 1, m_F = 0\rangle$ and $|\uparrow\rangle = |F = 1, m_F = -1\rangle$ in ^{41}K with a bias field of $B = 336.30(1)$ G where we have $\mathrm{d}\omega_0/\mathrm{d}B/(2\pi) < 1$ Hz/mG.

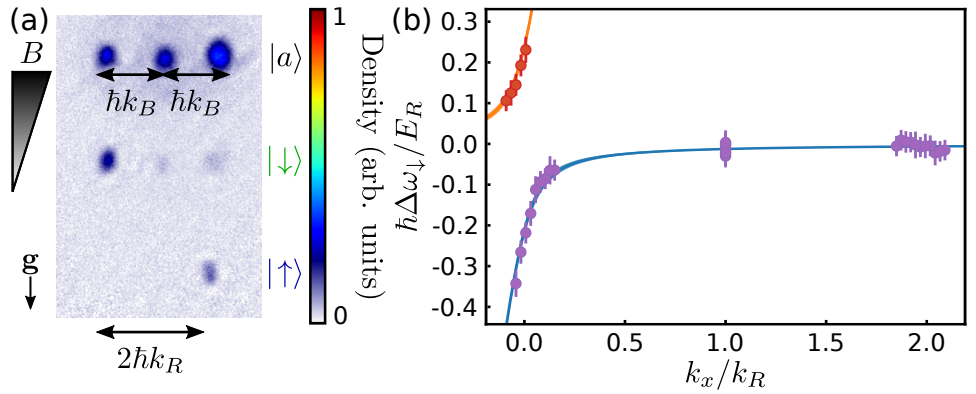

Figure 3.10: (a) The resonant frequency for transfer from the auxiliary state $|F = 1, m_F = 1\rangle \equiv |a\rangle$ to the Raman dressed bands is momentum-dependent so the transferred fraction of atoms at a given RF frequency is also momentum-dependent. For $k_x/k_R \approx 0$ the Raman dressed bands have close to equal projections onto the states $|\uparrow\rangle$ and $|\downarrow\rangle$ when $\hbar\delta_0/E_R \approx 0$ which allows for both significant transition strength and a detectable number of atoms in both spin states separated by momentum $2\hbar k_R \mathbf{e}_1$ in the laboratory frame after projection onto the bare state basis. (b) Shifts of the resonant transition frequencies from the auxiliary state $|F = 1, m_F = 1\rangle$ to the Raman dressed bands with respect to the $|a\rangle \rightarrow |\downarrow\rangle$ transition as a function of momentum for $\hbar\Omega/E_R = 0.45(3)$ and $\hbar\delta_0/E_R \approx 0$. The blue (orange) line shows the calculated shift for the lower (upper) dressed band and the shaded area reflects the uncertainty in the calculated shifts due to uncertainties in Ω and δ_0. Error bars correspond to the combination of the uncertainty of the fitted resonance frequency, and the uncertainty of the bare resonance frequency due to uncertainty in the magnetic field.

Figure 3.9(b) shows an absorption image corresponding to a value of δ_0 which gives some transfer between state $|\downarrow\rangle$ (moving to the left) and state $|\uparrow\rangle$ (moving to the right) but is not the resonant frequency. Note that the other two momentum components are not transferred to state $|\uparrow\rangle$ due to the momentum dependence of the coupling. Figure 3.9(c) shows the extracted quasimomentum as a function of wait time after the lattice pulse. For short wait times, we obtain a value close to the expected $k_x = k_R - k_B = -0.445k_R$. We fit the extracted quasimomentum with a third degree polynomial $k_x/k_R = p_3t^3 + p_2t^2 + p_1t + p_0$ with $p_3 = -11(2) \times 10^6$ s^{-3}, $p_2 = 9(2) \times 10^4$ s^{-2}, $p_1 = -17(20)$ s^{-1}, and $p_0 = -0.458(8)$. We assume equal magnitude of momentum in both directions.

We implement spin injection spectroscopy using a single auxiliary state $|\text{aux}\downarrow, \mathbf{k}\rangle = |F = 1, m_F = 1, \mathbf{k}\rangle \equiv |a, \mathbf{k}\rangle$. We have $\mathrm{d}\omega_{\downarrow,\text{aux}}/\mathrm{d}B/(2\pi) \approx 20$ Hz/mG. The choice to use only a single auxiliary state means that we are able to map the dispersion relations between $k_x \approx k_R - k_B$ and $k_x \approx k_R + k_B$ and we will only get a spectroscopic signal when $\langle \pm, \mathbf{k}| \downarrow', \mathbf{k}\rangle$ differs significantly from zero. Figure 3.10(a) shows an absorption image corresponding to all three momentum components being injected into the lower Raman dressed band. The significant differences in the fraction of atoms transferred for the different momentum components are a direct manifestation of the momentum-

dependent transition frequencies between the auxiliary state and the Raman dressed bands. For the component with quasimomentum $k_x/k_R \approx 0$ a portion of the atoms transferred into the dressed band are projected into state $|\uparrow\rangle$ with a laboratory frame momentum gain of $2\hbar k_R \mathbf{e}_1$.

Fig. 3.10(b) shows the measured difference between the transition frequencies between the auxiliary state and the Raman dressed bands and the bare transition frequency between the auxiliary state and state $|\downarrow', \mathbf{k}\rangle$, $\Delta\omega_\downarrow$, as a function of quasimomentum for $\hbar\Omega/E_R = 0.45(3)$ and $\hbar\delta_0/E_R = 0.0264(3)$. Spin injection spectroscopy does not directly indicate which dressed band is coupled and this information is inferred from the sign of $\Delta\omega_\downarrow$. Since the initial state, $|a, \mathbf{k}\rangle$, is not coupled by the Raman lasers we do not need to prepare any states adiabatically. For these measurements the Raman beams are switched on only after the lattice pulse and kept on for the spin injection RF pulse before being switched off again for the time of flight spin projection measurement. This means that the time during which the Raman beams are kept on is too short to allow for stabilising the power with the PID controllers.

From the measurements of $\Delta\omega_\pm$ (corresponding to positive or negative values of $\Delta\omega_\downarrow$), the Raman dressed dispersion relations can be inferred from $E_\pm = \hbar\Delta\omega_\pm + \hbar^2 \left(k_x - k_R\right)^2/(2m) + \hbar\delta_0/2$. Figure 3.11(a) shows measured dispersion relations for (top panel) $\hbar\Omega/E_R = 1.08(7)$ and $\hbar\delta_0/E_R = 0.0264(3)$, (middle panel) $\hbar\Omega/E_R = 0.45(3)$ and $\hbar\delta_0/E_R = 0.0264(3)$, and (bottom panel) $\hbar\Omega/E_R = 0.85(6)$ and $\hbar\delta_0/E_R = 0.9448(3)$. We see excellent agreement with the predicted dispersion relations without fitting parameters. Figure 3.11(b) shows the measured projections onto the bare spin states $|\downarrow\rangle$ and $|\uparrow\rangle$ for the same parameters as Fig. 3.11(a). For the lower band, the proportion of atoms projected into state $|\uparrow\rangle$ is only measurable for $k_x/k_R \approx 0$ and for the upper band the transition probability is close to zero for $k_x/k_R > 0$. As with the dispersion relations, the measured polarisations are in excellent agreement with the predicted values without fitting parameters.

3.5 Summary

In this chapter, I have introduced coherent coupling as a means of interaction control in a BEC. For a BEC dressed by RF, the elastic interactions have the same form as those of a BEC without coupling except with dependence on the parameters of the coupling field. When the BEC is coupled with a pair of laser beams in a Raman configuration, the dressed states become momentum-dependent. In the next chapter, I will show how the dynamics of a topological gauge theory known as the chiral BF theory can be encoded in the dynamics of matter in a BEC with unusual interactions and in Ch. 5 I will demonstrate how the momentum dependence of the interactions in the lower dressed band can be used to simulate the chiral BF theory. In Ch. 6 and Ch. 7, I will show how the momentum-dependent dressed states and interactions can be used to produce an exotic state of matter known as a supersolid.

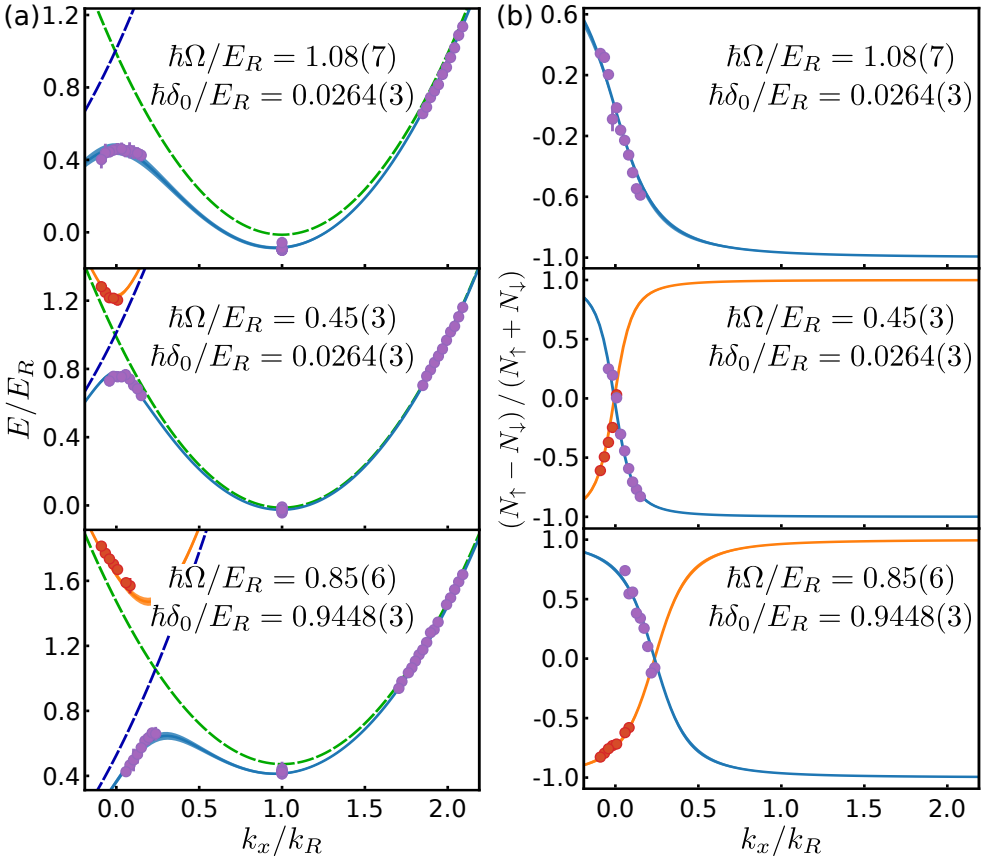

Figure 3.11: (a) Dispersion relations measured using spin injection spectroscopy for $\hbar\Omega/E_R = 1.08(7)$ and $\hbar\delta_0/E_R = 0.0264(3)$ (top), $\hbar\Omega/E_R = 0.45(3)$ and $\hbar\delta_0/E_R = 0.0264(3)$ (middle), and $\hbar\Omega/E_R = 0.85(6)$ and $\hbar\delta_0/E_R = 0.9448(3)$ (bottom). In the bottom and middle panels, the energy gap between the upper and lower bands can be observed. Error bars correspond to the combined uncertainties of the fitted resonance frequency, momentum calibration, and bare resonance frequency. The dashed green (blue) line shows the bare dispersion $\epsilon_\downarrow(k_x)$ ($\epsilon_\uparrow(k_x)$) while the solid blue (orange) line shows the dressed dispersion relation $\varepsilon_-(k_x)$ ($\varepsilon_+(k_x)$) without fitting parameters. The uncertainties in Ω and δ_0 are reflected in the shaded areas. (b) Measured dressed state spin polarisations for $\hbar\Omega/E_R = 1.08(7)$ and $\hbar\delta_0/E_R = 0.0264(3)$ (top), $\hbar\Omega/E_R = 0.45(3)$ and $\hbar\delta_0/E_R = 0.0264(3)$ (middle), and $\hbar\Omega/E_R = 0.85(6)$ and $\hbar\delta_0/E_R = 0.9448(3)$ (bottom). Error bars correspond to the uncertainties in fitted atom number in each of the spin-momentum components. The population in state $|\uparrow'\rangle$ is below the detection threshold for $k_x/k_R \geq 1$. The solid blue (orange) line shows the predictions for the lower (upper) band without fitting parameters. The uncertainties in Ω and δ_0 are reflected in the shaded areas.

Chapter 4

Encoding Gauge Theories for Quantum Simulation

As described in Ch. 1, topological gauge theories are a special class of gauge theory where the gauge field does not have dynamics in the absence of matter and nontrivial gauge field configurations in the absence of matter are only possible in a space with nontrivial topology. In Ch. 5, I will present the experimental realisation of the quantum simulation of a one-dimensional topological gauge theory known as the chiral BF theory. In this chapter, I will introduce the chiral BF theory in Lagrangian form and derive an encoded Hamiltonian form of a gauge theory where gauge degrees of freedom are eliminated using local constraints. The content of this chapter is a result of theoretical collaborations between myself, Dr. Anika Frölian, Dr. Elettra Neri, Dr. Ramón Ramos, Prof. Dr. Leticia Tarruell, and Dr. Alessio Celi and is included in the publication "Encoding a one-dimensional topological gauge theory in a Raman-coupled Bose-Einstein condensate" [118]. It has also been discussed in the PhD thesis of Dr. Anika Frölian [218] and the publication "Realizing a 1D topological gauge theory in an optically dressed BEC" [132].

4.1 Dynamical and Topological Gauge Theories

Topological field theories play an important role in condensed matter physics [52, 53, 255]. Like dynamical gauge theories, the gauge fields are subject to coupling with the matter field and local symmetry constraints. The key difference between topological and dynamical gauge theories is that the gauge field of a topological gauge theory does not have dynamics in the absence of matter. Because of this property, a topological gauge theory can always be recast such that all properties are described in terms of matter degrees of freedom. Usually, recasting a topological gauge theory purely in terms of matter degrees of freedom results in unusual (and often nonlocal) interactions between particles. To illustrate the similarities and differences between dynamical and topological gauge theories clearly, this section examines one prototypical example of each: Maxwell theory and Chern-Simons theory, respectively.

4.1.1 Maxwell Theory

The most well known example of a dynamical gauge theory is electromagnetism, otherwise known as Maxwell theory. It is a $U(1)$ Abelian field theory meaning that the theory contains a conserved charge and gauge transformations commute [52]. Maxwell theory describes a matter field, Ψ, minimally coupled to a gauge field, $\mathbf{A}$. We label the components of the gauge field as A^μ where the Greek index labels the space-time coordinates $0, \ldots, d$ with 0 corresponding to time and $1, \ldots, d$ ($d \leq 3$) corresponding to the spatial components x, y, and z. We define the unit vector aligned with the spatial μ-axis as $\mathbf{e}_\mu$. We take the matter field to be non-relativistic and bosonic. The Lagrangian density of the theory is

$$\mathcal{L}_{\mathrm{M}} = -\frac{1}{4\mu_0} F_{\mu\nu} F^{\mu\nu} - e A_\mu J^\mu + \mathcal{L}_{\mathrm{matter}} \tag{4.1}$$

where μ_0 is the vacuum permeability, e is the electron charge, and

$$\mathcal{L}_{\mathrm{matter}} = i\hbar \Psi^* \partial_0 \Psi + \frac{\hbar^2}{2m} \Psi^* \nabla^2 \Psi - V_{\mathrm{int}}(n). \tag{4.2}$$

Here, the current density has time component $J^0 = c\Psi^*\Psi \equiv cn$ and spatial components $\mathbf{J} = J^\mu \mathbf{e}_\mu = \left[\Psi^* \left(\hbar\nabla - ie\mathbf{A}\right)\Psi - \Psi\left(\hbar\nabla + ie\mathbf{A}\right)\Psi^*\right]/(2im)$ where c is the speed of light, $\hbar$ is the reduced Planck constant, m is the mass of the matter particles, and $\nabla = \mathbf{e}_\mu \partial_\mu$ for $\mu > 0$. The electromagnetic field tensor is $F_{\mu\nu} = \partial_\mu A_\nu - \partial_\nu A_\mu$ and the matter-matter interactions are described by $V_{\mathrm{int}}(n)$ which is assumed to be polynomial in the density, n. In these expressions, repeated indices are summed and indices are raised and lowered with the mostly negative Minkowski metric.

We rewrite the Lagrangian density using the first order formalism of Faddeev and Jackiw [256, 257]. The first order formalism entails replacing the time derivative of a field with its conjugate momentum in order to obtain an expression which is at most linear in the time derivative of the field. A classical mechanics analogy is the Lagrangian of a particle of position q and velocity $\partial_0 q$ in the presence of a conservative potential $V(q)$. The Lagrangian of such a particle is $L = m\left(\partial_0 q\right)^2/2 - V(q)$ and in first order formalism we have $L = p\partial_0 q - \left[p^2/(2m) + V(q)\right] = p\partial_0 q - H(q,p)$ where p is the momentum of the particle and $H(q,p)$ is the classical Hamiltonian.

Using the first order formalism, we have

$$\begin{aligned}\mathcal{L}_{\mathrm{M}} = \frac{A^0}{\mu_0 c}\left(\nabla\cdot\mathbf{E} - \frac{en}{\epsilon_0}\right) - \epsilon_0 \mathbf{E}\cdot\partial_0\mathbf{A} - \frac{1}{2}\left(\epsilon_0\mathbf{E}^2 + \frac{1}{\mu_0}\mathbf{B}^2\right) \\ + i\hbar\Psi^*\partial_0\Psi + \frac{1}{2m}\Psi^*\left(\hbar\nabla - ie\mathbf{A}\right)^2\Psi - V_{\mathrm{int}}(n)\end{aligned} \tag{4.3}$$

where ϵ_0 is the vacuum permittivity and we have introduced the electric and magnetic fields $E^i = (\mathbf{E})^i = -cF^{0i} = -\left(\partial_0 A^i + c\partial_i A^0\right)$ and $B^i = (\mathbf{B})^i = (\nabla\times\mathbf{A})^i = -\epsilon^{ijk}F^{jk}/2$ where Latin indices indicate spatial coordinates and ϵ^{ijk} is the Levi-Civita symbol. We have neglected a term proportional to $\nabla\left(A^0\mathbf{E}\right)$ because it does not contribute to the action.

Eq. 4.3 does not contain terms of the form $\partial_\mu A^0$ so A^0 is a Lagrange multiplier which enforces the local conservation law (Gauss's law) which ensures gauge invariance

$$\nabla \cdot \mathbf{E} = \frac{en}{\epsilon_0}. \tag{4.4}$$

The equations of motion for the matter and gauge fields obtained from the Euler-Lagrange equations are

$$\begin{aligned} &i\hbar\partial_0\Psi + \frac{1}{2m}\left(\hbar\nabla - ie\mathbf{A}\right)^2\Psi - \frac{\mathrm{d}V_{\mathrm{int}}(n)}{\mathrm{d}n}\Psi = 0, \\ &\nabla\cdot\mathbf{E} = \frac{en}{\epsilon_0},\ \nabla\times\mathbf{B} - \frac{1}{c^2}\partial_0\mathbf{E} = \mu_0\mathbf{J}, \\ &\nabla\cdot\mathbf{B} = 0, \text{ and } \nabla\times\mathbf{E} + \partial_0\mathbf{B} = 0. \end{aligned} \tag{4.5}$$

The equations of motion for the gauge field are Maxwell's equations. In the absence of matter and for $d = 2$ or 3, divergenceless propagating solutions (electromagnetic waves) exist. Since the gauge field has dynamics in vacuum, electromagnetism is a dynamical gauge theory. If $d = 1$, a transverse field is not possible so there are no dynamics in the absence of matter and the gauge field is completely determined by the matter configuration and a choice of background field due to Gauss' law [258].

4.1.2 Chern-Simons Theory

While less well known than Maxwell theory, Chern-Simons theory is an archetypal example of a topological gauge theory. It is an emergent gauge theory used as an effective low energy and single particle description of fractional quantum Hall states in strongly correlated electron systems confined to a two-dimensional plane and subjected to a large external magnetic field perpendicular to the plane [52]. Like Maxwell theory, the Chern-Simons theory is a $U(1)$ Abelian gauge theory which builds upon Wilczek's idea of flux attachment [119, 121]. Flux attachment replaces the strongly correlated particles of the original system with weakly interacting composite particles which carry an integer number of magnetic flux quanta (flux tubes).

The Chern-Simons theory is a field theory describing the coupling of the particles to the vector potential corresponding to the magnetic field attached to the flux tubes. The composite particles consisting of the weakly interacting particles and flux tubes may have bosonic or fermionic exchange statistics or the exchange of two quasiparticles may result in an exchange phase corresponding to neither bosons nor fermions, so-called anyonic statistics [52]. The statistical exchange phase can be understood in terms of the Aharonov-Bohm phase, φ_{AB}, which is picked up upon exchange of flux tubes [121]. The number of flux tubes attached to each particle is given by the Chern-Simons level, $\bar{\kappa}$. The value of $\bar{\kappa}$ determines the fractional quantum Hall state described by the Chern-Simons theory corresponding to the filling of the Landau levels of the composite particles [121]. The concept of flux attachment and the Chern-Simons theory are illustrated in Fig. 4.1.

Assuming, no external fields are applied in addition to the internal Chern-Simons

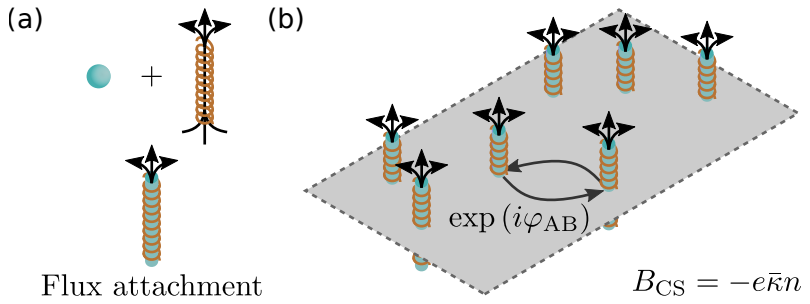

Figure 4.1: (a) Composite particles consist of an integer number of magnetic flux quanta attached to each matter particle. (b) The Chern-Simons theory is a topological gauge theory describing the coupling of composite particles to the vector potential created by the composite particles. The excitations in the system may have anyonic exchange statistics with the exchange phase, φ_{AB}, corresponding to the Aharonov-Bohm phase acquired by exchanging flux tubes.

magnetic field, the Lagrangian density of the theory is

$$\mathcal{L}_{\mathrm{CS}} = \frac{1}{4\bar{\kappa}}\epsilon^{\mu\nu\rho}A_\mu F_{\nu\rho} - eA_\mu J^\mu + \mathcal{L}_{\mathrm{matter}} \tag{4.6}$$

where we have $d = 2$ only. If, as we did for Maxwell theory, we assume a bosonic and nonrelativistic matter field, $\mathcal{L}_{\mathrm{CS}}$ is also known as the Jackiw-Pi model [259, 260].

We apply the Faddeev-Jackiw first order formalism, introducing the spatial components of the vector potential, $\mathbf{A}$, and magnetic field, $\mathbf{B} = B_{\mathrm{CS}}\mathbf{e}_3$, where the magnetic field has a single component perpendicular to the two-dimensional plane of the matter particles. The Lagrangian density is

$$\begin{aligned}\mathcal{L}_{\mathrm{CS}} = -cA^0\left(\frac{B_{\mathrm{CS}}}{\bar{\kappa}} + en\right) - \frac{1}{2\bar{\kappa}}\mathbf{A}\times\partial_0\mathbf{A} \\ + i\hbar\Psi^*\partial_0\Psi + \frac{1}{2m}\Psi^*\left(\hbar\nabla - ie\mathbf{A}\right)^2\Psi - V_{\mathrm{int}}(n)\end{aligned} \tag{4.7}$$

where we see the local conservation law and flux attachment condition $B_{\mathrm{CS}} = -e\bar{\kappa}n$. In the absence of matter, the equation of motion is $F_{\mu\nu} = 0$ so nontrivial solutions for the gauge field require a topological space and, unlike Maxwell theory, electromagnetic waves are not possible.

The equations of motion for the matter and gauge fields are

$$\begin{aligned}&i\hbar\partial_0\Psi + \frac{1}{2m}\left(\hbar\nabla - ie\mathbf{A}\right)^2\Psi - \frac{\mathrm{d}V_{\mathrm{int}}(n)}{\mathrm{d}n}\Psi = 0, \\ &\mathbf{E} - e\bar{\kappa}\mathbf{e}_3\times\mathbf{J} = \mathbf{0}, \text{ and } B_{\mathrm{CS}} + e\bar{\kappa}n = 0.\end{aligned} \tag{4.8}$$

Similarly to Maxwell theory, the equations of motion for the matter and gauge fields are linked but, unlike Maxwell theory, the equations of motion for the gauge fields become trivial in the absence of matter. Combining the equation for the electric field with the continuity equation for the matter field ($\partial_0 n + \nabla\cdot\mathbf{J} = 0$) gives the equation

of motion for the magnetic field. So the flux attachment conditions is both the local conservation law of the theory and the equation of motion of the gauge field. The equivalence of the local conservation law and equation of motion of the gauge field is common to all gauge theories which do not have propagating degrees of freedom, including Maxwell theory with $d = 1$.

4.2 The Chiral BF theory

The chiral BF theory is a member of a family of topological gauge theories which are possible one dimensional reductions of the Chern-Simons theory and is one of the simplest examples of a topological gauge theory [113–116]. The chiral BF theory was originally introduced during the 1990s as a possible model for one-dimensional anyons in the continuum [113–115] and corresponds to a field theoretic description of the Kundu linear anyon model in the limit of vanishing contact interactions [261, 262].

We obtain the chiral BF theory starting from the Jackiw-Pi model. We remove the dependence on the y spatial coordinate and set $A_2 = m\mathcal{B}$ where $\mathcal{B} = \mathcal{B}(t, x)$ is a bosonic scalar field. Making the field redefinition $A^0 \to A^0 - me\mathcal{B}^2/(2c)$ and defining $\kappa = \bar{\kappa}/\hbar$, the Lagrangian density is

$$\mathcal{L}_{\mathrm{BF}} = \frac{1}{2\kappa}\mathcal{B}\epsilon^{\mu\nu}F_{\mu\nu} - eA_\mu J^\mu + \mathcal{L}_{\mathrm{matter}} \tag{4.9}$$

where $\mu = 0, 1$ since we are now restricted to $d = 1$. The theory receives the name "BF" because of the gauge field term involving the product of the scalar bosonic field and the electromagnetic field tensor.

Since there are no derivatives of $\mathcal{B}$ in the Lagrangian density, $\mathcal{L}_{\mathrm{BF}}$, the equation of motion for the gauge field is $F_{\mu\nu} = 0$ even in the presence of matter. This means that both $\mathcal{B}$ and A_μ can be eliminated by redefining the matter field, Ψ, and all of the dynamics of the theory correspond to the matter field through $\mathcal{L}_{\mathrm{matter}}$. To endow the theory with nontrivial gauge field dynamics and reproduce the behaviour of a single edge of the two-dimensional Chern-Simons theory, Refs. [113–116] add a kinetic term for the scalar field of the self-dual form $\partial_0\mathcal{B}\partial_1\mathcal{B}$ [263]. As pointed out by Aglietti *et al.* [115], this kinetic term breaks Galilean invariance and is the simplest nonrelativistic combination that reproduces the edge dynamics of the Chern-Simons theory.

In two-dimensional quantum Hall systems, the edge modes come in pairs and have chiral dynamics, meaning that the dynamics depend on the propagation direction along the edge [264]. The paired edge modes have opposite chirality. Here, the self-dual kinetic term corresponds to one edge mode and the chirality is selected by the sign of a proportionality factor, λ, which we introduce along with the self-dual term. The self-dual term is referred to as the chiral boson term.

The Lagrangian density of the chiral BF theory is

$$\mathcal{L}_{\mathrm{cBF}} = \frac{1}{2\kappa}\mathcal{B}\epsilon^{\mu\nu}F_{\mu\nu} + \frac{\lambda}{2e^2c^2\kappa^2}\partial_0\mathcal{B}\partial_1\mathcal{B} - eA_\mu J^\mu + \mathcal{L}_{\mathrm{matter}}. \tag{4.10}$$

Specifying the electromagnetic field tensor in components and neglecting terms which

do not contribute to the action, we have

$$\mathcal{L}_{\mathrm{cBF}} = A^0\left(\frac{\partial_1\mathcal{B}}{\kappa} - ecn\right) - \frac{\mathcal{B}}{c\kappa}\partial_0 A + \frac{\lambda}{2e^2c^2\kappa^2}\partial_0\mathcal{B}\partial_1\mathcal{B} + i\hbar\Psi^*\partial_0\Psi + \frac{1}{2m}\Psi^*\left(\hbar\partial_1 - ieA\right)^2\Psi - V_{\mathrm{int}}(n), \quad (4.11)$$

where the spatial part of the vector potential is now a scalar, A, since we have $d = 1$. From Eq. 4.11 we can see that the local conservation law of the chiral BF theory is

$$\partial_1\mathcal{B} = ec\kappa n \quad (4.12)$$

which has the same role as the flux attachment condition in Chern-Simons theory and Gauss's law in electromagnetism.

The equations of motion for the matter and gauge fields read

$$i\hbar\partial_0\Psi + \frac{1}{2m}\left(\hbar\partial_1 - ieA\right)^2\Psi - \frac{\mathrm{d}V_{\mathrm{int}}(n)}{\mathrm{d}n}\Psi = 0,$$
$$\partial_0\mathcal{B} + ec\kappa J = 0,\ \partial_1\mathcal{B} - ec\kappa n = 0, \text{ and } E - \frac{\lambda}{e^2c\kappa}\partial_0\partial_1\mathcal{B} = 0 \quad (4.13)$$

where the electric field, E, and the spatial part of the current density, $J = \{\Psi^*(\hbar\partial_1 - ieA)\Psi - [(\hbar\partial_1 + ieA)\Psi^*]\Psi\}/(2im)$, are scalars since $d = 1$. Similarly to the Chern-Simons theory, the first equation describes a matter field, Ψ, coupled to a gauge potential, A. The next two equations can be combined to obtain the continuity equation for the matter field $\partial_0 n + \partial_1 J = 0$. The last equation is analogous to the equation of motion of the electromagnetic field tensor in Maxwell theory and can be rewritten as $F_{01} = E = \lambda\partial_0 n/e$. At the classical level, the conservation law $\partial_1\mathcal{B} = ec\kappa n$ is equivalent to $E = \lambda\partial_0 n/e$ or $A = -\lambda n/e + \partial_1\Lambda(x)$ where $\Lambda(x)$ is an arbitrary time-independent function.

As with the Chern-Simons theory, the gauge field of the chiral BF theory does not have dynamics in the absence of matter. The chiral boson term reproduces the edge dynamics of the Chern-Simons theory without changing the fact that the BF theories are topological gauge theories, a property which is inherited from the Chern-Simons theory.

4.3 Encoding Gauge Theories using First Order Formalism

In order to perform quantum simulation of the chiral BF theory with ultracold atoms, we need to derive a (second quantised) quantum Hamiltonian. The chiral BF theory is subject to the local constraint in Eq. 4.12. The relationships between $\partial_0 A$ and $\partial_0\mathcal{B}$ and the conjugate momenta of A and $\mathcal{B}$ are singular so cannot be inverted. This means that the Legendre transform of Eq. 4.11 is not straightforward. The first order approach of Faddeev and Jackiw [116, 256] allows us to separate the dynamics from local conservation laws by progressively eliminating the matter-dependent fields

at the level of the Lagrangian. In this way, we can derive a second quantised Hamiltonian which involves only the physical degrees of freedom with the gauge field dynamics encoded in the equations of motion of the matter field. This approach avoids the complex Dirac treatment of constraints [40, 258] and the resulting encoded Hamiltonian has a similar form to the one used in the simulation of the Schwinger model [265, 266].

Before deriving an encoded Hamiltonian for the chiral BF theory, we first apply the first order formalism to Maxwell theory to show that this approach produces the expected form of Coulomb's Hamiltonian and Gauss's law. In both cases, the price for eliminating the matter-dependent gauge field is the introduction of interaction terms beyond the simple contact interactions described by $V_{\text{int}}(n)$. In the case of Maxwell theory, the interactions are the well known infinite range Coulomb interactions and for the chiral BF theory, a chiral interaction which is not infinite range but also not the usual contact interaction of a BEC discussed in Ch. 2. The quantum simulation of the encoded Hamiltonian boils down to the engineering of the resulting interaction term in the experimental platform.

4.3.1 Encoding Maxwell Theory

We start from the Lagrangian density of the system which is Eq. 4.3 for Maxwell theory. The electric field can be decomposed into a divergenceless part, $\mathbf{E}_T$, and a part which is given by the gradient of a scalar function which we call the longitudinal part, $\mathbf{E}_L$, such that $\mathbf{E} = \mathbf{E}_L + \mathbf{E}_T$. We can write the longitudinal part of the electric field in terms of the matter field using Gauss's law[1] $\mathbf{E}_L = (e/\epsilon_0)\,\nabla\left(\nabla^{-2}n\right)$. If we also decompose the vector potential into transverse and longitudinal parts, $\mathbf{A} = \mathbf{A}_L + \mathbf{A}_T$ we find (neglecting terms which do not contribute to the action)

$$\begin{aligned}\mathcal{L}_{\text{M}} = {} & \epsilon_0 \mathbf{E}_T \cdot \partial_0 \mathbf{A}_T + i\hbar\Psi^*\partial_0\Psi + en\nabla^{-2}\left(\nabla\cdot\partial_0\mathbf{A}_L\right) \\ & - \frac{1}{2}\left(\epsilon_0\mathbf{E}_T^2 - \frac{e^2}{\epsilon_0}n\nabla^{-2}n + \frac{1}{\mu_0}\mathbf{B}^2\right) + \frac{1}{2m}\Psi^*\left(\hbar\nabla - ie\mathbf{A}\right)^2\Psi - V_{\text{int}}(n). \quad (4.14)\end{aligned}$$

This expression shows that the matter field and the transverse components of the gauge field are the dynamical degrees of freedom. The pairs $\mathbf{A}_T$ and $-\mathbf{E}_T$ and Ψ and $i\partial_0\Psi^*$ are equivalent to the position and momentum, q and p, of a mechanical system. The first two terms of Eq. 4.14 have the canonical form $p\partial_0 q$ but the third term does not because there is no momentum field conjugate to $\mathbf{A}_L$ since there is no polarisation along the propagation direction of light. This is because the longitudinal component of the vector potential is not physical. In the Faddeev-Jackiw approach, noncanonical terms can always be removed by redefining fields.

We apply a gauge transform to the matter field such that a new field, ϕ, is defined by $\Psi = \exp\left[ie\nabla^{-2}\left(\nabla\cdot\mathbf{A}_L\right)/\hbar\right]\phi$ and obtain

$$i\hbar\Psi^*\partial_0\Psi + en\nabla^{-2}\left(\nabla\cdot\partial_0\mathbf{A}_L\right) = i\hbar\phi^*\partial_0\phi \quad (4.15)$$

[1]Here, ∇^{-2} is the inverse Laplacian defined by its action on a test function, $f(\mathbf{r})$: $\nabla^{-2}\nabla^2 f(\mathbf{r}) = f(\mathbf{r})$ so that $(e/\epsilon_0)\,\nabla^{-2}n$ is minus the electrostatic potential.

and

$$\frac{1}{2m}\Psi^*\left(\hbar\nabla - ie\mathbf{A}_L\right)^2\Psi = \frac{\hbar^2}{2m}\phi^*\nabla^2\phi. \tag{4.16}$$

In the second expression we have used that fact that by construction $\mathbf{A}_L = \nabla f_L$ for some function, f_L. This means $\nabla\cdot\mathbf{A}_L = \nabla^2 f_L$ and $f_L = \nabla^{-2}\left(\nabla\cdot\mathbf{A}_L\right)$ which implies $\nabla\left[\nabla^{-2}\left(\nabla\cdot\mathbf{A}_L\right)\right] = \mathbf{A}_L$. With this gauge transformation, Eq. 4.14 becomes

$$\mathcal{L}_{\mathrm{M}} = \epsilon_0\mathbf{E}_T\cdot\partial_0\mathbf{A}_T + i\hbar\phi^*\partial_0\phi - \mathcal{H}_{\mathrm{C}}^{\mathrm{enc}} \tag{4.17}$$

where the encoded Hamiltonian density,

$$\mathcal{H}_{\mathrm{C}}^{\mathrm{enc}} = \frac{1}{2}\left(\epsilon_0\mathbf{E}_T^2 - \frac{e^2}{\epsilon_0}n\nabla^{-2}n + \frac{1}{\mu_0}\mathbf{B}^2\right) - \frac{1}{2m}\left(\hbar\nabla - ie\mathbf{A}_T\right)^2\phi, \tag{4.18}$$

is Coulomb's Hamiltonian. Note that we have chosen $V_{\mathrm{int}}(n) = 0$. The choice of interactions does not correspond to a gauge choice and no gauge choice was made to arrive to this result.

The derivation of the encoded Hamiltonian is also possible with $d = 1$ or $d = 2$. When we restrict ourselves to one spatial dimension, there is no transverse component of the electric field and the Hamiltonian contains only the kinetic term of the matter and the Coulomb interaction which is of infinite range. It has the same form as the interaction term in the lattice Hamiltonian of the Schwinger model after encoding by integrating out the gauge degrees of freedom using Gauss' law as a constraint [258]. When encoding the Schwinger model using Gauss's law, the integral of the density is replaced by a sum of charges which are represented as spins by a Jordan-Wigner transformation. The experimental implementation of such an interaction term is what makes the realisation of the encoded Hamiltonian density of Eq. 4.18 difficult but the interactions have been successfully implemented using trapped ions [40, 42]. Encoded formulations of Hamiltonians for Maxwell theory in a lattice which exploit electromagnetic duality have been proposed [267–270] and link model dual formulations have been investigated [271, 272].

4.3.2 Encoding the Chiral BF Theory

In this section, we derive a second quantised Hamiltonian for the chiral BF theory in encoded form. We apply the Faddeev-Jackiw formalism starting from Eq. 4.11. Since the chiral BF theory is a topological gauge theory, the only dynamical field is the matter field. We redefine the matter field using the gauge transformation

$$\Psi = \exp\left[i\frac{e}{\hbar}\left(\int_{x_0}^{x}\mathrm{d}\xi A(\xi,t) - c\int_{t_0}^{t}\mathrm{d}t' A^0(x_0,t') + \frac{\lambda}{2ce^2\kappa}\mathcal{B}(x_0,t)\right)\right]\phi \tag{4.19}$$

where x_0 and t_0 are arbitrary values of the space and time coordinates. With this gauge transformation, the Lagrangian density in Eq. 4.11 becomes

$$\mathcal{L}_{\mathrm{cBF}} = \tilde{A}^0\left(\frac{\partial_1\mathcal{B}}{\kappa} - ecn\right) - \frac{\lambda}{2e^2c^2\kappa}\partial_0\mathcal{B}(x_0,t)n + \frac{\lambda}{2\kappa^2}\partial_0\mathcal{B}\partial_1\mathcal{B} + i\hbar\phi^*\partial_0\phi + \frac{\hbar^2}{2m}\phi^*\partial_1^2\phi - V_{\mathrm{int}}(n) \tag{4.20}$$

where $\tilde{A}^0 = -\int_{x_0}^{x} \mathrm{d}\xi F_{01}(\xi,t)/c$ is a Lagrange multiplier representing the nondynamical part of the gauge field. The dynamical part of the gauge field is proportional to the bosonic field, $\mathcal{B}$, which remains subject to the constraint imposed by $\tilde{A}^0$: $\partial_1 \mathcal{B} = ec\kappa n$. The constraint imposed by $\tilde{A}^0$ can be written in the equivalent form

$$\mathcal{B}(x,t) = ec\kappa \int_{x_0}^{x} \mathrm{d}\xi n(\xi,t) + \mathcal{B}(x_0,t). \tag{4.21}$$

Equation 4.21 is the local conservation law of the chiral BF theory. Substituting Eq. 4.21 into Eq. 4.20 gives

$$\mathcal{L}_{\mathrm{cBF}} = i\phi^* \left(\hbar\partial_0 - i\frac{\lambda}{2} \int_{x_0}^{x} \mathrm{d}\xi \partial_0 n(\xi,t) \right) \phi + \frac{\hbar^2}{2m} \phi^* \partial_1^2 \phi - V_{\mathrm{int}}(n) \tag{4.22}$$

which is a Lagrangian density which depends only on the matter field.

The complete elimination of the gauge field was our goal here because it will make the quantum simulation of the chiral BF theory easier. This goal can be achieved because the chiral BF theory is topological so the gauge field dynamics are fully determined by the matter field. However, the resulting Lagrangian density is nonlocal and therefore not amenable to quantum simulation. Furthermore, the canonical quantisation of Eq. 4.22 would lead to a quantum field that is not bosonic. This is not surprising since, as discussed in Sec. 4.2, the chiral BF theory was originally introduced as a model for linear anyons, and the contact interactions $V_{\mathrm{int}}(n)$ do not alter the commutation relation of linear anyons [115, 116, 273].

To derive an encoded Hamiltonian suitable for the quantum simulation of the chiral BF theory, we remove the nonlocality of Eq. 4.22 by performing a Jordan-Wigner transformation

$$\phi = \exp\left(i\frac{\lambda}{2\hbar} \int_{x_0}^{x} \mathrm{d}\xi n(\xi,t) \right) \psi \tag{4.23}$$

which yields a bosonic matter field, ψ. We arrive at the local Lagrangian density (neglecting terms which do not contribute to the action)

$$\mathcal{L}_{\mathrm{cBF}}^{\mathrm{enc}} = i\hbar\psi^* \partial_0 \psi - \mathcal{H}_{\mathrm{cBF}}^{\mathrm{enc}} \tag{4.24}$$

where

$$\mathcal{H}_{\mathrm{cBF}}^{\mathrm{enc}} = -\frac{\hbar^2}{2m} \psi^* \partial_1^2 \psi + \tilde{V}_{\mathrm{int}}(n) + \frac{\lambda}{2} J n \tag{4.25}$$

where $J = \hbar\left[\psi^* \partial_1 \psi - (\partial_1 \psi^*)\,\psi\right]/(2im)$ is the spatial current for the nonrelativistic and bosonic matter field, ψ, which is not coupled to any gauge field and $\tilde{V}_{\mathrm{int}}(n) = V_{\mathrm{int}}(n) + \lambda^2 n^3/(8m)$. Since $V_{\mathrm{int}}(n)$ was only specified to be polynomial in the density, n, adding the additional three-body term does not change the physics of the Hamiltonian because we are still free to choose the polynomial form of $\tilde{V}_{\mathrm{int}}(n)$.

Similarly to the Maxwell case, the elimination of the gauge field through the local conservation law produces an unusual interaction term in the encoded Hamiltonian, which is of current-density form in this case. The current-density interaction is chiral and is the only term remaining in the encoded Hamiltonian which breaks Galilean invariance, meaning that it stems directly from the self-dual term added to Eq. 4.9

to obtain the chiral BF theory. To obtain a second-quantised Hamiltonian for the quantum chiral BF theory, it is sufficient to replace the fields in Eq. 4.25 with field operators with normal ordering [116, 273]

$$\hat{H}^{\text{enc}}_{\text{cBF}} = \int \mathrm{d}x \left(-\frac{\hbar^2}{2m} \hat{\psi}^\dagger \partial_x^2 \hat{\psi} + : \tilde{V}_{\text{int}}(\hat{n}) : + \frac{\lambda}{2} : \hat{J}\hat{n} : \right) \tag{4.26}$$

where $\hat{n} = \hat{\psi}^\dagger \hat{\psi}$. In Eq. 4.26, $: \cdot :$ denotes normal ordering and we have returned to the usual notation $\partial_1 \to \partial_x$. From now on, we will also use $\partial_0 \to \partial_t$. Using the local symmetry constraint, the expectation values of all observables, including the eliminated gauge field, can be determined. For the electric field, we have $\langle \hat{E} \rangle = -\langle \partial_t \hat{A}_{\text{BF}} \rangle = \lambda \langle \partial_t \hat{n} \rangle$ where the charge units have been absorbed into $\hat{A}_{\text{BF}}$ and $\hat{E}$. This relation is equivalent to the classical relation given in Sec. 4.2, as we would expect from Ehrenfest's theorem. A similar strategy was used to determine the electric field in the simulation of the encoded Schwinger model with trapped ions [40, 258].

Eq. 4.26 can also be written as

$$\hat{H}^{\text{enc}}_{\text{cBF}} = \int \mathrm{d}x \left[-\frac{\hbar^2}{2m} \psi^\dagger \left(\partial_x + \frac{i}{\hbar} \frac{\lambda}{2} \hat{n} \right) \hat{\psi} + V_{\text{int}}(\hat{n}) \right] \tag{4.27}$$

which features a density-dependent vector potential $\hat{A}_n = -\lambda \hat{n}/2$ which is related to the BF vector potential by $\hat{A}_n = \hat{A}_{\text{BF}}/2$. The correspondence between the density-dependent vector potential appearing in the encoded Hamiltonian at the mean-field level and the vector potential of the chiral BF theory at the classical level, $A = -\lambda n/e$ for the gauge choice $\Lambda(x) = 0$, inspired the first proposal for the implementation of the chiral BF theory in a Raman coupled BEC with unequal intrastate interactions [131] which will be described in the next section.

4.4 Quantum Simulation of the Chiral BF theory in a Bose-Einstein Condensate

The matter field in Eq. 4.26 and Eq. 4.27 is bosonic so, if the unusual current-dependent interactions or the equivalent density-dependent vector potential can be engineered, the encoded chiral BF Hamiltonian can be directly simulated in a BEC. Indeed, Edmonds *et al.* [131] have demonstrated that, in the mean-field limit, an equation of motion corresponding to the chiral BF theory can be produced in a two-component BEC with Raman coupling, as discussed in Ch. 3. Edmonds *et al.* [131] consider the eigenstates of the single particle Hamiltonian given in Eq. 3.14 under the position space adiabatic approximation with zero detuning, $\hbar\delta_0/E_R = 0$. In the position space adiabatic approximation, the Rabi frequency, Ω, dominates over all other energy scales and the atoms adiabatically follow the position-dependent atom-photon eigenstates given by

$$\begin{bmatrix} 0 & \exp(2ik_R x) \\ \exp(-2ik_R x) & 0 \end{bmatrix} |\pm(x)\rangle_{\text{adiabatic}} = E_{\pm,\text{adiabatic}} |\pm(x)\rangle_{\text{adiabatic}} \tag{4.28}$$

where $E_{\pm,\text{adiabatic}} = \pm\hbar\Omega/2$ and $|\pm(x)\rangle_{\text{adiabatic}} = [|\uparrow\rangle \pm \exp(-2ik_R x)|\downarrow\rangle]/\sqrt{2}$.

In the treatment of Edmonds *et al.* [131], the bare state interactions are included as first order perturbations to the dressed states. Projecting into the lower energy band with tight transverse confinement corresponding to a one-dimensional geometry results in a mean-field equation of motion for the corresponding wavefunction, $\phi_{\text{a}}(\mathbf{r}, t)$, given by

$$i\hbar\frac{\partial}{\partial t}\phi_{\text{a}} = \left[-\frac{\hbar^2}{2m}\left(\frac{\partial}{\partial x} + \frac{i}{\hbar}\frac{\lambda}{2}|\phi_{\text{a}}|^2\right)^2 + \frac{\lambda}{2}j_{\text{a}} + g_1|\phi_{\text{a}}|^2\right]\phi_{\text{a}} \tag{4.29}$$

where $j_{\text{a}} = \hbar\left(\phi_{\text{a}}^*\partial_x\phi_{\text{a}} - \phi_{\text{a}}\partial_x\phi_{\text{a}}^*\right)/(2im)$, $g_1 = (g_{\uparrow\uparrow} + g_{\downarrow\downarrow} + 2g_{\uparrow\downarrow})/4$, and $\lambda \propto (g_{\uparrow\uparrow} - g_{\downarrow\downarrow})$. Equation 4.29 is equivalent to the equation of motion for the matter field in Eq. 4.13 for properly chosen contact interactions, $V_{\text{int}}(n)$. In Ch. 5, I will show that, using a momentum space representation, a mapping between the BEC and the chiral BF theory can be achieved rigorously in the quantum regime at the level of the Hamiltonian including the modification of the free particle dispersion due to Raman coupling. In this section, I will review some of the key properties of the chiral BF theory which will serve as signatures of the successful experimental realisation in Ch. 5.

One of the most striking features of the chiral BF theory is the existence of chiral solitons [115, 131, 274–276]. Assuming $V_{\text{int}}(\hat{n}) = 0$, a chiral soliton is a matter wave packet which propagates without dispersion but only for one sign of the group momentum. Chiral solitons may be either bright or dark with the two possibilities existing for opposite signs of momentum and the latter requiring a phase jump of π to be imprinted upon the BEC [131]. The existence of the soliton solutions is easily understood from the perspective of the chiral BF gauge theory. We take a matter wave packet with group momentum $\hbar k_G\mathbf{e}_1$, which has a wavefunction of the form $\psi = \sqrt{n(x)}\exp(ik_G x)$ where $n(x) \in \mathbb{R}$. Inserting, this wavefunction into the nonlinear current term gives $jn = \hbar\lambda k_G n^2/(2m)$.

So we see that the current-density term is equivalent to a momentum-dependent two-body interaction and since the stability of a soliton stems from the balance between dispersion and nonlinear interactions [200], the sign of the momentum determines the stability of the soliton. If $V_{\text{int}}(\hat{n}) = g_s :\hat{n}^2:$, corresponding to standard two-body interactions, then the stability criteria for a bright soliton is shifted to $g_s + \hbar\lambda k_G/(2m) < 0$ [131]. For, $g_s + \hbar\lambda k_G/(2m) > 0$, no soliton solutions exist if no phase jump is present in the matter field. This means that the bright soliton is chiral and is the many-body analogue of the chiral edge states in quantum Hall systems. The chiral soliton dynamics are illustrated in Fig. 4.2(a).

A second important property of the chiral BF theory is a density-dependent electric field which can be seen in the relation $\langle\hat{E}\rangle = \lambda\langle\partial_t\hat{n}\rangle$. As illustrated in Fig. 4.2(b), the expectation value of the electric field operator can be directly inferred by observing temporal changes in the expectation value of the density operator and, importantly, changes in the density of the matter field induce electric forces which act back on the density and produce rich dynamics. In a harmonic trap, it has been shown that the current density term of Eq. 4.26 results in coupling between the monopole and dipole collective modes leading to chaotic dynamics for large amplitude oscillations [277–279].

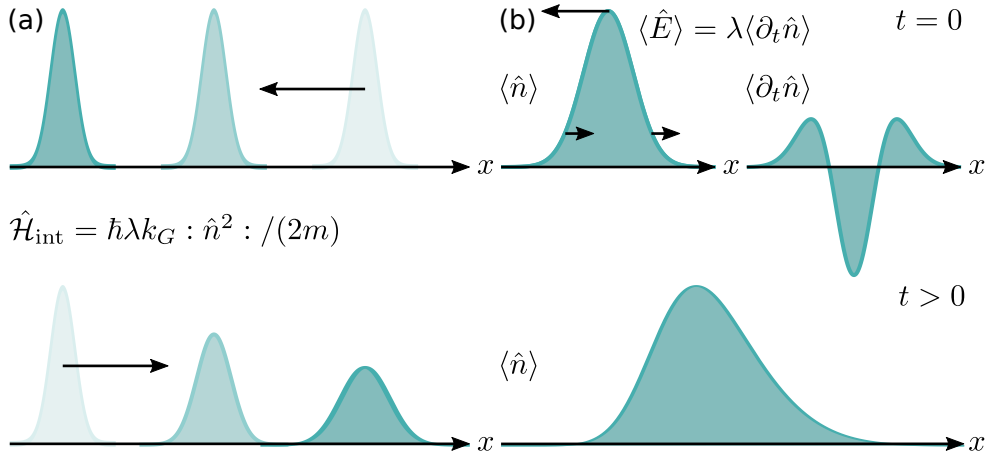

Figure 4.2: Dynamics of the chiral BF theory. (a) The current-density interaction term corresponds to a two-body contact interaction with interaction parameter proportional to the momentum of a wavepacket. When propagating to the left (top), the effective interactions are attractive and the wavepacket forms a self bound bright soliton. When propagating to the right (bottom) the effective interactions are repulsive and the wavepacket expands as a normal gas. (b) When a confined density distribution is suddenly allowed to expand, the sign and magnitude of the rate of change of the density varies between the centre and edges of the cloud. Since the chiral BF electric field is proportional to the time derivative of the density, an unevenly distributed effective electric force causes the density distribution to become skewed over time.

From the gauge theory perspective, it can be seen that the monopole mode corresponds to periodic compressions and expansions of the gas meaning periodic changes in density and a periodic electric driving force which couples to the centre of mass motion and excites the dipole mode.

Another manifestation of the density-dependent electric field can be seen in the dynamics of the matter density when the BEC is allowed to expand after being released from a confining potential. As the BEC expands, the sign of $\langle \partial_t \hat{n} \rangle$ is negative near the centre of the cloud and positive near the edges of the cloud. The simple expansion of the BEC results in an inhomogeneous distribution of electric forces acting on the BEC and over time, the back action of the gauge field will result in asymmetric expansion dynamics [131]. We have demonstrated chiral solitons and density-dependent asymmetric expansion experimentally [132] and these experiments will be discussed in Ch. 5.

4.5 Summary

In this chapter, I have introduced the chiral BF theory as a one dimensional reduction of the Chern-Simons theory used to describe fractional quantum Hall states in two dimensions. Both gauge theories are topological, meaning that the gauge fields do not have dynamics in the absence of matter and can be eliminated from the Hamiltonian

in favour of matter only terms with unusual interactions. Using the Faddeev-Jackiw approach, a second quantised encoded Hamiltonian for the chiral BF theory which is amenable to quantum simulation with BECs can be derived. In Ch 3, I introduced the theoretical framework and experimental methods required to engineer momentum-dependent interactions in a BEC. In Ch. 5 I will present the mapping of the Hamiltonian of a Raman coupled BEC with unequal intrastate interactions to the chiral interactions of Eq. 4.26 and the experimental realisation of the quantum simulation of the chiral BF theory.

Chapter 5

Realising the Chiral BF Theory in a Raman Coupled Bose-Einstein Condensate

In this chapter, I will demonstrate that the nontrivial momentum dependence of the interactions in the lower dressed band of a Raman coupled Bose-Einstein condensate introduced in Sec. 3.3.1 can be mapped to the chiral BF Hamiltonian. Furthermore, I will describe our experimental realisation of two key features of the chiral BF theory: chiral solitons which remain self-bound only when propagating in one direction and a density-dependent vector potential which is observed *via* the expansion dynamics of a BEC in an optical waveguide. Finally, I will examine the validity of the experimental mapping at the mean-field level using numerical simulations. The results presented in this chapter came as part of experimental collaborations between myself, Dr. Anika Frölian, Dr. Cesar Cabrera, Dr. Elettra Neri, Dr. Ramón Ramos, and Prof. Dr. Leticia Tarruell as well as theoretical collaborations with Dr. Alessio Celi. Parts of this chapter have been included in the publications "Realizing a 1D topological gauge theory in an optically dressed BEC" [132] and "Encoding a one-dimensional topological gauge theory in a Raman-coupled Bose-Einstein condensate" [118]. They have also been discussed in the PhD thesis of Dr. Anika Frölian [218].

5.1 Mapping a Raman Coupled Bose-Einstein Condensate to the Chiral BF Theory

As mentioned in Sec. 4.4, a mapping of a Raman coupled BEC to the chiral BF theory has been demonstrated at the mean-field level for very large values of Ω [131]. Such large values of the Raman Rabi frequency, Ω, would result in lifetimes on the order of 1 ms in a BEC of ^{39}K [207]. In this section, we will see how the mapping can be achieved at the quantum level without the requirement of very large Ω. We continue from the Raman coupled Hamiltonian restricted to the lower dressed band from Sec. 3.3.1: $\hat{H}_R = \hat{H}_{0,R} + \hat{V} + \hat{H}_{\mathrm{int},R}$ where, assuming a state-independent trapping

potential, $V(\mathbf{r})$,

$$\hat{H}_{0,R} = \int \frac{\mathrm{d}^3\mathbf{k}}{(2\pi)^3}\hat{\Phi}_-^\dagger(\mathbf{k})\varepsilon_-(\mathbf{k})\hat{\Phi}_-(\mathbf{k}), \tag{5.1}$$

$$\hat{V} = \int \frac{\mathrm{d}^3\mathbf{k}_2}{(2\pi)^3}\frac{\mathrm{d}^3\mathbf{k}_1}{(2\pi)^3}\hat{\Phi}_-^\dagger(\mathbf{k}_2)\tilde{V}(\mathbf{k}_1-\mathbf{k}_2)\left(C_1C_2+S_1S_2\right)\hat{\Phi}_-(\mathbf{k}_1) \tag{5.2}$$

with $\tilde{V}(\mathbf{k}_1-\mathbf{k}_2) = \int \mathrm{d}^3\mathbf{r}V(\mathbf{r})\exp\left[i\left(\mathbf{k}_1-\mathbf{k}_2\right)\cdot\mathbf{r}\right]$, and

$$\hat{H}_{\mathrm{int},R} = \int \frac{\mathrm{d}^3\mathbf{k}_1}{(2\pi)^3}\frac{\mathrm{d}^3\mathbf{k}_2}{(2\pi)^3}\frac{\mathrm{d}^3\mathbf{k}_3}{(2\pi)^3}\frac{\mathrm{d}^3\mathbf{k}_4}{(2\pi)^3}\hat{\Phi}_-^\dagger(\mathbf{k}_4)\hat{\Phi}_-^\dagger(\mathbf{k}_3)\hat{\Phi}_-(\mathbf{k}_2)\hat{\Phi}_-(\mathbf{k}_1) \times \chi(k_{x,1},k_{x,2},k_{x,3},k_{x,4})\delta^{(3)}\left(\mathbf{k}_3+\mathbf{k}_4-\mathbf{k}_1-\mathbf{k}_2\right) \tag{5.3}$$

with the screening function given by

$$\chi\left(k_{x,1},k_{x,2},k_{x,3},k_{x,4}\right) = g_{\uparrow\uparrow}C_2C_4C_1C_3 + g_{\downarrow\downarrow}S_2S_4S_1S_3 + g_{\uparrow\downarrow}\left(C_2C_4S_1S_3+S_2S_4C_1C_3\right). \tag{5.4}$$

Where, as defined in Ch. 3, $C_j = \cos\left[\theta(k_{x,j})\right]$ and $S_j = \sin\left[\theta(k_{x,j})\right]$ with $\cos\left[\theta(k_x)\right] = \left\{\left[1+\tilde{\delta}(k_x)/\tilde{\Omega}(k_x)\right]/2\right\}^{\frac{1}{2}}$ where $\hbar\tilde{\delta}(k_x)/E_R = \hbar\delta_0/E_R - 4k_x/k_R$ and $\tilde{\Omega}(k_x)^2 = \Omega^2 + \tilde{\delta}(k_x)^2$.

Assuming that the scalar potential, $V(\mathbf{r})$, does not confine the atoms too tightly in position space, the BEC will have a small spread in momentum space. Furthermore, we assume that $\hbar\Omega/E_R > 4$ such that the lower band dispersion has a single extremal value which is a global minimum located at quasimomentum $\hbar\mathbf{k} = \hbar k_{\min}\mathbf{e}_1 + 0\mathbf{e}_2 + 0\mathbf{e}_3$ where $k_{\min}$ is defined by $k_{\min}/k_R = -\tilde{\delta}(k_{\min})/\tilde{\Omega}(k_{\min})$. Taking $\hbar k_0\mathbf{e}_1$ to be an arbitrary quasimomentum which is close to the projection of the group quasimomentum of the atoms along the x-axis, we can make a series expansion of the terms depending on k_x around k_0 which will give us an accurate approximation of the Hamiltonian.

We start with the expansion of $\varepsilon_-(\mathbf{k})$. Letting $q = k_x - k_0$, we have

$$\frac{\varepsilon_-(\mathbf{k})}{E_R} = 1 + \frac{k_0^2+\mathbf{k}_\perp^2+2qk_0+q^2}{k_R^2} - \frac{\hbar\tilde{\Omega}(k_0)}{2E_R}f\left(\frac{qE_R}{\hbar\tilde{\Omega}(k_0)k_R}\right) \tag{5.5}$$

where

$$f(u) = \sqrt{1-8\tilde{\delta}(k_0)u/\tilde{\Omega}(k_0)+16u^2}. \tag{5.6}$$

Performing the Taylor expansion of $f(u)$ to third order in u gives

$$f(u) = 1 - 4\tilde{\delta}(k_0)u/\tilde{\Omega}(k_0) + 8\Omega^2u^2/\tilde{\Omega}(k_0)^2 + 32\tilde{\delta}(k_0)\Omega^2u^3/\tilde{\Omega}(k_0)^3 + \mathcal{O}(u^4). \tag{5.7}$$

Defining $\tilde{\delta}_0 = \tilde{\delta}(k_0)$ and $\tilde{\Omega}_0 = \tilde{\Omega}(k_0)$, we can write

$$\varepsilon_-(\mathbf{k}) \approx E_R + \frac{\hbar^2k_0^2}{2m} - \frac{\hbar\tilde{\Omega}_0}{2} + \frac{\hbar^2\mathbf{k}_\perp^2}{2m} + \frac{\hbar^2\left[q-A_q\right]^2}{2mm^*} + W_q \tag{5.8}$$

where $W_q = -\hbar^2A_q^2/(2mm^*)$, $mm^* = m\left[1-4E_R\Omega^2/\left(\hbar\tilde{\Omega}_0^3\right)\right]^{-1}$ is the effective mass[1], and $A_q = -m^*\left[k_0 + k_R\tilde{\delta}_0/\tilde{\Omega}_0 - 4E_R\tilde{\delta}_0\Omega^2q^2k_R/\left(m\tilde{\Omega}_0^5\right)\right]$ is the momentum-dependent

[1]Here, m^* is a dimensionless parameter which rescales the mass to the effective mass.

vector potential. Thus, dropping constant energy contributions, we have

$$\hat{H}_{0,R} \approx \int \mathrm{d}^3\mathbf{r}\hat{\phi'}_-^\dagger \left[\frac{\hbar^2\left(-i\partial_x - A_0\right)^2}{2mm^*} - \frac{\hbar^2}{2m}\nabla_\perp^2 + W_0\right]\hat{\phi'}_- \tag{5.9}$$

where $A_0 = -m^*\left[k_0 + k_R\tilde{\delta}_0/\tilde{\Omega}_0 + 4E_R\tilde{\delta}_0\Omega^2 k_R\partial_x^2/\left(m\tilde{\Omega}_0^5\right)\right]$, $W_0 = -\hbar^2 A_0^2/(2mm^*)$, $\nabla_\perp^2 = \partial_y^2 + \partial_z^2$, and $\hat{\phi'}_- = \hat{\phi}_- \exp\left(-ik_0x\right)$. The effective mass mm^*, applies only along the x-axis, reflecting the anisotropy imposed on the BEC by the Raman coupling [153]. The introduction of the effective mass is what allows us to drop the requirement of very large Raman Rabi frequency, Ω, needed in the derivation of Edmonds *et al.* [131].

Since we have done nothing more than perform a Taylor series expansion on $\varepsilon_-(\mathbf{k})$ to third order, we know that the error is bounded by the fourth order expansion term. We achieve a consistent level of approximation by expanding $\chi\left(k_{x,1}, k_{x,2}, k_{x,3}, k_{x,4}\right)$ to first order in q_j where $k_{x,j} = k_0 + q_j$ for $j = 1, 2, 3, 4$. We have

$$C_j = C_0\left[1 - 2u_j\left(1 - \tilde{\delta}_0/\tilde{\Omega}_0\right)\right] + \mathcal{O}(u_j^2) \tag{5.10}$$

and

$$S_j = S_0\left[1 + 2u_j\left(1 + \tilde{\delta}_0/\tilde{\Omega}_0\right)\right] + \mathcal{O}(u_j^2) \tag{5.11}$$

where $C_0 = \cos\left[\theta(k_0)\right]$, $S_0 = \sin\left[\theta(k_0)\right]$, and $u_j = q_jE_R/\left(\hbar\tilde{\Omega}_0k_R\right)$. Substituting these expressions into $\chi\left(k_{x,1}, k_{x,2}, k_{x,3}, k_{x,4}\right)$ and keeping only linear terms, we have

$$\chi\left(k_{x,1}, k_{x,2}, k_{x,3}, k_{x,4}\right) \approx g_{\mathrm{eff}}(k_0) + 2\left[\tilde{\delta}_0 g_{\mathrm{eff}}(k_0)/\tilde{\Omega}_0 + g_{\downarrow\downarrow}S_0^4 - g_{\uparrow\uparrow}C_0^4\right]\sum_{j=1}^{4} u_j \tag{5.12}$$

where $g_{\mathrm{eff}}(k_0) = \chi\left(k_0, k_0, k_0, k_0\right)$ is the momentum-dependent generalisation of the effective interaction g_{--} for a BEC with group quasimomentum $\hbar\left(k_0\mathbf{e}_1 + \mathbf{k}_\perp\right)$. Transforming to position space, we have $\hat{\mathcal{H}}_{\mathrm{int},R} \approx g_{\mathrm{eff}}(k_0)\hat{\phi'}_-^\dagger\hat{\phi'}_-^\dagger\hat{\phi'}_-\hat{\phi'}_- + \lambda\hat{\phi'}_-^\dagger\hat{j}'\hat{\phi'}_-$ where $\hat{j}' = \hbar\left[\hat{\phi'}_-^\dagger\partial_x\hat{\phi'}_- - \left(\partial_x\hat{\phi'}_-^\dagger\right)\hat{\phi'}_-\right]/(2imm^*)$ is the normal ordered current operator and $\lambda = \left(4m^*k_R/\tilde{\Omega}_0\right)\left[\tilde{\delta}_0 g_{\mathrm{eff}}(k_0)/\tilde{\Omega}_0 + g_{\downarrow\downarrow}S_0^4 - g_{\uparrow\uparrow}C_0^4\right]$.

The assumption that the BEC is not strongly compressed by the trap can be rephrased as saying that the trap varies slowly with $\mathbf{r}$ and is therefore very narrow in momentum space which means that we can approximate $\hat{V}$ using only zero order terms in u_j so that $\tilde{V}(\mathbf{k}_1 - \mathbf{k}_2)\left(C_1C_2 + S_1S_2\right) \approx \tilde{V}(\mathbf{k}_1 - \mathbf{k}_2)\left(C_0^2 + S_0^2\right) = \tilde{V}(\mathbf{k}_1 - \mathbf{k}_2)$ So, in position space, we have $\hat{V} \approx \int \mathrm{d}^3\mathbf{r}\hat{\phi'}_-^\dagger V(\mathbf{r})\hat{\phi'}_-$ and the total Hamiltonian is

$$\hat{H}_R \approx \int \mathrm{d}^3\mathbf{r}\hat{\phi'}_-^\dagger \left[\frac{\hbar^2\left(-i\partial_x - A_0\right)^2}{2mm^*} - \frac{\hbar^2}{2m}\nabla_\perp^2 + W_0 + V(\mathbf{r}) + \frac{g_{\mathrm{eff}}(k_0)}{2}\hat{\phi'}_-^\dagger\hat{\phi'}_- + \frac{\lambda}{2}\hat{j}'\right]\hat{\phi'}_-. \tag{5.13}$$

For a given value of k_0, we can choose the detuning, δ_0, such that $\hbar\tilde{\delta}_0/E_R = 0$. In this case, we have $m^* = \left[1 - 4E_R/(\hbar\Omega)\right]^{-1}$, $A_0 = -m^*k_0$, $g_{\mathrm{eff}}(k_0) = \left(g_{\uparrow\uparrow} + g_{\downarrow\downarrow} + 2g_{\uparrow\downarrow}\right)/4 \equiv$

g_1, and $\lambda = m^* k_R \left(g_{\downarrow\downarrow} - g_{\uparrow\uparrow}\right)/\Omega$. Thus, dropping constant energy contributions again,

$$\hat{H}_R \approx \int \mathrm{d}^3\mathbf{r}\hat{\psi}^\dagger \left[-\frac{\hbar^2}{2m}\left(\frac{1}{m^*}\frac{\partial^2}{\partial x^2} + \nabla_\perp^2\right) + V(\mathbf{r}) + \frac{g_1'}{2}\hat{\psi}^\dagger\hat{\psi} + \frac{\lambda}{2}\hat{j}\right]\hat{\psi} \tag{5.14}$$

where $\hat{\psi} = \hat{\phi}'_- \exp\left(im^* k_0 x\right)$, $\hat{j} = \hbar\left[\hat{\psi}^\dagger\partial_x\hat{\psi} - \left(\partial_x\hat{\psi}^\dagger\right)\hat{\psi}\right]/(2imm^*)$, and $g_1' = g_1 - \hbar\lambda k_0/m$.

Aside from the transverse kinetic terms, the Hamiltonian (Eq. 5.14) we have arrived to corresponds to the chiral BF Hamiltonian of Eq. 4.26. Thus, the only step left to simulate the chiral BF theory in a BEC is to prepare the lower Raman coupled dressed state in a regime where the assumptions used to arrive to Eq. 5.14 are valid and λ is sufficiently large to create measurable effects. The two main differences between the derivation presented here and the original derivation of Edmonds *et al.* [131] are that this mapping is valid in the quantum regime and that the derivation is valid at values of Ω just above the threshold of the single minimum regime ($\hbar\Omega/E_R = 4$) at the expense of defining an effective mass. In other words, the mean-field approximation of Eq. 5.14 reproduces the equation of motion of Edmonds *et al.* [131] in Eq. 4.29 with the addition of a negligibly small three-body interaction and under the additional approximation $m^* \approx 1$ which requires $\hbar\Omega/E_R \gtrsim 100$. Our derivation is valid for a BEC with group quasimomentum close to k_0 provided the detuning is set such that $\hbar\delta_0/E_R = 4k_0/k_R$ for any value of k_0.

In the chiral BF theory, contact interactions are only specified to be polynomial in density. Therefore, we can add a negligibly small three-body interaction term $\hat{H}_{3\mathrm{B}} = \int \mathrm{d}^3\mathbf{r}(\lambda^2/8mm^*)\hat{\psi}^\dagger\hat{\psi}^\dagger\hat{\psi}^\dagger\hat{\psi}\hat{\psi}\hat{\psi}$ to Eq. 5.14 without impacting the validity of our mapping. With the additional three-body term, we can rewrite the Hamiltonian as

$$\hat{H}_R \approx \int \mathrm{d}^3\mathbf{r}\hat{\psi}^\dagger \left\{-\frac{\hbar^2}{2m}\left[\frac{1}{m^*}\left(\frac{\partial}{\partial_x} + \frac{i}{\hbar}\frac{\lambda}{2}\hat{\psi}^\dagger\hat{\psi}\right)^2 + \nabla_\perp^2\right] + V(\mathbf{r}) + \frac{g_1'}{2}\hat{\psi}^\dagger\hat{\psi}\right\}\hat{\psi} \tag{5.15}$$

where we identify the density-dependent vector potential $\hat{A}_n = -\lambda\hat{\psi}^\dagger\hat{\psi}/2$ which is the same as the density-dependent vector potential in Eq. 4.27 and is related to the chiral BF vector potential through $\hat{A}_n = \hat{A}_{\mathrm{BF}}/2$. The density-dependent vector potential was the key point in the derivation by Edmonds *et al.* [131]. Here, we have taken a momentum space approach and found chiral interactions to be the key ingredient. As explained in Ch. 4 the density-dependent vector potential and chiral interactions are two equivalent descriptions of the chiral BF theory so it is no surprise that we are able to reformulate the Hamiltonian in Eq. 5.14 in terms of a density-dependent vector potential.

5.2 Experimental Realisation of the Chiral BF Theory in a Raman Coupled Bose-Einstein Condensate

In order to experimentally realise the chiral BF theory, we wish to make λ large so that the effects of the nonlinear current term in the Hamiltonian are significant. This

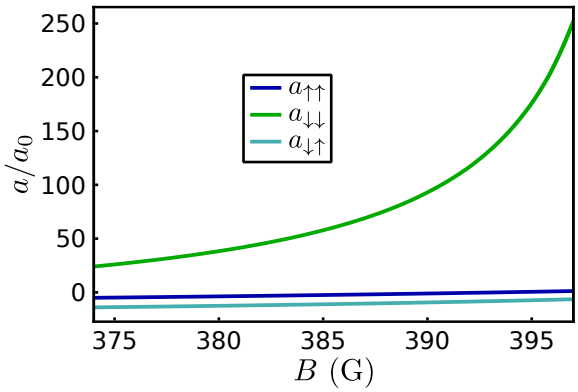

Figure 5.1: Magnetic field dependence of the interstate and intrastate scattering lengths for states $|\downarrow\rangle = |F = 1, m_F = 1\rangle$ and $|\uparrow\rangle = |F = 1, m_F = 0\rangle$ in ^{39}K.

requires keeping Ω relatively small since $\lambda \propto \Omega^{-1}$. Keeping Ω small will also help to achieve a lifetime of the BEC on the order of tens of milliseconds so that dynamics may be observed. Additionally, the difference between the bare intrastate interaction parameters, $|g_{\downarrow\downarrow} - g_{\uparrow\uparrow}|$, should be made as large as practically possible. Finally, we would like to be able to access regimes where $g_1 < 0$ so that we can observe the chiral solitons which have been theoretically predicted since the 1990s [115, 116, 131, 273–276] and also regimes where $g_1 > 0$ so that the density-dependent vector potential of Eq. 4.27 may be observed in an expanding BEC, as predicted by Edmonds *et al.* [131].

A suitable choice of isotope and states is ^{39}K with $|\downarrow\rangle = |F = 1, m_F = 1\rangle$ and $|\uparrow\rangle = |F = 1, m_F = 0\rangle$ with a bias magnetic field, $\mathbf{B} = B\mathbf{e}_3$, with B in the range 374 G - 397 G. The scattering lengths $a_{\uparrow\uparrow}$, $a_{\downarrow\downarrow}$, and $a_{\uparrow\downarrow}$ calculated by Prof. Dr. Andrea Simoni using the interaction potentials of Ref. [226] are shown in Fig. 5.1. We see that the difference $g_{\downarrow\downarrow} - g_{\uparrow\uparrow}$ is large and tunable in this field range and that $g_{\uparrow\uparrow}$ can be tuned from weakly repulsive to weakly attractive while $g_{\uparrow\downarrow}$ is always attractive. With these parameters, we are able to fulfil the requirements stated above. In this field range the sensitivity of the Zeeman splitting of the two states is $\mathrm{d}\omega_0/\mathrm{d}B/(2\pi) \approx 50$ Hz/mG so taking a high estimate of the magnetic field noise of 10 mG from Sec. 3.1.2 we estimate a detuning uncertainty of ~ 500 Hz.

The experiments shown in this chapter begin with a single-component BEC in a crossed optical dipole trap formed by laser beams with wavelength 1064 nm propagating along the $\mathbf{e}_1$ and $\mathbf{e}_3$ axes. The crossed dipole trap is modelled as a harmonic oscillator potential $V(\mathbf{r}) = m\left(\omega_x^2 x^2 + \omega_y^2 y^2 + \omega_z^2 z^2\right)/2$.

Preparing the lower dressed band with Raman coupling is straightforward in principle. For a BEC in state $|\downarrow\rangle$ at rest in the laboratory frame, we have $k_x/k_R = 1$ and

$$\lim_{\hbar\Omega/E_R \to 0} \langle \downarrow', k_x/k_R = 1 | -, k_x/k_R = 1 \rangle = \sqrt{\left[1 - \tilde{\delta}(k_R)/|\tilde{\delta}(k_R)|\right]/2} \tag{5.16}$$

so as long as $\hbar\delta_0/E_R < 4$, the lower band overlaps exactly with a BEC in state $|\downarrow\rangle$ at

rest in the laboratory frame in the limit of zero coupling and can be prepared simply by ramping up the optical power in the Raman beams smoothly starting from zero. In practice the restriction on detuning is made stronger by the need to keep the energy gap to the upper band significant enough to prevent coupling between the bands and to ensure that the minimum for $k_x/k_R > 0$ exists for all values of Ω. If $\hbar\delta_0/E_R > 0$, when the value of $\hbar\Omega/E_R$ reaches $4\left\{1 - [\hbar\delta_0/(4E_R)]^{2/3}\right\}^{3/2}$ the minimum of the lower band dispersion at positive quasimomentum will disappear.

In the presence of a confining potential, this would cause the BEC to diabatically evolve towards the minimum at negative quasimomentum and then oscillate in the trap [234]. The same arguments would hold with the sign of the detuning reversed if the initial state was $|\uparrow\rangle$ but we always start in $|\downarrow\rangle$ since, for our chosen states, this ensures that the BEC has repulsive interactions and is stable in the trap. In practice, we always set an initial negative detuning to ensure that magnetic field fluctuations do not tip the balance into the diabatic regime.

Aside from avoiding the diabatic evolution of the BEC upon disappearance of a minimum in the dispersion, it is desirable to adjust the Raman coupling parameters in such a way that the BEC follows the minimum of the dispersion to avoid dipole oscillations in the trap [280, 281]. For a harmonic trapping potential, this means that the time scales for ramps of Ω and δ_0 must be on the order of the trap period. To improve the preparation sequence, we take advantage of the fact that the minima of the lower band dispersion do not have a linear dependence on Ω and δ_0 to decrease the ramp up time and hence reduce the losses due to inelastic photon scattering during preparation. We choose a two step sequence where in the first step we ramp the Rabi frequency according to $\hbar\Omega(t)/E_R = 4\sqrt{(2 - t/\tau_1)\, t/\tau_1}$ with a fixed detuning, $\delta_{0,i}$, during a time τ_1. In the second step we perform simultaneous linear ramps of the Rabi frequency and detuning to their final values, Ω_f and $\delta_{0,f}$, in a time τ_2.

5.2.1 Observation of Chiral Solitons

In order to study the momentum dependence of the interactions in the presence of Raman coupling, we investigate the dynamics of the BEC propagating in the $\pm\mathbf{e}_1$ directions. To impart momentum on the BEC we adapt the experimental setup shown in Fig. 3.8(a) by adding two AOMs[2] between the BEC and the retroreflecting mirror. The original version of the setup was built during the Master's project of Philip Thomas [282]. The two AOMs are driven at frequencies $\omega_{B,1}$ and $\omega_{B,2}$, respectively. The retroreflected optical lattice is formed by the $+1$ and -1 double passed diffraction orders of the two AOMs so that rather than a standing wave, a running wave optical lattice is formed with translation frequency $2\,(\omega_{B,1} - \omega_{B,2}) \equiv \Delta\omega_B$ [282]. The adapted experimental setup is shown in Fig. 5.2.

We impart momentum $\pm\hbar k_B \mathbf{e}_1$ upon the Raman dressed BEC by switching off the dipole trap beam propagating in the $\mathbf{e}_3$ direction and pulsing the running wave lattice in the Bragg diffraction regime [72, 283, 284]. The propagation direction of the

[2]Intraaction, ATM-801A1

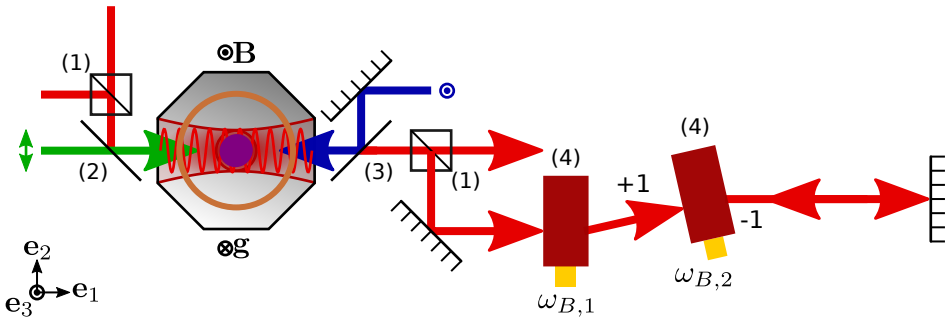

Figure 5.2: Experimental setup for Bragg diffraction. A BEC is initially held in a crossed optical dipole trap formed by laser beams propagating in the $\mathbf{e}_1$ and $\mathbf{e}_3$ directions. A running wave optical lattice with translation frequency $\Delta\omega_B = 2\left(\omega_{B,1} - \omega_{B,2}\right)$ is pulsed onto the BEC and the trapping beam propagating along the $\mathbf{e}_3$ direction is switched off. A momentum $\pm\hbar k_B \mathbf{e}_1$ is imparted onto the BEC by the lattice pulse with the direction determined by the sign of $\Delta\omega_B$. The optical components shown are (1) polarising beam splitter, QiOptiq G335525000; (2) dichroic mirror, Thorlabs DMSP1000L; (3) dichroic mirror, Thorlabs DMLP950L; (4) acousto-optic modulators, Intraaction ATM-801A1.

diffracted BEC is set by the translation direction of the running wave optical lattice and entering the Bragg regime requires matching the frequency $\Delta\omega_B$ to the change in kinetic energy. Assuming the BEC is initially at rest in the laboratory frame, a kick to the $\pm\mathbf{e}_1$ direction requires $\hbar|\Delta\omega_B| = \varepsilon_-(k_{\min}\mathbf{e}_1 \pm k_B\mathbf{e}_1) - \varepsilon_-(k_{\min}\mathbf{e}_1)$. For a BEC without Raman coupling, this reduces to $\hbar|\Delta\omega_B| = \hbar^2 k_B^2/(2m)$ while the required frequency difference in the presence of Raman coupling is dependent on Ω, δ_0, and the direction of the kick due to the fact that the Raman coupling breaks Galilean invariance. We are typically able to transfer more than 88 % of the atoms to the quasimomentum class $\hbar\left(k_{\min} \pm k_B\right)\mathbf{e}_1$ for given values of Ω and δ_0.

In the first series of experiments we prepare the BEC with trap frequencies $\omega_x/(2\pi) = 76(2)$ Hz, $\omega_y/(2\pi) = 128(2)$ Hz, and $\omega_z/(2\pi) = 55(5)$ Hz with a bias magnetic field $B = 374.29(1)$ G corresponding to $a_{\uparrow\uparrow} = -4.9a_0$, $a_{\downarrow\downarrow} = 24.6a_0$, and $a_{\uparrow\downarrow} = -13.8a_0$. The ramp times for preparing the Raman dressed state are $\tau_1 = 40$ ms and $\tau_2 = 5$ ms and the parameters of the Raman beams are $\hbar\delta_{0,i}/E_R = \hbar\delta_{0,f}/E_R = -2.62(6)$ and $\hbar\Omega_f/E_R = 5.3(3)$. When the dipole trapping beam propagating in the $\mathbf{e}_3$ direction is switched off the trap frequencies are quenched to $\omega_x/(2\pi) = 4(1)$ Hz, $\omega_y/(2\pi) = 98(2)$ Hz, and $\omega_z/(2\pi) = 55(5)$ Hz and the measured atom number is $N = 14(4) \times 10^3$.

Figure 5.3(a) and Fig. 5.3(b) show *in situ* images of the BEC kicked in the $-\mathbf{e}_1$ and $\mathbf{e}_1$ directions, respectively. The positions of the BEC for the two kick directions are shown in Fig. 5.3(c). The measured velocities are $\mathbf{v} = -8.83(2)\mathbf{e}_1$ mm/s and $\mathbf{v} = 17.39(4)\mathbf{e}_1$ mm/s, in good agreement with the expected values of $\mathbf{v} = -9.0(4)\mathbf{e}_1$ mm/s and $\mathbf{v} = 16.8(3)\mathbf{e}_1$ mm/s with the difference in absolute value for the two propagation directions reflecting the breaking of Galilean invariance by the

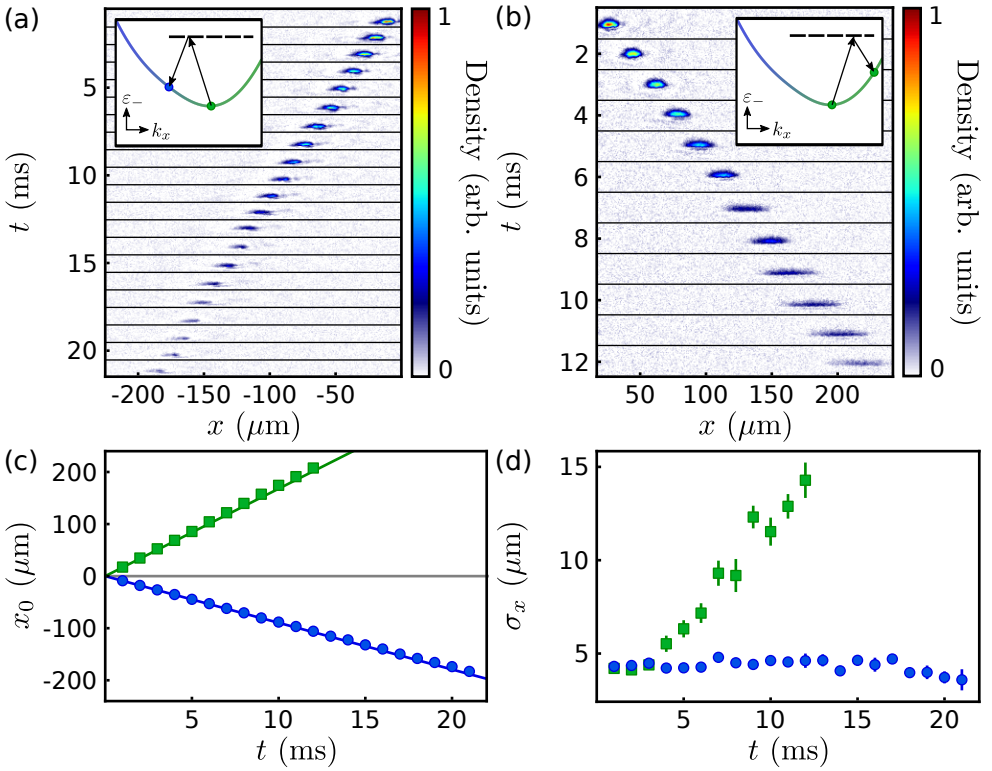

Figure 5.3: (a), (b) *In situ* density profiles of a Raman dressed BEC with $\hbar\Omega/E_R = 5.3(3)$, $\hbar\delta_0/E_R = -2.62(6)$, $a_{\uparrow\uparrow} = -4.9a_0$, $a_{\downarrow\downarrow} = 24.6a_0$, and $a_{\uparrow\downarrow} = -13.8a_0$ as a function of time, t, after a momentum kick $\pm\hbar k_B \mathbf{e}_1$ implemented *via* Bragg diffraction (insets). The slight deformation of the clouds in (a) is due to optical aberrations which are less visible with the larger clouds in (b). (c) Centre of mass position, x_0, and (d) width, σ_x, of the BEC kicked to the left (blue circles) and to the right (green squares). In (c), the blue and green lines illustrate the expected velocity of the cloud without fitting parameters while the grey line shows $x_0 = 0$ μm. For the BEC kicked to the left, the width does not evolve in time, indicating the formation of a bright soliton. Values and error bars correspond to the mean and standard deviation of three to five measurements.

Raman coupling. Figure 5.3(d) shows the widths extracted from Gaussian fits of the form $n = n_0 \exp\left[-(x-x_0)^2/(2\sigma_x^2) - y^2/(2\sigma_y^2)\right]$. We see that when the BEC is kicked to the left, σ_x remains constant in time[3], constituting the formation of a bright soliton [193, 194]. When the BEC is kicked to the right, σ_x grows by a factor of three in less than 15 ms. These observations are compatible with effective scattering lengths $a_{\text{eff}}(k_{\min} - k_B) = -2.7$ and $a_{\text{eff}}(k_{\min} + k_B) = 21.1$ where $g_{\text{eff}}(k_0) = 4\pi\hbar^2 a_{\text{eff}}(k_0)/m$.

[3]Within our optical resolution. As atoms are lost due to inelastic scattering of photons, one would expect a slight increase in the soliton width due to decreasing attractive contact interactions but the experimental time scale is approximately half of the 1/exp(1) lifetime. The slight decrease in width after 15 ms may indicate oscillations of the width on much longer time scales (see Appendix A).

The group quasimomentum, k_G, of the kicked BEC can be inferred from its relation to the velocity along the x-axis given by $v_-(k_G) = \partial_{k_x}\varepsilon_-/\hbar|_{k_x=k_G} = \hbar k_G/m + \left[\tilde{\delta}(k_G)/\tilde{\Omega}(k_G)\right]\hbar k_R/m$. Using the fitted velocities we obtain $k_G/k_R = -0.69(8)$ for the BEC kicked to the left and $k_G/k_R = 2.2(5)$ for the BEC kicked to the right. We can use the group quasimomentum and the width of the BEC to estimate the size of next order corrections in the low order momentum expansion, which is a measure of the quality of the mapping of the system to the chiral BF theory. Since we form chiral solitons, we assume that the system is quasi one-dimensional and we write down an approximation of the wavefunction describing the BEC at the mean-field level $\psi = \sqrt{N}\left(\pi\sigma_x^2\right)^{-1/4}\exp\left[-\left(x-x_0\right)^2/(2\sigma_x^2)\right]\exp\left(ik_G x\right)$. Taking $k_0/k_R = \hbar\delta_0/(4E_R)$, the expansion to third order in quasimomentum around k_0 of the lower band dispersion is (dropping constant terms) $\varepsilon_-(k_x) \approx \hbar^2\left[k_0\left(k_x-k_0\right)+\left(k_x-k_0\right)^2/m^*\right]/(2m) \equiv \varepsilon_1+\varepsilon_2$.

We compute the kinetic energy corresponding to motion along the x-axis by evaluating the expectation value of $\varepsilon_1+\varepsilon_2$ with the approximate wave function of the BEC

$$\frac{\langle\varepsilon_1+\varepsilon_2\rangle}{NE_R} = \frac{\left(k_G-k_0\right)\hbar\delta_0}{2E_R k_R} + \left(1-\frac{4E_R}{\hbar\Omega}\right)\left[\frac{1}{4k_R^2\sigma_x^2}+\frac{\left(k_G-k_0\right)^2}{k_R^2}\right]. \tag{5.17}$$

The next nonzero term in the expansion is to fourth order and we have

$$\frac{\langle\varepsilon_4\rangle}{NE_R} = \left(\frac{E_R}{\hbar\Omega}\right)^3\left[3+24\left(k_G-k_0\right)^2\sigma_x^2+16\left(k_G-k_0\right)^4\sigma_x^4\right]/\left(k_R\sigma_x\right)^4. \tag{5.18}$$

We can approximate the relative kinetic energy error caused by truncating the expansion at third order as $\Delta\varepsilon_{\text{kin}} = |\langle\varepsilon_4\rangle/\langle\varepsilon_1+\varepsilon_2\rangle|$. For the BEC kicked to the right we estimate $\Delta\varepsilon_{\text{kin}} \gtrsim 4$ and for the BEC kicked to the left we estimate $\Delta\varepsilon_{\text{kin}} \lesssim 10^{-3}$. We expect that the relative error in the interaction energy is on the same order as the relative error in the kinetic energy. Therefore, we have small corrections to the effective chiral BF Hamiltonian for the kick in the $-\mathbf{e}_1$ direction and we conclude that the observed bright solitons constitute an experimental realisation of chiral BF solitons [115, 116, 273].

To study the chiral properties of the Raman dressed soliton we add an optical barrier composed of an elliptical laser beam propagating in the $\mathbf{e}_3$ direction with wavelength $\lambda_{\text{barrier}} = 765$ nm and $1/\exp(2)$ radii $(w_x, w_y) \approx (14, 350)$ μm. At this wavelength the difference in polarisabilities for states $|\uparrow\rangle$ and $|\downarrow\rangle$ is ~ 1 % and we approximate the potential as state-independent. The barrier is positioned to the left of the initial position of the BEC and the optical power is set high enough to ensure that all atoms are reflected upon collision with the barrier. Figure 5.4(a) shows *in situ* images of the Raman dressed soliton as it propagates towards the barrier and reflects off of it. We can see that after reflection, the BEC begins to expand, directly revealing the chiral nature of the soliton.

For comparison Fig. 5.4(b) shows a similar experiment performed with a single-component bright soliton in state $|\uparrow\rangle$ with a bias magnetic field of $B = 385.62(1)$ G where the scattering length is $a_{\uparrow\uparrow} = -2.3a_0$. In contrast to the chiral soliton, the

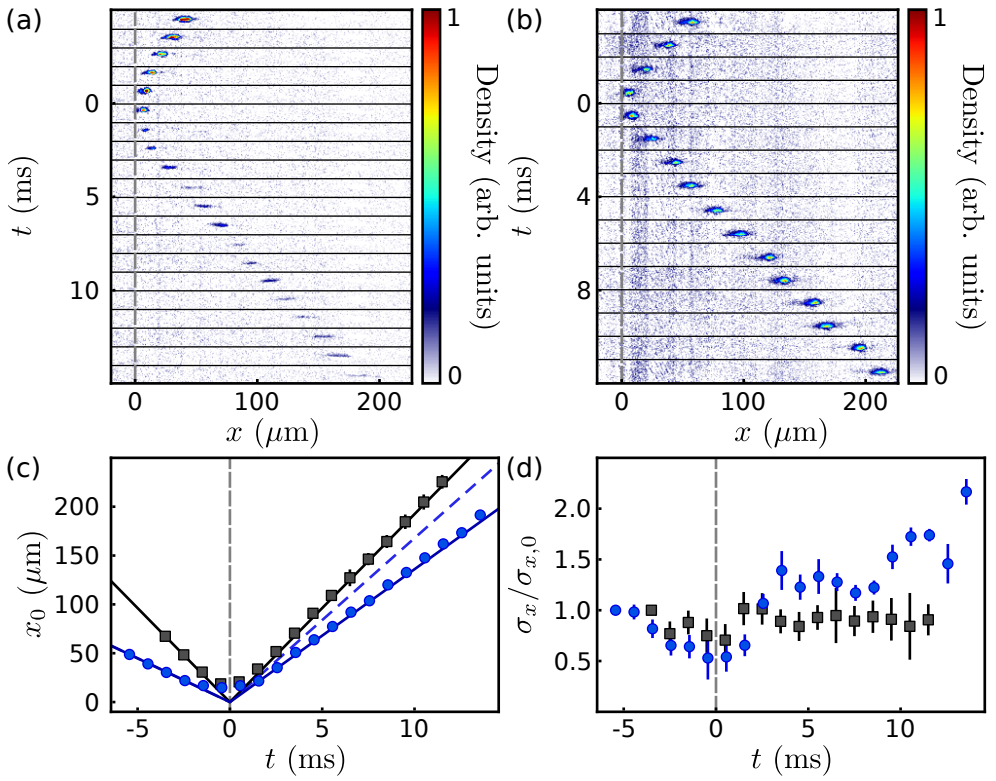

Figure 5.4: (a) *In situ* images of a chiral soliton reflecting from an optical barrier (dashed grey line) with the same parameters as Fig. 5.3(a). After reflecting from the barrier, the chiral soliton begins to expand. (b) *In situ* images of a single-component soliton in state $|\uparrow\rangle$ with $a_{\uparrow\uparrow} = -2.3a_0$ reflecting from an optical barrier. The width of the single-component soliton is unchanged after interaction with the barrier. (c) Positions and (d) widths of the chiral soliton (blue circles) and single-component soliton (grey squares). In (c), the solid blue and black lines show the predicted positions without fitting parameters for the chiral and single-component solitons, respectively. The dashed blue line shows the predicted position of the chiral soliton assuming quasi-momentum conservation. Values and error bars are the mean and standard deviation of three to five measurements.

single-component soliton maintains its width after reflection from the barrier, as we would expect. The positions and widths of the chiral and single-component solitons are shown in Fig. 5.4(c) and Fig. 5.4(d), respectively. The Hamiltonian describing the single-component soliton is Galilean invariant so, since the optical potential is conservative, the incoming and outgoing velocities have the same magnitude (black lines).

The chiral soliton does not have Galilean invariance so the incoming and outgoing velocities do not have the same magnitude. Furthermore, it is not possible to conserve both kinetic energy and quasimomentum upon reflection from the barrier. In this case, conservation of quasimomentum would imply $k_{\text{out}} = -k_{\text{in}} + 2k_{\text{min}}$ and the corre-

sponding velocity is indicated by the dashed blue line. We can see that the outgoing speed of the BEC is less than would be expected for quasimomentum conservation and the actual speed corresponds to conservation of kinetic energy (solid blue line). For both the chiral and single-component solitons, the BEC is slightly compressed during interaction with the barrier which is expected when the width of the barrier and the width of the soliton are comparable [285]. Numerical simulations of a chiral soliton bouncing from an optical barrier are given in Appendix A.

5.2.2 Density-Dependent Synthetic Vector Potential

Asymmetry From the Chiral BF Electric Field

Aside from the existence of chiral solitons, another key feature of the chiral BF theory is a density-dependent vector potential [115, 116, 131, 273]. The vector potential is a topological gauge field which does not have dynamics in the absence of matter and cannot be measured directly. Instead, we measure its impact on matter through the effective electric field[4] produced by time variations in the density-dependent vector potential $\langle \hat{E} \rangle = -\langle \partial_t \hat{A}_{\mathrm{BF}} \rangle = \lambda \langle \partial_t \hat{n} \rangle$. As shown in Fig. 4.2(b), since the effective electric field is proportional to the time derivative of the atomic density, for a wave packet initially held in a crossed optical dipole trap and then allowed to expand along the x-axis, we expect the electric force to point in the $\mathbf{e}_1$ direction at the edges of the BEC where the density increases during expansion and in the $-\mathbf{e}_1$ direction near the centre where the density decreases during expansion (assuming $\lambda > 0$). As well as pointing in different directions at the centre and edges of the cloud, the differential electric force has different magnitudes in different parts of the cloud. Over time, we expect this to result in an effectively faster expansion to the right compared to the left. Thus, an asymmetry in the atomic density profile after expansion would be a signature of the chiral BF electric field [131]. In addition to the density-dependent vector potential, in our mapping, the single particle synthetic vector potential includes a spatial derivative if $\hbar\delta_0/E_R \neq 4k_0/k_R$. This means that the expanding BEC can become asymmetric even if $g_{\downarrow\downarrow} = g_{\uparrow\uparrow}$ which would break the mapping to the chiral BF theory unless $\hbar\tilde{\delta}_0/E_R = 0$.

Kinetic Effects

A similar effect has already been demonstrated with ^{87}Rb where $k_R^2\lambda/\hbar \approx 0$ [236]. These experiments were understood in an alternative picture where the effective mass is momentum-dependent and expressed as[5] $1/\left[mM^*(k_x)\right] = \partial^2_{k_x}\varepsilon_-(k_x)/\hbar^2$ which gives $M^*(k_x) = 1/\left[1 - (4E_R/\hbar)\Omega^2/\tilde{\Omega}(k_x)^3\right]$. The experiments in ^{87}Rb were performed in the regime $\hbar\Omega/E_R < 4$ where the dispersion has two minima. The BEC was loaded

[4]Strictly speaking, this is an electric force since the charge units have been absorbed into $\hat{E}$ and $\hat{A}_{\mathrm{BF}}$, as in Ch. 4.

[5]Note that $M^*(k_x)$ has a similar physical meaning to the previously defined m^* but we use different notation to distinguish the momentum-dependent effective mass, $mM^*(k_x)$ from the effective mass which depends on k_0, mm^*.

into the minimum with $k_x/k_R < 0$ and allowed to expand into an optical waveguide. The mean-field repulsion of the condensate caused the BEC to grow in momentum space. The dispersion relation has an inflection point when $4E_R k_x/(\hbar k_R) = \delta_0 \pm \sqrt{(4E_R\Omega^2/\hbar)^{2/3} - \Omega^2}$ which means the effective mass, $mM^*(k_x)$, becomes negative and the quantum pressure acts as an attractive force similarly to the way negative effective mass stabilises gap bright solitons in a periodic potential [196]. Since the sign of the effective mass is momentum-dependent the quantum pressure is attractive only for atoms moving in one dimension and remains repulsive for atoms moving in the other direction resulting in asymmetric expansion [236]

The momentum-dependent effective mass picture also holds in the single minimum regime. In this case, $M^*(k_x)$ is always positive but we have

$$k_R \frac{\partial}{\partial k_x} M^*(k_x) = \frac{48 E_R^2 \Omega^2 \tilde{\delta}(k_x)}{\hbar^2 \tilde{\Omega}(k_x)^5} M^*(k_x)^2 \tag{5.19}$$

which is nonzero whenever $\hbar\tilde{\delta}(k_x)/E_R \neq 0$. If the derivative of the effective mass is nonzero then the atoms moving in one direction would be effectively more massive than the atoms moving in the other direction. For an expanding BEC with mass m, the width is expected to scale as $\sigma_x \propto m^{-2/5}$ [212] so we also expect asymmetric expansion when $\hbar\Omega/E_R > 4$ if $\hbar\tilde{\delta}(k_x)/E_R \neq 0$ since the effectively heavier atoms moving in one direction expand more slowly than the effectively lighter atoms moving in the opposite direction.

We investigate these kinetic asymmetric expansion effects numerically by simulating the equations of motion corresponding to the full two-component system in the presence of Raman coupling using the coupled stochastic partial differential equation solver XMDS2[6] [286]. The mean-field Gross-Pitaevskii equations of motion are

$$i\hbar\partial_t\phi'_\uparrow = \left\{ \frac{\hbar^2}{2m}\left[(i\partial_x + k_R)^2 - \nabla_\perp^2\right] - \frac{\hbar\delta_0}{2} + V(\mathbf{r}) + g_{\uparrow\uparrow}|\phi'_\uparrow|^2 + g_{\uparrow\downarrow}|\phi'_\downarrow|^2 \right\}\phi'_\uparrow + \frac{\hbar\Omega}{2}\phi'_\downarrow$$

and

$$i\hbar\partial_t\phi'_\downarrow = \left\{ \frac{\hbar^2}{2m}\left[(i\partial_x - k_R)^2 - \nabla_\perp^2\right] + \frac{\hbar\delta_0}{2} + V(\mathbf{r}) + g_{\downarrow\downarrow}|\phi'_\downarrow|^2 + g_{\uparrow\downarrow}|\phi'_\uparrow|^2 \right\}\phi'_\downarrow + \frac{\hbar\Omega}{2}\phi'_\uparrow. \tag{5.20}$$

To isolate the kinetic effect we simulate ^{41}K with $a_{\uparrow\uparrow} = a_{\downarrow\downarrow} = a_{\uparrow\downarrow} = 61a_0$. For simplicity we assume a harmonic trap with cylindrical symmetry where $\omega_y = \omega_z \equiv \omega_r$ which allows us to employ the Bessel transform for the numerical evaluation of the radial derivative[7] [287].

For numerical simulations, we fix $\hbar\Omega/E_R = 5.5$ and $N = \int |\phi_\uparrow|^2 + |\phi_\downarrow|^2 \mathrm{d}^3\mathbf{r} = 65000$. We compute the ground state using imaginary time evolution with $\omega_x/(2\pi) =$

[6] In this thesis, I do not take advantage of the capacity to solve stochastic differential equations. For more information about XMDS2, see http://www.xmds.org/ and https://xmds.sourceforge.net/.

[7] Python 3 functions for the handling of XMDS2 data and the application of Bessel transformations can be found online at https://github.com/CSChisholm/xmds2-tools and https://pypi.org/project/xmds2tools/1.0.0/.

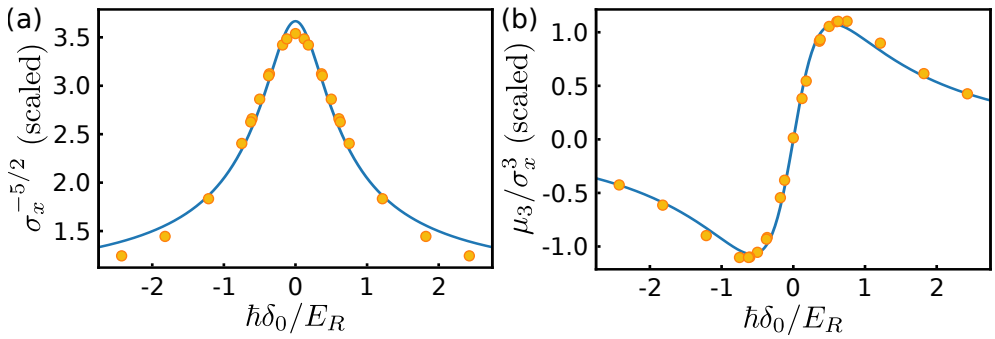

Figure 5.5: Numerical simulations revealing the momentum-dependent effective mass in a Raman coupled ^{41}K BEC with $\hbar\Omega/E_R = 5.5$. (a) The blue curve shows $M^*(k_{\min})$ and the orange points show the width of the numerically calculated density after 31 ms of expansion raised to the power of $-5/2$ scaled by an empirically determined factor of 19098 μm$^{5/2}$. (b) The blue curve shows $[k_R/M^*(k_x)]\,\partial_{k_x}M^*(k_x)|_{k_x=k_{\min}}$ and the orange points show the largest skewness obtained from the numerically calculated density profile scaled by an empirically determined factor of -5.284.

64 Hz and $\omega_r/(2\pi) = 130$ Hz for a given value of δ_0. To compute the expansion dynamics we quench to $\omega_x/(2\pi) = 5$ Hz and evolve the wavefunction in real time for 31 ms. In the simulations, the radial grid is defined on the interval $(0, 14)$ μm with 2^4 grid points and the x-axis is discretised on 2^{12} grid points with a grid spacing of 56.6 nm. From the total density, $n = |\phi_\uparrow|^2 + |\phi_\downarrow|^2$, we compute the central moments defined by $\mu_1 = \int x n \mathrm{d}^3\mathbf{r}/N$ and $\mu_j = \int (x-\mu_1)^j\, n \mathrm{d}^3\mathbf{r}/N$ for $j > 1$. The width of the BEC is related to the second central moment by $\sigma_x = \sqrt{\mu_2}$ and we quantify the asymmetry of the density profile using the skewness parameter, μ_3/σ_x^3.

For a single-component BEC we expect $\sigma_x^{-5/2} \propto m$ [212] and in Fig. 5.5(a) we see good agreement between the numerically determined values of $\sigma_x^{-5/2}$ after 31 ms of expansion (with an empirical scaling factor) and the curve $M^*(k_{\min})$. We would expect the agreement to improve for larger values of Ω and we have $M^*(k_x) = 1$ for all values of k_x and δ_0 for very large Ω. In the numerical simulations, we observe that the skewness does not necessarily grow monotonically and may reach a local (absolute) maximum depending on the interactions and traps. In Fig. 5.5(b) we take the skewness with the largest magnitude during the 31 ms expansion interval. We expect the skewness to be closely related to $-\partial_{k_x}M^*(k_x)|_{k_x=k_{\min}}$ and we find good agreement with the curve $[k_R/M^*(k_x)]\,\partial_{k_x}M^*(k_x)|_{k_x=k_{\min}}$ when the data points are scaled empirically.

In the low order quasimomentum expansion picture, the effective mass is not momentum-dependent and these kinetic effects are interpreted as stemming from the momentum-dependent density-independent vector potential which appears in Eq. 5.9 when $\hbar\tilde{\delta}_0/E_R \neq 0$ or, depending on the experimental parameters, additional terms which were truncated in the effective theory.

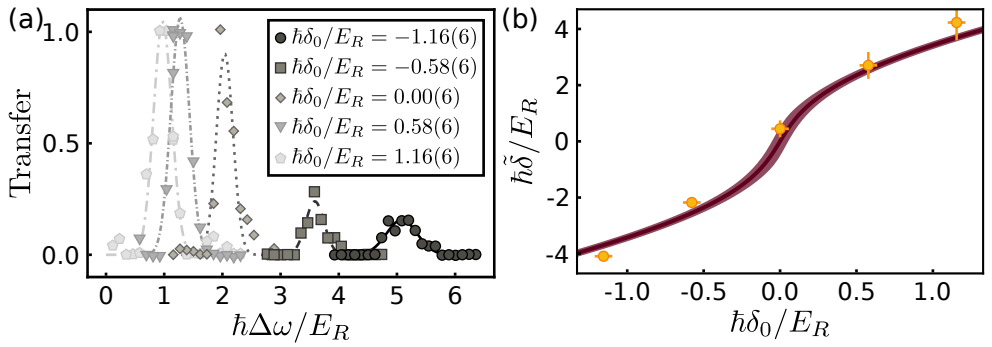

Figure 5.6: (a) RF spectroscopy of the $|-,\mathbf{k}\rangle$ to $|\text{aux},\uparrow,\mathbf{k}\rangle$ transition at various values of δ_0 with $\hbar\Omega/E_R = 4.5(3)$. (b) The generalised detuning inferred from the measured difference between the bare $|\uparrow,\mathbf{k}\rangle \leftrightarrow |\text{aux},\uparrow,\mathbf{k}\rangle$ transition frequency and the $|-,\mathbf{k}\rangle \leftrightarrow |\text{aux},\uparrow,\mathbf{k}\rangle$ transition frequency, $\Delta\omega$, (orange circles). The maroon line shows $\hbar\tilde{\delta}(k_{\text{min}})/E_R$ and the shaded area represents the uncertainty in the calculated value.

Experimental Realisation of the Chiral BF Electric Field

We prepare the Raman dressed ^{39}K BEC with $\omega_x/(2\pi) = 70(1)$ Hz, $\omega_y/(2\pi) = 147(2)$ Hz, $\omega_z/(2\pi) = 99(1)$ Hz, $\tau_1 = 30$ ms, $\tau_2 = 5$ ms, $\hbar\Omega_f/E_R = 4.5(3)$, $\hbar\delta_{0,i}/E_R = -0.46(6)$, and variable $\delta_{0,f}$. We set a bias magnetic field of $B = 397.01(1)$ G where we have $a_{\uparrow\uparrow} = 1.3a_0$, $a_{\downarrow\downarrow} = 252.7a_0$, and $a_{\uparrow\downarrow} = -6.3a_0$. At the end of the preparation sequence, the atom number is $N = 29(5) \times 10^3$. In this configuration, it is possible to observe skewness stemming from both kinetic effects and the chiral BF electric field. The kinetic effects are eliminated for $\hbar\tilde{\delta}(k_G)/E_R = 0$. For $\hbar\delta_0/E_R = 0$ we have $k_{\text{min}}/k_R = 0$ so for a BEC at rest we have $k_G/k_R = 0$. Similarly to the spin injection spectroscopy experiments discussed in Sec. 3.4.2, Wang *et al.* [247] have mapped the Raman dressed dispersion of a degenerate Fermi gas using spin ejection spectroscopy. To ensure that the BEC is at rest we perform spin ejection spectroscopy to the auxiliary state $|\text{aux},\uparrow,\mathbf{k}\rangle = |F = 1, m_F = -1\rangle$ to empirically determine the value of $\tilde{\delta}(k_G)$ after the preparation sequence.

As explained in Sec. 3.4.2, the difference between the bare $|\uparrow,\mathbf{k}\rangle \leftrightarrow |\text{aux},\uparrow,\mathbf{k}\rangle$ transition frequency and the $|-,\mathbf{k}\rangle \leftrightarrow |\text{aux},\uparrow,\mathbf{k}\rangle$ transition frequency is $\Delta\omega(k_x) = \left[\tilde{\Omega}(k_x) - \tilde{\delta}(k_x)\right]/2$. We spectroscopically measure $\Delta\omega(k_G)$ to infer the value of $\tilde{\delta}(k_G)$, as shown in Fig. 5.6. Table 5.1 shows the extracted value of $k_G - k_{\text{min}}$. From Eq. 5.15, we know that the density-dependent vector potential is expected to shift the effective value of k_{min}. We compute the groundstate corresponding to Eq. 5.20 and compute the expectation value of the quasimomentum, $\langle k_x\rangle$. The values of $\langle k_x\rangle - k_{\text{min}}$ are also shown in Tab. 5.1 for comparison to the experimental values. For the values of δ_0 shown in Tab. 5.1, the measured values of $k_G - k_{\text{min}}$ are compatible with zero and the values of $\langle k_x\rangle - k_{\text{min}}$ are smaller than the uncertainties in $k_G - k_{\text{min}}$. From these measurements, we conclude that the BEC is left as close to being at rest as is feasible after the preparation sequence.

To observe the expansion dynamics of the BEC, we quench the trap frequencies

Table 5.1: Group momentum experimentally extracted from spin ejection spectroscopy and numerically calculated from Eq. 5.20. Uncertainties in δ_0 and Ω are not included in the numerical values.

$\hbar\delta_0/E_R$	$k_G - k_{\min}$	$\langle k_x \rangle - k_{\min}$
$-0.58(6)$	$-0.9(9)$	-0.03
$0.00(6)$	$-0.1(2)$	-0.06
$0.58(6)$	$-0.04(16)$	-0.02

to $\omega_x/(2\pi) = 4(1)$ Hz, $\omega_y/(2\pi) = 129(2)$ Hz, and $\omega_z/(2/\pi) = 99(1)$ Hz and allow the BEC to evolve for a variable time, t. Figure 5.7(a) shows *in situ* images of the BEC in state $|-, \mathbf{k}\rangle$ with $\hbar\Omega/E_R = 4.5(3)$ and $\hbar\delta_0/E_R = -0.58(6)$ at various evolution times. We see that the BEC develops a sharp edge on the left and a long tail on the right, corresponding to $\mu_3/\sigma_x^3 > 0$. For comparison, Fig. 5.7(b) shows *in situ* images of a BEC in state $|\downarrow\rangle$ expanding without Raman coupling and without asymmetry.

For $\hbar\delta_0/E_R < 0$, a positive skewness is consistent with the kinetic effects already discussed. For the opposite detuning the kinetic effects are reversed and for $\hbar\delta_0/E_R = 0$ the kinetic effects are cancelled. For the experimentally chosen sign of λ, asymmetry arising from the chiral BF electric field would produce positive skewness independently of the sign of δ_0. This can be understood from a microscopic point of view by considering the momentum dependence of the spin polarisation and therefore interactions of the dressed state. Atoms moving to the right (left) have a larger projection onto state $|\downarrow'\rangle$ ($|\uparrow'\rangle$) so the expanding BEC can be seen as having a spin polarisation gradient. Furthermore, since we have chosen $g_{\downarrow\downarrow} > g_{\uparrow\uparrow}$, parts of the cloud with a locally stronger projection onto $|\downarrow'\rangle$ have effectively more repulsive interactions than other parts of the cloud and are therefore expected to expand faster.

Numerical determinations of μ_3 from experimental images are sensitive to noise because the $(x - \mu_1)^3$ term in the integrand gives a significant amount of weight to points far from the centre of mass of the BEC where the density is low and the relative noise is therefore large. We apply a low pass filter in Fourier space with an algorithmically determined cut off frequency for each image, taking care of low frequency components of the noise near the edges of the cloud in position space (see Appendix B). The experimental measurements of μ_3/σ_x^3 as a function of expansion time for $\hbar\delta_0/E_R = \pm 0.58(6)$ and $\hbar\delta_0/E_R = 0.00(6)$ are shown in Fig. 5.7(c). The solid coloured lines show the skewness corresponding to numerical solutions of Eq. 5.20 with $N = 29250$. To account for atom loss from the BEC due to inelastic photon scattering of the Raman beams, we add phenomenological loss terms, $i\Gamma/2$, corresponding to the measured $\Omega/\Gamma = 10(1) \times 10^3$ to Eq. 5.20. The dashed lines show the skewness corresponding to the numerical solutions with losses. For the numerical simulations, the x-axis is discretised on 2^{12} grid points with a grid spacing of 56.6 nm and the y-

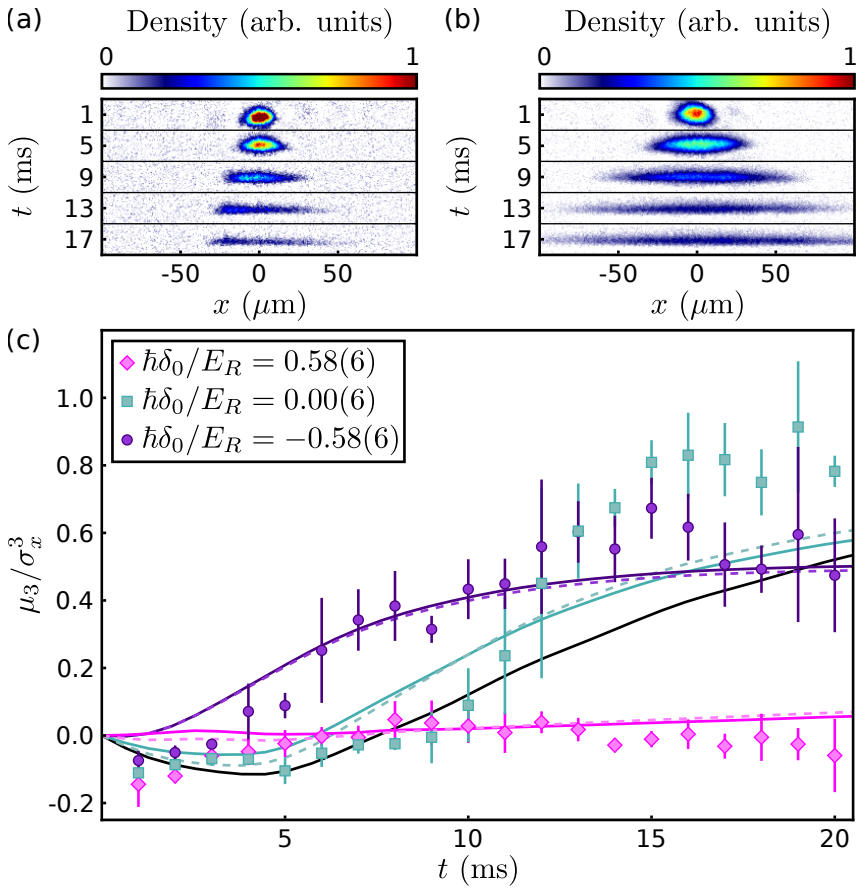

Figure 5.7: (a) *In situ* images during expansion for a Raman dressed BEC in state $|-\rangle$ with $\hbar\Omega/E_R = 4.5(3)$ and $\hbar\delta_0/E_R = -0.58(6)$. (b) Expansion of a BEC in state $|\downarrow\rangle$. (c) Skewness parameter, μ_3/σ_x^3. The solid coloured lines correspond to numerical solutions of Eq. 5.20 without losses and the dashed lines correspond to numerical solutions of Eq. 5.20 with $1/\Gamma = 40$ ms. The solid black line is the skewness obtained from the effective chiral BF model without losses. Values and error bars are the mean and standard deviation of four to five measurements.

and z-axes are discretised on 2^5 grid points each with a grid spacing of 0.675 μm.

We can see that the experimentally measured skewness is in good agreement with numerical calculations for $\hbar\delta_0/E_R \neq 0$ and that the skewness parameter is robust against atom loss. For $\hbar\delta_0/E_R = 0$, the skewness is sensitive to uncertainties in δ_0 as shown in Fig. 5.5(b) and also to residual mechanical momentum which is below our measurement resolution but still shows good qualitative agreement with the numerical simulations. The solid black line shows the skewness corresponding to the effective chiral BF Hamiltonian of Eq. 5.14. We observe good qualitative agreement between the full system Hamiltonian and the effective Hamiltonian with the discrepancy stemming from higher order terms in the quasimomentum expansion which are relevant at the low experimental Rabi frequency employed here. The corrections to the chiral BF

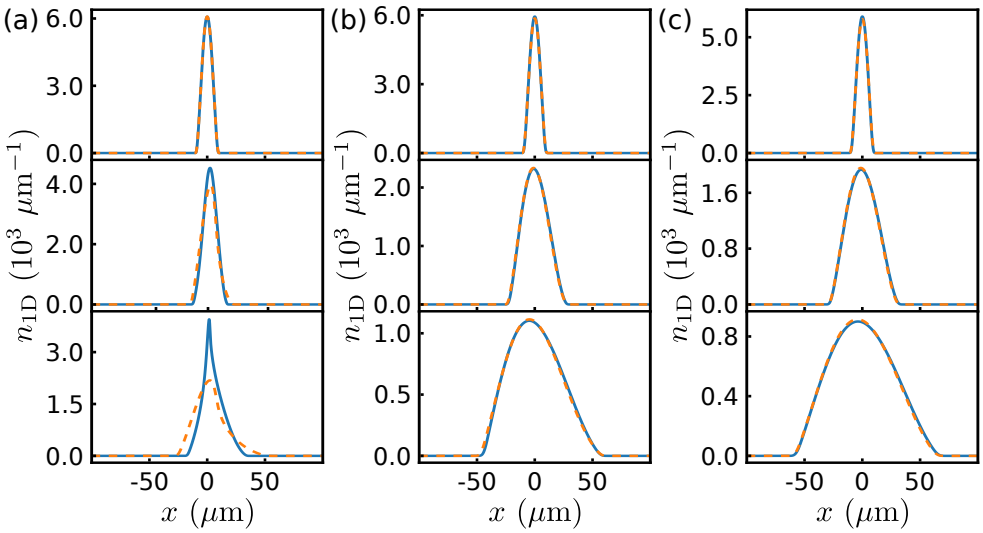

Figure 5.8: Density profiles corresponding to Eq. 5.21 (solid blue lines) and Eq. 5.20 (dashed orange lines) after an expansion time of $t = 0.0$ ms (top panel), $t = 7.5$ ms (middle panel), and $t = 15.0$ ms (bottom panel) with (a) $\hbar\Omega/E_R = 4.5$, (b) $\hbar\Omega/E_R = 7.0$, and (c) $\hbar\Omega/E_R = 10.0$. The dynamics of the full and effective systems are qualitatively similar for all values Ω. For $\hbar\Omega/E_R \geq 7.0$ the profiles are almost identical.

model decrease rapidly with increasing Ω, as will be discussed in Sec. 5.3.

5.3 Numerical Study of the Validity of Mapping to the Chiral BF Theory in the Mean-Field Regime

In order to characterise the quality of the mapping between the Raman dressed BEC and the chiral BF theory we use XMDS2 [286] to compare numerical solutions of Eq. 5.20 and the mean-field GPE corresponding to Eq. 5.14 with $k_0/k_R = 0$ and $\hbar\delta_0/E_R = 0$ which is

$$i\hbar\frac{\partial}{\partial t}\psi = \left[-\frac{\hbar^2}{2m}\left(\frac{1}{m^*}\frac{\partial^2}{\partial x^2} + \nabla_\perp^2\right) + V(\mathbf{r}) + g_1|\psi|^2 + \frac{\hbar\lambda}{imm^*}\psi^*\partial_x\psi\right]\psi. \tag{5.21}$$

We compute the groundstate with $\omega_x/(2\pi) = 70$ Hz, $\omega_y/(2\pi) = 147$ Hz, and $\omega_z/(2\pi) = 99$ Hz in imaginary time using the same grids as Fig. 5.7(c). The dynamics are computed with $\omega_x/(2\pi) = 5$ Hz, $\omega_y/(2\pi) = 129$ Hz, and $\omega_z/(2\pi) = 99$ Hz. Figure 5.8 shows the integrated density profiles, $n_{1D} = \int n(\mathbf{r})\,dydz$, corresponding to Eq. 5.20 and Eq. 5.21 for various expansion times and $N = 65000$ for (a) $\hbar\Omega/E_R = 4.5$, (b) $\hbar\Omega/E_R = 7.0$, and (c) $\hbar\Omega/E_R = 10.0$.

We see that for all of the values of Ω shown in Fig. 5.8, the effective chiral BF model qualitatively reproduces the dynamics of the full Raman coupled system, even when Ω is barely large enough to enter the single minimum regime. We can also

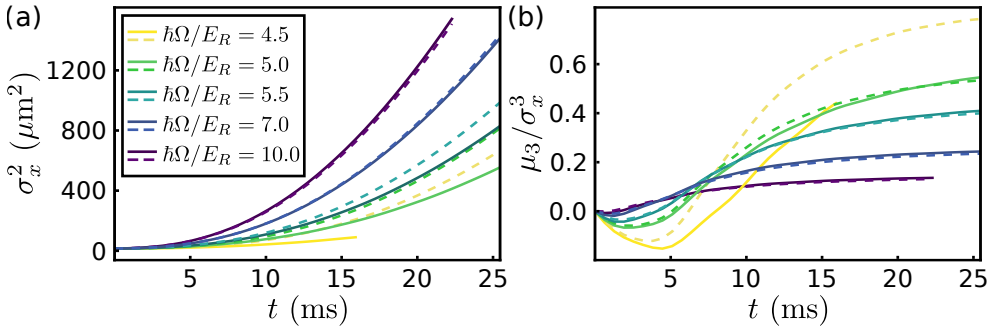

Figure 5.9: (a) Second central moment and (b) skewness corresponding to density profiles obtained by numerically solving Eq. 5.20 for the full Raman coupled system (dashed lines) and Eq. 5.21 for the effective chiral BF system (solid lines) for various values of Ω. We can see that the agreement between the effective model and the full system improves rapidly with increasing Ω. At $\hbar\Omega/E_R = 5.0$ the values of μ_3/σ_x^3 corresponding to the two density profiles are in excellent agreement. The second central moment is more sensitive to terms not included in Eq. 5.14 with agreement between the two models achieved for $\hbar\Omega/E_R \geq 7.0$.

see that the predictions of the effective chiral BF theory are quantitatively consistent with the full Raman coupled system for $\hbar\Omega/E_R = 7.0$, significantly lower than the $\hbar\Omega/E_R \gtrsim 100$ required for the adiabatic approximation in position space [131].

In Fig. 5.9 we compare the values of (a) σ_x^2 and (b) μ_3/σ_x^3 computed for the effective chiral BF model and the full Raman coupled system as functions of expansion time for various values of Ω. Note that σ_x^2 increases with increasing Ω, reflecting the decreasing effective mass while μ_3/σ_x^3 decreases with increasing Ω because $\lambda \propto \Omega^{-1}$. As in Fig. 5.8, for $\hbar\Omega/E_R \geq 7.0$ the computed values of the two models are practically indistinguishable. For $\hbar\Omega/E_R < 7.0$ we see that the skewness initially goes negative before increasing in time as we expect. This is because the interaction parameters, $g_{\downarrow\downarrow} \gg g_{\uparrow\uparrow}$, energetically favour a positive spin polarisation. In this context, the density-dependent vector potential in Eq. 5.15 can be seen as a mean-field many body detuning which is positive, as in the interpretation of Edmonds *et al.* [131]. As we have seen in Fig. 5.5(b), a positive detuning corresponds to kinetic contributions to the asymmetry which result in $\mu_3/\sigma_x^3 < 0$ because, in the momentum-dependent effective mass interpretation atoms moving to the right are effectively more massive than atoms moving to the left and therefore expand more slowly [236].

Comparing the numerically obtained values of the skewness for both the effective chiral BF model and the full Raman coupled system with $\hbar\Omega/E_R = 4.5$ in Fig. 5.7 where the atom number in the numerical simulations was fixed to $N = 29250$ and Fig. 5.9(b), we can see that the skewness has a slight dependence on the atom number. This is to be expected since the BF vector potential is proportional to the density which depends on the atom number ($n \propto N^{2/5}$ in the Thomas-Fermi regime). Yet, in Fig. 5.7, we have seen that the skewness is robust against atom losses. We investigate these facts further in Fig. 5.10.

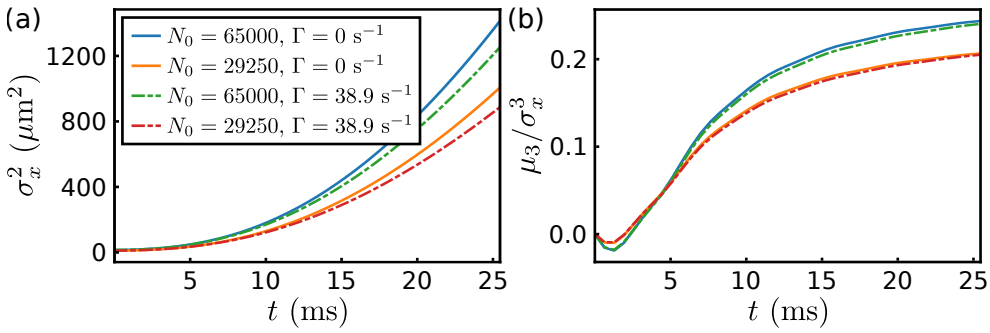

Figure 5.10: Effect of atomic losses on the expansion dynamics of the effective chiral BF model. (a) Second central moment, σ_x^2, and (b) skewness, μ_3/σ_x^3, corresponding to Eq. 5.21 with $\hbar\Omega/E_R = 7.0$ for initial atom number $N_0 = 29250$ (red and orange lines) and $N_0 = 65000$ (blue and green lines) without losses (solid lines) and with loss rate $\Gamma = 38.9$ s^{-1} (dashed-dotted lines).

We fix $\hbar\Omega/E_R = 7.0$ and the initial atom number to $N_0 = 29250$ or $N_0 = 65000$ and compute the expansion dynamics corresponding to Eq. 5.21 with and without losses. For the simulations with losses, we use the experimental value $\Omega/\Gamma = 10^4$ which corresponds to $\Gamma = 38.9$ s^{-1} for our chosen value of Ω. Figure 5.10(a) shows the computed values of σ_x^2. We see that the width of the BEC after a given expansion time is affected by both the initial atom number and atom losses. The skewness is shown in Fig. 5.10(b) and we see that while there is a slight dependence on the initial atom number, the value of μ_3/σ_x^3 over time is not strongly affected by losses. This is even more remarkable considering that the final atom number with $N_0 = 65000$ and $\Gamma = 38.9$ s^{-1} is less than 29250. We can therefore conclude that the skewness parameter is a robust experimental observable even in the presence of significant atom losses.

We conclude our numerical study of the validity of the mapping of a Raman coupled BEC to the chiral BF theory by numerically estimating the energy errors corresponding to terms in the quasimomentum expansion which have not been included in Eq. 5.14. We estimate the energy errors perturbatively by computing the next nonzero terms in the quasimomentum expansion. This corresponds to expansion to fourth order in the kinetic energy and second order in the interaction energy. We compare the expectation values of the next order terms to the terms kept in Eq. 5.14 but we neglect the transverse kinetic terms and the trapping potential to avoid biasing the energy error estimate to lower values. Given a wavefunction, ψ, numerically computed using Eq. 5.21, the estimated energy error is

$$\frac{\Delta\mathcal{E}}{\mathcal{E}} = \left| \frac{\Delta\mathcal{E}_{\text{kin}} + \Delta\mathcal{E}_{\text{int}}}{\int \psi^* \left[-\frac{\hbar^2}{2mm^*}\partial_x^2 + \frac{g_1}{2}|\psi|^2 + \frac{\hbar\lambda}{4imm^*}\left(\psi^*\partial_x\psi - \psi\partial_x\psi^*\right)\right]\psi \mathrm{d}^3\mathbf{r}} \right| \tag{5.22}$$

where

$$\Delta\mathcal{E}_{\text{kin}} = \frac{16E_R^4}{\hbar^3\Omega^3k_R^4}\int \psi^*\partial_x^4\psi \mathrm{d}^3\mathbf{r} \tag{5.23}$$

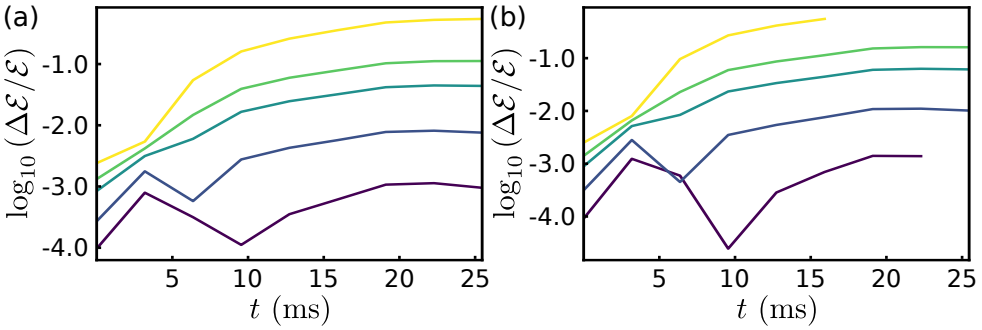

Figure 5.11: Perturbatively calculated energy errors corresponding to higher order terms in the quasimomentum expansion used to derive Eq. 5.14 for (a) $N = 29250$ and (b) $N = 65000$. The energy errors grow more rapidly for larger atom number because increased mean-field repulsion results in a larger spread of the BEC in momentum space after a given expansion time. For $\hbar\Omega/E_R = 7.0$, we have $\Delta\mathcal{E}/\mathcal{E} < 1$ % for all computed times. The colours of the lines correspond to the same values of Ω as in Fig. 5.9.

and

$$\Delta\mathcal{E}_{\text{int}} = \frac{2E_R^2}{\hbar^2\Omega^2k_R^2}\int \mathrm{d}^3\mathbf{r}\left[\psi^* g_1\left(\psi^*\partial_x^2\psi + \psi\partial_x^2\psi^* - 2\partial_x\psi^*\partial_x\psi\right)\psi - g_2\left(\psi^*\partial_x\psi + \psi\partial_x\psi^*\right)^2\right] \quad (5.24)$$

with $g_2 = \left(g_{\uparrow\uparrow} + g_{\downarrow\downarrow} - 2g_{\uparrow\downarrow}\right)/4$.

The computed values of $\Delta\mathcal{E}/\mathcal{E}$ for various values of Ω are shown in Fig. 5.11 for (a) $N = 29250$ and (b) $N = 65000$. For all values of Ω, the energy error grows faster for larger atom number. This is because larger atom number results in greater mean-field repulsion which causes the BEC to expand more rapidly in momentum space during expansion. The energy errors in the effective chiral BF model are expected to be larger when the BEC has a greater spread in momentum space. For most of the simulations shown, the energy errors stop increasing after approximately 20 ms of expansion, when the BEC enters the ballistic expansion regime [211, 212].

The exception is the data corresponding to $\hbar\Omega/E_R = 4.5$ with $N = 65000$. In this case the energy error approaches unity after approximately 15 ms of expansion. For longer expansion times, the numerics are effectively halted because the density profile acquires unphysically sharp features as seen in Fig. 5.8(a). For the parameters corresponding to our experimental measurements in Fig. 5.7(c) (with $\hbar\delta_0/E_R = 0$) the energy errors in the effective chiral BF model are below 10 % for the first few milliseconds of expansion. For comparison, in the position space adiabatic approximation [131], $m^* \approx 1$, kinetic energy errors are on the order of 100 % at $t = 0$ ms for the values of Ω used here. We conclude that our experimental realisation provides a good approximation of the chiral BF model. As indicated already by Fig. 5.8 and Fig. 5.9, a Raman coupled BEC with $\hbar\Omega/E_R \geq 7.0$ provides a near perfect mapping to the chiral BF theory, with energy errors remaining below 1 % for all computed times.

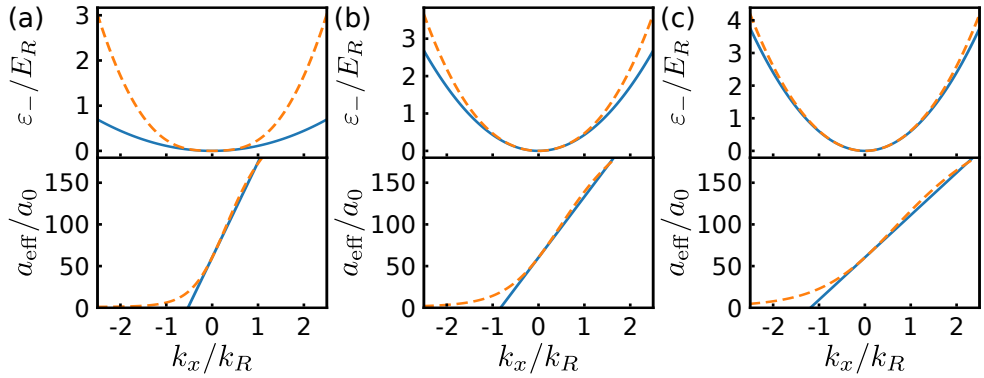

Figure 5.12: Exact value (dashed orange line) and third order expansion (solid blue line) of $\varepsilon_-(k_x)$ (top panel) and exact value (dashed orange line) and first order expansion (solid blue line) of $a_{\rm eff}(k_x)$ (bottom panel) for $k_0/k_R = 0$ and $\hbar\delta_0/E_R = 0$ with (a) $\hbar\Omega/E_R = 4.5$, (b) $\hbar\Omega/E_R = 7.0$, and (c) $\hbar\Omega/E_R = 10.0$. In the top panels, constant energy offsets have been removed.

These results can also be visualised simply without appealing to time consuming numerical simulations. In Fig. 5.12 the lower dressed dispersion, $\varepsilon_-(k_x)$, and the effective scattering length, $a_{\rm eff}(k_x) = mg_{\rm eff}(k_x)/(4\pi\hbar^2)$ are plotted with their expansions around $k_0/k_R = 0$ to third and first order respectively with $\hbar\delta_0/E_R = 0$ for various values of Ω. As can be expected, the agreement between the exact and approximate expressions improves for increasing Ω. In Fig. 5.11, we can see that while the BEC remains confined in a trap, the energy errors are below 1 % even for $\hbar\Omega/E_R = 4.5$. This is because a BEC naturally has a narrow momentum distribution and the energy error can be assessed to be small by visual assessment of Fig. 5.12. As previously mentioned, the mechanism for the increase of the energy error during the expansion dynamics is the conversion of mean-field energy into kinetic energy corresponding to an increasing spread in momentum space. By examining the dispersion, we can see that for smaller values of Ω, the same gain in kinetic energy results in a larger increase in momentum spread and at the same time, the third order expansion is valid for a narrower range of momenta.

We have seen the effect of the chiral BF electric field on a neutral BEC through the distortion of the density profile during expansion which is characterised by the skewness parameter, μ_3/σ_x^3. As we saw in Ch. 4, the electric field is completely characterised by the density and we can therefore directly compute the expectation value $\langle\hat{E}\rangle = \lambda\langle\partial_t\hat{n}\rangle$. Or, in the mean-field numerical simulations, $E = \lambda\partial_t n$. The electric field corresponding to $\hbar\Omega/E_R = 7.0$ and $N = 65000$ is shown in Fig. 5.13. We see that the direction of the electric field is reversed in the centre of the cloud where the density is decreasing compared to the edges of the cloud where the density is increasing. We can also see that as the inhomogeneous electric field skews the density profile, the electric field itself becomes skewed which is a direct reflection of the back action between the electric field and the matter density.

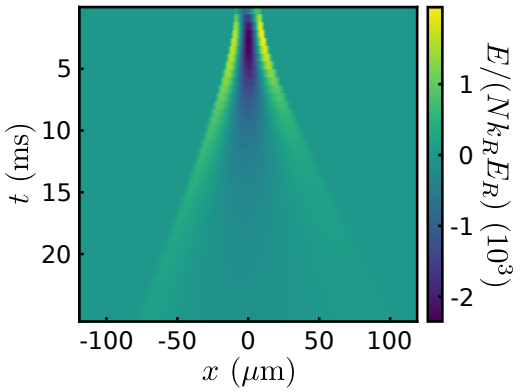

Figure 5.13: The chiral BF electric field generated by the time variation of the atomic density during expansion with $\hbar\Omega/E_R = 7.0$ and $N = 65000$.

5.4 Summary

In this chapter I have shown how the Raman coupling induced momentum dependence of interactions in a BEC can be used to derive a rigorous mapping between the BEC and the chiral BF Hamiltonian in the quantum regime. The mapping extends to values of Raman coupling strength far below the adiabatic limit in position space and which are experimentally accessible. I have reported the experimental realisation of chiral solitons and the observation of a density-dependent synthetic electric force. Using numerical simulations, I have shown that the skewness of a Raman-coupled BEC after expansion in an optical waveguide is an experimental observable which is resilient against atom losses which are inherent in Raman coupling experiments. I have used numerical simulations to quantify the quality of the mapping between the Raman coupled BEC and the chiral BF theory in the mean-field limit in experimentally accessible configurations.

With this chapter, I conclude the work on the quantum simulation of the chiral BF theory with Raman coupled BECs. In the next chapter I will show how moving into the double minimum regime enables the formation of a supersolid state in the so-called stripe phase. Using a similar momentum space approach as with the chiral BF theory, I will derive approximate expressions which describe both groundstate properties and collective oscillations of the supersolid.

Chapter 6

The Supersolid Stripe Phase

In the previous chapter, I have focused on the regime where the dispersion relation of a Raman-coupled BEC has a single minimum. In this chapter, I will focus on the regime where the Raman dressed dispersion has two minima at different quasimomenta and it is possible to form a supersolid state which combines features of solidity and superfluidity known as the stripe phase [67, 111, 112, 157, 168]. Taking inspiration from previous works [67, 166–168, 288], I will follow a similar approach as for the chiral BF theory to derive a spin mixture model. I will make analytic predictions of both static and dynamic properties of the supersolid stripe phase which I will compare to numerical simulations. The work presented in this chapter is derived from theoretical collaborations with Dr. Josep Cabedo, Dr. Ramón Ramos, Prof. Dr. Leticia Tarruell, and Dr. Alessio Celi.

6.1 Supersolids

In 1969 and 1970, three independent proposals were made on the existence of supersolidity, a state of matter featuring both the spontaneous translational symmetry breaking characteristic of solids and the frictionless flow of superfluids. Two of these, by Andreev and Lifshitz [102] and Chester [103], considered superfluid flow arising from tunnelling of vacancies frozen into solid ^{4}He at zero temperature. The other, by Leggett [104], considered superfluid flow arising from cooperative tunnelling of pairs of ^{4}He atoms without vacancies frozen into the solid. Shortly after these proposals, Guyer pointed out that nuclear magnetic resonance data available for solid ^{3}He and solid ^{3}He-^{4}He mixtures provided strong evidence against the existence of vacancies at zero temperature [142] and estimated the density of vacancies in solid ^{4}He to be less than 10^{-4} times the total density. Furthermore, Guyer concluded that low temperature experiments of the time would not be capable of observing superfluidity in ^{4}He based on Leggett's proposal [142].

In spite of pessimistic estimates of the detectability of supersolidty in ^{4}He, experiments pressed on with ^{4}He since it is the "most quantum" solid in nature [117]. In 1973, Suzuki investigated the plastic deformation of solid ^{4}He by measuring force

displacement curves corresponding to moving a steel ball through the helium sample at constant velocity [289]. No evidence of superfluidity was found in the experiment of Suzuki but no measurements were made below 0.5 K which is much higher than the < 0.1 mK required for cooperative tunnelling, as estimated by Guyer [142].

Calculations by Saslow [143, 144] obtained much higher estimates of the superfluid fraction and critical temperature for supersolidity than the estimates of Guyer [142] (on the order of 0.1 and 1 K, respectively). Bouyed by these updated estimates, Greywall [290] conducted an experiment where a small pressure difference was made between two samples of solid ^{4}He which were connected by a thin capillary. However, no evidence of superfluid flow through the capillary was detected down to 30 mK.

In 1997 Ho *et al.* [291] observed an anomaly in the acoustic attenuation of solid ^{4}He around 200 mK but Blackburn *et al.* [292] did not find evidence of anomalies in neutron diffraction experiments. In 2004, Kim and Chan [145, 146] reported the anomalous decrease of the moment of inertia of a torsional oscillator filled with ^{4}He, which was thought to be the first experimental evidence of supersolidity in ^{4}He. A similar experiment by Clark *et al.* [293] observed an increase in the torsional oscillator period of an apparatus filled with solid para-hydrogen but this effect was attributed to the motion of residual ortho-hydrogen molecules. In 2006 Sasaki *et al.* [294] reported superfluidity of grain boundaries in solid ^{4}He.

Due to a number of experimental results, many authors declared supersolidity to have been experimentally confirmed in ^{4}He by 2010 [295]. The declarations of experimental confirmation were made in spite of ongoing theoretical debates. Specifically, path integral Monte Carlo simulations [296, 297] contradicted the interpretation given to the experimental results of Kim and Chan [145, 146] and others. New experiments in 2012 showed that the reduction in the rotational inertia of a torsional oscillator filled with solid ^{4}He was actually due to elastic behaviour of solid ^{4}He [147]. To date, there is no conclusive evidence of the existence of supersolidity in ^{4}He [148, 298, 299].

While there is still current interest in the search for supersolidity in ^{4}He [148, 300, 301], atomic BECs started to garner theoretical interest in the early 2000s. Various proposals for systems which might display supersolid behaviour were made, including laser induced electrostriction [302], dipolar gases [303–305], and atoms weakly coupled to Rydberg states [306]. Supersolidity has been observed in BECs coupled to optical cavities where the cavities induce long range and spatially periodic interactions between atoms [105, 106] and in dipolar BECs where the long range dipolar interactions between atoms give rise to a roton minimum which goes soft with properly tuned contact interactions and trap geometries [107–109].

Supersolidity in Raman coupled BECs is also an active area of research. In 2004 Higbie and Stamper-Kurn introduced an effective model of a mixture of nonorthogonal dressed states corresponding to the two minima of a Raman coupled BEC and predicted spatial density modulations arising from interference between these two states [166]. In 2011, Lin *et al.* [67] observed a miscible to immiscible phase transition in the double minimum regime of a BEC with Raman coupling corresponding to the dependence of the effective interactions of the nonorthogonal dressed states on the Raman Rabi frequency, Ω.

Ho and Zhang [167] revisited the mixture model of Higbie and Stamper-Kurn [166] in light of the experiments by Lin *et al.* [67] and discussed spontaneous breaking of translational symmetry for effective interactions corresponding to miscible dressed states and two distinct spin polarised phases for immiscible interactions. Li *et al.* [168] developed a variational ansatz which provides an intuitive understanding of the phase diagram. The spontaneous formation of density modulations corresponds to a supersolid state called the stripe phase. The density modulations which characterise the supersolid stripe phase have been detected indirectly by Bragg diffraction of light [111, 112]. Following a theoretical study of the stripe phase in this chapter, I will present experimental results where we have used matterwave optics techniques to magnify and image the density modulations in Ch. 7.

6.1.1 The Stripe Phase

As described in the previous section, in the regime where the lower energy Raman dressed state has two minima in the dispersion, it is possible to produce a BEC at rest in the laboratory frame with group quasimomentum corresponding to either of the two minima. Two BECs corresponding to each of the two different minima in the dispersion have different projections onto the bare spin basis but are not orthogonal to each other [67, 166, 167]. If a BEC is produced with group quasimomentum corresponding to each of the two minima simultaneously as shown in Fig. 6.1(a) and the two dressed BECs are miscible, the dressed BECs overlap in position space. Due to matterwave interference between the nonorthogonal dressed BECs, periodic density modulations with fringe spacing determined by the difference in group quasimomentum of the two BECs form spontaneously [67, 111, 166, 167]. This concept is illustrated in Fig. 6.1(b) for the case of homogeneous BECs.

The periodic density modulation arising from the matterwave interference between the two nonorthogonal dressed states gives the total position space density profile a "striped" pattern, which is the origin of the name "stripe phase" and constitutes the spontaneous breaking of a continuous $U(1)$ symmetry. Namely, the spatial translational invariance along the Raman coupling axis. Coupled with the already broken internal $U(1)$ gauge symmetry of a BEC, we see that the stripe phase corresponds to two spontaneously broken continuous symmetries which manifest as periodic density modulations and superfluidity and thus constitutes a supersolid [111, 163]. As will be shown in Sec. 6.5, the stripe phase supports collective crystal modes which are illustrated in Fig. 6.1(c). In particular, a zero energy Goldstone mode corresponds to translations of the density modulations and oscillations of the fringe spacing can be excited [307, 308] while a massive Higgs mode corresponds to oscillations of the fringe contrast [106, 161, 164].

In the early experiments demonstrating a miscible to immiscible phase transition [67], the critical Raman Rabi frequency was very low. As we will see in Sec. 6.2, this is due to the inherent interactions of the chosen atomic species, ^{87}Rb, and results in a small contrast in the density modulation. The density modulations of the stripe phase have been detected experimentally through indirect Bragg scattering measure-

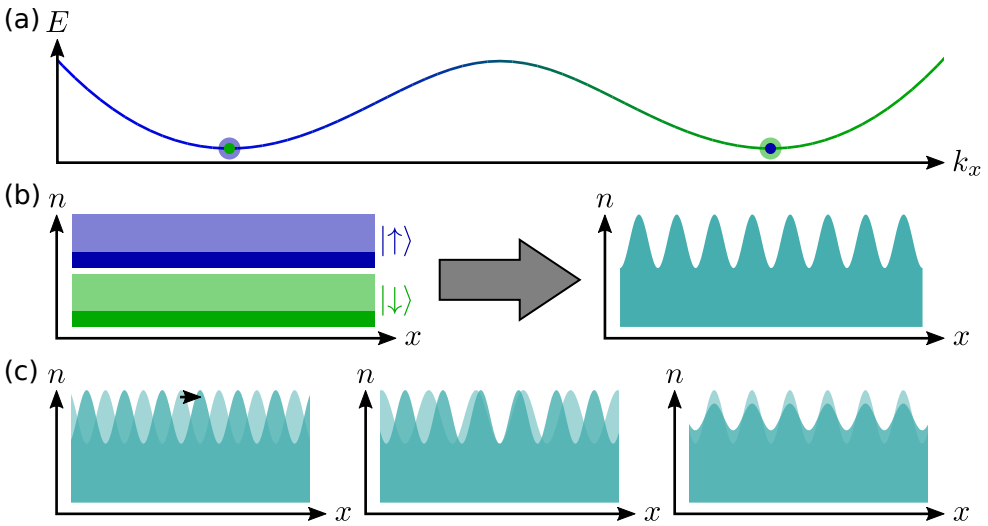

Figure 6.1: (a) The dispersion of the lower energy Raman dressed state can feature two energy minima where a BEC can be formed. (b) In position space, the two dressed BECs are stationary in the laboratory frame and each have nonzero overlap into each of the two bare spin states. The two dressed BECs are not orthogonal to one another and can manifest matterwave interference if they are miscible. The interference between the two dressed BECs results in a spontaneous breaking of translational invariance which is seen as a periodic modulation of the total density. (c) Collective crystal modes of the stripe phase. A Goldstone mode corresponds to translations of the stripes, oscillations of the fringe spacing can be excited, and a Higgs mode corresponds to oscillations of the fringe contrast.

ments [111, 112]. Li *et al.* [111] used ^{23}Na in different bands of an optical superlattice to tune the interactions into a more favourable configuration and Putra *et al.* [112] quenched the Rabi frequency to enhance the fringe contrast in ^{87}Rb in an out of equilibrium configuration.

6.2 Variational Approach to the Stripe Phase

Based on the intuition of two BECs with distinct quasimomenta interfering in position space, a variational ansatz based on a spinor wave function has been developed to study the groundstate properties of the stripe phase [168, 288]. In this section, I will explain some of the work done with this variational ansatz to understand the stripe phase. We assume a mean-field wavefunction of the form $\Psi = (\psi_\uparrow, \psi_\downarrow)^T$ corresponding to a uniform density, $\bar{n} = |\psi_\uparrow|^2 + |\psi_\downarrow|^2$, in the absence of stripes. We take

$$\Psi = \bar{n}\left[C_1\begin{pmatrix} -\sin\theta_1 \\ \cos\theta_1 \end{pmatrix}\exp(ik_1x) + C_2\begin{pmatrix} -\cos\theta_2 \\ \sin\theta_2 \end{pmatrix}\exp(-ik_2x)\right] \tag{6.1}$$

which we use to minimise the energy functional,

$$E[\Psi] = \int \Psi^\dagger \begin{bmatrix} -\frac{\hbar^2}{2m}\left(-i\partial_x + k_R\right)^2 - \frac{\hbar\delta_0}{2} & \frac{\hbar\Omega}{2} \\ \frac{\hbar\Omega}{2} & -\frac{\hbar}{2m}\left(-i\partial_x - k_R\right)^2 + \frac{\hbar\delta_0}{2} \end{bmatrix} \Psi \mathrm{d}^3\mathbf{r} + \int \frac{g_{\uparrow\uparrow}}{2}|\psi_\uparrow|^4 + \frac{g_{\downarrow\downarrow}}{2}|\psi_\downarrow|^4 + g_{\uparrow\downarrow}|\psi_\uparrow|^2|\psi_\downarrow|^2 \mathrm{d}^3\mathbf{r}, \quad (6.2)$$

with the six variational parameters C_1, θ_1, k_1, C_2, θ_2, and k_2 with $k_1, k_2 \geq 0$ and $C_1, C_2 \in \mathbb{C}$.

To simplify the variational procedure, we make the assumption that the spin polarisations are given by $\theta_\sigma = \arccos(k_\sigma)/2$ for $\sigma = 1, 2$. This assumption holds when k_1 and $-k_2$ do not differ substantially from the minima of the dispersion with $\hbar\delta_0/E_R = 0$. We have the normalisation condition $\int \Psi^\dagger\Psi \mathrm{d}^3\mathbf{r} = \int \bar{n}\mathrm{d}^3\mathbf{r} = N$ where N is the number of atoms. This provides a constraint $|C_1|^2 + |C_2|^2 = 1$. We write $C_\sigma = |C_\sigma|\exp(i\theta_{s,\sigma})$ and define $\theta_s = \theta_{s,1} - \theta_{s,2}$ and $S = |C_1|^2 - |C_2|^2 \Rightarrow -1 \leq S \leq 1$. We can write down the total density as

$$n = |\psi_\uparrow|^2 + |\psi_\downarrow|^2 = \bar{n} + (\bar{n}/2)\sqrt{1-S^2}\left[\sqrt{(1+k_1/k_R)(1-k_2/k_R)} + \sqrt{(1-k_1/k_R)(1+k_2/k_R)}\right]\cos\left[(k_1+k_2)x + \theta_s\right] \quad (6.3)$$

This density features modulations with period $\Delta s = 2\pi/(k_1+k_2)$ and contrast $\mathcal{C} = \sqrt{1-S^2}\left[\sqrt{(1+k_1/k_R)(1-k_2/k_R)} + \sqrt{(1-k_1/k_R)(1+k_2/k_R)}\right]/2$. The position of the fringes is determined solely by the relative phase between the two dressed BECs, θ_s [309]. Similarly, we can compute the spin density, s, and the spin polarisation, P, corresponding to this ansatz as

$$s = |\psi_\uparrow|^2 - |\psi_\downarrow|^2 = \frac{1-S}{2}\frac{k_2}{k_R} - \frac{1+S}{2}\frac{k_1}{k_R} + \sqrt{1-S^2}\sin(\theta_2-\theta_1)\cos\left[(k1+k2)+\theta_s\right] \quad (6.4)$$

and

$$P = \int s\mathrm{d}^3\mathbf{r}/N = \frac{1-S}{2}\frac{k_2}{k_R} - \frac{1+S}{2}\frac{k_1}{k_R}. \quad (6.5)$$

Note that for $k_1 \neq k_2$ there is also modulation in the spin density with contrast

$$\mathcal{C}_{\text{spin}} = \frac{k_R}{k_1(1+S) - k_2(1-S)}\mathcal{C} \quad (6.6)$$

which is always smaller than $\mathcal{C}$. Additionally, we may compute the transverse spin polarisation given by

$$P_{\text{transverse}} = 2\int \mathrm{Re}\left(\psi_\uparrow^*\psi_\downarrow\right)\mathrm{d}^3\mathbf{r}/N = -\left(\frac{1+S}{2k_R}\sqrt{k_R^2 - k_1^2} + \frac{1-S}{2k_R}\sqrt{k_R^2-k_2^2}\right). \quad (6.7)$$

Inserting the additional constraints into the energy functional yields

$$\begin{aligned}\frac{E[\Psi]}{NE_R} = 1 - \frac{1+S}{2}\frac{k_1^2}{k_2^2} + \frac{1-S}{2}\frac{k_2^2}{k_R^2} + \frac{\hbar\delta_0}{2E_R}\left(\frac{1+S}{2}\frac{k_1}{k_R} - \frac{1-S}{2}\frac{k_2}{k_R}\right) \\ - \frac{\hbar\Omega}{2E_R}\left(\frac{1+S}{2}\sqrt{1-\frac{k_1^2}{k_R^2}} + \frac{1-S}{2}\sqrt{1-\frac{k_2^2}{k_R^2}}\right) \\ + \frac{G_1}{E_R}\left[1 + \frac{1-S^2}{4}\left(1 - \frac{k_1k_2}{k_R^2} + \sqrt{1-\frac{k_1^2}{k_R^2}}\sqrt{1-\frac{k_2^2}{k_R^2}}\right)\right] \\ + \frac{G_2}{E_R}\left[\left(\frac{1+S}{2}\frac{k_1}{k_R} - \frac{1-S}{2}\frac{k_2}{k_R}\right)^2 + \frac{1-S^2}{4}\left(1 - \frac{k_1k_2}{k_R^2} - \sqrt{1-\frac{k_1^2}{k_R^2}}\sqrt{1-\frac{k_2^2}{k_R^2}}\right)\right] \\ + \frac{G_3}{E_R}\left(\frac{1+S}{2}\frac{k_1}{k_R} - \frac{1-S}{2}\frac{k_2}{k_R} + \frac{1-S^2}{4}\frac{k_1-k_2}{k_R}\right) \quad (6.8)\end{aligned}$$

where we have defined $G_1 = (g_{\uparrow\uparrow} + g_{\downarrow\downarrow} + 2g_{\uparrow\downarrow})\,\bar{n}/8$, $G_2 = (g_{\uparrow\uparrow} + g_{\downarrow\downarrow} - 2g_{\uparrow\downarrow})\,\bar{n}/8$, and $G_3 = (g_{\downarrow\downarrow} - g_{\uparrow\uparrow})\,\bar{n}/4$. Note that θ_s does not appear in Eq. 6.8 so there is no energy cost to sliding the stripes and stripe translation corresponds to a zero energy Goldstone mode [163]. We are left with just three variational parameters, k_1, k_2, and S.

In the case that $\hbar\delta_0/E_R = 0$ and $g_{\uparrow\uparrow} = g_{\downarrow\downarrow} \equiv g$, we can assume $k_1 = k_2$ and the energy functional can be minimised analytically under the constraint $0 \leq k_1/k_R \leq 1$ [168]. The system supports three distinct phases which are the stripe phase, the magnetised plane wave phase and the single minimum phase. The plane wave phase in fact corresponds to two degenerate states where the BEC occupies one of the minima of the dispersion or the other through a process of spontaneous symmetry breaking. For $\bar{n} < (g + g_{\uparrow\downarrow})\,E_R/\left[(g - g_{\uparrow\downarrow})\,g\right]$, the stripe phase is the groundstate of the system if $\hbar\Omega < 4\left[2G_2\left(E_R + G_1/2\right)\left(E_R - G_2\right)/\left(G_1 + 2G_2\right)\right]^{1/2} \equiv \hbar\Omega_c$ and the single minimum phase is the groundstate if $\hbar\Omega > 4\left(E_R - G_2\right)$ with the plane wave phase in between. Note that if $g_{\uparrow\downarrow} \neq g$ then $G_2/E_R \neq 0$ so the boundary to the single minimum phase is shifted from the value of $\hbar\Omega/E_R = 4$ found at the single particle level.

In the stripe phase we have $S = 0$ and $k_1/k_R = \sqrt{1 - \hbar^2\Omega^2/\left(4E_R + 2G_1\right)^2}$ which recovers the single particle value $k_{\min}/k_R = \sqrt{1 - \hbar^2\Omega^2/\left(4E_R\right)^2}$ in the limit $\bar{n} \to 0$. Note that the spacing between fringes tends to increase as Ω is increased, in contrast to density modulations present in a BEC in a shallow optical lattice which have spacing independent of the lattice intensity. According to the variational ansatz, the contrast of the stripes is given by $\mathcal{C} = \hbar\Omega/\left(4E_R + 2G_1\right)$.

Returning to the more general case where the values of δ_0, $g_{\uparrow\uparrow}$, and $g_{\downarrow\downarrow}$ can take arbitrary values, we can see that, as in the single minimum regime the term proportional to G_3 corresponds to a mean-field detuning which is nearly cancelled when $\hbar\delta_0 = -2G_3 = (g_{\uparrow\uparrow} - g_{\downarrow\downarrow})\,\bar{n}/2$. In the limit $\hbar\Omega/E_R \to 0$ we have $k_1/k_R = k_2/k_R = 1$ for any value of δ_0 and the energy functional becomes [288]

$$\lim_{\hbar\Omega/E_R \to 0} \frac{E[\Psi]}{N} = G_1 + \left(\frac{\hbar\delta_0}{2} + G_3\right)S + G_2S^2. \quad (6.9)$$

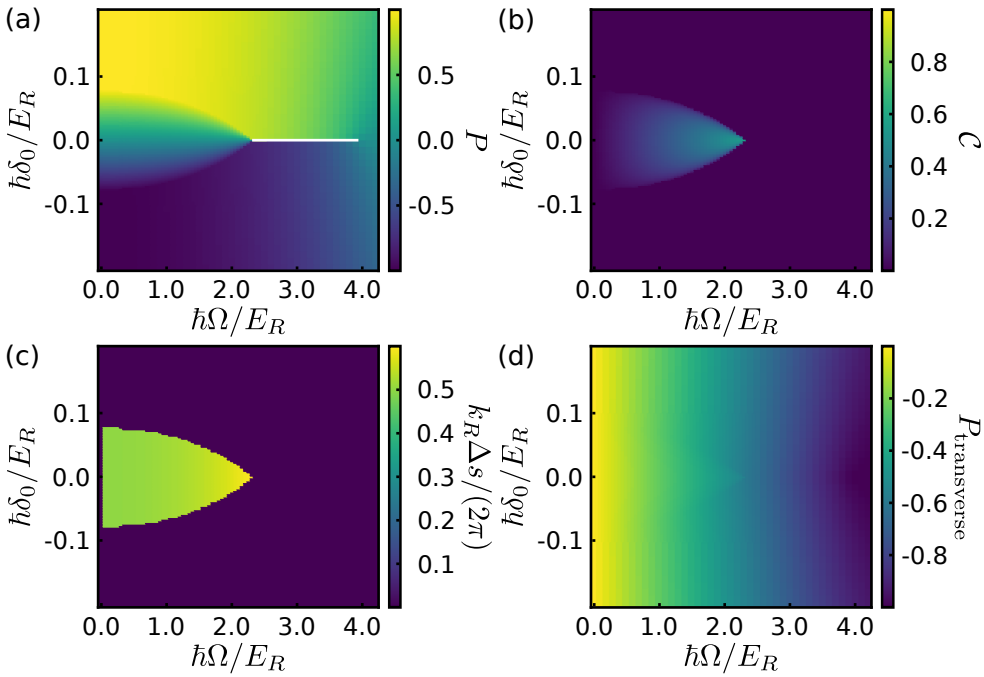

Figure 6.2: Variational results for an atom with the mass of ^{39}K where the scattering lengths are $a_{\uparrow\uparrow} = a_{\downarrow\downarrow} = 100a_0$ and $a_{\uparrow\downarrow} = 60a_0$ with density $\bar{n} = 10^{20}$ m^{-3}. (a) Spin polarisation, P, the white line indicates the parameters where the two plane wave phases with $S = \pm 1$ are degenerate. (b) Fringe contrast, $\mathcal{C}$. (c) Fringe spacing, Δs, unlike a BEC in a shallow optical lattice, the fringe spacing depends on the laser intensity *via* Ω. (d) Transverse spin polarisation, $P_{\text{transverse}}$.

Minimising with respect to S, we have

$$\lim_{\hbar\Omega/E_R \to 0} S = \begin{cases} -1, & \hbar\delta_0 > 4G_2 - 2G_3 \\ -\frac{\hbar\delta_0 + 2G_3}{4G_2}, & |\hbar\delta_0 + 2G_3| \leq 4G_2 \\ 1, & \hbar\delta_0 < -4G_2 - 2G_3. \end{cases} \tag{6.10}$$

Note that unlike the critical Rabi frequency, the phase boundary with respect to δ_0 does not depend on the value of k_R in the limit $\hbar\Omega/E_R \to 0$.

Aside from the particular results we have reviewed so far, analytic minimisation of Eq. 6.8 is not possible. Instead, we numerically minimise the energy functional under the three constraints $-1 \leq S \leq 1$, $0 \leq k_1/k_R \leq 1$, and $0 \leq k_2/k_R \leq 1$. Specifically, we perform a brute force search over the three variational parameters with 100 points along each axis. The brute force minimisation is then used as an initial guess for gradient descent minimisation. Figure 6.2 shows the variational results for an atom with the mass of ^{39}K where the scattering lengths are $a_{\uparrow\uparrow} = a_{\downarrow\downarrow} = 100a_0$ and $a_{\uparrow\downarrow} = 60a_0$ with density $\bar{n} = 10^{20}$ m^{-3}.

We can see that the width of the stripe phase with respect to δ_0 smoothly reduces from the maximum value given in Eq. 6.10 when $\hbar\Omega/E_R = 0$ to zero at the stripe to

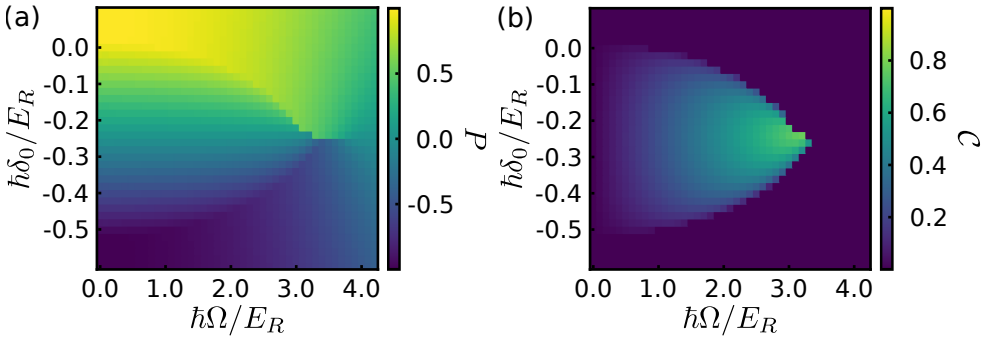

Figure 6.3: Variational results for ^{39}K where the scattering lengths are $a_{\uparrow\uparrow} = 1.3a_0$, $a_{\downarrow\downarrow} = 252.7a_0$, and $a_{\uparrow\downarrow} = -6.3a_0$ with density $\bar{n} = 10^{20}$ m^{-3}. (a) Spin polarisation, P. (b) Fringe contrast, $\mathcal{C}$.

plane wave transition, the fringe contrast and fringe spacing are both maximised at the stripe to plane wave transition at $\hbar\delta_0/E_R = 0$, and the transverse spin polarisation does indicate the stripe to plane wave transition but is most suited for investigating the plane wave to single minimum transition.

The scattering lengths used in Fig. 6.2 do not correspond to any real alkali atom and are an idealised case. If $g_{\uparrow\uparrow} \approx g_{\downarrow\downarrow} \approx g_{\uparrow\downarrow}$, as is commonly the case in the absence of Feshbach resonances, then $G_2/E_R \approx 0$ and $\hbar\Omega_c/E_R \approx 0$. For this reason, previous experiments working with ^{87}Rb have the stripe phase as the groundstate of the system only for small values of Ω and δ_0 where the fringe spacing does not differ significantly from the value corresponding to a shallow optical lattice with lattice spacing π/k_R, the fringe contrast is $\mathcal{C} \approx 10^{-2}$, and the system is highly sensitive to magnetic field fluctuations [67, 112]. This limitation could be avoided by partially separating the bare spins in a direction which is orthogonal to the Raman coupling axis to decrease the effective interstate interactions [310]. Experimentally, a similar technique has been implemented with ^{23}Na by using bands of an optical superlattice as pseudospins where the effective value of $g_{\uparrow\downarrow}$ is small due to the spatial separation of the pseudospins. However, this technique induces additional heating which is sensitive to the alignment between the optical superlattice and the Raman beams [111]. The density modulation in ^{87}Rb can also be enhanced and stabilised by implementing momentum space hopping by means of an additional optical lattice but in this case translational symmetry is not spontaneously broken and the stripe phase is not a supersolid state [157, 311, 312].

Figure 6.3 shows the spin polarisation and fringe contrast according to the variational ansatz for ^{39}K at a density of $\bar{n} = 10^{20}$ m^{-3} with the scattering lengths used in Ch. 5: $a_{\uparrow\uparrow} = 1.3a_0$, $a_{\downarrow\downarrow} = 252.7a_0$, and $a_{\uparrow\downarrow} = -6.3a_0$. The variational calculation predicts that the stripe phase is stable over large ranges of both Ω and δ_0 and that the fringe contrast can reach very high values.

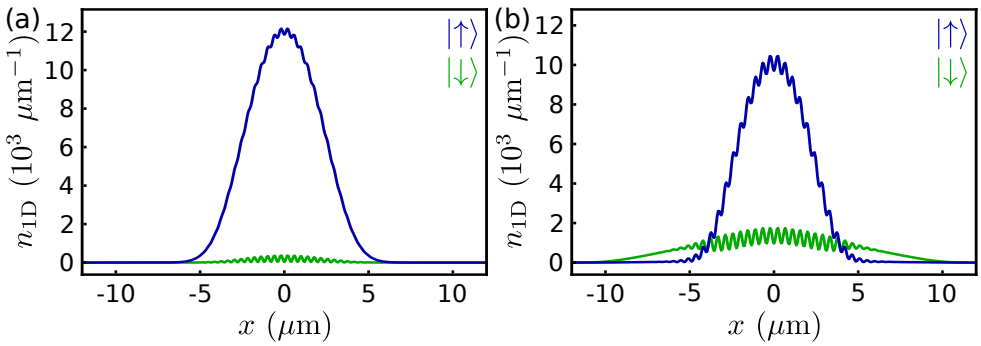

Figure 6.4: Integrated density profiles for the two spin components $|\uparrow\rangle$ (blue line) and $|\downarrow\rangle$ (green line) of ^{39}K with $a_{\uparrow\uparrow} = 1.3a_0$, $a_{\downarrow\downarrow} = 252.7a_0$, $a_{\uparrow\downarrow} = -6.3a_0$, and $N = 6.5 \times 10^4$ corresponding to Eq. 5.20 for (a) $\hbar\Omega/E_R = 0.9$ and $\hbar\delta_0/E_R = 0.0$ and (b) $\hbar\Omega/E_R = 2.0$ and $\hbar\delta_0/E_R = -0.1$.

6.3 Zero Order Mixture Picture

For a finite system, the envelope of the density profile must be taken into account. Figure 6.4 shows the integrated density profiles for each of the two spin components found by solving Eq. 5.20 in imaginary time for (a) $\hbar\Omega/E_R = 0.9$ and $\hbar\delta_0/E_R = 0$ and (b) $\hbar\Omega/E_R = 2.0$ and $\hbar\delta_0/E_R = -0.1$ in a cylindrically symmetric harmonic trap with $\omega_x/(2\pi) = 65$ Hz, $\omega_r/(2\pi) = 130$ Hz, $N = 6.5 \times 10^4$, and scattering lengths from Fig. 6.3. For these simulations we employ the Bessel transform for the radial derivative where the radial grid is defined on the interval $(0, 9.63)$ μm with 2^4 grid points and the x-axis is discretised on 2^{13} grid points with a grid spacing of 60.2 nm.

For $\hbar\delta_0/E_R = 0$, the profiles of the two spin components are similar in shape and have good overlap but the contrast of the fringes is limited because the centre of the stripe phase is significantly shifted due to the large value of G_3. In this case, we have $S \approx -1$ meaning almost all of the atoms have momentum $k_x/k_R < 0$ and $P \approx 1$. For $\hbar\delta_0/E_R = -0.1$, we have $S \approx 0$ but the actual contrast is significantly lower than that predicted by the variational ansatz because the two spin components have very different density profiles and there is little spatial overlap between them. In this section, I will develop an effective model of the stripe phase which will allow for simple analytic approximations with relevant experimental parameters, including unequal intrastate interactions and harmonic trapping potentials.

As has been shown previously, we can treat the two dressed BECs corresponding to the two minima of the Raman dressed dispersion as a pseudospin mixture with interaction strengths depending on the Raman coupling parameters [67, 166, 167, 239, 313, 314]. Here, we modify the momentum space based approach applied for the quantum simulation of the chiral BF theory in Ch. 5 to a two component system to develop an understanding of the stripe phase in a finite size system. We label the two minima of the Raman dressed dispersion, $\varepsilon_-(\mathbf{k})$, as $k_l/k_R = -\tilde{\delta}(k_l)/\tilde{\Omega}(k_l)$ for $l = 1, 2$ with $k_1/k_R > 0$ and $k_2/k_R < 0$. Note that k_2 is defined with a minus sign with respect

to the variational ansatz. We write the lower dressed state field operator as a a spinor, $\hat{\phi}_-(\mathbf{r}) = [\hat{\varphi}_1(\mathbf{r}), \hat{\varphi}_2(\mathbf{r})]^T$. For convenience, we will refer to $\hat{\varphi}_1^\dagger(\mathbf{r})$ and $\hat{\varphi}_2^\dagger(\mathbf{r})$ as the field creation operators corresponding to the positive and negative momentum wells, respectively.

The second order Taylor expansion of the Raman dressed dispersion around k_l is

$$\varepsilon_-(\mathbf{k}) \approx E_R + \frac{\hbar^2}{2m}\left(k_l^2 + \mathbf{k}_\perp^2\right) + \frac{\hbar^2}{2mm_l^*}\left(k_x - k_l\right)^2 \tag{6.11}$$

where the effective mass, mm_l^*, is given by

$$1/m_l^* = 1 - 4\frac{k_l/k_R}{4k_l/k_R - \hbar\delta_0/E_R}\left(1 - k_l^2/k_R^2\right). \tag{6.12}$$

Let $\Delta = \varepsilon_-(k_2\mathbf{e}_1 + \mathbf{k}_\perp) - \varepsilon_-(k_1\mathbf{e}_1 + \mathbf{k}_\perp)$ and $\hat{\varphi}_l'(\mathbf{r}) = \exp\left(-ik_l x\right)\hat{\varphi}_l(\mathbf{r})$. Then, the single particle part of the Raman dressed Hamiltonian can be approximated as

$$\begin{aligned}\hat{H}_{0,R} \approx \int \mathrm{d}^3\mathbf{r} \Bigg[&\hat{\varphi}_1'^\dagger(\mathbf{r})\left(-\frac{\hbar^2}{2mm_1^*}\frac{\partial^2}{\partial x^2} - \frac{\hbar^2}{2m}\nabla_\perp^2 - \frac{\Delta}{2}\right)\hat{\varphi}_1'(\mathbf{r}) \\ &+\hat{\varphi}_2'^\dagger(\mathbf{r})\left(-\frac{\hbar^2}{2mm_2^*}\frac{\partial^2}{\partial x^2} - \frac{\hbar^2}{2m}\nabla_\perp^2 + \frac{\Delta}{2}\right)\hat{\varphi}_2'(\mathbf{r})\Bigg].\end{aligned} \tag{6.13}$$

For the interaction part of the Hamiltonian, $\hat{H}_{\mathrm{int},R}$, we expand to zero order in momentum to be consistent with the second order expansion in kinetic energy. Due to momentum conservation, the only allowed collisions are of the form $\hat{\varphi}_l'^\dagger(\mathbf{r})\hat{\varphi}_l'^\dagger(\mathbf{r})\hat{\varphi}_l'(\mathbf{r})\hat{\varphi}_l'(\mathbf{r})$, corresponding to intrawell collisions and the four combinations $\hat{\varphi}_1'^\dagger(\mathbf{r})\hat{\varphi}_2'^\dagger(\mathbf{r})\hat{\varphi}_1'(\mathbf{r})\hat{\varphi}_2'(\mathbf{r})$, $\hat{\varphi}_1'^\dagger(\mathbf{r})\hat{\varphi}_2'^\dagger(\mathbf{r})\hat{\varphi}_2'(\mathbf{r})\hat{\varphi}_1'(\mathbf{r})$, $\hat{\varphi}_2'^\dagger(\mathbf{r})\hat{\varphi}_1'^\dagger(\mathbf{r})\hat{\varphi}_1'(\mathbf{r})\hat{\varphi}_2'(\mathbf{r})$, and $\hat{\varphi}_2'^\dagger(\mathbf{r})\hat{\varphi}_1'^\dagger(\mathbf{r})\hat{\varphi}_2'(\mathbf{r})\hat{\varphi}_1'(\mathbf{r})$, corresponding to interwell collisions.

We compute the well-wise interaction strengths by expanding Eq. 5.4 to zero order in momentum around k_1 and k_2 and by exploiting the symmetry of $\chi\left(k_{1,x}, k_{2,x}, k_{3,x}, k_{4,x}\right)$ with respect to the exchanges $k_{1,x} \leftrightarrow k_{3,x}$ and $k_{2,x} \leftrightarrow k_{4,x}$. We get

$$\begin{aligned}\hat{H}_{\mathrm{int},R} \approx \frac{1}{2}\int \mathrm{d}^3\mathbf{r} \Big[&g_{11}\hat{\varphi}_1'^\dagger(\mathbf{r})\hat{\varphi}_1'^\dagger(\mathbf{r})\hat{\varphi}_1'(\mathbf{r})\hat{\varphi}_1'(\mathbf{r}) + g_{22}\hat{\varphi}_2'^\dagger(\mathbf{r})\hat{\varphi}_2'^\dagger(\mathbf{r})\hat{\varphi}_2'(\mathbf{r})\hat{\varphi}_2'(\mathbf{r}) \\ &+2g_{12}\hat{\varphi}_1'^\dagger(\mathbf{r})\hat{\varphi}_2'^\dagger(\mathbf{r})\hat{\varphi}_1'(\mathbf{r})\hat{\varphi}_2'(\mathbf{r})\Big].\end{aligned} \tag{6.14}$$

where

$$g_{11} = \frac{1}{4}\left[g_{\uparrow\uparrow}\left(1 - \frac{k_1}{k_R}\right)^2 + g_{\downarrow\downarrow}\left(1 + \frac{k_1}{k_R}\right)^2 + 2g_{\uparrow\downarrow}\left(1 - \frac{k_1^2}{k_R^2}\right)\right], \tag{6.15}$$

$$g_{22} = \frac{1}{4}\left[g_{\uparrow\uparrow}\left(1 - \frac{k_2}{k_R}\right)^2 + g_{\downarrow\downarrow}\left(1 + \frac{k_2}{k_R}\right)^2 + 2g_{\uparrow\downarrow}\left(1 - \frac{k_2^2}{k_R^2}\right)\right], \tag{6.16}$$

and

$$\begin{aligned}g_{12} = &\frac{g_{\uparrow\uparrow}}{2}\left(1 - \frac{k_1}{k_R}\right)\left(1 - \frac{k_2}{k_R}\right) + \frac{g_{\downarrow\downarrow}}{2}\left(1 + \frac{k_1}{k_R}\right)\left(1 + \frac{k_2}{k_R}\right) \\ &+ \frac{g_{\uparrow\downarrow}}{2}\left[1 - \frac{k_1 k_2}{k_R^2} + \sqrt{\left(1 - \frac{k_1^2}{k_R^2}\right)\left(1 - \frac{k_2^2}{k_R^2}\right)}\right].\end{aligned} \tag{6.17}$$

With interactions expanded to zero order in momentum, the total Hamiltonian, $\hat{H}_R = \hat{H}_{0,R} + \hat{H}_{\mathrm{int},R}$, has the approximate form of a mixture of two bosonic species with species and direction-dependent effective masses and two-body interactions. For this reason, I will refer to this model as the zero order mixture picture. As in the case of the mapping to the chiral BF theory in the single minimum regime, these approximations are valid for a BEC with small spread in momentum space which corresponds to small densities with repulsive interactions.

By writing, the mean-field wavefunctions of the pseudospins in polar form, $\varphi_l' = |\varphi_l| \exp(i\theta_{s,l})$, we can express the wavefunctions corresponding to the bare spin states in terms of the pseudospins as

$$\phi_\downarrow = \frac{1}{\sqrt{2}} \left[\sqrt{1 + \frac{k_1}{k_R}} |\varphi_1| \exp(i\theta_{s,1} - ik_1 x) + \sqrt{1 + \frac{k_2}{k_R}} |\varphi_2| \exp(i\theta_{s,2} - ik_2 x) \right] \quad (6.18)$$

and

$$\phi_\uparrow = \frac{-1}{\sqrt{2}} \left[\sqrt{1 - \frac{k_1}{k_R}} |\varphi_1| \exp(i\theta_{s,1} - ik_1 x) + \sqrt{1 - \frac{k_2}{k_R}} |\varphi_2| \exp(i\theta_{s,2} - ik_2 x) \right] \quad (6.19)$$

which allows us to express the total mean-field density as

$$\begin{aligned} n(\mathbf{r}) = |\phi_\downarrow(\mathbf{r})|^2 + |\phi_\uparrow(\mathbf{r})|^2 &= |\varphi_1(\mathbf{r})|^2 + |\varphi_2(\mathbf{r})|^2 \\ &+ |\varphi_1(\mathbf{r})||\varphi_2(\mathbf{r})| \left[\sqrt{(1 + k_1/k_R)(1 + k_2/k_R)} \right. \\ &\left. + \sqrt{(1 - k_1/k_R)(1 - k_2/k_R)} \right] \cos[(k_1 - k_2)x + \theta_s]. \end{aligned} \quad (6.20)$$

Note that the zero order mixture picture does not contain any terms which allow the transfer of atoms between the two momentum wells. This means that

$$S = \frac{\langle \hat{\varphi}_1'^\dagger \hat{\varphi}_1' - \hat{\varphi}_2'^\dagger \hat{\varphi}_2' \rangle}{\langle \hat{\varphi}_1'^\dagger \hat{\varphi}_1' + \hat{\varphi}_2'^\dagger \hat{\varphi}_2' \rangle} = \frac{1}{N} \int \mathrm{d}^3\mathbf{r} \left[|\varphi_1(\mathbf{r})|^2 - |\varphi_2(\mathbf{r})|^2 \right] \quad (6.21)$$

is a conserved quantity at this order of approximation. So when the two components of the zero order mixture picture have uniform mean-field densities we can write $|\varphi_1(\mathbf{r})|^2 = (1 + S)\,\bar{n}/2$ and $|\varphi_2(\mathbf{r})|^2 = (1 - S)\,\bar{n}/2$ and we recover the same density given by the variational ansatz of Ref. [288] up to the minus sign in the definition of k_2.

Using the fact the S is a conserved quantity at this order of approximation, we can use the zero order mixture picture to construct an energy functional where we express the mean-field wave functions using a single mode approximation but without assuming a uniform density: $\varphi_1(\mathbf{r}) = \sqrt{(1 + S)\,n(\mathbf{r})/2} \exp(i\theta_{s_1})$ and $\varphi_2(\mathbf{r}) = \sqrt{(1 - S)\,n(\mathbf{r})/2} \exp(i\theta_{s_2})$. Under this assumption, the mean-field energy functional

is

$$E\left[n(\mathbf{r}),S\right]=\int \mathrm{d}^3\mathbf{r}\sqrt{n(\mathbf{r})}\left[\frac{1+S}{2}\left(-\frac{\hbar^2}{2mm_1^*}\frac{\partial^2}{\partial x^2}-\frac{\hbar^2}{2m}\nabla_\perp^2-\frac{\Delta}{2}\right)\right.$$
$$\left.+\frac{1-S}{2}\left(-\frac{\hbar^2}{2mm_2^*}\frac{\partial^2}{\partial x^2}-\frac{\hbar^2}{2m}\nabla_\perp^2+\frac{\Delta}{2}\right)\right]\sqrt{n(\mathbf{r})}+\left[\frac{g_{11}}{2}\left(\frac{1+S}{2}\right)^2\right.$$
$$\left.+\frac{g_{22}}{2}\left(\frac{1-S}{2}\right)^2+g_{12}\frac{1-S^2}{4}\right]n(\mathbf{r})^2. \quad (6.22)$$

If we take $\hbar\delta_0/E_R=0\Rightarrow k_1=-k_2=k_R\sqrt{1-\left[\hbar\Omega/(4E_R)\right]^2}$, $m_1^*=m_2^*=1/\{1-\left[\hbar\Omega/(4E_R)\right]^2\}\equiv m^*$ and minimise the energy functional with respect to S, we obtain $S=\left(g_{22}-g_{11}\right)/\left(g_{11}+g_{22}-2g_{12}\right)$. Alternatively, we can assume a uniform density $n(\mathbf{r})=\bar{n}$ which gives

$$S=\frac{g_{22}-g_{11}+2\Delta/\bar{n}}{g_{11}+g_{22}-2g_{12}} \quad (6.23)$$

which is the same as the result without assuming uniform density with $\hbar\delta_0/E_R=0$. Since the constraint $-1\leq S\leq 1$ applies, the boundary between the stripe phase and plane wave phases can be determined by finding the points where $S=\pm1$ or S is undefined. In the case of $\hbar\delta_0/E_R=0$ and $g_{\uparrow\uparrow}=g_{\downarrow\downarrow}\equiv g$ we have $g_{11}=g_{22}=g+\left[\hbar\Omega/(4E_R)\right]^2\left(g_{\uparrow\downarrow}-g\right)/2$ and $S=0$ for $g_{12}=g_{\uparrow\downarrow}+\left[\hbar\Omega/(4E_R)\right]^2 g<g_{11}$ and undefined S for $g_{12}=g_{11}\Rightarrow\hbar\Omega/E_R=4\sqrt{2}\sqrt{\left(g_{\uparrow\downarrow}-g\right)/\left(g_{\uparrow\downarrow}-3g\right)}$ which is the low density limit of $\hbar\Omega_c/E_R$ [167, 168]. So, for symmetric interactions and zero detuning, the stripe to plane wave transition corresponds to a miscible to immiscible phase transition of the Raman dressed states, consistent with the interpretation of Lin *et al.* [67].

In an immiscible two-component BEC coherently coupled by a resonant radio frequency (RF) electromagnetic field, as described in Ch. 3, the groundstate of the system is an effective single-component BEC with vanishing spin polarisation in the bare spin basis when the Rabi frequency dominates over the interaction energy scale [315, 316]. For smaller Rabi frequencies, the system tends to minimise its energy by becoming spin polarised, as has been observed experimentally by Zibold *et al.* [315]. This is possible because the RF dressed system has only one chemical potential meaning that there is conservation of total particle number but not of the individual bare spin components. In the zero order mixture picture, we have conservation of the ratio of atoms in the two momentum wells, S.

If $\hbar\delta_0/E_R=0$ and $g_{11}>g_{22}$ then $S=-1$ when $g_{12}=g_{22}$ meaning that it becomes energetically favourable for all of the atoms to occupy the negative momentum well[1]. Note that this is not a miscible to immiscible transition but rather a magnetic phase transition to a polarised state [317]. In an experimental platform, S can be set to an arbitrary value since there are no well changing collisions at our order of approximation and metastable stripes could be observed with $g_{12}>g_{22}$ but the stripe phase would not be the ground state. As will be discussed shortly, a confining potential does promote

[1]The physics is similar for $g_{11}<g_{22}$ but in this case $S=1$ when $g_{12}=g_{11}$.

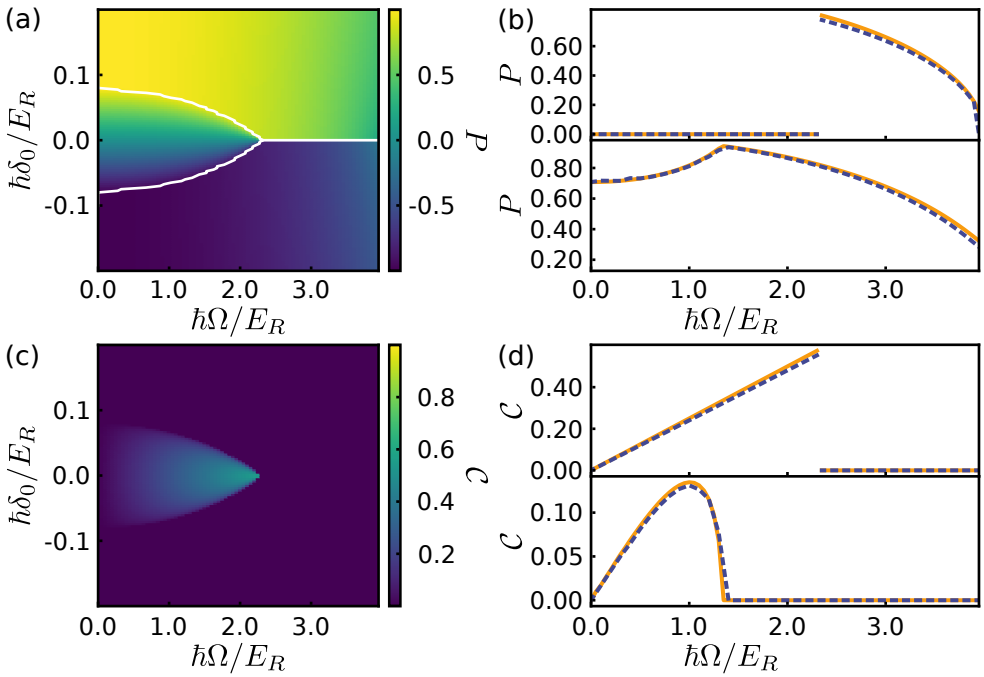

Figure 6.5: (a) Polarisation, P, calculated using the zero order mixture picture for an atom with the mass of ^{39}K with $a_{\uparrow\uparrow} = a_{\downarrow\downarrow} = 100a_0$, $a_{\uparrow\downarrow} = 60a_0$, and $\bar{n} = 10^{20}$ m^{-3}. The white line shows the phase boundary extracted numerically from Fig. 6.2. (b) Slices of P versus $\hbar\Omega/E_R$ for $\hbar\delta_0/E_R = 0.000$ (top panel) and $\hbar\delta_0/E_R = 0.056$ (bottom panel) from the zero order mixture picture (solid orange line) and the variational ansatz (dashed blue line). (c) Contrast, $\mathcal{C}$, calculated from the zero order mixture picture. (d) Slices of $\mathcal{C}$ versus $\hbar\Omega/E_R$ for $\hbar\delta_0/E_R = 0.000$ (top panel) and $\hbar\delta_0/E_R = 0.056$ (bottom panel) from the zero order mixture picture (solid orange line) and the variational ansatz (dashed blue line).

particle exchange between the two wells [239] and a thermal component would also mediate the exchange of particles between the two wells. In Ch. 7 I will report on experiments in the stripe phase where we have observed that mechanisms enabling exchange of particles between the two wells are not significant on our experimental timescales.

In the uniform density case, we can express the polarisation in the bare state basis as $P = -k_1(1+S)/2 - k_2(1-S)/2$ and the contrast can be read off from Eq. 6.20 for $\hbar\delta_0/E_R = 0$ as $\mathcal{C} = \sqrt{1-S^2}\hbar\Omega/(4E_R)$ which is also the low density limit of the variational expression. Since the zero order mixture picture gives predictions corresponding to the low density limit with $\hbar\delta_0/E_R$, we expect discrepancies to emerge at high densities for all detunings. Figure 6.5 shows the polarisation, P, and the contrast, $\mathcal{C}$, calculated using the zero order mixture picture as a function of Ω and δ_0 for an atom with the mass of ^{39}K with $a_{\uparrow\uparrow} = a_{\downarrow\downarrow} = 100a_0$ and $a_{\uparrow\downarrow} = 60a_0$ with a density of $\bar{n} = 10^{20}$ m^{-3}, which is a realistic density for a trapped BEC.

We can see that the zero order mixture picture slightly underestimates the Rabi

frequency corresponding to the stripe phase to plane wave phase transition for all detunings and the zero order mixture picture does not show the decrease in the Rabi frequency corresponding to the plane wave phase to single minimum phase transition seen in the variational ansatz. Overall, the values of P and $\mathcal{C}$ calculated from the zero order mixture picture are in good quantitative agreement with the variational ansatz for the parameters used in Fig. 6.5.

To understand the density profiles of ^{39}K shown in Fig. 6.4(b), we use the mean-field Gross-Pitaevskii equations of motion corresponding to the zero order mixture picture which are

$$i\hbar\frac{\partial}{\partial t}\varphi_1' = \left[-\frac{\hbar^2}{2mm_1^*}\frac{\partial^2}{\partial x^2} - \frac{\hbar^2}{2m}\nabla_\perp^2 - \frac{\Delta}{2} + V_1(\mathbf{r}) + g_{11}|\varphi_1'|^2 + g_{12}|\varphi_2'|^2\right]\varphi_1'$$

and

$$i\hbar\frac{\partial}{\partial t}\varphi_2' = \left[-\frac{\hbar^2}{2mm_2^*}\frac{\partial^2}{\partial x^2} - \frac{\hbar^2}{2m}\nabla_\perp^2 + \frac{\Delta}{2} + V_2(\mathbf{r}) + g_{22}|\varphi_2'|^2 + g_{12}|\varphi_1'|^2\right]\varphi_2' \tag{6.24}$$

where we have included trapping potentials $V_l(\mathbf{r})$. The trapping potentials are determined by adding a state-dependent trapping term to the Hamiltonian as in Sec. 3.3.2. Projecting into the two pseudospins corresponding to the two momentum wells and expanding to zero order in momentum under the assumption that the trap does not confine too tightly in position space, we find

$$\hat{V} \approx \int \mathrm{d}^3\mathbf{r}\begin{bmatrix}\hat{\varphi}_1'^\dagger(\mathbf{r}) & \hat{\varphi}_2'^\dagger(\mathbf{r})\end{bmatrix}\begin{bmatrix}V_1(\mathbf{r}) & V_{12}(\mathbf{r})\\ V_{12}(\mathbf{r}) & V_2(\mathbf{r})\end{bmatrix}\begin{bmatrix}\hat{\varphi}_1'(\mathbf{r})\\ \hat{\varphi}_2'(\mathbf{r})\end{bmatrix} \tag{6.25}$$

where

$$V_l(\mathbf{r}) = V_\uparrow(\mathbf{r})\frac{1-k_l/k_R}{2} + V_\downarrow(\mathbf{r})\frac{1+k_l/k_R}{2} \tag{6.26}$$

and

$$V_{12}(\mathbf{r}) = V_\uparrow(\mathbf{r})\frac{\sqrt{1-k_1/k_R}\sqrt{1-k_2/k_R}}{2} + V_\downarrow(\mathbf{r})\frac{\sqrt{1+k_1/k_R}\sqrt{1+k_2/k_R}}{2}. \tag{6.27}$$

It is interesting to note that even when $V_\uparrow(\mathbf{r}) = V_\downarrow(\mathbf{r})$, the trap promotes exchange of atoms between the two momentum wells [239]. We will see in Sec. 6.5 that this coupling is typically small for realistic experimental parameters. As $\hbar\Omega$ is increased towards $4E_R$, the two pseudospins start to see the same potential even for $V_\uparrow(\mathbf{r}) \neq V_\downarrow(\mathbf{r})$ as would be expected since the two wells become one in the single minimum phase. This mixing of the state-dependent potentials has important consequences for schemes which aim to increase the stability of the stripe phase through geometric separation of the two bare components to effectively reduce $g_{\uparrow\downarrow}$ [310, 318] although this effect was not significant in the experiments of Li *et al.* [111] since the Raman Rabi frequency was restricted to $\lesssim 0.5E_R$.

6.4 Experimental Considerations for Interactions

Figure 6.6(a) shows the density profiles $|\varphi_1'(\mathbf{r})|^2$ and $|\varphi_2'(\mathbf{r})|^2$ evaluated by solving Eq. 6.24 in imaginary time with $V_\uparrow(\mathbf{r}) = V_\downarrow(\mathbf{r}) \equiv V(\mathbf{r}) \Rightarrow V_1(\mathbf{r}) = V_2(\mathbf{r}) = V(\mathbf{r})$

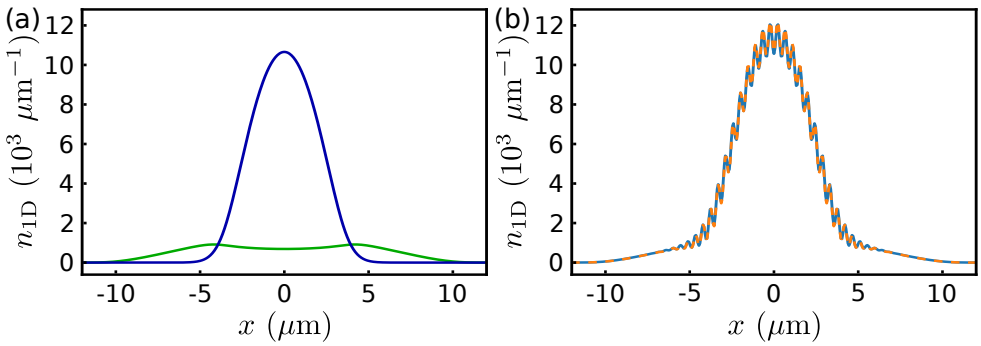

Figure 6.6: (a) Density profiles of the effective zero order mixture picture calculated from Eq. 6.24 for ^{39}K with the parameters of Fig. 6.4(b). The green line shows the $k_x/k_R > 0$ component and the blue line shows the $k_x/k_R < 0$ component. (b) Comparison between the total density calculated from Eq. 5.20 (dashed orange line) and the effective zero order mixture picture calculated from Eq. 6.20 (solid blue line).

using the same parameters as Fig. 6.4(b). Using the pseudospin density profiles, we can evaluate the total density using Eq. 6.20. Figure 6.6(b) shows the total density calculated using the zero order mixture picture and the total density corresponding to Fig. 6.4(b). We can see that the two density profiles are almost identical in spite of the large difference in $g_{\uparrow\uparrow}$ and $g_{\downarrow\downarrow}$.

Note that the zero order mixture picture shows that the pseudospins violate the uniform density miscibility condition with $g_{12}^2 > g_{11}g_{22}$. In the trap, the effect is that $|\varphi_1'|^2$ is concave up in the centre of the trap, indicating buoyancy [204]. I have verified for general anisotropic traps without imposing any symmetries upon the wavefunctions that there is no cylindrical symmetry breaking [319].

Since the spatial overlap of the density profiles of ^{39}K at $B = 397.01$ G limits the contrast of the stripes to a few percent, there is no clear experimental advantage to using ^{39}K at this magnetic field compared to previous experiments with ^{87}Rb [67, 112]. To improve the spatial overlap between the two spin components, we would like to have $g_{\uparrow\uparrow} \approx g_{\downarrow\downarrow}$. The scattering lengths of ^{39}K at $B = 57.28$ G used in Sec. 3.2.2 are closer to satisfying this condition but the large three-body losses affecting state $|\downarrow\rangle = |F = 1, m_F = 0\rangle$ would result in rapid losses which, unlike in the RF dressing case, would alter the spin polarisation, P, since they would have a much greater effect on $\hat{\varphi}_1'$ than $\hat{\varphi}_2'$. Fortunately, there is a pair of Feshbach resonances for ^{41}K affecting the $|F = 1, m_F = -1\rangle \leftrightarrow |F = 1, m_F = -1\rangle$ and $|F = 1, m_F = 0\rangle \leftrightarrow |F = 1, m_F = -1\rangle$ scattering lengths at $B = 51.1(2)$ G and $B = 51.92(8)$ G, respectively [244]. These Feshbach resonances allow us to tune the scattering lengths much closer to the desired configuration.

Choosing $|\uparrow\rangle = |F = 1, m_F = -1\rangle$ and $|\downarrow\rangle = |F = 1, m_F = 0\rangle$ in ^{41}K gives theoretically predicted scattering lengths of $a_{\uparrow\uparrow} = 102.0a_0$, $a_{\downarrow\downarrow} = 64.3a_0$, and $a_{\uparrow\downarrow} = 18.5a_0$ at $B = 51.765$ G [244]. Figure 6.7(a) shows the density profiles of the two bare state spin components calculated by numerically solving Eq. 5.20 in imaginary time

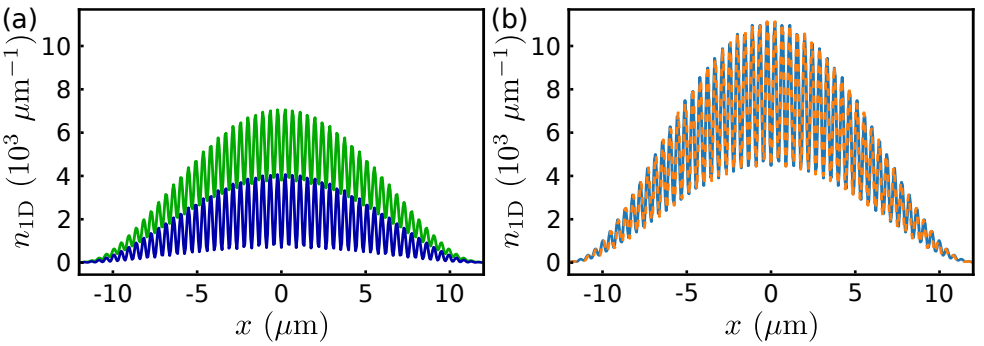

Figure 6.7: (a) Integrated density profiles for the two spin components $|\uparrow\rangle$ (blue line) and $|\downarrow\rangle$ (green line) of ^{41}K with $a_{\uparrow\uparrow} = 102.0a_0$, $a_{\downarrow\downarrow} = 64.3a_0$, $a_{\uparrow\downarrow} = 18.5a_0$, and $N = 10^5$ corresponding to Eq. 5.20 for $\hbar\Omega/E_R = 2$ and $\hbar\delta_0/E_R = 0$. (b) Comparison between the total density calculated from Eq. 5.20 (dashed orange line) and the effective zero order mixture picture calculated from Eq. 6.20 (solid blue line).

with $\hbar\Omega/E_R = 2$ and $\hbar\delta_0/E_R = 0$ in a cylindrically symmetric harmonic trap with $\omega_x/(2\pi) = 65$ Hz, $\omega_r/(2\pi) = 130$ Hz, and $N = 10^5$ using the same grid as Fig. 6.4. We can observe that the single mode approximation is much more accurate in this case than for ^{39}K and the increased spatial overlap results in a much higher fringe contrast. Figure 6.7(b) shows the comparison between the total density corresponding to Eq. 5.20 and the zero order mixture picture. As with ^{39}K, the two density profiles are practically indistinguishable.

It has been shown that the variational ansatz can be compared to numerical solutions of the GPEs by using the density at the trap centre in place of the uniform density in the variational ansatz [168]. The density does not appear in the analytical expressions arising from the zero order mixture picture. In Fig. 6.8 we make quantitative comparisons between the variational ansatz, the zero order mixture picture and the numerical results of Eq. 5.20 for various values of $\hbar\Omega/E_R$ using the parameters of Fig. 6.7. For these simulations we employ the Bessel transform for the radial derivative where the radial grid is defined on the interval $(0, 9.39)$ μm with 2^4 grid points and the x-axis is discretised on 2^9 grid points with a grid spacing of 58.7 nm.

To extract the proportion of atoms in each momentum well, S, from the numerical solutions, we evaluate

$$N_1 = \int_{-\infty}^{\infty} \frac{\mathrm{d}k_z}{2\pi} \int_{-\infty}^{\infty} \frac{\mathrm{d}k_y}{2\pi} \int_{0}^{\infty} \frac{\mathrm{d}k_x}{2\pi} \left[|\Phi'_\uparrow(\mathbf{k})|^2 + |\Phi'_\downarrow(\mathbf{k})|^2 \right] \tag{6.28}$$

and

$$N_2 = \int_{-\infty}^{\infty} \frac{\mathrm{d}k_z}{2\pi} \int_{-\infty}^{\infty} \frac{\mathrm{d}k_y}{2\pi} \int_{-\infty}^{0} \frac{\mathrm{d}k_x}{2\pi} \left[|\Phi'_\uparrow(\mathbf{k})|^2 + |\Phi'_\downarrow(\mathbf{k})|^2 \right]. \tag{6.29}$$

Similarly, to determine k_1 and k_2, we evaluate

$$k_1 = \frac{1}{N_1} \int_{-\infty}^{\infty} \frac{\mathrm{d}k_z}{2\pi} \int_{-\infty}^{\infty} \frac{\mathrm{d}k_y}{2\pi} \int_{0}^{\infty} \frac{\mathrm{d}k_x}{2\pi} k_x \left[|\Phi'_\uparrow(\mathbf{k})|^2 + |\Phi'_\downarrow(\mathbf{k})|^2 \right] \tag{6.30}$$

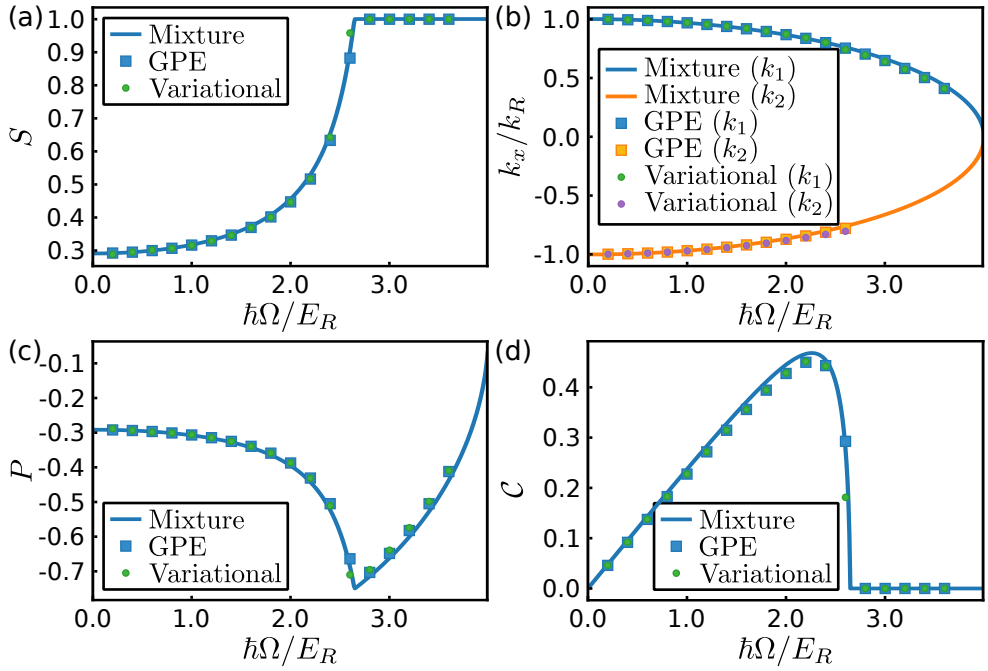

Figure 6.8: Comparison between the variational ansatz, zero order mixture picture, and numerical solutions of the GPEs for ^{41}K with $a_{\uparrow\uparrow} = 102.0a_0$, $a_{\downarrow\downarrow} = 64.3a_0$, $a_{\uparrow\downarrow} = 18.5a_0$, and $N = 10^5$ for various values of $\hbar\Omega/E_R$ with $\hbar\delta_0/E_R = 0$. (a) Momentum well population ratio, S. (b) Group momenta of the two dressed BECs, $\hbar k_1$ and $\hbar k_2$. (c) Spin polarisation in the bare spin basis, P. (d) Fringe contrast, $\mathcal{C}$.

and

$$k_2 = \frac{1}{N_2}\int_{-\infty}^{\infty}\frac{\mathrm{d}k_z}{2\pi}\int_{-\infty}^{\infty}\frac{\mathrm{d}k_y}{2\pi}\int_{-\infty}^{0}\frac{\mathrm{d}k_x}{2\pi}k_x\left[|\Phi'_\uparrow(\mathbf{k})|^2 + |\Phi'_\downarrow(\mathbf{k})|^2\right]. \tag{6.31}$$

To evaluate the contrast, we fit the integrated total density profile, $n_{1\mathrm{D}}$, with a modulated Gaussian function

$$G_s(x) = A\exp\left[-\frac{(x-x_0)^2}{2\sigma_x}\right]\left[1 + \mathcal{C}\cos\left(k_s x + \theta_s\right)\right]. \tag{6.32}$$

We see good agreement between values corresponding to the zero order mixture picture, the variational ansatz, and the GPE solutions for all of the parameters shown in Fig. 6.8 for this experimentally realistic configuration. The largest discrepancies between the variational ansatz and the numerical results appear just below the stripe phase to plane wave phase transition.

6.5 Collective Mode Dynamics of the Stripe Phase

Long before the first experimental realisations of supersolids, the collective excitation spectrum was proposed as a key signature of supersolidity [320]. A large number

of theoretical and experimental works have addressed the use of collective modes to probe supersolidity in dipolar [158, 159, 164, 321–324], cavity [106, 325, 326], and Raman coupled [153, 163, 307–309, 316, 327–329] systems. Gapless Goldstone modes are associated with the spontaneous breaking of continuous symmetries [158, 160].

In a supersolid, one expects a Goldstone excitation associated with breaking of phase invariance as in a normal superfluid as well as an additional Goldstone mode for each broken translational symmetry (each spatial axis with spontaneous density modulations) which results in additional collective mode frequencies [158, 164, 322]. Each of the broken symmetries in a supersolid corresponds to a distinct physical phonon mode [330, 331]. This means, in a supersolid with spontaneous density modulations in one direction, we expect to see two speeds of sound corresponding to the phase invariance and the crystal structure.

Goldstone modes have been observed experimentally as zero energy translations of density modulations in dipolar supersolids [159, 322] and supersolid properties can also be inferred from nonclassical rotational inertia, in analogy with early attempts to detect supsersolidity in ^{4}He [323]. Zero energy translations of the density modulation have also been detected cavity supersolids [105, 106, 325] but in this case the symmetry breaking arises from global interactions between all of the atoms in the ensemble mediated by cavity photons and as such there are no propagating phonon modes associated with the crystal structure [325, 332].

In Raman coupled BECs, the Goldstone modes in the supersolid stripe phase have not been investigated experimentally yet. Numerical studies have shown additional modes associated to spin excitations emerging in the supersolid stripe phase [307, 308, 328] and the appearance of a low energy mode has been confirmed by the spin dipole mode violating the upper bound on the lowest excitation frequency set by a sum-rule [307] due to the divergence of the magnetic susceptibility at the stripe phase to plane wave phase transition [333]. The sound velocities associated to the two Goldstone modes have been determined by exact numerical calculations [327] and analytic estimates have been made through a perturbative treatment [163].

In this section, I will apply the zero order mixture picture to build an intuitive understanding of the collective excitation behaviour of Raman coupled BECs in harmonic traps. Specifically, I will follow the Ehrenfest approach outlined in Refs. [334, 335] to make an analytic approximation of the dipole and spin dipole frequencies which can also be used to infer the collective breathing frequency both in the supersolid stripe phase and the magnetised plane wave phase. Additionally, I will use well known results from incoherent spin mixtures to make analytic approximations of the sound velocities in the supersolid stripe phase. All of the analytical predictions make good approximations of numerical simulations.

6.5.1 Collective Oscillation Frequencies

Chen *et al.* have calculated the excitation spectrum of a Raman dressed BEC with $a_{\uparrow\uparrow} = a_{\downarrow\downarrow} = 101.8a_0$, $a_{\uparrow\downarrow} = 71.3a_0$, $N = 2000$, $\hbar\delta_0/E_R = 0$, and the mass of ^{87}Rb in an effectively one-dimensional harmonic trap with $\hbar\delta_0/E_R = 0$ in all three

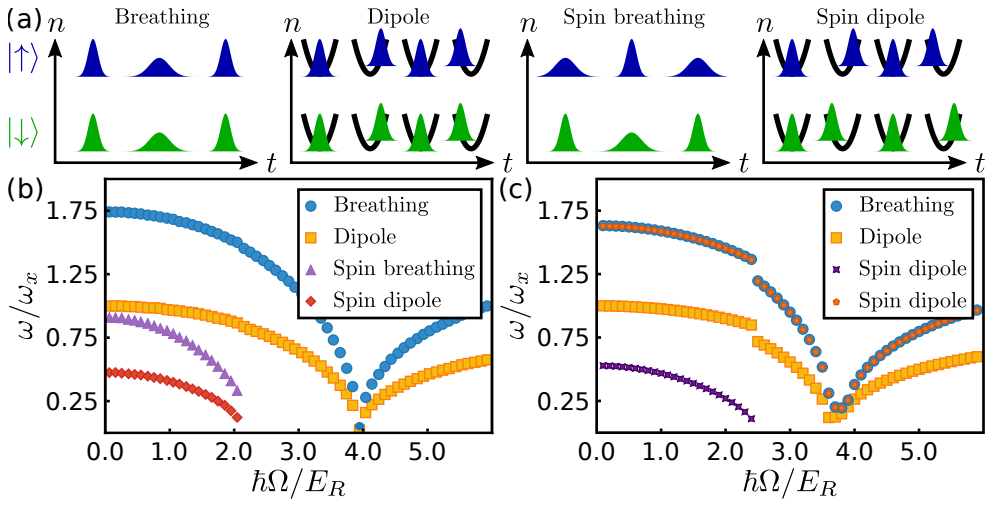

Figure 6.9: (a) Collective modes for the two spin components. The breathing mode corresponds to in phase breathing, the dipole mode corresponds to in phase centre of mass oscillations, the spin breathing mode corresponds to out of phase breathing, and the spin dipole mode corresponds to out of phase centre of mass oscillations. Density modulations have been omitted for clarity. (b) Collective mode frequencies of a Raman coupled BEC determined by Chen *et al.* [328] by solving the Bogoliubov de Genes equations. The numerical values have been taken from Figure 1 in Ref. [328]. (c) Collective mode frequencies of a Raman coupled BEC determined by Geier *et al.* [307] by numerically solving the coupled Gross-Pitaevskii equations. The numerical values have been taken from Figure 1 in Ref. [307].

phases by numerically solving the Bogoliubov de Genes equations [328]. The two lowest energy density modes are the dipole mode and the breathing mode. They are characterised by oscillations in the observables $\langle x\rangle = \int x n_{1\mathrm{D}}(x)\mathrm{d}x/N$ and $\langle x^2\rangle = \int (x-\langle x\rangle)^2 n_{1\mathrm{D}}(x)\mathrm{d}x/N$ and are illustrated in Fig. 6.9(a). Some of the numerical results of Chen *et al.* [328] are shown in Fig. 6.9(b).

For the parameters used in the calculations of Chen *et al.* [328], the frequencies of the dipole and breathing modes decrease monotonically from $\omega_D/\omega_x = 1$ and $\omega_B/\omega_x = \sqrt{3}$ at $\hbar\Omega/E_R = 0$ to $\omega_D/\omega_x = \omega_B/\omega_x = 0$ at $\hbar\Omega/E_R = 4$ before increasing into the single minimum regime with $\omega_B > \omega_D$ for all values of $\hbar\Omega/E_R$. In addition, two spin modes, the spin dipole mode and the spin breathing mode which are also illustrated in Fig. 6.9(a), corresponding to the observables $\langle x\rangle_\uparrow - \langle x\rangle_\downarrow$ and $\sqrt{\langle x^2\rangle_\uparrow} - \sqrt{\langle x^2\rangle_\downarrow}$ where $\langle x\rangle_\sigma = \int x|\phi_\sigma|^2\mathrm{d}^3\mathbf{r}/N_\sigma$ and $\langle x^2\rangle_\sigma = \int (x-\langle x\rangle_\sigma)^2 |\phi_\sigma|^2\mathrm{d}^3\mathbf{r}/N_\sigma$ for $\sigma = \uparrow,\downarrow$ start from $\omega_{SD} < \omega_D$ and $\omega_{SB} < \omega_B$ and vanish outside of the stripe phase. Finally, a near zero energy mode exists in the stripe phase, corresponding to the translation of the stripes [163, 309].

Geier *et al.* have numerically investigated some of the collective modes in a two dimensional BEC with $a_{\uparrow\downarrow} = a_{\downarrow\downarrow} = 100a_0$, $a_{\uparrow\downarrow} = 60a_0$, $N = 10^4$, $\hbar\delta_0/E_R = 0$, and the mass of ^{87}Rb by numerically solving the time-dependent equations of motion after removing various perturbing potentials which were applied during the calculation

of the groundstate [307]. The numerical results of Geier *et al.* [307] are shown in Fig. 6.9(c).

There are a number of differences between the results of Chen *et al.* [328] and Geier *et al.* [307]. A perturbation designed to excite the breathing mode was found to excite the breathing mode with $\omega_B/\omega_x \approx 1.6$ at $\hbar\Omega/E_R = 0$ and also to excite the spin dipole mode with two frequencies, ω_B and ω_{SD}, in the stripe phase and a single frequency, ω_B, in the plane wave and single minimum phases. Geier *et al.* [307] observed a larger jump in the breathing and dipole mode frequencies at the stripe phase to plane wave phase transition. Finally, the dipole and breathing modes did not go to zero at $\hbar\Omega/E_R = 4$ and instead reached a nonzero minimum frequency with $\hbar\Omega/E_R < 4$.

The observation of a nonzero minimum frequency is consistent with the experimental results of Zhang *et al.* [281] and the apparent discrepancy with the results of Chen *et al.* [328] can be explained by the difference in trapping potentials and atom numbers. The configuration of Geier *et al.* [307] corresponds to a significantly higher density than that of Chen *et al.* [328] and therefore results in a stronger shift in the plane wave phase to single minimum phase transition, as illustrated by variational calculations [168, 288, 309]. The difference in breathing frequency at $\hbar\Omega/E_R = 0$ can also be explained by the difference in density.

Ehrenfest Approach

To understand the dynamics of the spin dipole mode and the dependence of oscillation frequencies on Ω, we can employ the zero order mixture picture as well as the Ehrenfest theorem for the equations of motion of $\langle x\rangle_l = \int x|\varphi_l'|^2 \mathrm{d}^3\mathbf{r}/N_l$ where $l = 1, 2$ as was recently shown for mixtures of ^{41}K and ^{87}Rb [334, 335]. Assuming $\langle x^m\rangle_\uparrow \approx \langle x^m\rangle_2$ and $\langle x^m\rangle_\downarrow \approx \langle x^m\rangle_1$ for $m \in \mathbb{N}$, the results for the mixture picture can be applied to understand the behaviour of the bare spin components by following the method developed in Refs. [334, 335]. As a starting point, we take the mean-field equations of motion for the zero order mixture picture from Eq. 6.24. We assume $\hbar\delta_0/E_R = 0$ which means $k_1 = -k_2 = k_R\sqrt{1 - [\hbar\Omega/(4E_R)]^2}$, $m_1^* = m_2^* = 1/\left(k_1/k_R\right)^2 \equiv m^*$, $g_{ll} = \left[g_{\uparrow\uparrow}\left(1 - k_l/k_R\right)^2 + g_{\downarrow\downarrow}\left(1 + k_l/k_R\right)^2 + 2g_{\uparrow\downarrow}\left(1 - k_l^2/k_R^2\right)\right]/4$, $g_{12} = g_{\uparrow\downarrow} + \left(g_{\uparrow\uparrow} + g_{\downarrow\downarrow}\right)\left[\hbar\Omega/(4E_R)\right]^2/2$, and $\Delta/E_R = 0$.

For a state-independent trapping potential, $V(\mathbf{r}) = m\left(\omega_x^2x^2 + \omega_y^2y^2 + \omega_z^2z^2\right)/2$, each of the pseudospin components sees an effective potential given by $V_{\mathrm{tot},l}(\mathbf{r}, t) = V(\mathbf{r}) + g_{ll}|\varphi_l'(\mathbf{r}, t)|^2 + g_{12}|\varphi_p'(\mathbf{r}, t)|^2$ for $l, p = 1, 2$ with $p \neq l$. Let $\delta x_l = \langle x\rangle_l$. The Ehrenfest theorem tells us that expectation values follow classical laws so we have [335]

$$\begin{aligned}\partial_t^2\delta x_l &= -\langle\partial_x V_{\mathrm{tot},l}\rangle_l/(mm^*)\\ &= -\omega_x'^2\delta x_l - \frac{g_{ll}}{mm^*N_l}\int|\varphi_l'|^2\partial_x|\varphi_l'|^2\mathrm{d}^3\mathbf{r} - \frac{g_{12}}{mm^*N_l}\int|\varphi_l'|^2\partial_x|\varphi_p'|^2\mathrm{d}^3\mathbf{r}\end{aligned} \tag{6.33}$$

where we have defined $\omega_x' = \omega_x/\sqrt{m^*}$. Note that $\int|\varphi_l'|^2\partial_x|\varphi_l'|^2\mathrm{d}^3\mathbf{r} = |\varphi_l'|^4|_{-\infty}^{\infty} - \int|\varphi_l'|^2\partial_x|\varphi_l'|^2\mathrm{d}^3\mathbf{r} \Rightarrow \int|\varphi_l'|^2\partial_x|\varphi_l'|^2\mathrm{d}^3\mathbf{r} = 0$. Let $n_{l0} = |\varphi_l'(\mathbf{r}, 0)|^2$, assuming small am-

plitude and rigid oscillations we have $|\varphi_l'(\mathbf{r},t)|^2 \approx n_{l0} - \delta x_l \partial_x n_{l0}$ [335] so

$$\begin{aligned}\int |\varphi_l'|^2 \partial_x |\varphi_p'|^2 \mathrm{d}^3\mathbf{r} &\approx \int \left(n_{l0} - \delta x_l \partial_x n_{l0}\right) \partial_x \left(n_{p0} - \delta x_p \partial_x n_{p0}\right) \mathrm{d}^3\mathbf{r} \\ &= -\delta x_l \int \partial_x n_{l0} \partial_x n_{p0} \mathrm{d}^3\mathbf{r} - \delta x_p \int n_{l0} \partial_x^2 n_{p0} \mathrm{d}^3\mathbf{r}\end{aligned} \tag{6.34}$$

where we have assumed that n_{l0} and n_{p0} are even functions. We have $\int n_{l0}\partial_x^2 n_{p0}\mathrm{d}^3\mathbf{r} = n_{l0}\partial_x n_{p0}|_{-\infty}^{\infty} - \int \partial_x n_{l0}\partial_x n_{p0}\mathrm{d}^3\mathbf{r} = -\int \partial_x n_{l0}\partial_x n_{p0}\mathrm{d}^3\mathbf{r}$ so

$$\int |\varphi_l'|^2 \partial_x |\varphi_p'|^2 \mathrm{d}^3\mathbf{r} \approx -\left(\delta x_l - \delta x_p\right) \int \partial_x n_{l0} \partial_x n_{p0} \mathrm{d}^3\mathbf{r}. \tag{6.35}$$

Let $\eta_l = g_{12} I/(m m^* N_l)$ where $I = \int \partial_x n_{l0}\partial_x n_{p0}\mathrm{d}^3\mathbf{r}$ then $\partial_x^2 \delta x_l \approx -\omega_x'^2 \delta x_l - \eta_l \delta x_p + \eta_l \delta x_l$ which we can express in matrix form as

$$\frac{\partial^2}{\partial t^2}\begin{pmatrix}\delta x_1 \\ \delta x_2\end{pmatrix} \approx -\begin{pmatrix}\omega_x'^2 - \eta_1 & \eta_1 \\ \eta_2 & \omega_x'^2 - \eta_2\end{pmatrix}\begin{pmatrix}\delta x_1 \\ \delta x_2\end{pmatrix} \equiv -M_{\mathrm{dipole}}\begin{pmatrix}\delta x_1 \\ \delta x_2\end{pmatrix}. \tag{6.36}$$

To evaluate the integral, I, we need to determine n_{10} and n_{20}. We can solve Eq. 6.24 in imaginary time to determine φ_l' for a given value of $\hbar\Omega/E_R$. For an analytic estimate of I, we use the single mode approximation in the Thomas-Fermi regime. We write the groundstate mean-field wavefunctions in polar form, $\varphi_l' = \sqrt{n_{0l}}\exp\left(i\theta_{s,l}\right)$ with $\theta_{s,l} = \theta_{0,l} - \mu_l t/\hbar$ where μ_l is the chemical potential of pseudospin l. We have $\theta_s = \theta_{s,1} - \theta_{s,2} = \theta_{0,1} - \theta_{0,2} + (\mu_2 - \mu_1)t/\hbar$ which means that the stripes translate at a rate of $(\mu_2 - \mu_1)/\hbar$.

Assuming that the stripes are stationary in the groundstate, we must have $\mu_1 = \mu_2 \equiv \mu$ so the mean-field equations of motion reduce to

$$\mu\varphi_1' = \left[-\frac{\hbar^2}{2mm^*}\frac{\partial^2}{\partial x^2} - \frac{\hbar^2}{2m}\nabla_\perp^2 + V(\mathbf{r}) + g_{11}|\varphi_1'|^2 + g_{12}|\varphi_2'|^2\right]\varphi_1'$$

and

$$\mu\varphi_2' = \left[-\frac{\hbar^2}{2mm^*}\frac{\partial^2}{\partial x^2} - \frac{\hbar^2}{2m}\nabla_\perp^2 + V(\mathbf{r}) + g_{22}|\varphi_2'|^2 + g_{12}|\varphi_1'|^2\right]\varphi_2'. \tag{6.37}$$

Using the single mode approximation, we have $n_{10} = (1+S)\,n_0/2$ and $n_{20} = (1-S)\,n_0/2$ where $S = \left(g_{22} - g_{11}\right)/\left(g_{11} + g_{22} - 2g_{12}\right)$. We are left with one equation which we can solve using the Thomas-Fermi approximation to yield

$$n_0 = \frac{\mu}{\beta}\max\left[1 - \left(\frac{x}{\sigma_{T,x}}\right)^2 - \left(\frac{y}{\sigma_{T,y}}\right)^2 - \left(\frac{z}{\sigma_{T,z}}\right)^2, 0\right] \tag{6.38}$$

where $\beta = \left(g_{11}g_{22} - g_{12}^2\right)/\left(g_{11} + g_{22} - 2g_{12}\right)$ and $\sigma_{T,j} = \sqrt{2\mu/(m\omega_j^2)}$ for $j = x, y, z$. The normalisation condition, $\int n_0 \mathrm{d}^3\mathbf{r} = N$, gives us

$$\mu = \left(\frac{15\beta m^{3/2}\bar{\omega}^3 N}{16\sqrt{2}\pi}\right)^{2/5} \tag{6.39}$$

where $\bar{\omega}^3 = \omega_x\omega_y\omega_z$.

So, we have $I = (1-S^2)m\omega_x^2 N/(4\beta) \Rightarrow \eta_l = (1-S^2)g_{12}N\omega_x'^2/(4\beta N_l)$. The eigenvalues of the $M_{\rm dipole}$ are $\omega_x'^2$ and $\omega_x'^2 - \eta_1 - \eta_2 = \omega_x'^2\,(1-g_{12}/\beta)$ with corresponding eigenvectors $(1,\,1)^T$ and $[1,\,-(g_{11}-g_{12})/(g_{22}-g_{12})]^T$. The first eigenmode is the in phase dipole mode with frequency $\omega_D = \omega_x'$ and the second eigenmode corresponds to the out of phase spin dipole mode with the phase difference between δx_1 and δx_2 equal to π when $g_{\uparrow\uparrow} = g_{\downarrow\downarrow}$. The frequency of the spin dipole mode is $\omega_{SD} = \omega_x'\sqrt{1-g_{12}/\beta}$.

Since we have assumed rigid oscillations, the breathing of the BECs has been neglected in the above derivation of the dipole and spin dipole frequencies. A BEC will be in the weakly interacting regime for low densities and the Thomas-Fermi regime for higher densities. It has been shown that for a single-component BEC in a cylindrical trap, the axial breathing frequency is $\omega_B = \sqrt{3}\omega_x$ in the weakly interacting regime and $\omega_B = \sqrt{2.5}\omega_x \approx 1.58\omega_x$ in the Thomas-Fermi regime [336] with similar results for a two dimensional trap [337]. For a two-component BEC with symmetric interactions, $g_{\uparrow\uparrow} = g_{\downarrow\downarrow} \equiv g$, and balanced atom number, the groundstate density profiles are identical and for in phase modes (the dipole mode and the breathing mode), the system can be described by an effective single-component equation of motion with interaction parameter $(g + g_{\uparrow\downarrow})/2$.

Assuming that the $\hbar\Omega/E_R = 0$ results apply to the pseudospin mixture, we can infer that the breathing frequency is given by $\omega_B = \sqrt{2.5}\omega_D$ in the Thomas-Fermi regime and $\omega_B = \sqrt{3}\omega_D$ in the weakly interacting regime. Since the dipole frequency, ω_D, does not depend on the density profiles of the pseudospin components we do not need to calculate the weakly interacting density profiles to determine ω_D and ω_B. We can also see that if the BECs are breathing and translating at the same time then the breathing frequency would appear as a driving force acting on the spin dipole mode through the integral, I, which explains the beating observed in numerical simulations by Geier *et al.* [307]. In the zero order mixture picture, the spin dipole mode would not be excited by a change in trap frequency without also moving the trap but this is accounted for by next order corrections to the zero order mixture picture which couple the density and the current density, as in the effective chiral BF model.

Numerical Study of Collective Modes

In order to investigate the various collective modes numerically, we construct a series of spin-dependent perturbations, $V_{\rm pert,\uparrow}$ and $V_{\rm pert,\downarrow}$, given in Tab. 6.1. For convenience, we label the perturbations as I, II, III, and IV. Perturbation I excites the breathing mode by applying an equal compression to both bare spin components. Perturbation II excites the dipole mode by displacing the two bare spin components by the same amount. Perturbation III excites the spin dipole mode by displacing the two bare spin components in opposite directions. Perturbation IV excites the spin breathing mode by compressing one bare spin component while decompressing the other. The dynamics are simulated by calculating the groundstate in the presence of the trapping potential $V(\mathbf{r}) = m\omega_x^2x^2/2 + m\omega_r^2(y^2+z^2)/2$ plus one of the perturbations in imaginary time and then simulating the real time evolution of the system after

Table 6.1: Spin dependent perturbations which are added to the potential $V(\mathbf{r}) = m\omega_x^2 x^2/2 + m\omega_r^2(y^2+z^2)/2$ in order to excite collective modes in numerical simulations. The perturbations correspond to I breathing, II dipole, III spin dipole, and IV spin breathing.

Label	$V_{\mathrm{pert},\uparrow}$	$V_{\mathrm{pert},\downarrow}$
I	$\frac{1}{2}m\Delta\omega_x\left(\Delta\omega_x + 2\omega_x\right)x^2$	$\frac{1}{2}m\Delta\omega_x\left(\Delta\omega_x + 2\omega_x\right)x^2$
II	$\frac{1}{2}m\omega_x^2 x_0\left(x_0 - 2x\right)$	$\frac{1}{2}m\omega_x^2 x_0\left(x_0 - 2x\right)$
III	$\frac{1}{2}m\omega_x^2\frac{x_0}{2}\left(\frac{x_0}{2} + x\right)$	$\frac{1}{2}m\omega_x^2\frac{x_0}{2}\left(\frac{x_0}{2} - x\right)$
IV	$-\frac{1}{2}m\Delta\omega_x^2 x^2$	$\frac{1}{2}m\Delta\omega_x^2 x^2$

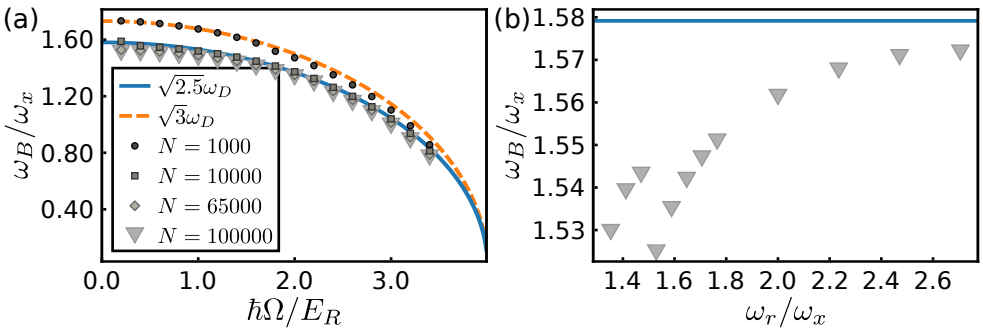

Figure 6.10: (a) Breathing frequency, ω_B, as a function of Rabi frequency for various values of N. The solid blue line and dashed orange line show the zero order mixture picture estimates of $\omega_B = \sqrt{2.5}\omega_D$ and $\omega_B = \sqrt{3}\omega_D$, respectively. (b) Breathing frequency as a function of radial trapping frequency for $N = 10^5$ and $\hbar\Omega/E_R = 0.2$. The solid blue line shows the zero order mixture picture estimate, $\omega_B = \sqrt{2.5}\omega_D$.

removing the perturbation.

Figure 6.10(a) shows the numerically determined values of ω_B corresponding to solving Eq. 5.20 for various values of N with $\hbar\delta_0/E_R = 0$ for an atom with the mass of ^{39}K with $a_{\uparrow\uparrow} = a_{\downarrow\downarrow} = 100a_0$, $a_{\uparrow\downarrow} = 60a_0$, $\omega_y/(2\pi) = \omega_z/(2\pi) \equiv \omega_r/(2\pi) = 130$ Hz, and $\omega_x/(2\pi) = 85$ Hz after removing the perturbation I in Tab. 6.1 with $\Delta\omega_x/(2\pi) = -15$ Hz. To extract ω_B from the numerical data we evaluate $\sqrt{\langle x^2\rangle}$ and fit the result with a sinusoidal curve. For these simulations we employ the Bessel transform for the radial derivative and the radial grid is defined on the interval $(0, 9.63)$ μm with 2^4 grid points and the x-axis is discretised on 2^9 grid points with a grid spacing of 60.2 nm.

We can see that all of the numerical data points are well approximated by one of the two curves $\omega_B = \sqrt{3}\omega_D$ ($N = 10^3$) and $\omega_B = \sqrt{2.5}\omega_D$ ($N = 10^4$, $N = 6.5 \times 10^4$, and $N = 10^5$). For $N = 10^5$ the numerical values are slightly below $\omega_B = \sqrt{2.5}\omega_D$, this is due to dynamic coupling to the radial breathing mode due to the small ratio of ω_r/ω_x [336]. In Fig. 6.10(b) the breathing frequency is plotted as a function of ω_r for

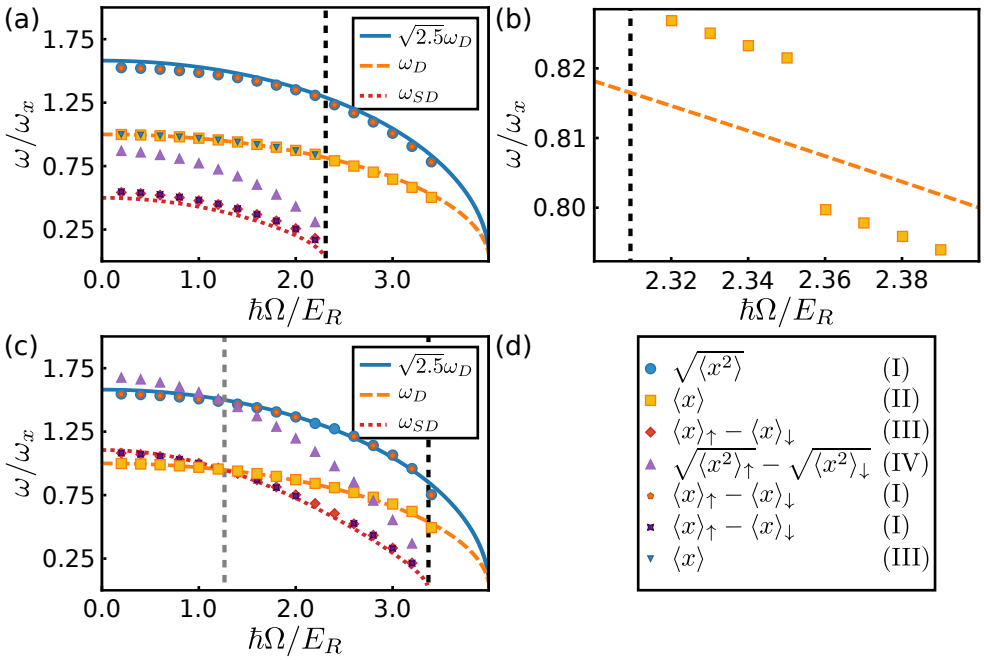

Figure 6.11: (a) Collective mode frequencies corresponding to the parameters of Fig. 6.10(a) ($a_{\uparrow\uparrow} = a_{\downarrow\downarrow} = 100a_0$, $a_{\uparrow\downarrow} = 60a_0$, $N = 10^5$). The dashed black line indicates the stripe phase to plane wave phase transition predicted by the zero order mixture picture. The solid blue line, dashed orange line and dotted red line show the frequencies of the breathing, dipole, and spin dipole modes predicted by the zero order mixture picture. (b) Yellow squares show the dipole mode frequency close to the stripe phase to plane wave phase transition. We see a small jump in frequency at the phase transition which occurs at a slightly higher Rabi frequency than that predicted by the zero order mixture picture due to density-dependent corrections. (c) Collective mode frequencies for $a_{\uparrow\uparrow} = a_{\downarrow\downarrow} = 30a_0$ and $a_{\uparrow\downarrow} = -3a_0$. The spin excitation frequencies cross the density excitation frequencies when the sign of g_{12} changes (dashed grey line). (d) Key of the markers in panels (a)-(c) and the observables that they correspond to. The perturbations from Tab. 6.1 are given in parentheses.

$N = 10^5$ and $\hbar\Omega/E_R = 0.2$. We can see that that ω_B/ω_x increases towards $\sqrt{2.5}\omega_D$ as ω_r/ω_x is increased with a near resonance in the dynamic coupling for $\omega_r/\omega_x \approx \sqrt{2.5}$. In order to completely neglect the dynamic coupling we should have $\omega_r/\omega_x > 10$ [336].

In Fig. 6.11(a) the frequencies corresponding to various observables are plotted for the parameters of Fig. 6.10(a) ($N = 10^5$). The perturbation parameters are $\Delta\omega_x/(2\pi) = -15$ Hz and $x_0 = 0.385$ μm. We see good agreement with the analytic expressions for $\omega_B = \sqrt{2.5}\omega_D$, ω_D, and ω_{SD} corresponding to the zero order mixture picture and the spin breathing mode behaves in a qualitatively similar way to the spin dipole mode. As shown by Geier *et al.* [307], the breathing perturbation, I, excites the spin dipole mode with two frequencies, ω_{SD} and ω_B. When we excite the spin dipole mode using the spin dipole perturbation, III, we see a single frequency oscillation, consistent with the zero order mixture picture. The dipole mode is also excited by the

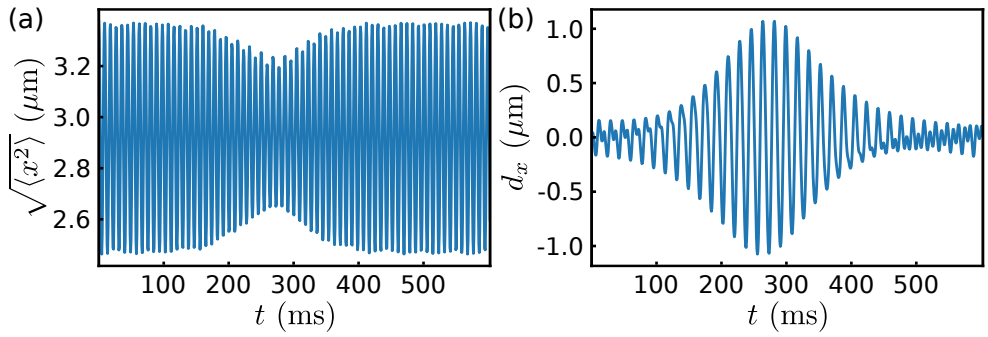

Figure 6.12: (a) The width of the total density, $\sqrt{\langle x^2 \rangle}$, and (b) the separation between the two spin components, d_x, corresponding to the parameters of Fig. 6.11(c) with $\hbar\Omega/E_R = 2.2$. There is clear evidence of energy transfer between the modes.

spin dipole perturbation because of higher order corrections to the mixture picture which mean that the second eigenvector of M_{dipole} differs from $(1, -1)^T$. Note that the spin breathing perturbation, IV, alters the groundstate ratio of atoms in the two pseudospins because the differential compression makes it energetically favourable to put more atoms into the less compressed state. Removing the perturbing potential resets the groundstate ratio to $S = 0$ so the imbalance which remains during the computation of real time dynamics corresponds to a differential mean-field shift. I have verified that forcing the bare spin polarisation to zero in the imaginary time evolution has a negligible effect on the extracted frequencies.

Figure 6.11(b) shows the dipole mode from Fig. 6.11(a) close to the stripe phase to plane wave phase transition. The black dashed line indicates the value of Ω_c according to the zero order mixture picture. We can see a small density-dependent shift in Ω_c, corresponding to the predictions of Li *et al.* [168], and a small jump in the oscillation frequencies at the phase transition. The jump in oscillation frequency is significantly smaller than that observed by Geier *et al.* [307] and this is likely related to the atomic density since we have used a density corresponding to a similar atom number and trap geometry as used for the experiments in Ch. 7 which is smaller than the density used by Geier *et al.* [307]. The jump in oscillation frequencies at the phase transition has been attributed to the first order nature of the stripe phase to plane wave phase transition [307] and is not captured by the zero order mixture picture.

In Fig. 6.11(c) we repeat the calculations of Fig. 6.11(a) with the scattering lengths changed to $a_{\uparrow\uparrow} = a_{\downarrow\downarrow} = 30a_0$ and $a_{\uparrow\downarrow} = -3a_0$. when $g_{\uparrow\downarrow}$ is negative, the zero order mixture picture predicts $\omega_{SD} = \omega_D$ when $\hbar\Omega/E_R = 4\sqrt{-2g_{\uparrow\downarrow}/(g_{\uparrow\uparrow} + g_{\downarrow\downarrow})}$. We see that the spin dipole frequency and spin breathing frequency match the dipole frequency and breathing frequency near the predicted value of $\hbar\Omega/E_R = 1.265$ with the spin excitations at higher frequency than the density excitations for smaller Rabi frequencies. The spin excitation frequencies shift upwards (downwards) when g_{12} is negative (positive) because each BEC sees an effectively tighter (looser) trap due to the attractive (repulsive) potential imposed by the other BEC [338]. The attractive interaction between the two bare components inhibits the excitation of the dipole mode

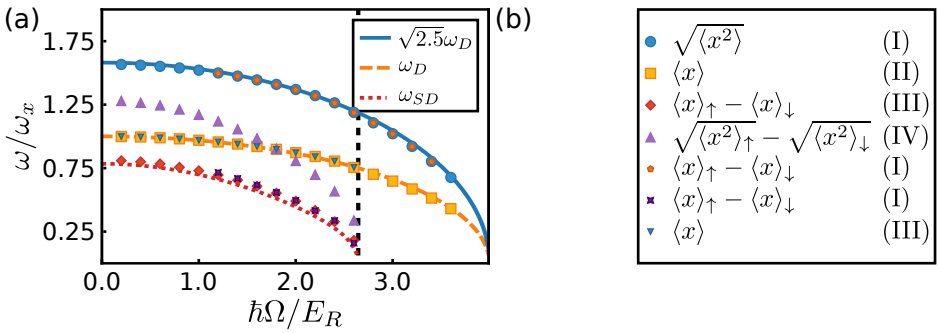

Figure 6.13: (a) Collective mode frequencies of ^{41}K with $a_{\uparrow\uparrow} = 102.0a_0$, $a_{\downarrow\downarrow} = 64.3a_0$, $a_{\uparrow\downarrow} = 18.5a_0$, and $N = 10^5$. The dashed black line indicates the stripe phase to plane wave phase transition predicted by the zero order mixture picture. The solid blue line, dashed orange line and dotted red line show the frequencies of the breathing, dipole, and spin dipole modes predicted by the zero order mixture picture. (b) Key of the markers in panel (a) and the observables that they correspond to. The perturbations from Tab. 6.1 are given in parentheses.

by perturbation III.

The width of the total density, $\sqrt{\langle x^2\rangle}$, and the separation between the spin components, d_x, corresponding to the parameters of Fig. 6.11(c) with $\hbar\Omega/E_R = 2.2$ where $\omega_B \approx 2\omega_{SD}$ are shown in Fig. 6.12(a) and Fig. 6.12(b), respectively. We can see evidence of coupling between the breathing mode and the spin dipole mode manifesting as energy transfer between the two modes [309] in addition to the beating observed by Geier *et al.* [307]. Modelling of this energy transfer process goes far beyond the applicability of the zero order mixture picture and modes which are subject to significant coupling are excluded from the numerical data shown here.

As with the groundstate, one of the strengths of the zero order mixture picture is the ability to predict dynamic properties without the assumption $g_{\uparrow\uparrow} = g_{\downarrow\downarrow}$. Figure 6.13 shows the numerically determined collective mode frequencies for ^{41}K with $a_{\uparrow\uparrow} = 102.0a_0$, $a_{\downarrow\downarrow} = 64.3a_0$, $a_{\uparrow\downarrow} = 18.5a_0$, $\hbar\delta_0/E_R = 0$, $N = 10^5$, $\omega_x/(2\pi) = 65$ Hz, and $\omega_r/(2\pi) = 130$ Hz. For these simulations we employ the Bessel transform for the radial derivative where the radial grid is defined on the interval $(0, 9.39)$ μm with 2^4 grid points and the x-axis is discretised on 2^9 grid points with a grid spacing of 58.7 nm. We excite the collective modes using the perturbations of Tab. 6.1 with $\Delta\omega_x/(2\pi) = 15$ Hz and $x_0 = 0.376$ μm. The numerical simulations show resonant coupling between the breathing mode and the spin dipole mode for $\hbar\Omega/E_R \leq 1$ but the predictions of the zero order mixture picture are in overall good agreement with the numerical data.

It has been shown that the two Goldstone modes of the supersolid stripe phase are each associated to either spin or density excitations and that the zero energy translation of the stripes corresponds to the spin branch through the relative phase of the two components [163]. Geier *et al.* [308] have pointed out that the spin dipole oscillation is accompanied by changes in the fringe spacing. Here, we inspect the

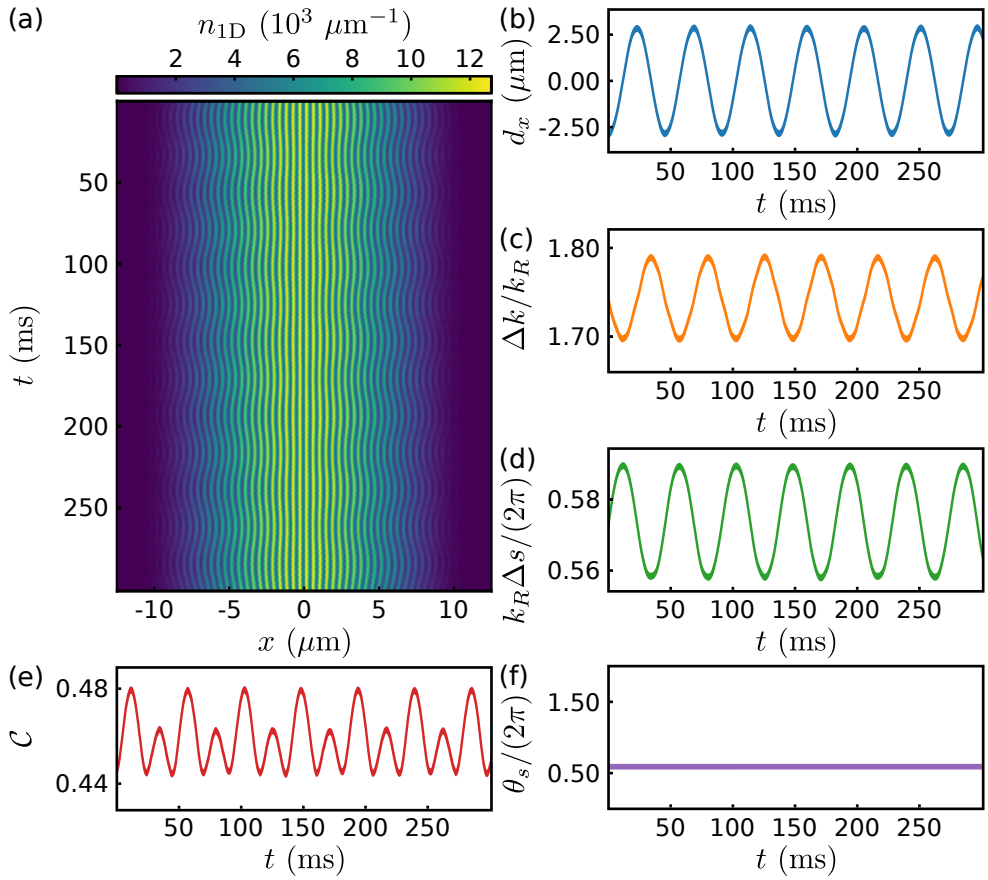

Figure 6.14: (a) Integrated density profile, n_{1D}, corresponding to perturbation III, which excites the spin dipole mode, in Fig. 6.11(a) with $\hbar\Omega/E_R = 2$. (b) The separation between spin components, $d_x \equiv \langle x\rangle_\uparrow - \langle x\rangle_\downarrow$. (c) The dimensionless difference in group quasimomentum of the two pseudospin components, $\Delta k/k_R \equiv (k_{1,G} - k_{2,G})/k_R$. (d) The scaled fringe spacing, $k_R\Delta s/(2\pi)$, which scales as $1/\Delta k$. (d) The fringe contrast, $\mathcal{C}$, oscillates in time with two frequencies which are the spin dipole frequency and double the spin dipole frequency corresponding to an amplitude (Higgs) mode. (e) The fringe phase, θ_s, is constant in time.

dynamics associated to the spin perturbation operators in more detail and look for Goldstone and Higgs (amplitude) modes.

Figure 6.14(a) shows the integrated density profile, n_{1D}, corresponding to perturbation III in Fig. 6.11(a) for $\hbar\Omega/E_R = 2$. We can see the periodic changes in the fringe spacing in the total density profile but the fringes do not slide. In Fig. 6.14(b)-(f) the values of the separation between spin components, $d_x \equiv \langle x\rangle_\uparrow - \langle x\rangle_\downarrow$, the difference in group quasimomentum of the two pseudospin components[2], $\Delta k \equiv k_{1,G} - k_{2,G}$, the

[2]Here, the symbols $k_{1,G}$ and $k_{2,G}$ are defined in the same way as k_1 and k_2 in Eqs. 6.30 and 6.31 but now they do not correspond to the groundstate values defined by $k_l/k_R = -\tilde{\delta}(k_l)/\tilde{\Omega}(k_l)$ because we have dynamics.

fringe spacing, Δs, the fringe contrast, $\mathcal{C}$, and the fringe phase, θ_s, corresponding to Fig. 6.14(a) are plotted. To extract the fringe spacing, fringe contrast, and fringe phase we fit $n_{1\mathrm{D}}$ with Eq. 6.32. We can see that the amplitude of d_x is not equal to x_0 because of the mixing of the spin-dependent potentials, as seen in Eq. 6.26, and the repulsion between the pseudospin components. The difference of the momenta of the two pseudospin components oscillates at the same frequency as d_x with a phase shift of $\pi/2$, as we would expect. From Eq. 6.20, we know that $\Delta s \propto 1/\Delta k$ resulting in an oscillation of Δs at the same frequency as d_x with a phase shift of π with respect to Δk.

We can also see oscillations in the amplitude, corresponding to a Higgs mode [106, 161, 164], which results from the changing spatial overlap of the two pseudospin components as well as the changing projection of each of the two pseudo spin components onto the bare spins. The spatial overlap oscillates between maximum and minimum twice for every period of d_x while the spin projections oscillate approximately sinusoidally with the same frequency as d_x. Thus, we see the beat of the spin dipole frequency and double the spin dipole frequency in the oscillations of $\mathcal{C}$. The relative phase of the two components does not evolve during the dynamics and the fringes therefore do not slide.

Figure 6.15(a) shows the integrated density profile corresponding to perturbation IV in Fig. 6.11(a) for $\hbar\Omega/E_R = 2$. This perturbation corresponds to the spin breathing mode and here we can see that the fringes slide without changing spacing. In Fig. 6.15(b)-(f) the values of the difference in widths of the bare spin components, $d_\sigma \equiv \sqrt{\langle x^2\rangle_\uparrow} - \sqrt{\langle x^2\rangle_\downarrow}$, the difference in group quasimomentum of the two pseudospin components, $\Delta k \equiv k_{1,G} - k_{2,G}$, the fringe spacing, Δs, the fringe contrast, $\mathcal{C}$, and the fringe phase, θ_s, corresponding to Fig. 6.15(a) are plotted. In this case, since there is no spin dipole mode, the values of Δk and Δs are static. The Higgs mode is again present due to the changing spatial overlap of the components. Since the differential compression applied during the imaginary time evolution creates a population imbalance in the groundstate, there is a mean-field shift between the two components. That is, we have $\mu_1 \neq \mu_2$ and the fringes slide, corresponding to a Goldstone mode [160, 163].

If the bare state spin polarisation, P, is fixed to zero during the imaginary time evolution, the mean-field shift is not present upon removal of the perturbing potential and the fringes do not slide. Conversely, the Goldstone mode may be excited by forcing an out of equilibrium bare spin polarisation during the imaginary time evolution without applying a perturbation operator. These effects demonstrate that the sliding of the fringes is a direct consequence of a difference in the chemical potentials of the two dressed BECs.

6.5.2 Sound Propagation in the Stripe Phase

We have seen evidence of the collective Goldstone excitation [162] manifesting as a translation of the density modulations due to a spin excitations [163]. The stripe phase appears similar to supersolid-like states created in BECs inside optical cavities [106]

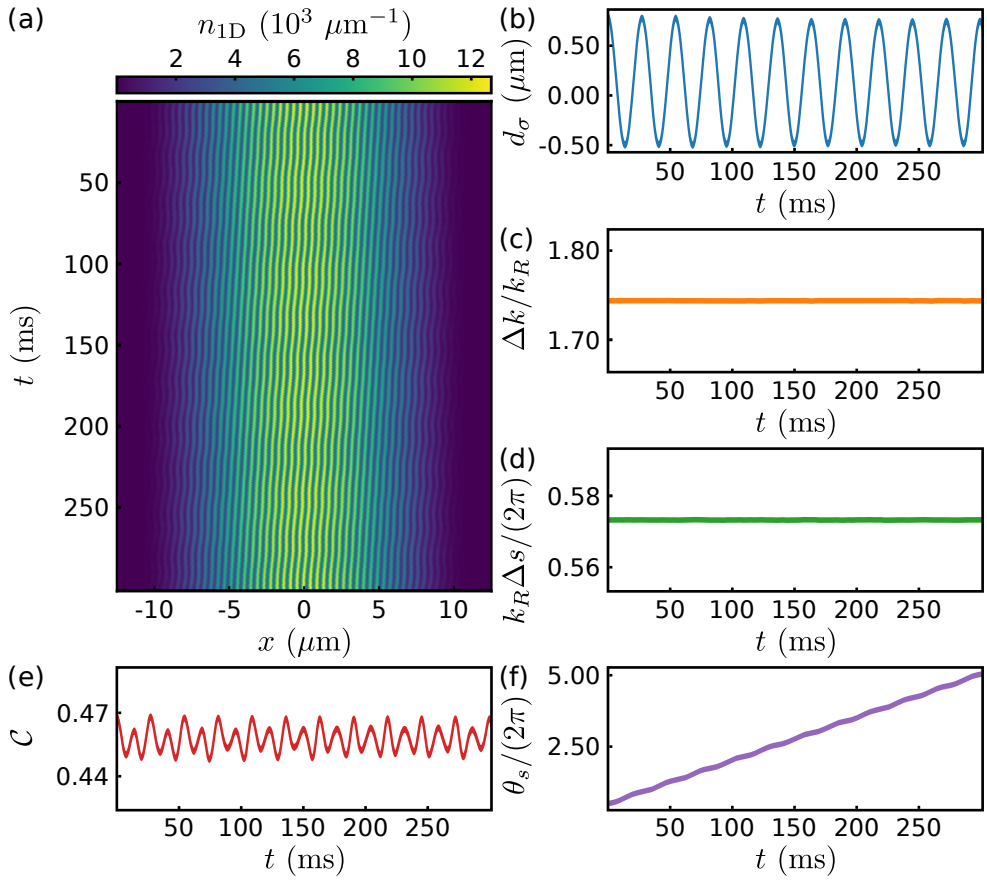

Figure 6.15: (a) Integrated density profile, n_{1D}, corresponding to perturbation IV, which excites the spin breathing mode, in Fig. 6.11(a) with $\hbar\Omega/E_R = 2$. (a) The difference in widths of the bare spin components, $d_\sigma \equiv \sqrt{\langle x^2\rangle_\uparrow} - \sqrt{\langle x^2\rangle_\downarrow}$. (b) The dimensionless difference in group quasimomentum of the two pseudospin components, $\Delta k/k_R \equiv (k_{1,G} - k_{2,G})/k_R$, (c) Since the dipole mode is not excited there are no dynamics in Δk and the scaled fringe spacing, $k_R\Delta s/(2\pi)$, is constant in time. (d) The fringe contrast, $\mathcal{C}$, oscillates due to the changing spatial overlap of the two components so there is a weak excitation of an amplitude (Higgs) mode. (e) The fringe phase, θ_s, evolves linearly in time which means the fringes translate with respect to the centre of mass corresponding to a Goldstone mode.

since the cavity system also has degeneracy in the fringe phase and both systems depend on light addressing the BEC. However, in the cavity system, interactions are global so there are no propagating sound modes [105, 325]. In contrast, the stripe phase has two Goldstone modes which each have an associated speed of sound [163], similarly to supersolids in dipolar systems [107, 159, 322]. In the stripe phase, the two speeds of sound correspond to the spin and density excitation branches [163]. In this section, I will numerically demonstrate sound propagation in the stripe phase.

The zero order mixture picture treats the stripe phase as an incoherent mixture of

two (nonorthogonal) BECs. This means that with $g_{\uparrow\uparrow} = g_{\downarrow\downarrow} \equiv g$ and $\hbar\delta_0/E_R = 0$ we have $m_1^* = m_2^* = 1/\{1 - [\hbar\Omega/(4E_R)]\} \equiv m^*$, $g_{11} = g_{22} = g + [\hbar\Omega/(4_E R)]^2 (g_{\uparrow\downarrow} - g)/2$, and $g_{12} = g_{\uparrow\downarrow} + [\hbar\Omega/(4E_R)]^2 g$. We can use the results of a spin mixture to predict the speeds of sound associated with the spin and density branches, c_s and c_d, as [169, 177, 317, 339]

$$\frac{m}{\hbar k_R} c_s = \sqrt{\frac{2m\bar{n}}{4E_R m m^*}(g_{11} - g_{12})}$$

and

$$\frac{m}{\hbar k_R} c_d = \sqrt{\frac{m\bar{n}}{4E_R m m^*}(g_{11} + g_{12})}. \tag{6.40}$$

Note that the nonorthogonality of the pseudospins in the zero order mixture picture is crucial here since although an incoherent spin mixture has two speeds of sound, there is normally no spontaneous translational symmetry breaking in such a system [340]. In an incoherent spin mixture both Goldstone modes are associated with gauge invariance and one of them becomes massive in the presence of RF coupling [340].

The speeds of sound estimated in Eq. 6.40 correspond to the low density limit of exact numerical calculations [327] and analytic estimates made through a perturbative treatment [163]. Since the stripe phase to plane wave phase transition corresponds to $g_{11} = g_{12}$ in the zero order mixture picture, we can see that the spin sound vanishes at the phase transition, as shown in previous works [163, 327].

To study the Goldstone modes numerically, we simulate a Raman dressed BEC of an atom with the mass of ^{39}K with $a_{\uparrow\uparrow} = a_{\downarrow\downarrow} = 100a_0$ and $a_{\uparrow\downarrow} = 60a_0$ in a trapping potential defined by

$$V_{\text{box}}(\mathbf{r}) = \begin{cases} 0, & |x| < \frac{L}{2} \text{ and } y^2 + z^2 < \frac{L}{2} \\ 8000E_R, & \text{else} \end{cases} \tag{6.41}$$

where $L = 30.8$ μm. We set $N = 2.295 \times 10^6$ corresponding to an average density of $\bar{n} = 10^{20}$ m^{-3}. We employ the Bessel transform for the radial derivative and the radial grid is defined on the interval $(0, 19.25)$ μm with 2^5 grid points and the x-axis is discretised on 2^{10} grid points with a grid spacing of 60.2 nm.

To create a phonon excitation in the BEC we calculate the groundstate in imaginary time in the presence of an additional potential such that [341]

$$V_{\text{perturbed}}(\mathbf{r}) = V_{\text{box}}(\mathbf{r}) + V_p \exp\left(-2\frac{x^2}{\sigma_p^2}\right) \tag{6.42}$$

and then compute the real time dynamics without the perturbation. To create an excitation in the spin, we additionally give spatial dependence to the Rabi frequency such that[3]

$$\Omega(x) = \Omega\left[1 + 0.1\exp\left(-2\frac{x^2}{\sigma_p^2}\right)\right]. \tag{6.43}$$

[3]This perturbation is not an obvious choice in an experimental setting and has been chosen because it excites the spin mode without exciting the density mode. Most experimentally realistic perturbations couple to both branches simultaneously due to the hybridisation of the spin and density branches in the stripe phase [163].

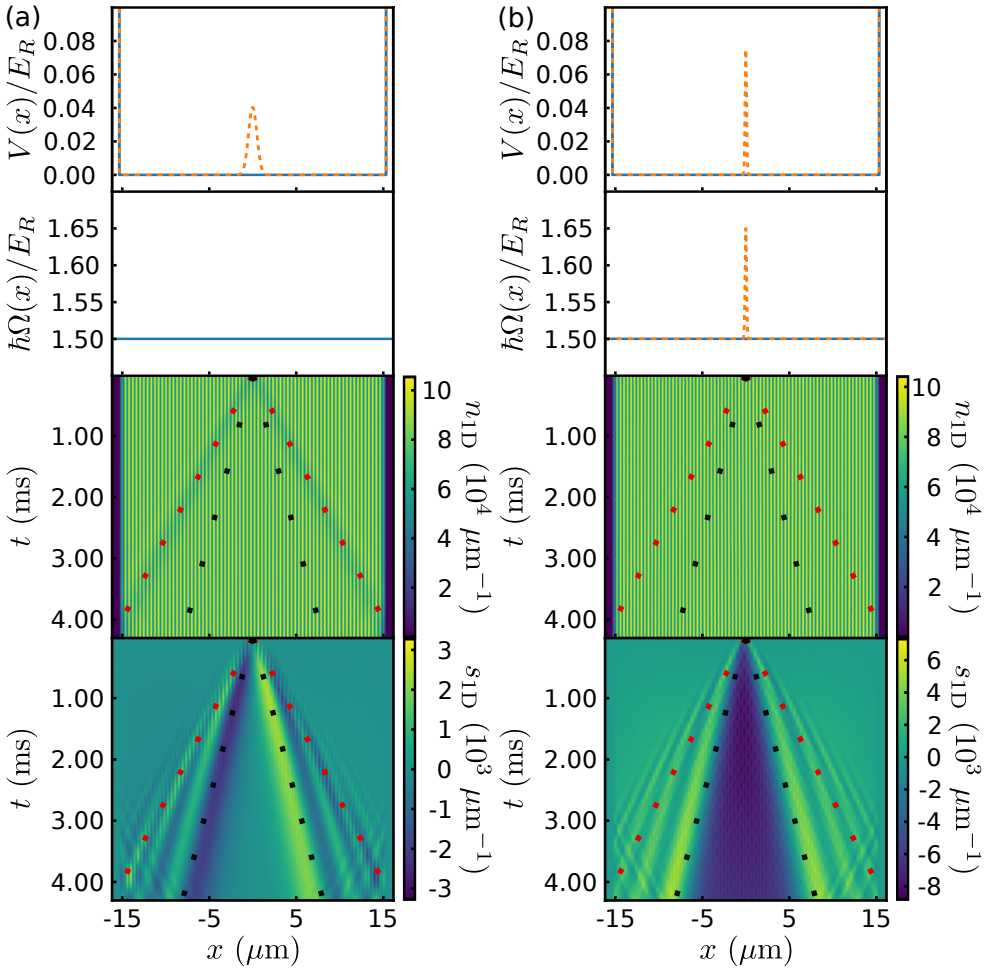

Figure 6.16: (Top panel) perturbed potential, $V(x) = V_{\text{perturbed}}(x, 0, 0)$, (dashed orange line) and unperturbed potential, $V(x) = V_{\text{box}}(x, 0, 0)$, (solid blue line). (Second panel) Rabi frequency, $\Omega(x)$. (Third panel) integrated density, n_{1D}. And (bottom panel) integrated spin density, s_{1D}, for (a) density excitation with $\hbar\Omega/E_R = 1.5$, $V_p/E_R = 0.04$, and $\sigma_p = 1$ μm and (b) spin excitation with $\hbar\Omega/E_R = 1.5$, $V_p/E_R = 0.075$, and $\sigma_p = \sqrt{2}/k_R$. The dotted red and black lines represent the density and spin speeds of sound, c_d and c_s, given in Eq. 6.40.

In Fig. 6.16(a) the integrated density, $n_{1D} = \int n(\mathbf{r})\mathrm{d}y\mathrm{d}z$, and integrated spin density, $s_{1D} = \int |\phi_\uparrow|^2 - |\phi_\downarrow|^2 \mathrm{d}y\mathrm{d}z$, are shown for the density excitation with $\hbar\Omega/E_R = 1.5$, $V_p/E_R = 0.04$, and $\sigma_p = 1$ μm. The density propagation propagates at the density speed of sound, c_d, predicted in Eq. 6.40 and there are perturbations in the integrated spin density which are approximately bounded by c_d and c_s due to the hybridisation of spin and density excitations [163].

In Fig. 6.16(b) the integrated density, $n_{1D} = \int n(\mathbf{r})\mathrm{d}y\mathrm{d}z$, and integrated spin density, $s_{1D} = \int |\phi_\uparrow|^2 - |\phi_\downarrow|^2 \mathrm{d}y\mathrm{d}z$ are shown for the spin density excitation with

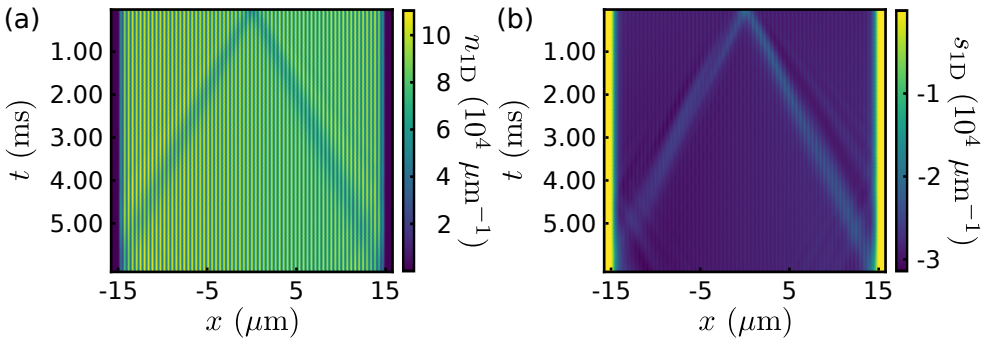

Figure 6.17: (a) Integrated density, n_{1D}, and (b) integrated spin density, s_{1D}, of ^{41}K with $a_{\uparrow\uparrow} = 102.0a_0$, $a_{\downarrow\downarrow} = 64.3a_0$, $a_{\uparrow\downarrow} = 18.5a_0$, $\hbar\Omega/E_R = 2$, and the same perturbation as Fig. 6.16(a). The density disturbance propagates slightly faster to the left than to the right, in contrast to Fig. 6.16 where $g_{\uparrow\uparrow} = g_{\downarrow\downarrow}$.

$\hbar\Omega/E_R = 1.5$, $V_p/E_R = 0.075$, and $\sigma_p = \sqrt{2}/k_R$. For these parameters, there is no excitation in the integrated density and we see a significant dip in the integrated spin density which spreads out from the initial perturbation at the spin speed of sound, c_s, predicted in Eq. 6.40.

Interestingly, the disturbances in the n_{1D} and s_{1D} shown in Fig. 6.16 propagate with the same speed in both directions. In the plane wave phase, the speed of sound is different in the $\mathbf{e}_1$ and $-\mathbf{e}_1$ directions if $G_2/E_R \neq 0$ [153, 154]. The integrated density and integrated spin density for ^{41}K with $a_{\uparrow\uparrow} = 102.0a_0$, $a_{\downarrow\downarrow} = 64.3a_0$, $a_{\uparrow\downarrow} = 18.5a_0$, $\hbar\Omega/E_R = 2$, and the same perturbation as Fig. 6.16(a) are shown in Fig. 6.17(a) and Fig. 6.17(b), respectively. For ^{41}K we have $G_3/E_R \neq 0$ and the speed of sound is slightly faster moving to the left than to the right which indicates the importance of terms beyond the zero order mixture picture. Also note that stripes are visible in the spin density because $g_{\uparrow\uparrow} \neq g_{\downarrow\downarrow} \Rightarrow |k_1| \neq |k_2|$, in agreement with the variational ansatz [288].

6.5.3 Time-Dependent Detuning

So far, we have seen that we can derive analytic expressions which provide good approximations of collective mode frequencies from the zero order mixture picture at zero detuning, $\hbar\delta_0/E_R = 0$. An important consideration from an experimental perspective is to have $\hbar\delta_0/E_R \neq 0$ and in particular to understand the effects of a time-dependent detuning, due to magnetic field noise at 50 Hz as discussed in Sec. 3.1.2, for example. To model 50 Hz noise in numerical simulations, we make the replacement $\delta_0 \to \delta_0 + \delta_1 \sin(\omega_{50} t)$ where $\omega_{50}/(2\pi) = 50$ Hz. In Fig. 6.18 we examine the dynamics after removing perturbation I with the parameters of Fig. 6.11(a) (mass of ^{39}K, $a_{\uparrow\uparrow} = a_{\downarrow\downarrow} = 100a_0$, $a_{\uparrow\downarrow} = 60a_0$, and $N = 10^5$) with $\hbar\Omega/E_R = 1$ and $\hbar\delta_0/E_R = -0.04, 0.0, 0.04$, and $\hbar\delta_1/E_R = 0.0, 0.02, 0.04$. We can see that both $\sqrt{\langle x^2 \rangle}$ and d_x are sensitive to δ_0 but are remarkably insensitive to δ_1 even when $|\delta_1| \geq |\delta_0|$ and the fluctuations in detuning cross the stripe phase to plane wave phase transition

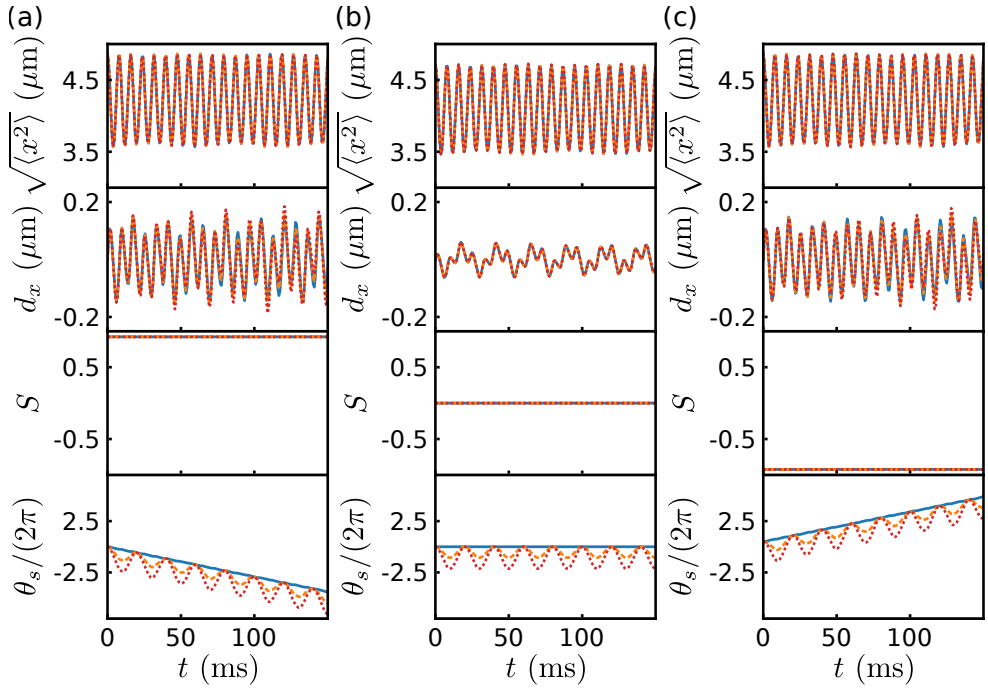

Figure 6.18: (Top panel) Width, $\sqrt{\langle x^2 \rangle}$, (second panel) separation between spin components, d_x, (third panel) well polarisation, S, and (bottom panel) fringe phase, θ_s, for the parameters of Fig. 6.11(c) with $\hbar\Omega/E_R = 1$ and (a) $\hbar\delta_0/E_R = -0.04$, (b) $\hbar\delta_0/E_R = 0.00$, and (c) $\hbar\delta_0/E_R = 0.04$. The dynamics are calculated in the presence of 50 Hz noise with amplitude $\hbar\delta_1/E_R = 0.00$ (solid blue line), $\hbar\delta_1/E_R = 0.02$ (dashed orange line), and $\hbar\delta_1/E_R = 0.04$ (dotted red line).

according to Fig. 6.2.

We can understand the insensitivity to detuning fluctuations by once again invoking the zero order mixture picture. For small values of $\hbar\delta_0/E_R$, k_1 and k_2 are relatively insensitive to changes in detuning meaning that the oscillation of the detuning does not create any significant changes in the effective interaction parameters or the effective mass. Additionally we can see that there are no dynamics in the relative well population, S, for any of the calculated combinations of δ_0 and δ_1. This makes sense since the only way[4] to exchange atoms between the two pseudospins, $\hat{\varphi}_1'$ and $\hat{\varphi}_2'$, is through trap mediated exchange which is negligible for experimentally realistic parameters.

For $\hbar\delta_1/E_R = 0$ and $\hbar\delta_0/E_R \neq 0$, the fringe phase evolves linearly in time with the propagation direction dependent on the sign of δ_0, similarly to the observations of Geier *et al.* [307, 308]. This is because there is a mean-field shift between φ_1' and φ_2' stemming from the population imbalance between the two pseudospin components as well as a small difference between g_{11} and g_{22}. The evolution of the fringe phase is not

[4]In an experimental setting, thermal atoms may also mediate exchange between momentum wells but this effect is not included in the numerical simulations.

present if the perturbation, I, is kept on for the real time dynamics (or never included in the first place) because, in the groundstate, $\mu_1 = \mu_2$ even when $\hbar\delta_0/E_R \neq 0$. When the perturbation is removed, the system is excited out of the groundstate and the mean-field energies of the two pseudospin components are shifted with respect to one another by an amount proportional to the detuning, δ_0.

When $\hbar\delta_1/E_R \neq 0$, we can see that the fringe phase oscillates with frequency, ω_{50}, and that the oscillation is additive with the linear phase evolution. For simplicity, we consider the system without perturbation. For small values of $\hbar\delta_0/E_R$ and $\hbar\delta_1/E_R$, we have $\Delta \approx -\hbar\delta_0 - \hbar\delta_1 \sin(\omega_{50}t)$ so the equations of motion are

$$i\hbar\frac{\partial}{\partial t}\varphi_1' \approx \Bigg[-\frac{\hbar^2}{2mm_1^*}\frac{\partial^2}{\partial x^2} - \frac{\hbar^2}{2m}\nabla_\perp^2 + \frac{\hbar\delta_0}{2} + \frac{\hbar\delta_1}{2}\sin(\omega_{50}t) + V(\mathbf{r}) + g_{11}|\varphi_1'|^2 + g_{12}|\varphi_2'|^2\Bigg]\varphi_1'$$

and

$$i\hbar\frac{\partial}{\partial t}\varphi_2' \approx \Bigg[-\frac{\hbar^2}{2mm_2^*}\frac{\partial^2}{\partial x^2} - \frac{\hbar^2}{2m}\nabla_\perp^2 - \frac{\hbar\delta_0}{2} - \frac{\hbar\delta_1}{2}\sin(\omega_{50}t) + V(\mathbf{r}) + g_{22}|\varphi_2'|^2 + g_{12}|\varphi_1'|^2\Bigg]\varphi_2'. \tag{6.44}$$

In the ground state these equations would be written as

$$\mu_1\varphi_1' \approx \left[-\frac{\hbar^2}{2mm_1^*}\frac{\partial^2}{\partial x^2} - \frac{\hbar^2}{2m}\nabla_\perp^2 + \frac{\hbar\delta_0}{2} + V(\mathbf{r}) + g_{11}|\varphi_1'|^2 + g_{12}|\varphi_2'|^2\right]\varphi_1'$$

and

$$\mu_2\varphi_2' \approx \left[-\frac{\hbar^2}{2mm_2^*}\frac{\partial^2}{\partial x^2} - \frac{\hbar^2}{2m}\nabla_\perp^2 - \frac{\hbar\delta_0}{2} + V(\mathbf{r}) + g_{22}|\varphi_2'|^2 + g_{12}|\varphi_1'|^2\right]\varphi_2'. \tag{6.45}$$

Since the interaction parameters and effective masses are not significantly altered for small values of $\hbar\delta_1/E_R$ we can substitute Eq. 6.45 into Eq. 6.44 to get

$$i\hbar\frac{\partial}{\partial t}\varphi_1' \approx \left[\mu_1 + \frac{\hbar\delta_1}{2}\sin(\omega_{50}t)\right]\varphi_1'$$

and

$$i\hbar\frac{\partial}{\partial t}\varphi_2' \approx \left[\mu_2 - \frac{\hbar\delta_1}{2}\sin(\omega_{50}t)\right]\varphi_2' \tag{6.46}$$

from which we can infer $\partial_t\theta_s \approx (\mu_2 - \mu_1)/\hbar - \delta_1\sin(\omega_{50}t)$, which is consistent with the numerical observations.

In the numerical simulations of Geier *et al.* [308], a linear evolution of the fringe phase in time was also observed after ramping $\hbar\delta_0/E_R$ from a finite initial value to zero in addition to oscillations of the total bare spin polarisation, P, around an out of equilibrium value [307]. In the framework of the zero order mixture picture, we understand that both effects are explained by the lack of exchange of particles between the two pseudospin components. The ratio of atoms in the two pseudospin components and the projections of the pseudopsins onto the bare states determine the total bare spin polarisation and an out of equilibrium ratio corresponds to a difference in chemical potentials ($\mu_1 \neq \mu_2$) leading to a linear evolution of the fringe phase.

6.6 Summary

In this chapter, I have introduced the supersolid stripe phase in the double minimum regime of a Raman coupled BEC. I have discussed the origin of the spontaneous translational symmetry breaking in terms of interference between two nonorthogonal dressed BECs [67, 166, 167]. Through numerical simulations, I have demonstrated the existence of a zero energy Goldstone mode corresponding to the sliding of the stripes. I have also presented a mixture model using the same momentum space expansion which I employed to map the Raman dressed BEC in the single minimum regime to the chiral BF theory in Ch. 5. Using the mixture model, I have made analytic predictions for collective mode frequencies and the spin and density speeds of sound which I have benchmarked against numerical simulations of the Raman dressed BEC in the mean-field regime. Additionally, I have used the mixture model to explain the out of equilibrium spin locking observed in numerical simulations by Geier *et al.* [307]. In the next chapter, I will present experimental results exploring the stripe phase in ^{41}K.

Chapter 7

Experimental Exploration of the Stripe Phase

In the previous chapter, I introduced the stripe phase of a Raman coupled BEC as a system with supersolid properties which can be accessed and understood using the same techniques as the chiral BF theory. In this chapter, I will present experimental results from the realisation of the stripe phase in ^{41}K. Following Lin *et al.* [67], I will present time of flight measurements which provide information about spin and momentum distributions which can be compared to the zero order mixture picture developed in Ch. 6. Finally, I will show how matterwave optics techniques [342, 343] can be adapted to the stripe phase to image the density modulations for the first time in Raman coupled BECs. The results presented in this chapter come from experimental collaborations with Dr. Ramón Ramos and Prof. Dr. Letica Tarruell with theory support from Dr. Josep Cabedo and Dr. Alessio Celi.

7.1 Supersolids in Bose-Einstein Condensates

The stripe phase has been experimentally detected *via* diffraction of light from the atomic cloud, revealing the existence of density modulations which are too small to image optically [111, 112]. Bersano *et al.* [157] have created optically detectable fringes in a Raman coupled BEC by employing an optical lattice to enable momentum space hopping. However, since the translational symmetry in this system is broken by the optical lattice and not spontaneously, it should be considered as "supersolid-like" [157].

Around the same time as the first detection of stripes in a Raman coupled BEC, a supersolid state was formed by coupling a BEC symmetrically to two optical cavities [105]. As in the stripe phase, the fringes of the cavity supersolid are too small to image optically and the presence of density modulations was inferred from light leaking from the cavities and the atomic momentum distribution in time of flight images. The realisation of supersolids in dipolar BECs [107–109] resulted in optically observable density modulations but in this case, the number of fringes is small since the crystal spacing is is not much smaller than the size of the BEC [159]. In this chapter, I will

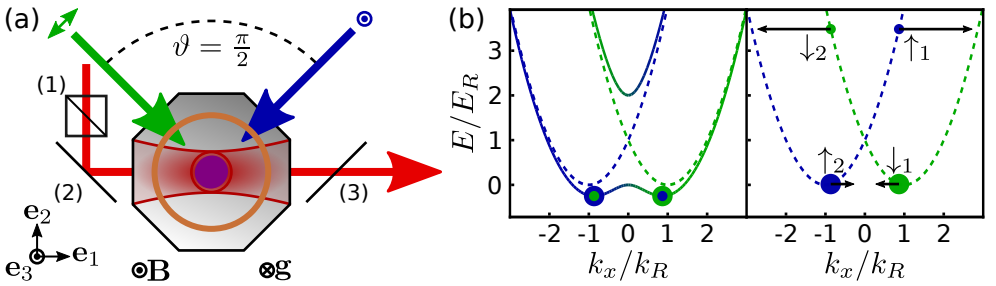

Figure 7.1: (a) Experimental configuration with an angle $\vartheta = \pi/2$ between the Raman beams, the optical elements shown are (1) polarising beam splitter, QiOptiq G335525000; (2) dichroic mirror, Thorlabs DMSP1000L; (3) dichroic mirror, Thorlabs DMLP950L. (b) The dashed lines show the bare state dispersion relations, $\epsilon_\uparrow$ and $\epsilon_\downarrow$, while the coloured lines show the Raman dressed dispersion relations, ε_- and ε_+, with $\hbar\Omega/E_R = 2$ and $\hbar\delta_0/E_R = 0$. In the lower band two nonorthogonal dressed BECs can be formed at rest in the laboratory frame with distinct quasimomenta. When the Raman beams are suddenly switched off, the two dressed BECs are projected onto the bare state dispersions without changing quasimomentum resulting in four components with distinct momenta in the laboratory frame. The black arrows in the right panel indicate the velocities of the four projected components as given by $\partial_{k_x}\epsilon_\uparrow$ and $\partial_{k_x}\epsilon_\downarrow$.

first investigate the momentum space distributions of atoms in the stripe phase and then employ matterwave optics to magnify the fringes to a size which can be directly imaged.

7.2 Time of Flight Measurements

Our experiments in the stripe phase are conducted in ^{41}K with a bias magnetic field of[1] $B = 51.766(5)$ mG. We choose $|\uparrow\rangle = |F = 1, m_F = -1\rangle$ and $|\downarrow\rangle = |F = 1, m_F = 0\rangle$ so that $a_{\uparrow\uparrow} = 102.0a_0$, $a_{\downarrow\downarrow} = 64.3a_0$, $a_{\uparrow\downarrow} = 18.1a_0$ [244], and $\mathrm{d}B/\mathrm{d}\omega_0/(2\pi) \approx 580$ Hz/mG. For the experiments in this chapter we set the angle between the Raman beams to be $\vartheta = \pi/2$ as shown in Fig. 7.1(a) so that $2\pi/k_R = \sqrt{2}\lambda_R = 1.088$ μm and the single photon recoil energy is given by $E_R/(2\pi\hbar) = 4.12$ kHz. The $1/\exp(2)$ radii of the Raman beams are ~ 200 μm. For the experiments presented in this chapter, we use a crossed optical dipole trap consisting of two laser beams with wavelength 1064 nm propagating along the $\mathbf{e}_1$ and $\mathbf{e}_3$ axes. The approximate harmonic oscillator trap frequencies are $\omega_x/2\pi = 63(1)$ Hz, $\omega_y/2\pi = 147(5)$ Hz, and $\omega_z/2\pi = 103(2)$ Hz.

Figure 7.1(b) illustrates the procedure for examining the momentum space density of the stripe phase. When the two dressed BECs are at rest in the laboratory frame, their group quasimomenta are $\hbar k_1\mathbf{e}_1$ and $\hbar k_2\mathbf{e}_1$, where k_1 and k_2 are the minima of the dressed dispersion, $\varepsilon_-(k_x)$, as defined in Sec. 6.3. When the Raman beams are suddenly switched off, the dressed BECs are projected onto the bare spin states and

[1]For the uncertainty in magnetic field we do not consider the 50 Hz noise because we have seen that these oscillations do not impact the dynamic properties of the stripe phase in Sec. 6.5.

quasimomentum is conserved. Thus the BEC is split into four momentum components (two for each spin state) which all have different velocities in the laboratory frame and which we have labelled $\downarrow_1$, $\uparrow_1$, $\downarrow_2$, and $\uparrow_2$ in Fig. 7.1(b). In state $|\uparrow\rangle$, the laboratory frame momenta of the two components are $\uparrow_1$: $\hbar k_x^{(\mathrm{lab})}\mathbf{e}_1 = \hbar\left(k_1 + k_R\right)\mathbf{e}_1$ and $\uparrow_2$: $\hbar k_x^{(\mathrm{lab})}\mathbf{e}_1 = \hbar\left(k_2 + k_R\right)\mathbf{e}_1$ and in state $|\downarrow\rangle$, the laboratory frame momenta are $\downarrow_1$: $\hbar k_x^{(\mathrm{lab})}\mathbf{e}_1 = \hbar\left(k_1 - k_R\right)\mathbf{e}_1$ and $\downarrow_2$: $\hbar k_x^{(\mathrm{lab})}\mathbf{e}_1 = \hbar\left(k_2 - k_R\right)\mathbf{e}_1$. Since $0 \leq k_1/k_R \leq 1$ and $-1 \leq k_2/k_R \leq 0$ for $\hbar\Omega/E_R < 4$, both components of state $|\uparrow\rangle$ ($|\downarrow\rangle$) move in the $\mathbf{e}_1$ ($-\mathbf{e}_1$) direction.

After switching off the Raman beams, we release the atoms from the trap and allow the atoms to evolve in time of flight which maps the laboratory frame velocities into horizontal displacements. This means that the spin resolved momentum distribution can be measured with a single absorption image with a Stern-Gerlach gradient applied during time of flight. To prepare the stripe phase, we need to start with a mixture of the bare spin states since we have

$$\lim_{\hbar\Omega/E_R\to 0}\langle\downarrow', k_x/k_R = 1|-, k_x/k_R = 1\rangle = \sqrt{\left[1 - \tilde{\delta}(k_R)/|\tilde{\delta}(k_R)|\right]/2}$$

and

$$\lim_{\hbar\Omega/E_R\to 0}\langle\uparrow', k_x/k_R = -1|-, k_x/k_R = -1\rangle = \sqrt{\left[1 + \tilde{\delta}(-k_R)/|\tilde{\delta}(-k_R)|\right]/2}. \quad (7.1)$$

We prepare a BEC in state $|\downarrow', k_x/k_R = 1\rangle$ with an initial atom number, N_0, and apply a resonant RF pulse with Rabi frequency $\Omega_{\mathrm{RF}}/(2\pi) = 14.6(2)$ kHz for a duration of τ_{pulse}. We add a short wait time to allow the different bare state interactions to cause the RF dressed states to decohere and ramp the Raman Rabi frequency linearly from zero to its final value in 15 ms with $\hbar\delta_0/E_R = 0.0(7)$. We keep the atoms in the trap with the Raman beams at constant power for a time, t_{hold}, before switching off the Raman beams. The trap is switched off 1.2 ms after the Raman beams.

Figure 7.2(a) show the measured momentum distributions for various values of $\hbar\Omega/E_R$ with $N_0 = 1.0(2)\times 10^5$, $\tau_{\mathrm{pulse}} = 15$ μs, $t_{\mathrm{hold}} = 1.2$ ms and 14 ms time of flight. We can see the expected four components with displacements in the expected directions but we also see scattering halos around the expected clouds due to collisions between the different components immediately following the switch off of the Raman beams since the two dressed BECs were initially overlapped in position. To reduce scattering between components, we decrease the atomic density by reducing the initial atom number to $N_0 = 2.0(4)\times 10^4$, as shown in Fig. 7.2(b). We have verified that the power is ramped slowly enough to avoid populating the upper band by ramping up the power, waiting for variable times and ramping down the power. We observe that the final mixture is the same as the initial mixture for various values of τ_{pulse}.

In Fig. 7.2(a), the components corresponding to quasimomentum $\hbar k_1\mathbf{e}_1$ ($\hbar k_2\mathbf{e}_1$) are marked with green (blue) boxes for $\hbar\Omega/E_R = 2.5$ and the vertically displaced bare spin components are labelled. By fitting the positions and atom numbers in the four components for each value of $\hbar\Omega/E_R$ shown in Fig. 7.2(b), we can infer the group quasimomenta and the bare state spin polarisation, P for each of the dressed BECs and the ratio of atoms in the two dressed BECs, S. These quantities are shown

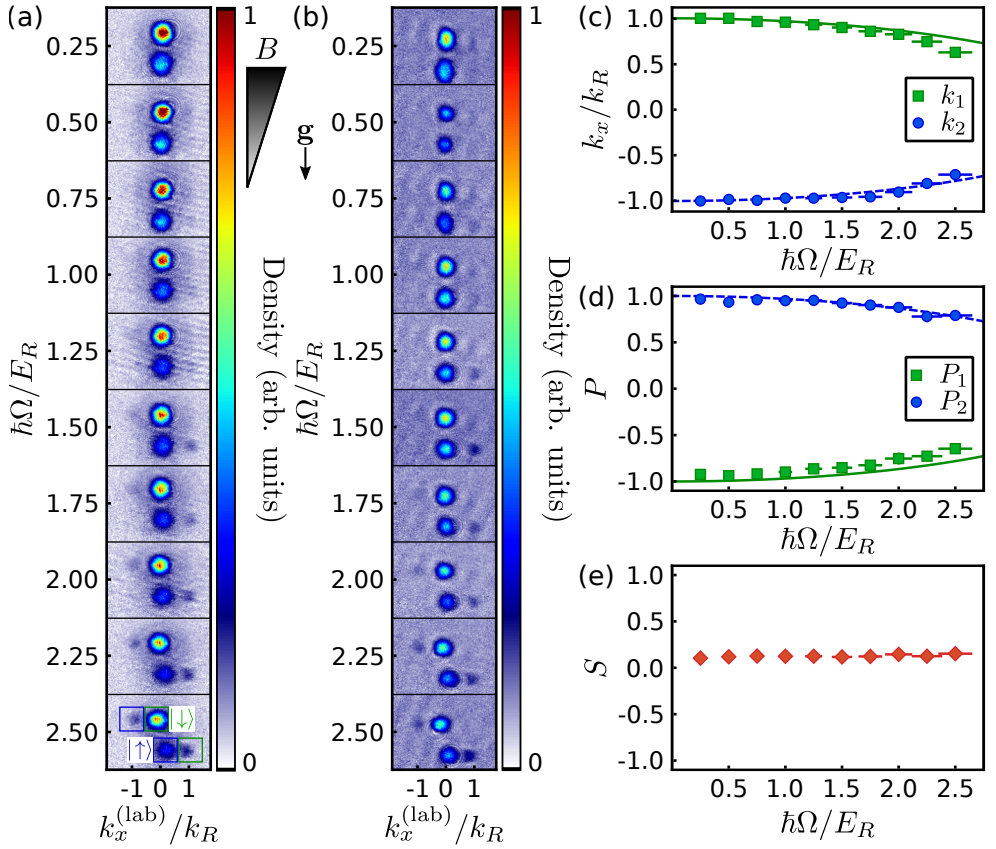

Figure 7.2: (a) Collage of atomic densities with initial atom number $N_0 = 1.0(2) \times 10^5$, an RF pulse time of $\tau_{\mathrm{pulse}} = 15$ μs, $\hbar\delta_0/E_R = 0.0(7)$ and various values of $\hbar\Omega/E_R$ after projection onto the bare spin states and 14 ms time of flight in the presence of a magnetic field gradient. For $\hbar\Omega/E_R = 2.5(2)$ the bare spin states are labelled and the components corresponding to initial quasimomentum $k_x/k_R \approx 1$ ($k_x/k_R \approx -1$) are marked with green (blue) boxes. (b) Collage of atomic densities with initial atom number $N_0 = 2.0(4) \times 10^4$, an RF pulse time of $\tau_{\mathrm{pulse}} = 15$ μs, and various values of $\hbar\Omega/E_R$ after projection onto the bare spin states and 14 ms time of flight in the presence of a magnetic field gradient. (c) Group quasimomentum extracted from time of flight images with initial atom number $N_0 = 2.0(4) \times 10^4$. The solid green line and dashed blue line show $k_1/k_R = \sqrt{1 - [\hbar\Omega/(4E_R)]}$ and $k_2 = -k_1$, respectively. (d) Polarisation of each momentum well corresponding to initial atom number $N_0 = 2.0(4) \times 10^4$. The solid green line shows $P_1 = \tilde{\delta}(k_1)/\tilde{\Omega}(k_1)$ and the dashed blue line shows $P_2 = \tilde{\delta}(k_2)/\tilde{\Omega}(k_2)$. (e) Ratio of atoms in the two momentum wells, S, corresponding to initial atom number $N_0 = 2.0(4) \times 10^4$. For (a), (b), and (c) data points and vertical error bars correspond to the mean and standard deviation of 10 measurements and horizontal error bars reflect the upper bound of 6 % systematic uncertainty in Ω.

in Fig. 7.2(c), (d), and (e), respectively. We can see that for the largest measured values of $\hbar\Omega/E_R$ the absolute value of the group quasimomentum is smaller than the

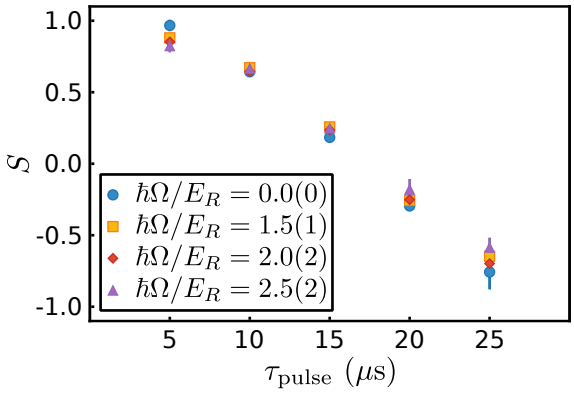

Figure 7.3: Ratio of atoms in the two momentum wells, S, as a function of pulse time, τ_{pulse}, with an RF field of Rabi frequency $\Omega_{\mathrm{RF}}/(2\pi) = 14.6(2)$ kHz for various values of $\hbar\Omega/E_R$. Data points and error bars are the mean and standard deviation of five measurements.

prediction of the zero order mixture picture for both dressed BECs.

The deviation in the measured group momenta from the predicted values cannot be accounted for by a mean-field shift or the uncertainty in δ_0 because, in these cases, the group momenta of the two dressed BECs would be shifted in the same direction, in contrast to the experimental observation. Here, the lifetime of the BEC is longer than in Ch. 5 due to the reduction in the value of E_R and the decreased magnetic field [207] but the reduced initial atom number limits the losses we can tolerate before detection of the fast moving components with a minority of the atoms becomes problematic. Minimising losses due to inelastic photon scattering is the reason for the relatively short ramp time of 15 ms which generates the mechanical momentum leading to the observed deviations in the group momenta.

From Fig. 7.2(e), we can see that for our experimental parameters and timescales, the ratio of atoms in the two dressed BECs is independent of $\hbar\Omega/E_R$ which tells us that the initial bare state mixture dictates the population of the two dressed BECs, as predicted in Ch. 6. Figure 7.3 shows the ratio of atoms in the two dressed BECs, S, as a function of the RF pulse time, τ_{pulse}, for various values of $\hbar\Omega/E_R$ with $\hbar\delta_0/E_R = 0.0(7)$. All of the measurements fall onto the same curve, further confirming that S does not freely evolve on our experimental time scales. The fact that S can be controlled independently of the bare state interactions in our experiments opens the possibility of creating metastable stripe phases where one of g_{11} or g_{22} is smaller than g_{12} such that the groundstate would be the plane wave phase but $g_{12}^2 < g_{11}g_{22}$ such that stripes can be formed if $S \neq 0$. In this chapter, we restrict experiments to $\hbar\Omega/E_R < \hbar\Omega_c/E_R \approx 2.65$ so that the true groundstate is the supersolid stripe phase.

Figure 7.4 shows (a) the magnitude of the difference in quasimomentum, $\hbar\delta k_x$, of the two dressed BECs, (b) the bare state spin polarisation, P, of each of the two dressed BECs, (c) the ratio of atoms, S, in the two dressed BECs, and (d) the bare state spin polarisation, P, of the full system for the parameters of Fig. 7.2(b) as a

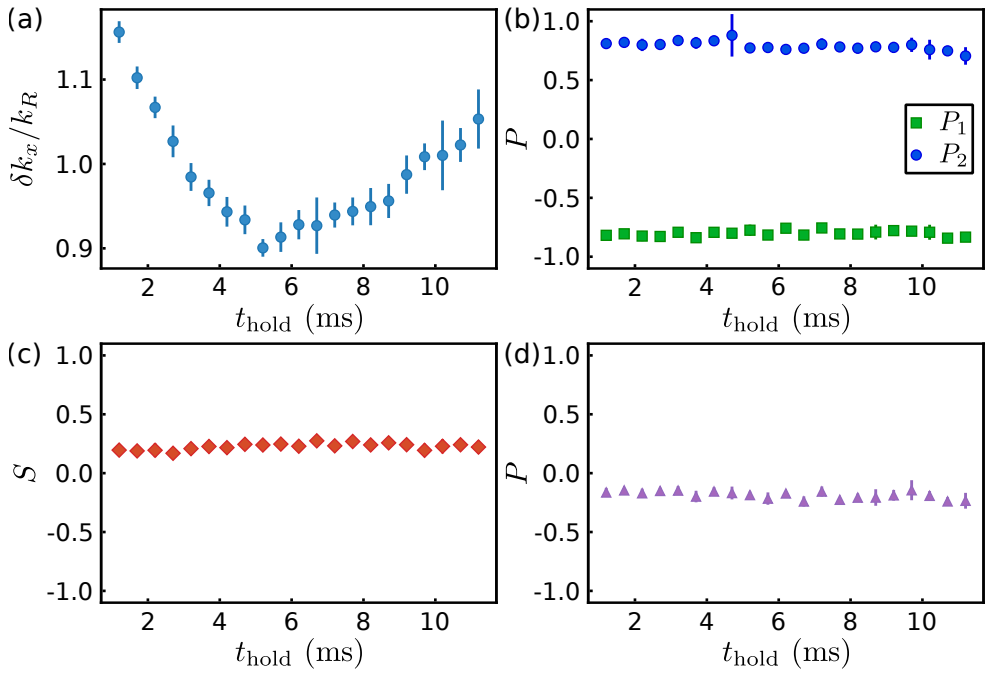

Figure 7.4: A Raman dressed BEC with initial atom number $N_0 = 2.0(4) \times 10^4$ and $\hbar\Omega/E_R = 2.5(2)$ is held in a crossed dipole trap for a time, t_{hold}, before projection onto the bare states and 14 ms time of flight. (a) Difference in group quasimomentum of the dressed BECs in the two momentum wells, δk_x. (b) Bare spin polarisation of the dressed BECs in the two momentum wells, P_1 and P_2. (c) Ratio of atoms in the two momentum wells, S. (d) Total bare spin polarisation, P. Data points and error bars are the mean and standard deviation of five measurements.

function of t_{hold} with $\hbar\Omega/E_R = 2.5(2)$. We can see that δk_x appears to oscillate in time, as we would expect [280, 281]. The oscillation of δk_x does not appear to be sinusoidal which implies the excitation of both the dipole and spin dipole modes although the maximum hold time is too short to resolve the frequencies. Once again, we see in Fig. 7.4(c) that S is conserved. We expect oscillation in P_1, P_2, and P with the same period as δk_x, however the two dressed BECs are nearly spin polarised in the double minimum regime and these oscillations are therefore small.

7.3 Matterwave Lensing to Image Stripes

In our *in situ* imaging system, the spatial resolution is ~ 1.5 μm [170, 227] which is approximately three times larger than the expected fringe spacing in the stripe phase, $\lim_{\hbar\Omega/E_R \to 0} \Delta s = \pi/k_R = \lambda_R/\sqrt{2} = 544$ nm. In the previous section, we have used time of flight imaging to map the momentum distribution of the BEC to position space [211] and infer some properties of the stripe phase. The mapping of the momentum distribution to position space can also be achieved by using a harmonic

trap as a "matterwave lens" for the atomic density distribution [342, 344].

The ballistic expansion of an ultracold gas is directly analogous to Fraunhofer diffraction in optics [344]. The intensity distribution of light far from a source is the Fourier transform of the intensity distribution at the source. If the light passes through a lens which produces a spatially quadratic phase shift on the light, the far-field Fourier plane is brought to the focal plane of the lens [344]. Pulsing a spatial varying optical potential onto a BEC imprints a spatially varying phase onto the BEC [177, 198, 199]. Thus, pulsing a harmonic oscillator potential of the form $V_{\rm lens} = m\omega_{\rm lens}^2 \mathbf{r}^2/2$ onto a BEC for one quarter trap period $(\pi/(2\omega_{\rm lens}))$ focuses the BEC and maps the momentum distribution to position space and vice versa without the need of a long time of flight [342].

Asteria *et al.* [343] have combined the concept of matterwave focusing with the time of flight measurement technique to create a quantum gas magnifier where the initial spatial distribution is mapped into position space with a magnification factor of $\omega_{\rm lens} t_{\rm tof}$ where $t_{\rm tof}$ is the time of flight. Here, we apply the technique to image density modulations in the stripe phase. In the experiments of Asteria *et al.* [343] atoms were released from a two-dimensional optical lattice into a harmonic potential of the form $V_{\rm lens} = m\omega_{\rm lens}\left(x^2 + y^2\right)/2$ and then imaged along the z-axis.

To magnify a single-component BEC in a harmonic trap, one can simply quench the harmonic trap frequency to $\omega_{\rm lens}$ which has the same effect as releasing from one trap into another. Assuming $\omega_{\rm lens}$ is greater than the original trap frequency, quenching the trap frequency will cause the BEC to expand in momentum space. For a Raman dressed BEC in the double minimum regime, it is possible for the BEC to expand sufficiently in momentum space such that parts of the cloud enter the negative effective mass regime which may induce shock waves [345].

Our procedure to magnify the stripes is to switch off the Raman beams and quench the trap frequency simultaneously. This projects the two dressed BECs into the four spin and momentum components which we have investigated in time of flight. To model the lensing sequence, we initially consider the four components without interactions. We allow for mechanical momentum by assuming that at the moment before the Raman beams are switched off the two dressed BECs have group quasimomenta k_{x1} and k_{x2} with $k_{x1}/k_R > 0$ and $k_{x2}/k_R < 0$ with the two group quasimomenta close to but not necessarily equal to the minima of the Raman dressed dispersion.

Since we allow for mechanical momentum, we must also allow for spatial displacements of the two dressed BECs, we denote the centre of mass positions of the two dressed BECs at the moment the Raman beams are switched off as x_1 and x_2. When the Raman beams are switched off and the harmonic trap is compressed, the four projected components will undergo simple harmonic motion, according to Ehrenfest's theorem. The positions and group momenta of the projected components as functions of time in the compressed trap are given in Tab. 7.1.

The compressed trap slows down the four components such that they come to rest in the laboratory frame after a time $t = \pi/(2\omega_{\rm lens})$. Due to the momentum gained from projection out of the Raman dressed states onto the bare spin states, the two components in the $|\uparrow\rangle$ $(|\downarrow\rangle)$ state end up displaced in the $\mathbf{e}_1$ $(-\mathbf{e}_1)$ direction with the

Table 7.1: Centre of mass positions and group momenta of projected spin components after suddenly switching off the Raman beams. The labelling of the projected components is the same as in Fig. 7.1(b).

Component	Position	Group momentum
$\downarrow_1$	$\frac{\hbar(k_{x1}-k_R)}{m\omega_{\rm lens}}\sin(\omega_{\rm lens}t)+x_1$	$(k_{x1}-k_R)\cos(\omega_{\rm lens}t)+k_R$
$\downarrow_2$	$\frac{\hbar(k_{x2}-k_R)}{m\omega_{\rm lens}}\sin(\omega_{\rm lens}t)+x_2$	$(k_{x2}-k_R)\cos(\omega_{\rm lens}t)+k_R$
$\uparrow_1$	$\frac{\hbar(k_{x1}+k_R)}{m\omega_{\rm lens}}\sin(\omega_{\rm lens}t)+x_1$	$(k_{x1}+k_R)\cos(\omega_{\rm lens}t)-k_R$
$\uparrow_2$	$\frac{\hbar(k_{x2}+k_R)}{m\omega_{\rm lens}}\sin(\omega_{\rm lens}t)+x_2$	$(k_{x2}+k_R)\cos(\omega_{\rm lens}t)-k_R$

displacements depending on the value of $\omega_{\rm lens}$ and group quasimomenta of the dressed BECs before switching off the Raman beams.

When the lensing potential is suddenly switched off, the four components expand in position space and overlap with each other after a sufficiently long expansion time. As the components expand, interference between the two pairs of components with matching spin restores the density modulations of the stripe phase [177, 346]. For a given time, t, in the compressed trap and after an expansion time, t_e with $t_e^2 \gg 1/\omega_{\rm lens}^2$, the fringe spacing is [347]

$$\Delta s \approx \frac{2\pi\hbar t_e}{m}\left[\left|x_1-x_2+\hbar\left(k_{x1}-k_{x2}\right)\sin\left(\omega_{\rm lens}t\right)/(m\omega_{\rm lens})\right|\right. \\ \left.+\hbar t_e\left|\left(k_{x1}-k_{x2}\right)\cos\left(\omega_{\rm lens}t\right)/m\right|\right]^{-1}. \quad (7.2)$$

For $\omega_{\rm lens}t=\pi/2$ we have

$$\Delta s = \frac{2\pi\hbar t_e}{m\left|x_1-x_2+\hbar\left(k_{x1}-k_{x2}\right)/(m\omega_{\rm lens})\right|}. \quad (7.3)$$

So we see that if $k_R(x_1-x_2)=0$ we obtain the expected magnification factor of $\omega_{\rm lens}t_e$ [343] but mechanical momentum can cause a change in the magnification factor as well as the initial fringe spacing.

In the experiments of Asteria *et al.* [343], lensing was achieved using a magnetic potential which is naturally smooth and harmonic since the curvature is determined by the size of the coils used to generate the field. For our chosen states of ^{41}K, we have different magnetic moments for the $|\uparrow\rangle$ and $|\downarrow\rangle$ components which means a magnetic trap would not work. Instead, we create the lensing potential by suddenly increasing the power of the dipole trap beam propagating in the $\mathbf{e}_3$ direction by a factor of 16 (from 15 mW to 240 mW) while leaving the other beam unchanged corresponding to estimated trapping frequencies of $\omega_x/(2\pi)\equiv\omega_{\rm lens}/(2\pi)=252(4)$ Hz, $\omega_y/(2\pi)=285(10)$ Hz, and $\omega_z/(2\pi)=103(2)$ Hz. We have defined the trap frequency along the x-axis to be $\omega_{\rm lens}$ since the anisotropic traps will not allow lensing to be performed on more than one-axis simultaneously and our goal is to magnify the stripes along the x-axis. The matterwave lensing sequence is illustrated in Fig. 7.5.

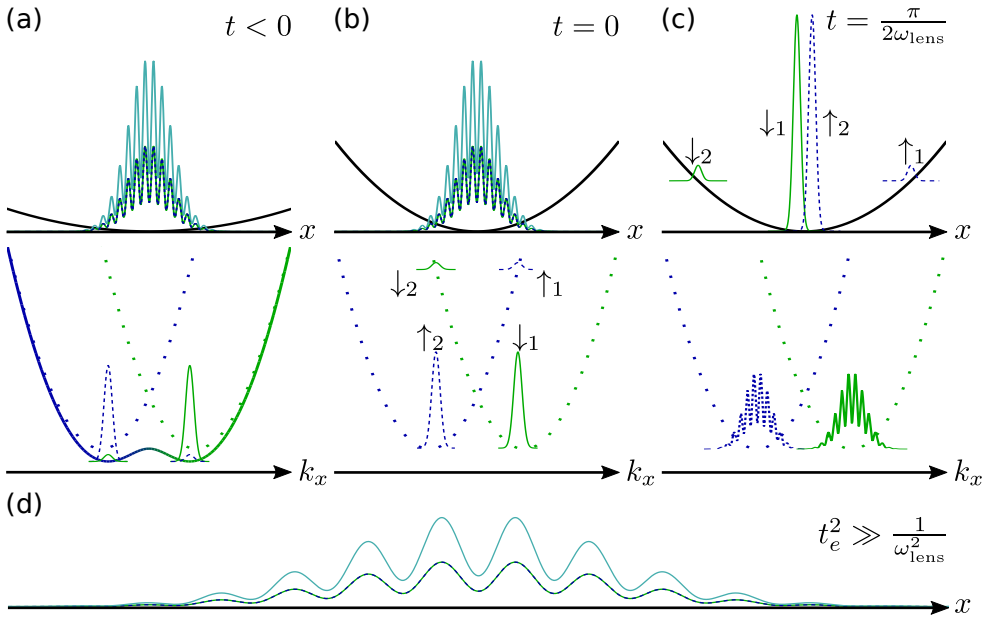

Figure 7.5: Matterwave lensing of stripes. (a) A harmonically trapped BEC in the stripe phase at rest in the laboratory frame corresponds to two nonorthogonal dressed BECs at the minima of the Raman dressed dispersion $\varepsilon_-(k_x)$ (coloured line). (b) The Raman beams are suddenly switched off and the harmonic trap is compressed simultaneously. In momentum space, the dressed BECs are projected onto the bare state dispersions (dotted lines) resulting in four spin and momentum components. The density is unchanged in the first instant. (c) After one quarter period in the compressed trap, all components come to rest in the laboratory frame resulting in interference fringes in momentum space corresponding to displacements in position space. (d) After a long expansion time, the four components in position space overlap and form matterwave interference fringes with spacing proportional to the expansion time. In (b) and (c), the projected components have been labelled as in Fig. 7.1(b).

Since we want to use our *in situ* imaging system which images the atomic density along the $\mathbf{e}_3$ direction [170], we must keep the trapping beam propagating in the $\mathbf{e}_1$ direction on during the expansion time to prevent the atoms from falling out of the focus of the imaging objective under the influence of gravity. This means that the width along the y-axis will oscillate during the expansion time and we won't have a rapid initial expansion of the BEC which would allow us to neglect interactions [343]. Repulsive interactions will tend to increase the observed fringe spacing [347] and we have seen that scattering halos from colliding components after switching off the Raman beams obscure the density of unscattered atoms. Therefore, as we did for time of flight measurements we restrict ourselves to small initial atom numbers $N_0 = 2.0(4) \times 10^4$.

As described in Sec. 2.4.1, we use an off-resonant phase contrast imaging technique in the presence of a bias magnetic field for *in situ* imaging [170]. This can cause problems when trying to image matterwave interference patterns since light passing through a spatially periodic structure will be influenced by the Talbot effect [348,

349]. For off-resonant light passing through the spatially modulated BEC, the fringe contrast and fringe spacing can both be modified [350]. To avoid this effect, we reduce the bias magnetic field to ~ 1.2 G during the expansion phase[2], optically pump the atoms into the low field state $|F = 2, m_F = 2\rangle$, and apply resonant absorption imaging.

The $1/\exp(2)$ radius of the dipole trap beam propagating in the $\mathbf{e}_3$ direction is 51.6(3) μm. This means that for the momentum imparted onto the fast moving components during the projection from Raman dressed BECs to bare spin states, we expect to see significant anharmonicity in the trapping potential for $\omega_{\text{lens}}t = \pi/2$. This can be somewhat compensated by reducing the lensing time such that the fast moving components do not move as far into the anharmonic region of the trap. The consequence of having $\omega_{\text{lens}}t < \pi/2$ is that the BECs do not come to rest during the compression phase and the spin components move in opposite directions during the expansion phase. So, for sufficiently long t_e, we not only magnify the stripes but also separate spin components which allows for spin resolved imaging.

7.3.1 Calibration

To calibrate the matterwave lensing sequence, we use the running wave optical lattice used to Bragg diffract atoms in Sec. 5.2.1. If we take a single-component BEC with N atoms, pulsing the lattice for a time τ_{Bragg} will impart a momentum $\hbar k_B \mathbf{e}_1$ onto γN atoms where $0 \leq \gamma \leq 1$ depends on the length of the pulse. After the pulse but before the diffracted component has time to move away, the diffracted and undiffracted atoms overlap in position space with a momentum difference of k_B and form matter wave interference fringes with wavelength $2\pi/k_B$.

We have $2\pi/k_B = \lambda_L/2 = 532$ nm which is similar to $\pi/k_R = \lambda_R/\sqrt{2} = 544$ nm for $\vartheta = \pi/2$. Therefore, we can apply matterwave lensing to Bragg diffracted atoms to calibrate the technique. When the harmonic trap frequency is compressed to ω_{lens}, the diffracted portion of the atoms will come to rest after time $t = \pi/(2\omega_{\text{lens}})$ and the separation between the diffracted and undiffracted components will be $\hbar k_B/(m\omega_{\text{lens}})$. When the lensing potential is released and the two BECs expand for a time t_e such that $t_e^2 \gg 1/\omega_{\text{lens}}^2$, the BECs will overlap and interfere with fringe spacing $\Delta s = 2\pi\omega_{\text{lens}}t_e/k_B$ and contrast $\mathcal{C} = 2\sqrt{\gamma(1-\gamma)}$ [177, 347].

Starting with a BEC of ^{41}K in state $|\downarrow\rangle = |F = 1, m_F = 0\rangle$ with $B = 51.766(5)$ G and $N = 1.2(3)\times 10^4$ at rest in the laboratory frame, we apply the running wave lattice for a variable pulse time, τ_{Bragg}, and measure the proportion of diffracted atoms, γ, after a 14 ms time of flight. Figure 7.6(a) shows the fraction of diffracted atoms as a function of pulse duration.

The value of ω_{lens} is not precisely known and the quench of trap frequency is not infinitely sharp because the intensity of the dipole trapping beam is stabilised by a PID controller with a bandwith of ~ 1 kHz. To find the time corresponding to $\omega_{\text{lens}}t = \pi/2$, we apply the lensing sequence for variable compression times and optimise the observed fringe contrast after an expansion time of $t_e = 7$ ms which

[2]The magnetic field takes ~ 2 ms to stabilise, limited by eddy currents in the steel vacuum chamber.

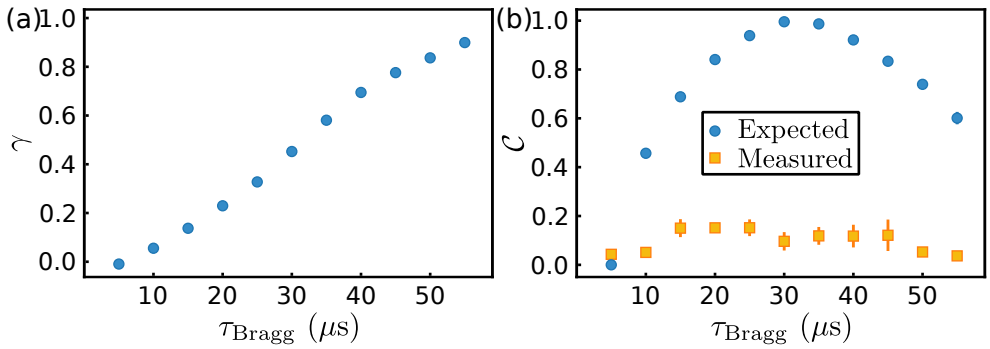

Figure 7.6: (a) Fraction of atoms, γ, transferred to momentum $\hbar k_B \mathbf{e}_1$ by a running wave lattice as a function of Bragg pulse time, τ_{Bragg}, measured in time of flight. (b) Expected contrast, $\mathcal{C}$, from time of flight ratio, γ, and measured contrast from matterwave lensing. Data points and error bars are means and standard deviations of three (five) measurements for time of flight (matterwave lensing). For the time of flight measurements, error bars are smaller than the data markers.

corresponds to a compromise between a large magnification factor and a good signal to noise ratio in absorption images. We find optimal contrast with a compression time of 900 μs. To extract the contrast, we fit the integrated *in situ* images of the atomic density after matterwave lensing with

$$n_{1\mathrm{D}}(x) = A \exp\left[-\left(x - x_0\right)^2 / \left(2\sigma_x^2\right)\right] \left[1 + \mathcal{C} \cos\left(2\pi x/\Delta s + \theta_B\right)\right]. \tag{7.4}$$

The fitted values of $\mathcal{C}$ as a function of τ_{Bragg} are shown in Fig. 7.6(b) along with the expected fringe contrast inferred from the experimentally determined values of γ. We can see that the measured contrast after lensing is significantly smaller than the expected contrast. One reason for this is that the interactions distort the fringes [347]. We have $a_{\downarrow\downarrow} = 64.3 a_0$ and for a fixed pulse time of $\tau_{\mathrm{Bragg}} = 25$ μs, we measure $\mathcal{C} = 0.16(7)$ where the value and uncertainty correspond to the mean and standard deviation of 28 measurements. If instead we use state $|\uparrow\rangle = |F = 1, m_F = -1\rangle$ with $a_{\uparrow\uparrow} = 102.0 a_0$ we find $\mathcal{C} = 0.08(3)$ corresponding to the mean and standard deviation of 25 measurements.

The interactions in the BEC have a clear impact of the measured contrast. For state $|\uparrow\rangle$, we measure a magnified fringe spacing of $\Delta s = 6.8(3)$ μm corresponding to a magnification factor of 12.7(6) and for state $|\downarrow\rangle$ we measure $\Delta s = 6.9(3)$ μm corresponding to a magnification factor of 13.0(5). From these results, we conclude that, for our experimental parameters, interactions do not make a significant impact on measured fringe spacing.

Another factor which can impact measured fringe contrast is the optical resolution of the imaging system. We have a spatial resolution of ~ 1.5 μm [170, 227]. To estimate the effect of optical resolution on the measured contrast, we plot the ideal density profile

$$n(x, y) = \exp\left[-x^2/\left(2\sigma_x^2\right) - y^2/\left(2\sigma_y^2\right)\right] \left[1 + \mathcal{C} \cos\left(2\pi x/\Delta s\right)\right] \tag{7.5}$$

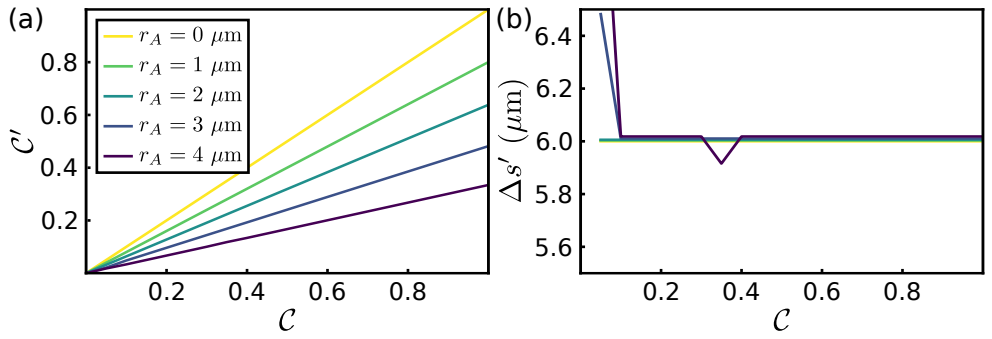

Figure 7.7: (a) Fitted contrast, $\mathcal{C}'$, and (b) fitted fringe spacing, $\Delta s'$, as functions of contrast, $\mathcal{C}$, for an ideal modulated density profile convolved with Airy disk point spread functions of various radii, r_A.

with $\sigma_x = 23$ μm, $\sigma_y = 3$ μm, and $\Delta s = 6$ μm. We convolve Eq. 7.5 with an Airy disk of radius[3] r_A and integrate over the y-axis. We fit the result with Eq. 7.4 for various values of $\mathcal{C}$ and r_A to extract the effective contrast, $\mathcal{C}'$, and fringe spacing, $\Delta s'$.

Figure 7.7(a) and (b) show $\mathcal{C}'$ and $\Delta s'$ as functions of $\mathcal{C}$ for various values of r_A. We can see that the fringe spacing is negligibly affected by the optical resolution for the parameters shown[4] but the measured contrast is significantly reduced by finite optical resolution. We observe that $\mathcal{C}'$ is linear in $\mathcal{C}$ for all values of r_A shown which means that although the finite imaging resolution reduces the measured fringe contrast, relative values of the fringe contrast are not impacted by the imaging resolution. The expected reduction in contrast due to finite imaging resolution is less than what we have measured with Bragg diffraction which is consistent with the observation that the interatomic interactions have a clear impact on observed contrast.

7.3.2 Imaging the Stripe Phase

Figure 7.8(a) shows matterwave lensing images in the stripe phase with $\hbar\Omega/E_R = 2.5(2)$ and $\hbar\delta_0/E_R$ for various values of τ_{pulse} with a compression time of 0.7 ms and an expansion time of $t_e = 7$ ms. The preparation procedure is the same as for the time of flight data and the wait time between reaching the final Rabi frequency and the matterwave lensing sequence is $t_{\text{hold}} = 1.2$ ms. We can see that, as expected, the BEC separates into spin components with the atoms in state $|\uparrow\rangle$ ($|\downarrow\rangle$) moving to the right (left) because the compression time is less than $\pi/(2\omega_{\text{lens}})$. The contrast of fringes observed in the two components is dependent on the ratio of atoms in the dressed BECs, S, and is impacted by the optical resolution and interactions.

The dependence of the contrast on S can be understood in terms of the populations of the different projected BECs which expand and interfere in the last part of the lensing sequence. When $|S| \approx 1$ almost all of the atoms are in one momentum well so the contrast corresponding to the majority spin component is limited by the small

[3]The position of the first zero of the first order Bessel function of the first kind.
[4]The sharp changes for low contrast are numerical artefacts and are on the order of 100 nm.

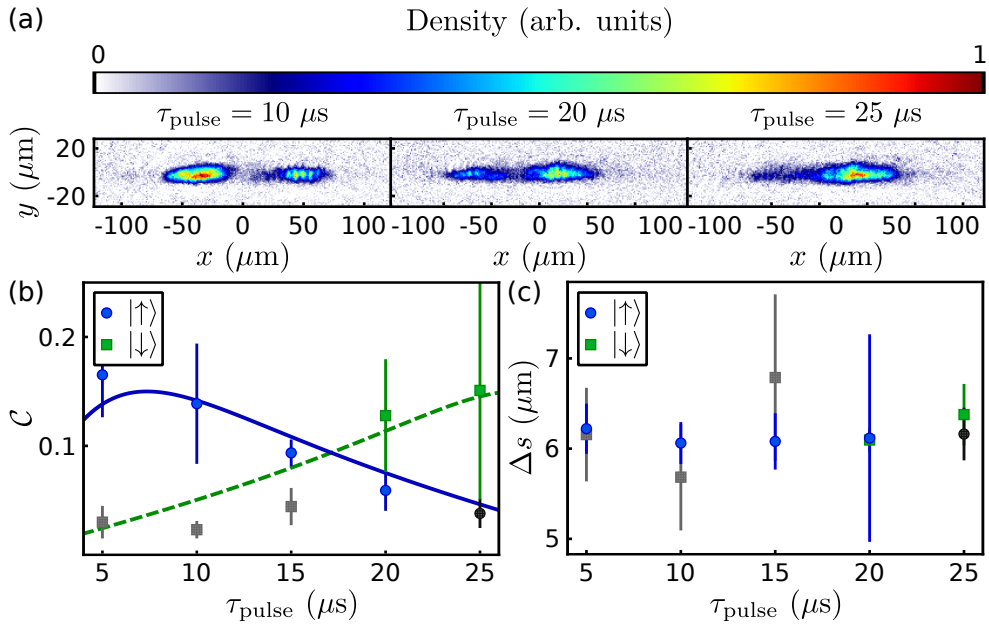

Figure 7.8: (a) Exemplary images of matterwave lensing applied to the stripe phase with $N_0 = 2.0(4) \times 10^4$, $\hbar\Omega/E_R = 2.5(2)$, and $\hbar\delta_0/E_R = 0.0(7)$ for various RF pulse times, $\tau_{\rm pulse}$. Due to residual momentum after projection onto the bare states, the two spin components spatially separate and the contrast in each component is dependent on the ratio of atoms in the two momentum wells which is set by the RF pulse time before ramping on the Raman beams, $\tau_{\rm pulse}$. (b) Fitted contrast, $\mathcal{C}$, in each of the two spin components as a function of RF pulse time. The solid blue (dashed green) line shows the contrast in state $|\uparrow\rangle$ ($|\downarrow\rangle$) calculated using the zero order mixture picture with an ad-hoc scaling factor of 0.15 to account for finite imaging resolution and blurring by interactions. (c) Fitted fringe spacing, Δs, in each of the two components as a function of RF pulse time. Data points and error bars are means and standard deviations of 10 measurements. Data points with fringe contrast too small to distinguish by visual inspection have been converted to grey scale.

admixture of that spin in the almost unpopulated momentum well. On the other hand, the minority spin component corresponds in part to most of the atoms in the almost unpopulated momentum well and in part to the small admixture from the more populated momentum well. Thus, the minority spin component is approximately evenly distributed between the two projected momenta leading to high contrast.

To quantify the fringe contrast and extract the magnified fringe spacing we find the centre of mass with respect to the y-axis by integrating the experimental image along the x-axis and finding the first central moment of the resulting profile. We sum the three rows of pixels[5] from the experimental image around the centre of mass to get an approximation of the integrated density profile, $n_{\rm 1D}(x)$. We fit the integrated

[5]This does not cover the full extent of the BEC but does not change the result for a Gaussian transverse profile. By only summing the highest density part of the cloud, we increased the signal to noise ratio in $n_{\rm 1D}(x)$.

profile with

$$n_{1\mathrm{D}}(x) = A_\uparrow \exp\left[-\left(x - x_{0\uparrow}\right)^2 / \left(2\sigma_{x\uparrow}^2\right)\right] \left[1 + \mathcal{C}_\uparrow \cos\left(k_\uparrow x + \theta_{s\uparrow}\right)\right] + A_\downarrow \exp\left[-\left(x - x_{0\downarrow}\right)^2 / \left(2\sigma_{x\downarrow}^2\right)\right] \left[1 + \mathcal{C}_\downarrow \cos\left(k_\downarrow x + \theta_{s\downarrow}\right)\right]. \quad (7.6)$$

Figure 7.8(b) shows the fitted contrasts of the two spin components as a function of τ_{pulse}. We see that $\mathcal{C}_\uparrow$ ($\mathcal{C}_\downarrow$) decreases (increases) with increasing pulse time because the ratio of atoms in the two momentum components projected into state $|\uparrow'\rangle$ ($|\downarrow'\rangle$) increases (decreases) as S is decreased from 1 to -1. The solid blue (dashed green) line shows the expect value of $\mathcal{C}_\uparrow$ ($\mathcal{C}_\downarrow$) according to the zero order mixture picture with an ad-hoc scaling factor of 0.15 to account for finite optical resolution and blurring by interactions. Figure 7.8(c) shows the fringe spacing $\Delta s_\sigma = 2\pi/k_\sigma$ ($\sigma = \uparrow, \downarrow$) as a function of τ_{pulse}. The fringe spacing is not impacted by the value of S because it is set by the positions and momenta of the components at the end of the compression, as shown in Eq. 7.2.

The compression time of 0.7 ms has been selected to empirically optimise the observed fringe contrast in Fig. 7.8 in the presence of the bandwidth limited PID. By preparing fringes in state $|\downarrow\rangle$ with $\tau_{\mathrm{Bragg}} = 25$ μs and setting the compression time to 0.7 ms, we measure $\mathcal{C} = 0.06(3)$ and $\Delta s = 5.0(4)$ μm corresponding to the mean and standard deviation of 17 measurements. We estimate an effective magnification factor of 9.5(7) for the fringes prepared by Bragg diffraction. Based on Fig. 7.4 the initial momentum difference between the dressed BECs with $\hbar\Omega/E_R = 2.5(2)$ is $\delta k_x \approx k_R$ so the initial fringe spacing is $\Delta s \approx 2\pi/k_R \approx 1$ μm. A magnification factor of 9.5 would correspond to a measured fringe spacing of $\Delta s \approx 10$ μm which is larger than the measured value of $\Delta s \approx 6$ μm. We know that the preparation of the stripe phase has imparted mechanical momentum onto the BEC which means that the initial displacement between the dressed BECs is not necessarily zero and from Eq. 7.2, we know that this displacement will lower the measured fringe spacing. An initial displacement of a few microns would account for the discrepancy between the measured and expected fringe spacing, this is not unrealistic given the amplitude of oscillations estimated from Fig. 7.4.

Mechanical momentum affects the effective magnification factor of the matterwave lens. Varying the wait time between ramping on the Raman lasers and the matter wave lensing sequence will vary both the initial displacement between the dressed BECs and the initial difference in their group quasimomenta. Figure 7.9(a) and (b) show the fitted contrast and fringe spacing corresponding to the $|\uparrow\rangle$ component as a function of t_{hold} for the parameters of Fig. 7.8 with $\tau_{\mathrm{pulse}} = 15$ μs. Since we do not see any significant change in either parameter, we conclude that there is a compensation between the changing displacement and momentum difference between the dressed BECs and that the effective magnification is not strongly altered during the wait time.

Figure 7.10(a) shows a collage of matterwave lensing images as a function of Ω with $N_0 = 2.0(4) \times 10^4$, $\hbar\delta_0/E_R = 0.0(7)$, $t_{\mathrm{hold}} = 1.2$ ms, and $\tau_{\mathrm{pulse}} = 15$ μs. For $\hbar\Omega/E_R < 2$ the residual momentum remaining after the compression time of 0.7 ms

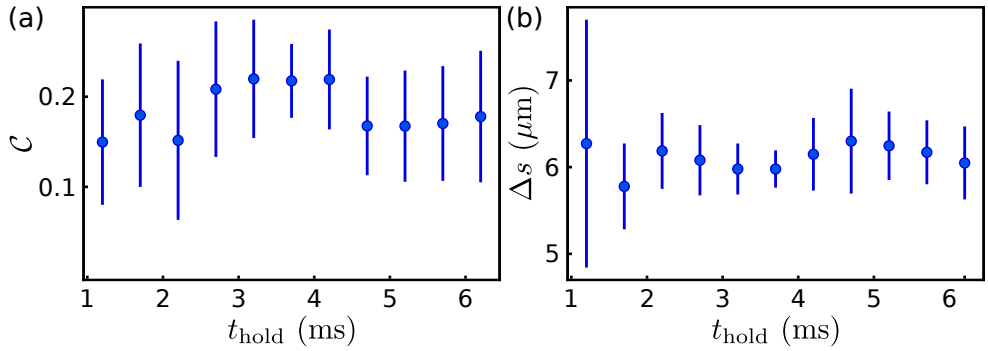

Figure 7.9: (a) Contrast, $\mathcal{C}$, and (b) fringe spacing, Δs, as a function of hold time, t_{hold}, before matterwave lensing with $N_0 = 2.0(4) \times 10^4$, $\hbar\Omega/E_R = 2.5$, $\hbar\delta_0/E_R = 0.0(7)$, and $\tau_{\mathrm{pulse}} = 15$ μs. Data points and error bars are means and standard deviations of 20 measurements. From this plot, we conclude that we are not able to observe oscillations in fringe spacing due to mechanical momentum because the initial displacements at the beginning of the lensing sequence compensate the changes in momentum.

is not sufficient to achieve full spatial separation of the spin components during the expansion time, $t_e = 7$ ms. We can see fringes on the right in the $|\uparrow\rangle$ component and not on the left in the $|\downarrow\rangle$ component, which is consistent with Fig. 7.8.

For analysis, we focus on $\hbar\Omega/E_R \geq 2$, where we have clear separation between the spin components. Figure 7.10(b) shows the fitted contrast of the $|\uparrow\rangle$ component as a function of Ω as well as the predictions for the groundstate (solid blue line) and the experimental ratio $S = 0.13(6)$ (dashed orange line) according to the zero order mixture picture. For the theory curves we have applied an ad-hoc scaling factor of 0.15 as in Fig. 7.8(b) to account for the finite imaging resolution and interactions. We see the expected increase in contrast with increasing Ω due to the increasing overlap of the two dressed BECs with respect to their bare spin compositions in agreement with the predicted values.

Figure 7.10(c) shows the fitted fringe spacing of the $|\uparrow\rangle$ component as a function of Ω as well as the prediction of the zero order mixture picture and the values corresponding to the quaismomenta inferred from time of flight measurements in Fig. 7.2(c). The predicted fringe spacing and the inferred fringe spacing have been scaled by a factor of 6 which is an estimated magnification factor based on the data in Fig. 7.9(b). The measured values are in good agreement with the inferred values given the uncertainty in the magnification factor. Both the measured and inferred fringe spacing are slightly higher than the prediction of the zero order mixture picture which is consistent with mechanical momentum reducing the difference in the group quasimomenta of the dressed BECs.

The measured fringe spacing after matterwave lensing shown in Fig. 7.10(c) demonstrates the increase in fringe spacing with increasing Raman Rabi frequency which has been predicted theoretically [168, 288] but not observed experimentally until now.

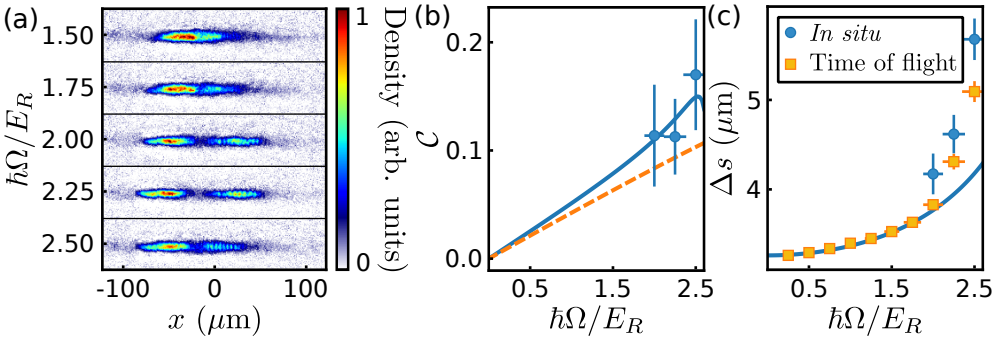

Figure 7.10: (a) Collage of density profiles after matterwave lensing with $N_0 = 2.0(4) \times 10^4$, $\hbar\delta_0/E_R = 0.0(7)$, $t_{\text{hold}} = 1.2$ ms, and $\tau_{\text{pulse}} = 15$ μs for various values of $\hbar\Omega/E_R$. (b) Fringe contrast, $\mathcal{C}$, corresponding to the $|\uparrow\rangle$ component. The solid blue line is the prediction for the groundstate from the zero order mixture picture and the dashed orange line is the prediction accounting for the measured ratio of atoms in the two momentum wells, $S = 0.13(6)$, which does not change during the experiment. Both lines have been scaled by an ad-hoc factor of 0.15 to account for finite imaging resolution and blurring due to interactions. (c) Fringe spacing, Δs, corresponding to the $|\uparrow\rangle$ component measured *in situ* with matterwave lensing and predicted from quasimomenta inferred from time of flight measurements in Fig. 7.2(c). The blue line shows the prediction of the zero order mixture picture without accounting for mechanical momentum. The time of flight and zero order mixture picture predictions have been scaled by a factor of 6 to account for the matterwave lensing magnification. Data points and vertical error bars are means and standard deviations of 20 (10) measurements for *in situ* (time of flight) data and horizontal error bars correspond to the upper bound of 6 % systematic uncertainty in Ω.

The change in fringe spacing with increasing Rabi frequency clearly sets the stripe phase apart from density modulations formed by a shallow optical lattice and can be taken as evidence of spontaneous symmetry breaking since the laser wavelength sets a length scale for the fringes but does not completely determine the fringe spacing. Since the matterwave lensing procedure results in effectively spin resolved images, it should be feasible to excite the spin dipole mode and observe spin dipole oscillations while simultaneously observing the oscillations in fringe spacing predicted in Ref. [308] and Fig. 6.14 in future experiments.

7.4 Summary

In this chapter, I have presented experimental measurements of the supersolid stripe phase in ^{41}K. Using time of flight measurements, I have examined the spin resolved momentum distribution of the Raman coupled system and measured quantities are consistent with the predictions made in Ch. 6. I have presented matterwave optics as a tool to magnify the density modulations associated with spontaneous breaking of translational symmetry in the stripe phase and presented the first optical images of these magnified stripes. The matterwave lensing images empirically demonstrate the

change in fringe spacing with changing optical power, in contrast to density modulations which would be induced by a shallow optical lattice. In the next chapter, I will outline potential future research directions and give some concluding remarks.

Chapter 8

Conclusion and Outlook

8.1 Thesis Summary

In this thesis I have described the quantum simulation of a topological gauge theory known as the chiral BF theory and an exotic state of matter known as a supersolid. In both cases, experiments have been implemented in two-component BECs of ^{39}K or ^{41}K. The two key ingredients linking the two sets of experiments described in this thesis are state-dependent and tunable two-body interactions and optical coherent coupling between the spin states. I have supplemented experimental results with extensive mean-field numerical simulations.

In Ch. 2, I introduced the experimental apparatus used in this thesis. In Ch. 3, I have presented coherent coupling as a means of controlling interactions of atoms in dressed states, as has been described in more detail in Ref. [217]. Building from the use of coherent coupling to control interactions, I have described our implementation of Raman coupling to create momentum-dependent dressed states and control the interactions in a dressed BEC by controlling the group momentum of the BEC.

In Ch. 4, I have followed Ref. [118] and shown how the chiral BF theory, which is a dimensional reduction of the Chern-Simons theory used to describe fractional quantum Hall states, preserves the chiral edge dynamics of the Chern-Simons theory in the form of chiral solitons. Since the chiral BF theory is a topological gauge theory, the gauge field does not have dynamics in the absence of matter. Following the Faddeev-Jackiw formalism, all of the dynamics of the theory can be encoded in the dynamics of the matter coupled to a density-dependent gauge field yielding a second quantised Hamiltonian which is amenable to quantum simulation.

In Ch. 5, I have shown how the momentum-dependent interactions of a BEC under the influence of Raman coupling can be mapped to the encoded Hamiltonian of the chiral BF theory as in Ref. [118]. I have also reported the experimental realisation of chiral solitons which are matter wave packets which propagate without dispersion when moving in one direction but not the other and the experimental observation of a density-dependent vector potential which manifests as asymmetric expansion dynamics. The experimental results in Ch. 5 have been published in Ref. [132]. I have

evaluated the quality of the mapping of the Raman coupled BEC using mean-field numerical simulations in the XMDS2 package [286] and found good agreement at coupling strengths much lower than those required for the proposal of Edmonds *et al.* in the position space adiabatic approximation [131]. Some of the numerical results in Ch. 5 have been published in Ref. [118].

In Ch. 6, I have focused on the regime of small Raman Rabi frequencies where the dressed state dispersion relation features two minima allowing for the simultaneous condensation of two nonorthogonal dressed BECs [67, 166, 167]. The two nonorthogonal dressed BECs correspond to distinct quasimomenta but are at rest in the laboratory frame which allows for a spontaneous breaking of translational symmetry due to matterwave interference for appropriate interactions. The striped pattern corresponding to the translational symmetry breaking combined with the superfluid properties of the dressed BECs constitute a supersolid state known as the stripe phase [111, 168].

We have developed a mixture model for the two dressed BECs following the same formalism as the mapping of the Raman coupled BEC to the chiral BF theory. Using this mixture model, I have derived analytic expressions for the phase boundaries of the stripe phase and for the frequencies of collective modes in the stripe phase and the magnetised plane wave phase. I have benchmarked the analytical expressions against a variational ansatz [168, 288] and mean-field numerical simulations and found them to be valid at atomic densities corresponding to typical experimental parameters.

Finally, in Ch. 7, I have presented experiments in the stripe phase. First, we investigated the spin-resolved momentum distribution of atoms in the stripe phase using time of flight measurements. Then, we employed matterwave lensing techniques [342, 343] to magnify the density modulations of the stripe phase and directly image them for the first time. In doing so, we have shown that the fringe spacing is dependent on the Raman coupling strength. The dependence of the fringe spacing on the coupling strength is in contrast to density modulations formed in a shallow optical lattice.

8.2 Future Directions

Much has been learned about matterwave bright solitons from their collision dynamics [351]. The dynamics of collisions between pairs of single-component solitons are integrable, meaning that the solitons either bounce off of each other or pass through each other unperturbed, depending on the relative phase between them [274]. Chiral solitons have been predicted to have nonintegrable dynamics meaning that the collision dynamics depend not only on the phase but also on the relative atom number of the two solitons [274, 352].

During the collision, the solitons may bounce off or pass through each other similarly to normal solitons if the two-body contact interactions are much stronger than the current-density interaction [274]. If the current-density term is the dominant interaction, atoms may be transferred from one soliton to another, the solitons may merge, or the collision may result in soliton fission with more outgoing solitons than incoming solitons [274]. A technical challenge for studying chiral soliton collisions is that they only exist propagating in one direction which means that the collision

should take place with the two solitons moving in the same direction but with different momenta [274]. This condition would be complicated to implement using Bragg diffraction as we have done in Ch. 5 but a laser based accelerator would allow for precise control of the relative momentum of two or more solitons [353].

The chiral BF theory was introduced as a model for linear anyons [113, 114], one-dimensional particles which are neither bosonic nor fermionic but acquire a phase jump upon exchange of two particles [354, 355]. The chiral BF theory corresponds to a continuum theory for linear anyons in a regime where both two- and three-body interactions are important and the contact interactions and current-density interaction have a proper dependence on the exchange phase [262]. For small values of the exchange phase, corresponding to "almost-bosonic" anyons, this theory corresponds to the Kundu linear anyon model [261].

Strong interactions can be achieved in one-dimensional BECs. Strong interactions would enable the observation of quantum effects in the chiral BF theory but would also increase the momentum spread of the BEC and therefore require a greater Raman Rabi frequency to simulate the chiral BF theory. A current project by Dr. Josep Cabedo, Prof. Dr. Leticia Tarruell, and Dr. Alessio Celi indicates that larger exchange phases can be obtained by realising the chiral BF theory in a lattice with strong interactions.

In two-dimensions, a two-component BEC with angular momentum-dependent interactions stemming from Raman coupling has been mapped to the Chern-Simons theory in the position space adiabatic limit [356]. Almost-bosonic anyons in two-dimensions appear as quantised vortices [357]. In the adiabatic limit in position space, the chiral BF theory is expected to support density-dependent chiral persistent currents on a ring [131]. A current project by Claudio Iacovelli, Prof. Dr. Leticia Tarruell, and Dr. Alessio Celi aims to apply a similar approach to the one used in Ch. 5 to map a BEC in a ring trap with angular momentum Raman coupling to the chiral BF theory with periodic boundary conditions as an intermediate step to performing the mapping for the two-dimensional Chern-Simons theory. In the ring geometry, the topological gauge field can not be completely eliminated which results in an extra Aharonov-Bohm phase for particles moving around the ring. The density dependence of the residual magnetic field is responsible for the density dependence of the persistent currents.

Coupling the angular momentum of the atoms would require spatial shaping of the Raman beams, which could be achieved using a spatial light modulator [37] or a digital micromirror device [39], for example. Spatial control of the Raman beam intensity profiles would open the door for the quantum simulation of analogue gravity. For example, arbitrary event horizon configurations could be generated in one dimension [358] and charged phonons coupled to both gravitational and electromagnetic fields could be produced in two dimensions [359].

Turning towards the supersolid stripe phase, one possible research direction is to revisit previous experiments performed in our group studying quantum liquid droplets stabilised by beyond mean-field effects [99]. It has been shown numerically that beyond mean-field effects stabilise the stripe phase for a wider range of parameters than predicted at the mean-field level for sufficiently high atomic densities [360]. Furthermore, it is possible to produce a quantum liquid droplet in the stripe phase [361–363].

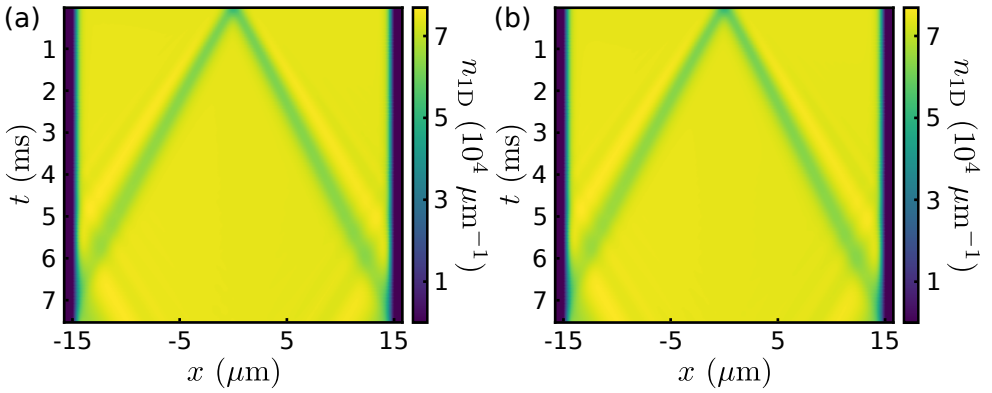

Figure 8.1: Integrated density profiles corresponding to chiral sound propagation using the same parameters as Fig. 6.17 except $\hbar\Omega/E_R = 10$. The density profiles have been calculated using (a) Eq. 5.20 and (b) Eq. 5.21.

At the mean-field level, there remains a large amount of experimental work to be done on both the static properties and the collective modes of the stripe phase. In particular, one would like to collect a large amount of statistics on the fringe position across various experimental realisations to demonstrate the randomness of the fringe phase. Furthermore, studies on the coherence of the stripe phase could be performed using Talbot-interferometry [112, 364] and matterwave lensing.

Aside from measuring the collective mode frequencies in the stripe phase, an important feature showing that the stripes are not rigid (as they would be in an optical lattice) is the predicted oscillations of fringe spacing and contrast. In the same spirit, it would be fascinating to directly observe the zero energy Goldstone mode by tracking the fringe phase as a function of time using matterwave lensing. Since our imaging technique is destructive, and matterwave lensing is incompatible with minimally destructive imaging techniques [365], this would require using a shallow optical lattice which is nearly commensurate with the fringe spacing in the stripe phase to pin the initial phase before releasing it.

Measurements of the speed of sound in the stripe phase could be used to estimate the superfluid fraction [366, 367] and, as shown in Fig. 6.17, would reveal chiral properties in the stripe phase. Figure 8.1 shows the integrated density profiles corresponding to the same parameters as Fig. 6.17 except $\hbar\Omega/E_R = 10$ for (a) the full two-component system corresponding to Eq. 5.20 and (b) the effective chiral BF mapping corresponding to Eq. 5.21. We can see that sound propagates slightly faster to the left than to the right and the full and effective profiles are practically indistinguishable, this shows that chiral sound is a feature of the chiral BF theory.

The next order corrections to the zero order mixture picture include third order kinetic energy contributions as well as intrawell and interwell current-density interaction terms similar to the current-density interaction of the chiral BF theory. Additionally, the two-dimensional Chern-Simons theory supports supersolid states [368]. These results hint at a gauge theory description of the supersolid stripe phase.

Appendix A

Numerical Simulation of a Chiral Soliton Reflecting from an Optical Barrier

For an additional insight into the dynamics of the chiral soliton bouncing from an optical barrier, we numerically simulate the equations of motion corresponding to the full two-component system in the presence of Raman coupling, corresponding to Eq. 5.20, using XMDS2 [286]. We discretise the x-axis with 2^{11} grid points and a grid spacing of 56.3 nm and we discretise the y and z-axes with 2^5 grid points and a grid spacing of 675.3 nm. We consider a simplified version of the experiment where we completely neglect the 1 % difference in polarisabilities for the bare spin states at the barrier wavelength.

For the simulation shown in this appendix, we use a tighter Gaussian potential in place of the barrier in Fig. 5.4 given by

$$V_{\text{barrier}}(\mathbf{r}) = \frac{A}{\sqrt{1-(z/z_x)^2}\sqrt{1-(z/z_y)^2}} \exp\left[-2\frac{(x-x_0)^2}{w_x^2} - 2\frac{y^2}{w_y^2}\right] \tag{A.1}$$

where $A/E_R = 10$, $x_0 = -93.6$ μm, $w_x = 4.25$ μm, $w_y = 200$ μm, and $z_j = \pi w_j^2/\lambda_{\text{barrier}}$ for $j = x, y$. We set $\hbar\Omega/E_R = 5.3$, $\hbar\delta_0/E_R = -2.832$, $N = \int |\phi_\uparrow|^2 + |\phi_\downarrow|^2 \mathrm{d}^3\mathbf{r} = 4000$, and $V(\mathbf{r}) = V_{\text{barrier}}(\mathbf{r}) + m\left(\omega_x^2 x^2 + \omega_y^2 y^2 + \omega_z^2 z^2\right)/2$.

We compute the groundstate in imaginary time with $\omega_x/(2\pi) = 75.5$ Hz, $\omega_y/(2\pi) = 97.8$ Hz, and $\omega_z/(2\pi) = 51.4$ Hz. To approximate the kick with the running lattice, we set $\omega_x/(2\pi) = 0$ Hz and add a potential given by $V_{\text{kick}}(x) = \hbar k_B x/\Delta t$ for a duration $\Delta t = 0.32$ ms. After the kick time, we remove the potential, $V_{\text{kick}}(x)$, and compute the real time dynamics. The position and width of the BEC are given by μ_1 and $\sigma_x = \sqrt{\mu_2}$, respectively where μ_j is the j^{th} central moment of the total density. We compute the group momentum of the BEC as $\langle k_x \rangle = \int k_x \left[|\Phi'_\uparrow(\mathbf{k})|^2 + |\Phi'_\downarrow(\mathbf{k})|^2\right] \mathrm{d}^3\mathbf{k} / \left[N\,(2\pi)^3\right]$.

Figure A.1 shows the integrated density, $n_{1\text{D}} = \int n(\mathbf{r})\mathrm{d}y\mathrm{d}z$, and Fig. A.2 shows (a) the position, μ_1, (b) the group momentum, $\langle k_x \rangle$, (c) the spin polarisation, P, and (d)

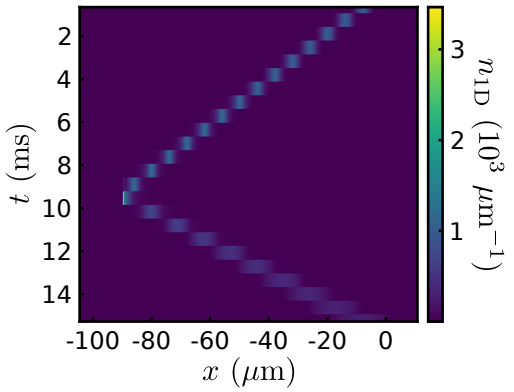

Figure A.1: Integrated density, $n_{1D} = \int n(\mathbf{r})\mathrm{d}y\mathrm{d}z$, of a Raman dressed BEC accelerated towards an optical barrier with $\hbar\Omega/E_R = 5.3$, $\hbar\delta_0/E_R = -2.832$, $N = 4000$, $a_{\uparrow\uparrow} = -4.9a_0$, $a_{\downarrow\downarrow} = 24.6a_0$, and $a_{\uparrow\downarrow} = -13.9a_0$.

the width, σ_x, of the BEC as it approaches and reflects from the potential, $V_{\mathrm{barrier}}(\mathbf{r})$. We can see that the position and group momentum of the BEC before collision with the barrier are consistent with the expected group momentum $\hbar k_{\mathrm{in}} = \hbar(k_{\mathrm{min}} - k_B)$ and group velocity $v_{\mathrm{in}} = \partial_{k_x}\varepsilon_-/\hbar|_{k_x=k_{\mathrm{in}}}$. Likewise, the position and group momentum of the BEC after reflection from the barrier are consistent with an outgoing group momentum defined by $\varepsilon_-(k_{\mathrm{out}}) = \varepsilon_-(k_{\mathrm{in}})$ corresponding to group velocity $v_{\mathrm{out}} = \partial_{k_x}\varepsilon_-/\hbar|_{k_x=k_{\mathrm{out}}}$. The polarisation is close to $P = 0$ before reflecting from the barrier because $\hbar\tilde{\delta}(k_{\mathrm{in}})/E_R = 0$. There are small oscillations in the polarisation because of the sudden removal of $V_{\mathrm{kick}}(x)$ (see inset of Fig. A.2(c)). After reflection from the barrier we have $P \approx -0.9$ because $\tilde{\delta}(k_{\mathrm{out}}) \approx -2\Omega$.

The initial width of the BEC is significantly smaller than the soliton shown in Fig. 5.3(a). This is because, for the imaginary time evolution, we have confinement along the x-axis and $g_{\mathrm{eff}}(k_{\mathrm{min}})N$ is small compared to $\hbar\omega_x$ so the size of the BEC is close to the harmonic oscillator length, $\sqrt{\hbar/(m\omega_x)}$. In the experiment, the initial width is larger because of the dynamics during the preparation of the Raman dressed BEC. In Fig. A.2(d), the width is slowly increasing before colliding with the barrier because the initial width is smaller than the equilibrium size of the soliton. The increase in the width is small because the excess kinetic energy has to work against the attractive interactions. The time scale of oscillations of the soliton width are on the order of 100 ms. In contrast, the experimental width in Fig. 5.3(c) is initially constant because the out of equilibrium initial width is close to the equilibrium width after the interaction quench. The slight decrease in width after $t = 15$ ms in Fig. 5.3(c) is attributed to slow oscillations of the width.

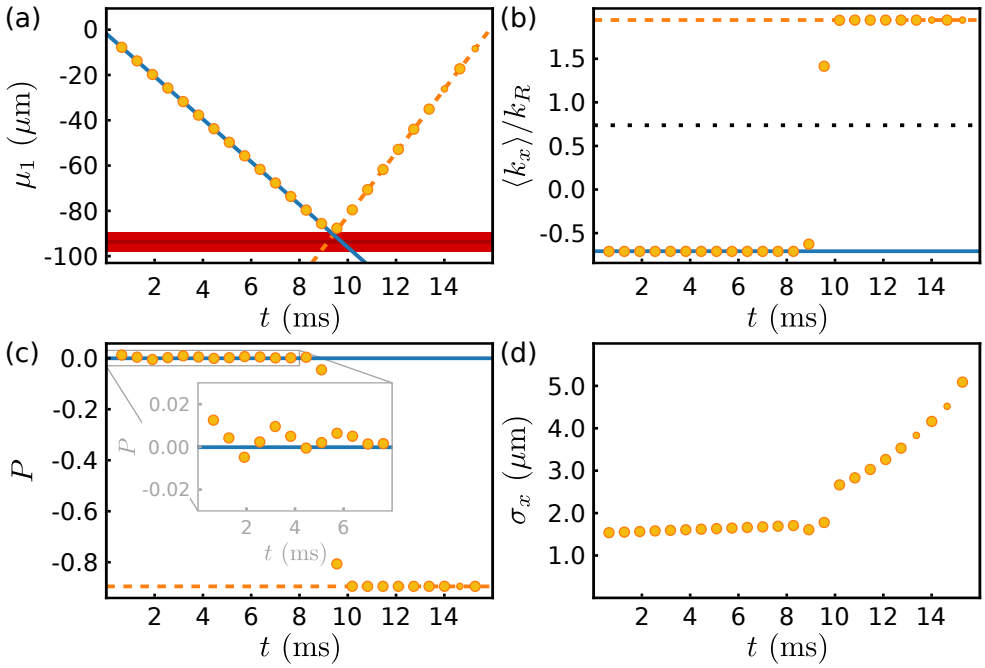

Figure A.2: Numerical simulation of a Raman dressed BEC accelerated towards an optical barrier with $\hbar\Omega/E_R = 5.3$, $\hbar\delta_0/E_R = -2.832$, $N = 4000$, $a_{\uparrow\uparrow} = -4.9a_0$, $a_{\downarrow\downarrow} = 24.6a_0$, and $a_{\uparrow\downarrow} = -13.9a_0$. (a) Position, μ_1, of the BEC, the slope of the solid blue line is v_{in} and the slope of the dashed orange line is v_{out}. The solid red line indicates the position of the optical barrier and the red shaded area indicates the $1/\exp(2)$ radius of the barrier. (b) Group momentum, $\langle k_x \rangle$, the solid blue line, dashed orange line and dotted black line show k_{in}, k_{out}, and k_{min}, respectively. (c) Spin polarisation, P, the solid blue line shows $P(k_{\text{in}}) = \tilde{\delta}(k_{\text{in}})/\tilde{\Omega}(k_{\text{in}})$ and the dashed orange line shows $P(k_{\text{out}}) = \tilde{\delta}(k_{\text{out}})/\tilde{\Omega}(k_{\text{out}})$. The inset shows the initial oscillations in the polarisation after acceleration. (d) The width, σ_x, of the BEC increases slowly before colliding with the barrier due to being below the equilibrium value. During interaction with the barrier there is slight compression of the BEC followed by rapid expansion after reflection.

Appendix B

Asymmetry Extracted From Experimental Images

In this appendix, I will explain the procedure used to extract the values of skewness shown in Fig. 5.7(c) from experimental images. As explained in Sec. 2.4.1, the *in situ* images shown in Fig. 5.7(a) correspond to integrating the three-dimensional density distribution over the z-axis. We are interested in the density distribution along the x-axis only, the skewness extraction process starts with summing over the rows of the *in situ* images which approximates integration over the y-axis. We take the Fourier transform of the integrated density profile and enforce that the power spectral density is smooth at low spatial frequencies in order to remove any constant offset from the density profile.

The evaluation of central moments is sensitive to noise at large values of x and negative values in the density profile can result in unphysical evaluations of $\sigma_x^2 < 0$. This means it is necessary to further process the data. We choose a cut off frequency by finding a local minimum in the power spectral density where the value of the power spectral density is less than 1 % of the maximum value. In the case of two or more minima meeting this criterion, we choose the one corresponding to the lowest spatial frequency. We use the algorithmically determined cut off frequency to low pass filter the data.

This low pass filtering method is not able to remove low frequency noise from the images. To improve upon the low pass filtering, we detect the edges of the density profile in a two step process. First, we divide the data into segments defined by the zero-crossings of the data. Since negative density is unphysical we set the value in all of the segments except the segment containing the maximum value to zero. Then, we look for local minima in the data and split the data into segments with edges defined by the points where the value of a local minimum is less than 3 % of the peak value and set the segments which don't include the peak to zero. Finally we normalise the profile and extract the central moments. The image processing work flow is illustrated in Fig. B.1 using the *in situ* image of a Raman coupled BEC with $\hbar\Omega/E_R = 4.5(3)$ and $\hbar\delta_0/E_R = -0.58(6)$ after 8 ms of expansion in an optical waveguide as an example.

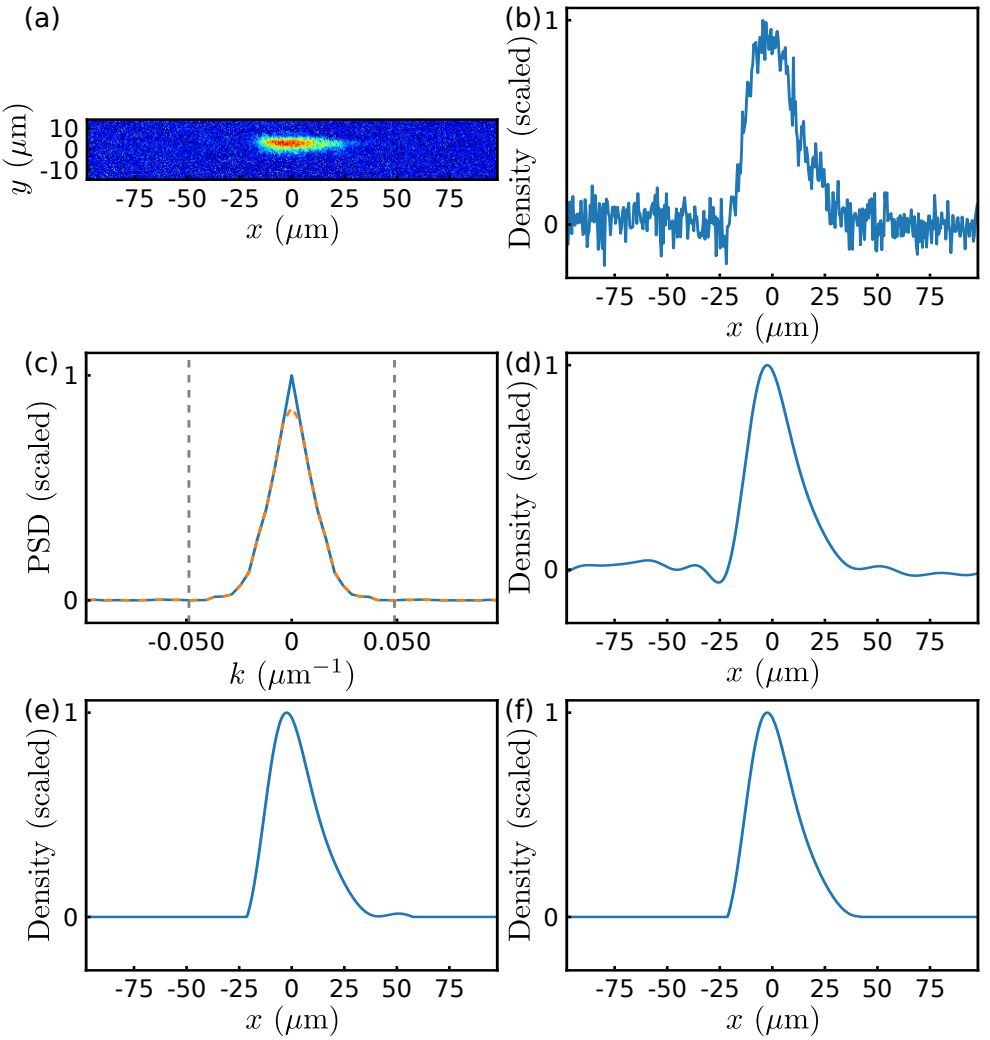

Figure B.1: Image filtering sequence for skewness extraction. (a) *In situ* image of a Raman coupled BEC with $\hbar\Omega/E_R = 4.5(3)$ and $\hbar\delta_0/E_R = -0.58(6)$ after 8 ms of expansion in an optical waveguide. (b) Integrated density profile before the filtering process with the maximum value scaled to unity. (c) Power spectral density (PSD) of the integrated density profile (solid blue line). The dashed orange line shows the PSD after forcing smoothness at low spatial frequency to remove the constant offset from the density profile. The dashed grey lines mark the algorithmically determined cut off frequency as described in the text. (d) Integrated density profile after low pass filtering with the maximum value rescaled to unity. (e) Filtered density profiles with values outside of the central nodes set to zero. (f) Second pass edge detection using a local minimum with value less than 3 % of the peak density to arrive at the filtered density from which central moments can be extracted.

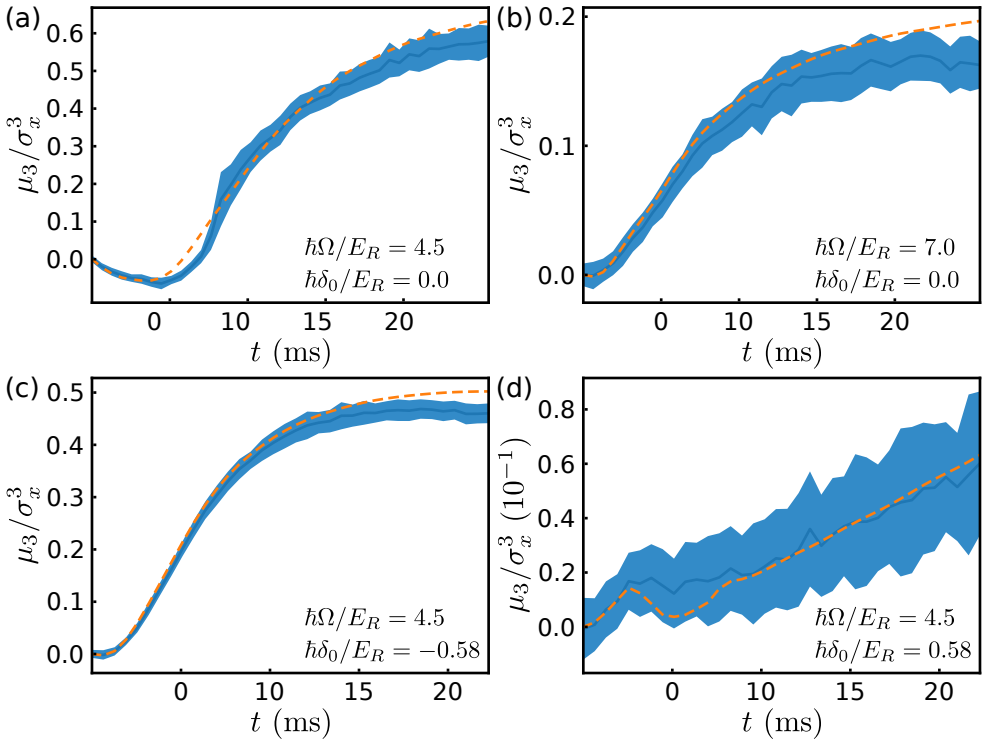

Figure B.2: Comparing the skewness extracted from numerical density profiles with and without noise for (a) $\hbar\Omega/E_R = 4.5$ and $\hbar\delta_0 = 0.0$, (b) $\hbar\Omega/E_R = 7.0$ and $\hbar\delta_0 = 0.0$, (c) $\hbar\Omega/E_R = 4.5$ and $\hbar\delta_0 = -0.58$, and (d) $\hbar\Omega/E_R = 4.5$ and $\hbar\delta_0 = 0.58$. The orange dashed lines show the skewness without noise and the solid blue lines show the skewness averaged over 100 noise realisations. The blue shaded area represents the standard deviation over 100 noise realisations.

To test the filtering process, we take integrated asymmetric density profiles from numerical simulations where the skewness can be evaluated without noise. We add uniformly distributed pseudorandom numbers with zero mean and peak to peak amplitude equal to 10 % of the peak integrated density at $t = 0$. We apply the same filtering algorithm as with the experimental images and compute the skewness, which we compare to the skewness calculated without adding noise. Figure B.2 shows the results for various values of Ω and δ_0 corresponding to simulations which do not include atom losses. We create 100 independent noise realisations for each numerical density profile and average the extracted skewness after filtering over all realisations.

We find good agreement between the skewness extracted without added noise and the skewness extracted with added noise after filtering which demonstrates the robustness of the filtering. I have additionally verified the filtering method using noise extracted from experimental images in place of the pseudorandom numbers.

References

[1] R. P. Feynman, International Journal of Theoretical Physics **21**, 467 (1982) (Cited on pages 1, 2, and 4).

[2] J. Preskill, Quantum **2**, 79 (2018) (Cited on page 1).

[3] J. W. Z. Lau, K. H. Lim, H. Shrotriya, and L. C. Kwek, AAPPS Bulletin **32**, 27 (2022) (Cited on page 1).

[4] T. Freeth, Y. Bitsakis, X. Moussas, J. H. Seiradakis, A. Tselikas, H. Mangou, M. Zafeiropoulou, R. Hadland, D. Bate, A. Ramsey, M. Allen, A. Crawley, P. Hockley, T. Malzbender, D. Gelb, W. Ambrisco, and M. G. Edmunds, Nature **444**, 587 (2006) (Cited on page 1).

[5] D. E. Cartwright, *Tides. A Scientific History* (Cambridge University Press. 2001) (Cited on page 1).

[6] B. J. Copeland. In: *The Stanford Encyclopedia of Philosophy*. Ed. by E. N. Zalta (Metaphysics Research Lab, Stanford University. Winter 2020. 2020) (Cited on page 1).

[7] J. A. Graf, The Military Engineer **49**, 365 (1957) (Cited on page 1).

[8] V. Saxena, X. Wu, I. Srivastava, and K. Zhu, Journal of Low Power Electronics and Applications **8**, 34 (2018) (Cited on page 1).

[9] J. I. Cirac and P. Zoller, Nature Physics **8**, 264 (2012) (Cited on page 2).

[10] A. Trabesinger, Nature Physics **8**, 263 (2012) (Cited on page 2).

[11] I. M. Georgescu, S. Ashhab, and F. Nori, Reviews of Modern Physics **86**, 153 (2014) (Cited on page 2).

[12] A. Aspuru-Guzik and P. Walther, Nature Physics **8**, 285 (2012) (Cited on page 2).

[13] A. Micheli, G. K. Brennen, and P. Zoller, Nature Physics **2**, 341 (2006) (Cited on page 2).

[14] M. Lewenstein, Nature Physics **2**, 309 (2006) (Cited on page 2).

[15] E. Manousakis, Journal of Low Temperature Physics **126**, 1501 (2002) (Cited on page 2).

[16] H. Weimer, M. Müller, I. Lesanovsky, P. Zoller, and H. P. Büchler, Nature Physics **6**, 382 (2010) (Cited on page 2).

[17] H. Labuhn, D. Barredo, S. Ravets, S. de Léséleuc, T. Macrì, T. Lahaye, and A. Browaeys, Nature **534**, 667 (2016) (Cited on page 2).

[18] D. Barredo, S. de Léséleuc, V. Lienhard, T. Lahaye, and A. Browaeys, Science **354**, 1021 (2016) (Cited on page 2).

[19] H. Bernien, S. Schwartz, A. Keesling, H. Levine, A. Omran, H. Pichler, S. Choi, A. S. Zibrov, M. Endres, M. Greiner, V. Vuletić, and M. D. Lukin, Nature **551**, 579 (2017) (Cited on pages 2 and 5).

[20] A. A. Houck, H. E. Türeci, and J. Koch, Nature Physics **8**, 292 (2012) (Cited on page 2).

[21] R. Blatt and C. F. Roos, Nature Physics **8**, 277 (2012) (Cited on page 2).

[22] M. Lewenstein, A. Sanpera, V. Ahufinger, B. Damski, A. Sen(De), and U. Sen, Advances in Physics **56**, 243 (2007) (Cited on pages 2 and 3).

[23] I. Bloch, J. Dalibard, and W. Zwerger, Reviews of Modern Physics **80**, 885 (2008) (Cited on page 2).

[24] I. Bloch, J. Dalibard, and S. Nascimbène, Nature Physics **8**, 267 (2012) (Cited on page 2).

[25] M. H. Anderson, J. R. Ensher, M. R. Matthews, C. E. Wieman, and E. A. Cornell, Science **269**, 198 (1995) (Cited on pages 2, 9, and 21).

[26] K. B. Davis, M.-O. Mewes, M. R. Andrews, N. J. van Druten, D. S. Durfee, D. M. Kurn, and W. Ketterle, Physical Review Letters **75**, 3969 (1995) (Cited on pages 2 and 9).

[27] C. C. Bradley, C. A. Sackett, J. J. Tollett, and R. G. Hulet, Physical Review Letters **75**, 1687 (1995) (Cited on pages 2 and 9).

[28] S. Inouye, M. R. Andrews, J. Stenger, H.-J. Miesner, D. M. Stamper-Kurn, and W. Ketterle, Nature **392**, 151 (1998) (Cited on pages 2 and 9).

[29] Ph. Courteille, R. S. Freeland, D. J. Heinzen, F. A. van Abeelen, and B. J. Verhaar, Physical Review Letters **81**, 69 (1998) (Cited on pages 2 and 9).

[30] S. L. Cornish, N. R. Claussen, J. L. Roberts, E. A. Cornell, and C. E. Wieman, Physical Review Letters **85**, 1795 (2000) (Cited on pages 2 and 9).

[31] C. Chin, R. Grimm, P. Julienne, and E. Tiesinga, Reviews of Modern Physics **82**, 1225 (2010) (Cited on pages 2 and 9).

[32] M. Ueda, *Fundamentals and new frontiers of Bose-Einstein condensation* (World Scientific. Singapore. 2010) (Cited on pages 2 and 6).

[33] M. C. Fischer, K. W. Madison, Q. Niu, and M. G. Raizen, Physical Review A **58**, R2648 (1998) (Cited on pages 2 and 6).

[34] K. W. Madison, M. C. Fischer, R. B. Diener, Q. Niu, and M. G. Raizen, Physical Review Letters **81**, 5093 (1998) (Cited on pages 2 and 6).

[35] M. Greiner, I. Bloch, O. Mandel, T. W. Hänsch, and T. Esslinger, Physical Review Letters **87**, 160405 (2001) (Cited on pages 2, 6, and 39).

[36] J. Hecker Denschlag, J. E. Simsarian, H. Häffner, C. McKenzie, A. Browaeys, D. Cho, K. Helmerson, S. L. Rolston, and W. D. Phillips, Journal of Physics B: Atomic, Molecular and Optical Physics **35**, 3095 (2002) (Cited on pages 2 and 6).

[37] V. Boyer, R. M. Godun, G. Smirne, D. Cassettari, C. M. Chandrashekar, A. B. Deb, Z. J. Laczik, and C. J. Foot, Physical Review A **73**, 031402 (2006) (Cited on pages 2 and 139).

[38] K. Henderson, C. Ryu, C. MacCormick, and M. G. Boshier, New Journal of Physics **11**, 043030 (2009) (Cited on page 2).

[39] G. Gauthier, I. Lenton, N. M. Parry, M. Baker, M. J. Davis, H. Rubinsztein-Dunlop, and T. W. Neely, Optica **3**, 1136 (2016) (Cited on pages 2 and 139).

[40] E. A. Martinez, C. A. Muschik, P. Schindler, D. Nigg, A. Erhard, M. Heyl, P. Hauke, M. Dalmonte, T. Monz, P. Zoller, and R. Blatt, Nature **534**, 516 (2016) (Cited on pages 2, 5, 53, 54, and 56).

[41] N. Klco, E. F. Dumitrescu, A. J. McCaskey, T. D. Morris, R. C. Pooser, M. Sanz, E. Solano, P. Lougovski, and M. J. Savage, Physical Review A **98**, 032331 (2018) (Cited on page 2).

[42] C. Kokail, C. Maier, R. van Bijnen, T. Brydges, M. K. Joshi, P. Jurcevic, C. A. Muschik, P. Silvi, R. Blatt, C. F. Roos, and P. Zoller, Nature **569**, 355 (2019) (Cited on pages 2, 5, and 54).

[43] H.-H. Lu, N. Klco, J. M. Lukens, T. D. Morris, A. Bansal, A. Ekström, G. Hagen, T. Papenbrock, A. M. Weiner, M. J. Savage, and P. Lougovski, Physical Review A **100**, 012320 (2019) (Cited on page 2).

[44] C. Schweizer, F. Grusdt, M. Berngruber, L. Barbiero, E. Demler, N. Goldman, I. Bloch, and M. Aidelsburger, Nature Physics **15**, 1168 (2019) (Cited on pages 2 and 5).

[45] F. Görg, K. Sandholzer, J. Minguzzi, R. Desbuquois, M. Messer, and T. Esslinger, Nature Physics **15**, 1161 (2019) (Cited on pages 2, 3, and 5).

[46] A. Mil, T. V. Zache, A. Hegde, A. Xia, R. P. Bhatt, M. K. Oberthaler, P. Hauke, J. Berges, and F. Jendrzejewski, Science **367**, 1128 (2020) (Cited on pages 2 and 5).

[47] B. Yang, H. Sun, R. Ott, H.-Y. Wang, T. V. Zache, J. C. Halimeh, Z.-S. Yuan, P. Hauke, and J.-W. Pan, Nature **587**, 392 (2020) (Cited on pages 2 and 5).

[48] Y. Y. Atas, J. Zhang, R. Lewis, A. Jahanpour, J. F. Haase, and C. A. Muschik, Nature Communications **12**, 6499 (2021) (Cited on page 2).

[49] W. N. Cottingham and D. A. Greenwood, *An Introduction to the Standard Model of Particle Physics* (Cambridge University Press. Cambridge. Second. 2007) (Cited on page 2).

[50] G. Altarelli, *Collider Physics within the Standard Model: A Primer*. Ed. by J. Wells (Springer Nature. Cham. 2017) (Cited on page 2).

[51] M. E. Peskin and D. V. Schroeder, *An Introduction to Quantum Field Theory* (CRC Press. Boca Raton. 2018) (Cited on page 2).

[52] X.-G. Wen, *Quantum field theory of many-body systems. from the origin of sound to an origin of light and electrons* (Oxford University Press. New York. 2004) (Cited on pages 2, 4, 47, 48, and 49).

[53] E. Fradkin, *Field Theories of Condensed Matter Physics* (Cambridge University Press. Cambridge. Second. 2013) (Cited on pages 2 and 47).

[54] K. W. Madison, F. Chevy, W. Wohlleben, and J. Dalibard, Physical Review Letters **84**, 806 (2000) (Cited on page 2).

[55] K. W. Madison, F. Chevy, W. Wohlleben, and J. Dalibard, Journal of Modern Optics **47**, 2715 (2000) (Cited on page 2).

[56] J. R. Abo-Shaeer, C. Raman, J. M. Vogels, and W. Ketterle, Science **292**, 476 (2001) (Cited on page 2).

[57] P. Engels, I. Coddington, P. C. Haljan, V. Schweikhard, and E. A. Cornell, Physical Review Letters **90**, 170405 (2003) (Cited on page 2).

[58] P. E. Parks and R. J. Donnelly, Physical Review Letters **16**, 45 (1966) (Cited on page 2).

[59] E. J. Yarmchuk and R. E. Packard, Journal of Low Temperature Physics **46**, 479 (1982) (Cited on page 2).

[60] N. R. Cooper, Advances in Physics **57**, 539 (2008) (Cited on page 2).

[61] A. L. Fetter, Reviews of Modern Physics **81**, 647 (2009) (Cited on page 2).

[62] J. Stenger, S. Inouye, D. M. Stamper-Kurn, H.-J. Miesner, A. P. Chikkatur, and W. Ketterle, Nature **396**, 345 (1998) (Cited on page 2).

[63] J. Higbie and D. M. Stamper-Kurn, Physical Review Letters **88**, 090401 (2002) (Cited on pages 2, 6, 7, and 33).

[64] N. Goldman, G. Juzeliūnas, P. Öhberg, and I. B. Spielman, Reports on Progress in Physics **77**, 126401 (2014) (Cited on pages 2 and 33).

[65] Y.-J. Lin, R. Compton, A. Perry, W. Phillips, J. Porto, and I. Spielman, Physical Review Letters **102**, 130401 (2009) (Cited on pages 3, 7, 38, and 39).

[66] Y.-J. Lin, R. L. Compton, K. Jiménez-García, J. V. Porto, and I. B. Spielman, Nature **462**, 628 (2009) (Cited on page 3).

[67] Y.-J. Lin, K. Jiménez-García, and I. B. Spielman, Nature **471**, 83 (2011) (Cited on pages 3, 7, 33, 83, 84, 85, 90, 91, 94, 97, 117, 119, and 138).

[68] L. W. Clark, B. M. Anderson, L. Feng, A. Gaj, K. Levin, and C. Chin, Physical Review Letters **121**, 030402 (2018) (Cited on pages 3 and 5).

[69] K.-X. Yao, Z. Zhang, and C. Chin, Nature **602**, 68 (2022) (Cited on pages 3 and 5).

[70] P. Roushan, C. Neill, A. Megrant, Y. Chen, R. Babbush, R. Barends, B. Campbell, Z. Chen, B. Chiaro, A. Dunsworth, A. Fowler, E. Jeffrey, J. Kelly, E. Lucero, J. Mutus, P. J. J. O'Malley, M. Neeley, C. Quintana, D. Sank, A. Vainsencher, J. Wenner, T. White, E. Kapit, H. Neven, and J. Martinis, Nature Physics **13**, 146 (2017) (Cited on page 3).

[71] V. Lienhard, P. Scholl, S. Weber, D. Barredo, S. de Léséleuc, R. Bai, N. Lang, M. Fleischhauer, H. P. Büchler, T. Lahaye, and A. Browaeys, Physical Review X **10**, 021031 (2020) (Cited on pages 3 and 5).

[72] O. Morsch and M. Oberthaler, Reviews of Modern Physics **78**, 179 (2006) (Cited on pages 3 and 66).

[73] M. Greiner, O. Mandel, T. Esslinger, T. W. Hänsch, and I. Bloch, Nature **415**, 39 (2002) (Cited on page 3).

[74] R. Jördens, N. Strohmaier, K. Günter, H. Moritz, and T. Esslinger, Nature **455**, 204 (2008) (Cited on page 3).

[75] U. Schneider, L. Hackermüller, S. Will, Th. Best, I. Bloch, T. A. Costi, R. W. Helmes, D. Rasch, and A. Rosch, Science **322**, 1520 (2008) (Cited on page 3).

[76] L. Tarruell, D. Greif, T. Uehlinger, G. Jotzu, and T. Esslinger, Nature **483**, 302 (2012) (Cited on page 3).

[77] A. Celi, P. Massignan, J. Ruseckas, N. Goldman, I. B. Spielman, G. Juzeliūnas, and M. Lewenstein, Physical Review Letters **112**, 043001 (2014) (Cited on page 3).

[78] B. K. Stuhl, H.-I. Lu, L. M. Aycock, D. Genkina, and I. B. Spielman, Science **349**, 1514 (2015) (Cited on page 3).

[79] M. Mancini, G. Pagano, G. Cappellini, L. Livi, M. Rider, J. Catani, C. Sias, P. Zoller, M. Inguscio, M. Dalmonte, and L. Fallani, Science **349**, 1510 (2015) (Cited on page 3).

[80] T. Chalopin, T. Satoor, A. Evrard, V. Makhalov, J. Dalibard, R. Lopes, and S. Nascimbene, Nature Physics **16**, 1017 (2020) (Cited on page 3).

[81] B. Paredes, A. Widera, V. Murg, O. Mandel, S. Fölling, I. Cirac, G. V. Shlyapnikov, T. W. Hänsch, and I. Bloch, Nature **429**, 277 (2004) (Cited on page 3).

[82] T. Kinoshita, T. Wenger, and D. S. Weiss, Science **305**, 1125 (2004) (Cited on page 3).

[83] Z. Hadzibabic, P. Krüger, M. Cheneau, B. Battelier, and J. Dalibard, Nature **441**, 1118 (2006) (Cited on page 3).

[84] P. Cladé, C. Ryu, A. Ramanathan, K. Helmerson, and W. Phillips, Physical Review Letters **102**, 170401 (2009) (Cited on page 3).

[85] S. Tung, G. Lamporesi, D. Lobser, L. Xia, and E. A. Cornell, Physical Review Letters **105**, 230408 (2010) (Cited on page 3).

[86] R. Desbuquois, L. Chomaz, T. Yefsah, J. Léonard, J. Beugnon, C. Weitenberg, and J. Dalibard, Nature Physics **8**, 645 (2012) (Cited on page 3).

[87] T. Kinoshita, T. Wenger, and D. S. Weiss, Nature **440**, 900 (2006) (Cited on page 3).

[88] L. E. Sadler, J. M. Higbie, S. R. Leslie, M. Vengalattore, and D. M. Stamper-Kurn, Nature **443**, 312 (2006) (Cited on page 3).

[89] C. N. Weiler, T. W. Neely, D. R. Scherer, A. S. Bradley, M. J. Davis, and B. P. Anderson, Nature **455**, 948 (2008) (Cited on page 3).

[90] A. Polkovnikov, K. Sengupta, A. Silva, and M. Vengalattore, Reviews of Modern Physics **83**, 863 (2011) (Cited on page 3).

[91] J. Smith, A. Lee, P. Richerme, B. Neyenhuis, P. W. Hess, P. Hauke, M. Heyl, D. A. Huse, and C. Monroe, Nature Physics **12**, 907 (2016) (Cited on page 3).

[92] T. Langen, T. Gasenzer, and J. Schmiedmayer, Journal of Statistical Mechanics: Theory and Experiment **2016**, 064009 (2016) (Cited on page 3).

[93] M. Prüfer, P. Kunkel, H. Strobel, S. Lannig, D. Linnemann, C.-M. Schmied, J. Berges, T. Gasenzer, and M. K. Oberthaler, Nature **563**, 217 (2018) (Cited on page 3).

[94] S. Erne, R. Bücker, T. Gasenzer, J. Berges, and J. Schmiedmayer, Nature **563**, 225 (2018) (Cited on page 3).

[95] M. Tolosa-Simeón, Á. Parra-López, N. Sánchez-Kuntz, T. Haas, C. Viermann, M. Sparn, N. Liebster, M. Hans, E. Kath, H. Strobel, M. K. Oberthaler, and S. Floerchinger, Physical Review A **106**, 033313 (2022) (Cited on page 3).

[96] C. Viermann, M. Sparn, N. Liebster, M. Hans, E. Kath, Á. Parra-López, M. Tolosa-Simeón, N. Sánchez-Kuntz, T. Haas, H. Strobel, S. Floerchinger, and M. K. Oberthaler, Nature **611**, 260 (2022) (Cited on page 3).

[97] I. Ferrier-Barbut, H. Kadau, M. Schmitt, M. Wenzel, and T. Pfau, Physical Review Letters **116**, 215301 (2016) (Cited on page 3).

[98] L. Chomaz, S. Baier, D. Petter, M.-J. Mark, F. Wächtler, L. Santos, and F. Ferlaino, Physical Review X **6**, 041039 (2016) (Cited on pages 3 and 9).

[99] C. R. Cabrera, L. Tanzi, J. Sanz, B. Naylor, P. Thomas, P. Cheiney, and L. Tarruell, Science **359**, 301 (2018) (Cited on pages 3, 13, and 139).

[100] G. Semeghini, G. Ferioli, L. Masi, C. Mazzinghi, L. Wolswijk, F. Minardi, M. Modugno, G. Modugno, M. Inguscio, and M. Fattori, Physical Review Letters **120**, 235301 (2018) (Cited on pages 3 and 13).

[101] C. D'Errico, A. Burchianti, M. Prevedelli, L. Salasnich, F. Ancilotto, M. Modugno, F. Minardi, and C. Fort, Physical Review Research **1**, 033155 (2019) (Cited on page 3).

[102] A. F. Andreev and L. M. Lifshitz, Zhur Eksper Teoret Fiziki **56**, 2057 (1969) (Cited on pages 3, 6, and 83).

[103] G. V. Chester, Physical Review A **2**, 256 (1970) (Cited on pages 3, 6, and 83).

[104] A. J. Leggett, Physical Review Letters **25**, 1543 (1970) (Cited on pages 3, 6, and 83).

[105] J. Léonard, A. Morales, P. Zupancic, T. Esslinger, and T. Donner, Nature **543**, 87 (2017) (Cited on pages 3, 6, 84, 100, 111, and 119).

[106] J. Léonard, A. Morales, P. Zupancic, T. Donner, and T. Esslinger, Science **358**, 1415 (2017) (Cited on pages 3, 7, 84, 85, 100, and 110).

[107] L. Tanzi, E. Lucioni, F. Famà, J. Catani, A. Fioretti, C. Gabbanini, R. N. Bisset, L. Santos, and G. Modugno, Physical Review Letters **122**, 130405 (2019) (Cited on pages 3, 6, 84, 111, and 119).

[108] F. Böttcher, J.-N. Schmidt, M. Wenzel, J. Hertkorn, M. Guo, T. Langen, and T. Pfau, Physical Review X **9**, 011051 (2019) (Cited on pages 3, 6, 84, and 119).

[109] L. Chomaz, D. Petter, P. Ilzhöfer, G. Natale, A. Trautmann, C. Politi, G. Durastante, R. van Bijnen, A. Patscheider, M. Sohmen, M. Mark, and F. Ferlaino, Physical Review X **9**, 021012 (2019) (Cited on pages 3, 6, 84, and 119).

[110] F. Böttcher, J.-N. Schmidt, J. Hertkorn, K. S. H. Ng, S. D. Graham, M. Guo, T. Langen, and T. Pfau, Reports on Progress in Physics **84**, 012403 (2020) (Cited on pages 3 and 6).

[111] J.-R. Li, J. Lee, W. Huang, S. Burchesky, B. Shteynas, F. Çağrı Top, A. O. Jamison, and W. Ketterle, Nature **543**, 91 (2017) (Cited on pages 3, 6, 7, 83, 85, 86, 90, 96, 119, and 138).

[112] A. Putra, F. Salces-Cárcoba, Y. Yue, S. Sugawa, and I. B. Spielman, Physical Review Letters **124**, 053605 (2020) (Cited on pages 3, 6, 7, 83, 85, 86, 90, 97, 119, and 140).

[113] S. J. Rabello, Physics Letters B **363**, 180 (1995) (Cited on pages 3, 51, and 139).

[114] S. J. B. Rabello, Physical Review Letters **76**, 4007 (1996) (Cited on pages 3, 51, and 139).

[115] U. Aglietti, L. Griguolo, R. Jackiw, S.-Y. Pi, and D. Seminara, Physical Review Letters **77**, 4406 (1996) (Cited on pages 3, 51, 55, 57, 65, 69, and 71).

[116] R. Jackiw, Journal of Nonlinear Mathematical Physics **4**, 261 (1997) (Cited on pages 3, 51, 52, 55, 56, 65, 69, and 71).

[117] M. Boninsegni and N. V. Prokof'ev, Reviews of Modern Physics **84**, 759 (2012) (Cited on pages 3, 5, 6, and 83).

[118] C. S. Chisholm, A. Frölian, E. Neri, R. Ramos, L. Tarruell, and A. Celi, Physical Review Research **4**, 043088 (2022) (Cited on pages 4, 5, 47, 61, 137, and 138).

[119] F. Wilczek, Physical Review Letters **49**, 957 (1982) (Cited on pages 4 and 49).

[120] J. K. Jain, Physical Review Letters **63**, 199 (1989) (Cited on page 4).

[121] Z. F. Ezawa, *Quantum Hall Effects: Field Theoretical Approach and Related Topics. Field Theorectical Approach and Related Topics* (World Scientific Publishing Company. Singapore. Second. 2008), 700 (Cited on pages 4 and 49).

[122] K. Fukushima and T. Hatsuda, Reports on Progress in Physics **74**, 014001 (2011) (Cited on page 4).

[123] J. Berges, M. P. Heller, A. Mazeliauskas, and R. Venugopalan, Reviews of Modern Physics **93**, 035003 (2021) (Cited on page 4).

[124] C. Weeks, G. Rosenberg, B. Seradjeh, and M. Franz, Nature Physics **3**, 796 (2007) (Cited on page 5).

[125] U.-J. Wiese, Annalen der Physik **525**, 777 (2013) (Cited on page 5).

[126] N. H. Nguyen, M. C. Tran, Y. Zhu, A. M. Green, C. H. Alderete, Z. Davoudi, and N. M. Linke, PRX Quantum **3**, 020324 (2022) (Cited on page 5).

[127] F. M. Surace, P. P. Mazza, G. Giudici, A. Lerose, A. Gambassi, and M. Dalmonte, Physical Review X **10**, 021041 (2020) (Cited on page 5).

[128] Z.-Y. Zhou, G.-X. Su, J. C. Halimeh, R. Ott, H. Sun, P. Hauke, B. Yang, Z.-S. Yuan, J. Berges, and J.-W. Pan, Science **377**, 311 (2022) (Cited on page 5).

[129] H.-Y. Wang, W.-Y. Zhang, Z.-Y. Yao, Y. Liu, Z.-H. Zhu, Y.-G. Zheng, X.-K. Wang, H. Zhai, Z.-S. Yuan, and J.-W. Pan, *Interrelated Thermalization and Quantum Criticality in a Lattice Gauge Simulator*. arXiv 2210.17032. (2022) (Cited on page 5).

[130] H.-N. Dai, B. Yang, A. Reingruber, H. Sun, X.-F. Xu, Y.-A. Chen, Z.-S. Yuan, and J.-W. Pan, Nature Physics **13**, 1195 (2017) (Cited on page 5).

[131] M. J. Edmonds, M. Valiente, G. Juzeliūnas, L. Santos, and P. Öhberg, Physical Review Letters **110**, 085301 (2013) (Cited on pages 5, 56, 57, 58, 61, 63, 64, 65, 71, 78, 80, 138, and 139).

[132] A. Frölian, C. S. Chisholm, E. Neri, C. R. Cabrera, R. Ramos, A. Celi, and L. Tarruell, Nature **608**, 293 (2022) (Cited on pages 5, 25, 47, 58, 61, and 137).

[133] P. Kapitza, Nature **141**, 74 (1938) (Cited on page 5).

[134] J. F. Allen and A. D. Misener, Nature **142**, 643 (1938) (Cited on page 5).

[135] L. Landau, Physical Review **60**, 356 (1941) (Cited on page 5).

[136] Z. Hadzibabic and J. Dalibard, La Rivista del Nuovo Cimento **34**, 389 (2011) (Cited on page 6).

[137] P. A. Crowell and J. D. Reppy, Physical Review Letters **70**, 3291 (1993) (Cited on page 6).

[138] D. G. Henshaw and A. D. B. Woods, Physical Review **121**, 1266 (1961) (Cited on page 6).

[139] S. V. Iordanskiĭ and L. P. Pitaevskiĭ, Soviet Physics Uspekhi **23**, 317 (1980) (Cited on page 6).

[140] L. P. Pitaevskiĭ, Zhur Eksper Teoret Fiziki **39**, 423 (1984) (Cited on page 6).

[141] Y. Pomeau and S. Rica, Physical Review Letters **72**, 2426 (1994) (Cited on page 6).

[142] R. A. Guyer, Physical Review Letters **26**, 174 (1971) (Cited on pages 6, 83, and 84).

[143] W. M. Saslow, Physical Review Letters **36**, 1151 (1976) (Cited on pages 6 and 84).

[144] W. M. Saslow, Physical Review B **15**, 173 (1977) (Cited on pages 6 and 84).

[145] E. Kim and M. H. W. Chan, Nature **427**, 225 (2004) (Cited on pages 6 and 84).

[146] E. Kim and M. H. W. Chan, Science **305**, 1941 (2004) (Cited on pages 6 and 84).

[147] D. Y. Kim and M. H. W. Chan, Physical Review Letters **109**, 155301 (2012) (Cited on pages 6 and 84).

[148] J. Beamish and S. Balibar, Reviews of Modern Physics **92**, 045002 (2020) (Cited on pages 6 and 84).

[149] T. Donner, Physics **12**, 38 (2019) (Cited on page 6).

[150] D. H. J. O'Dell, S. Giovanazzi, and G. Kurizki, Physical Review Letters **90**, 110402 (2003) (Cited on page 6).

[151] L. Santos, G. V. Shlyapnikov, and M. Lewenstein, Physical Review Letters **90**, 250403 (2003) (Cited on page 6).

[152] W. Zheng and Z. Li, Physical Review A **85**, 053607 (2012) (Cited on page 6).

[153] G. I. Martone, Y. Li, L. P. Pitaevskii, and S. Stringari, Physical Review A **86**, 063621 (2012) (Cited on pages 6, 63, 100, and 114).

[154] S.-C. Ji, L. Zhang, X.-T. Xu, Z. Wu, Y. Deng, S. Chen, and J.-W. Pan, Physical Review Letters **114**, 105301 (2015) (Cited on pages 6, 7, and 114).

[155] R. Mottl, F. Brennecke, K. Baumann, R. Landig, T. Donner, and T. Esslinger, Science **336**, 1570 (2012) (Cited on page 6).

[156] M. Kulkarni, B. Öztop, and H. E. Türeci, Physical Review Letters **111**, 220408 (2013) (Cited on page 6).

[157] T. M. Bersano, J. Hou, S. Mossman, V. Gokhroo, X.-W. Luo, K. Sun, C. Zhang, and P. Engels, Physical Review A **99**, 051602 (2019) (Cited on pages 6, 7, 83, 90, and 119).

[158] L. Tanzi, S. M. Roccuzzo, E. Lucioni, F. Famà, A. Fioretti, C. Gabbanini, G. Modugno, A. Recati, and S. Stringari, Nature **574**, 382 (2019) (Cited on pages 6, 7, and 100).

[159] M. Guo, F. Böttcher, J. Hertkorn, J.-N. Schmidt, M. Wenzel, H. P. Büchler, T. Langen, and T. Pfau, Nature **574**, 386 (2019) (Cited on pages 6, 7, 100, 111, and 119).

[160] J. Goldstone, Il Nuovo Cimento **19**, 154 (1961) (Cited on pages 6, 100, and 110).

[161] P. W. Higgs, Physical Review Letters **13**, 508 (1964) (Cited on pages 7, 85, and 110).

[162] S. Saccani, S. Moroni, and M. Boninsegni, Physical Review Letters **108**, 175301 (2012) (Cited on pages 7 and 110).

[163] G. I. Martone and S. Stringari, SciPost Physics **11**, 092 (2021) (Cited on pages 7, 33, 85, 88, 100, 101, 108, 110, 111, 112, and 113).

[164] J. Hertkorn, F. Böttcher, M. Guo, J. N. Schmidt, T. Langen, H. P. Büchler, and T. Pfau, Physical Review Letters **123**, 193002 (2019) (Cited on pages 7, 85, 100, and 110).

[165] I. B. Spielman, Physical Review A **79**, 063613 (2009) (Cited on pages 7, 32, 33, and 36).

[166] J. Higbie and D. M. Stamper-Kurn, Physical Review A **69**, 053605 (2004) (Cited on pages 7, 83, 84, 85, 91, 117, and 138).

[167] T.-L. Ho and S. Zhang, Physical Review Letters **107**, 150403 (2011) (Cited on pages 7, 83, 85, 91, 94, 117, and 138).

[168] Y. Li, L. P. Pitaevskii, and S. Stringari, Physical Review Letters **108**, 225301 (2012) (Cited on pages 7, 83, 85, 86, 88, 94, 98, 102, 107, 133, and 138).

[169] C. R. Cabrera Córdova. PhD thesis. Universitat Politècnica de Catalunya, Insitut de Ciències Fotòniques. 2018 (Cited on pages 9, 17, 18, 19, 20, 22, 28, and 112).

[170] J. Sanz Sánchez. PhD thesis. Universitat Politècnica de Catalunya, Insitut de Ciències Fotòniques. 2020 (Cited on pages 9, 17, 18, 22, 23, 24, 25, 29, 30, 31, 32, 124, 127, and 129).

[171] S. Jochim, M. Bartenstein, A. Altmeyer, G. Hendl, S. Riedl, C. Chin, J. Hecker Denschlag, and R. Grimm, Science **302**, 2101 (2003) (Cited on page 9).

[172] M. Greiner, C. A. Regal, and D. S. Jin, Nature **426**, 537 (2003) (Cited on page 9).

[173] M. W. Zwierlein, C. A. Stan, C. H. Schunck, S. M. F. Raupach, S. Gupta, Z. Hadzibabic, and W. Ketterle, Physical Review Letters **91**, 250401 (2003) (Cited on page 9).

[174] S. O. Demokritov, V. E. Demidov, O. Dzyapko, G. A. Melkov, A. A. Serga, B. Hillebrands, and A. N. Slavin, Nature **443**, 430 (2006) (Cited on page 9).

[175] H. Deng, H. Haug, and Y. Yamamoto, Reviews of Modern Physics **82**, 1489 (2010) (Cited on page 9).

[176] J. Klaers, J. Schmitt, F. Vewinger, and M. Weitz, Nature **468**, 545 (2010) (Cited on page 9).

[177] C. J. Pethick and H. Smith, *Bose-Einstein condensation in dilute gases* (Cambridge University Press. Cambridge. Second. 2008) (Cited on pages 9, 10, 11, 12, 13, 112, 125, 126, and 128).

[178] T. Fukuhara, S. Sugawa, Y. Takasu, and Y. Takahashi, Physical Review A **79**, 021601 (2009) (Cited on page 9).

[179] S. Stellmer, M. K. Tey, B. Huang, R. Grimm, and F. Schreck, Physical Review Letters **103**, 200401 (2009) (Cited on page 9).

[180] P. G. Mickelson, Y. N. Martinez de Escobar, M. Yan, B. J. DeSalvo, and T. C. Killian, Physical Review A **81**, 051601 (2010) (Cited on page 9).

[181] S. Stellmer, M. K. Tey, R. Grimm, and F. Schreck, Physical Review A **82**, 041602 (2010) (Cited on page 9).

[182] M. Lu, N. Q. Burdick, S. H. Youn, and B. L. Lev, Physical Review Letters **107**, 190401 (2011) (Cited on page 9).

[183] K. Aikawa, A. Frisch, M. Mark, S. Baier, A. Rietzler, R. Grimm, and F. Ferlaino, Physical Review Letters **108**, 210401 (2012) (Cited on page 9).

[184] Y. Tang, N. Q. Burdick, K. Baumann, and B. L. Lev, New Journal of Physics **17**, 045006 (2015) (Cited on page 9).

[185] E. T. Davletov, V. V. Tsyganok, V. A. Khlebnikov, D. A. Pershin, D. V. Shaykin, and A. V. Akimov, Physical Review A **102**, 011302 (2020) (Cited on page 9).

[186] Y. Miyazawa, R. Inoue, H. Matsui, G. Nomura, and M. Kozuma, Physical Review Letters **129**, 223401 (2022) (Cited on page 9).

[187] T. G. Tiecke, *Properties of Potassium*. Version 1.03, available online at https://tobiastiecke.nl/archive/PotassiumProperties.pdf. June 2019 (Cited on pages 9, 13, 14, 15, 17, and 19).

[188] C. J. Foot, *Atomic physics* (Oxford University Press. 2005) (Cited on pages 9, 13, 14, and 26).

[189] L. Pitaevskii and S. Stringari, *Bose-Einstein Condensation (The International Series of Monographs on Physics)* (Oxford University Press, USA. New York. 2003) (Cited on pages 10 and 11).

[190] H. R. Brown and P. Holland, American Journal of Physics **72**, 34 (2004) (Cited on page 10).

[191] M. Olshanii, Physical Review Letters **81**, 938 (1998) (Cited on page 11).

[192] L. Salasnich, A. Parola, and L. Reatto, Physical Review A **65**, 043614 (2002) (Cited on page 11).

[193] K. E. Strecker, G. B. Partridge, A. G. Truscott, and R. G. Hulet, Nature **417**, 150 (2002) (Cited on pages 11 and 68).

[194] L. Khaykovich, F. Schreck, G. Ferrari, T. Bourdel, J. Cubizolles, L. D. Carr, Y. Castin, and C. Salomon, Science **296**, 1290 (2002) (Cited on pages 11 and 68).

[195] V. M. Pérez-García, H. Michinel, and H. Herrero, Physical Review A **57**, 3837 (1998) (Cited on pages 11 and 12).

[196] B. Eiermann, Th. Anker, M. Albiez, M. Taglieber, P. Treutlein, K.-P. Marzlin, and M. K. Oberthaler, Physical Review Letters **92**, 230401 (2004) (Cited on pages 12 and 72).

[197] A. D. Jackson, G. M. Kavoulakis, and C. J. Pethick, Physical Review A **58**, 2417 (1998) (Cited on page 12).

[198] S. Burger, K. Bongs, S. Dettmer, W. Ertmer, K. Sengstock, A. Sanpera, G. V. Shlyapnikov, and M. Lewenstein, Physical Review Letters **83**, 5198 (1999) (Cited on pages 12 and 125).

[199] J. Denschlag, J. E. Simsarian, D. L. Feder, C. W. Clark, L. A. Collins, J. Cubizolles, L. Deng, E. W. Hagley, K. Helmerson, W. P. Reinhardt, S. L. Rolston, B. I. Schneider, and W. D. Phillips, Science **287**, 97 (2000) (Cited on pages 12 and 125).

[200] B. P. Anderson, P. C. Haljan, C. A. Regal, D. L. Feder, L. A. Collins, C. W. Clark, and E. A. Cornell, Physical Review Letters **86**, 2926 (2001) (Cited on pages 12 and 57).

[201] L. Salasnich, A. Parola, and L. Reatto, Physical Review A **66**, 043603 (2002) (Cited on page 12).

[202] L. D. Carr and Y. Castin, Physical Review A **66**, 063602 (2002) (Cited on page 12).

[203] P. Ao and S. T. Chui, Physical Review A **58**, 4836 (1998) (Cited on page 13).

[204] D. S. Hall, M. R. Matthews, J. R. Ensher, C. E. Wieman, and E. A. Cornell, Physical Review Letters **81**, 1539 (1998) (Cited on pages 13 and 97).

[205] D. S. Petrov, Physical Review Letters **115**, 155302 (2015) (Cited on page 13).

[206] T. G. Tiecke. PhD thesis. Universiteit van Amsterdam. 2009 (Cited on pages 14 and 27).

[207] R. Wei and E. J. Mueller, Physical Review A **87**, 042514 (2013) (Cited on pages 14, 36, 37, 39, 40, 61, and 123).

[208] G. Breit and I. I. Rabi, Physical Review **38**, 2082 (1931) (Cited on pages 14 and 27).

[209] R. Grimm, M. Weidemüller, and Y. B. Ovchinnikov. In: *Advances In Atomic, Molecular, and Optical Physics* (Elsevier. 2000), 95 (Cited on pages 15, 16, 17, and 36).

[210] L. J. LeBlanc. PhD thesis. University of Toronto. 2011 (Cited on pages 15, 16, and 36).

[211] W. Ketterle, D. S. Durfee, and D. M. Stamper-Kurn. In *Bose-Einstein Condensation in Atomic Gases: Proceedings of the International School of Physics "Enrico Fermi", Course CXL*. Ed. by M. Ignuscio, S. Stringari, and C. E. Wieman (IOS Press. Amsterdam. 1999) (Cited on pages 21, 22, 80, and 124).

[212] Y. Castin and R. Dum, Physical Review Letters **77**, 5315 (1996) (Cited on pages 21, 31, 72, 73, and 80).

[213] L. Saemisch, *Development of an imaging system for a quantum gas experiment*. Erasmus internship, Institut de Ciències Fotòniques, Universitat Politècnica de Catalunya. 2015 (Cited on page 23).

[214] J. Sanz Sánchez. Master's thesis. Universitat Politècnica de Catalunya, Insitut de Ciències Fotòniques. 2015 (Cited on page 23).

[215] C. C. Bradley, C. A. Sackett, and R. G. Hulet, Physical Review Letters **78**, 985 (1997) (Cited on page 23).

[216] M. Gajdacz, P. L. Pedersen, T. Mørch, A. J. Hilliard, J. Arlt, and J. F. Sherson, Review of Scientific Instruments **84**, 083105 (2013) (Cited on page 23).

[217] J. Sanz, A. Frölian, C. S. Chisholm, C. R. Cabrera, and L. Tarruell, Physical Review Letters **128**, 013201 (2022) (Cited on pages 25, 28, 31, 32, and 137).

[218] A. Frölian. PhD thesis. Universitat Politècnica de Catalunya, Insitut de Ciències Fotòniques. 2022 (Cited on pages 25, 47, and 61).

[219] C. P. Search and P. R. Berman, Physical Review A **63**, 043612 (2001) (Cited on pages 25, 29, and 30).

[220] D. A. Steck, *Quantum and Atom Optics*. Revision 0.13.15, available online at http://steck.us/teaching. 28 July 2022 (Cited on pages 26, 33, and 39).

[221] N. F. Ramsey, Physical Review **78**, 695 (1950) (Cited on page 27).

[222] J. R. Ramos Benitez. PhD thesis. University of Toronto. 2019 (Cited on page 27).

[223] E. Nicklas, H. Strobel, T. Zibold, C. Gross, B. A. Malomed, P. G. Kevrekidis, and M. K. Oberthaler, Physical Review Letters **107**, 193001 (2011) (Cited on page 30).

[224] E. Nicklas, W. Muessel, H. Strobel, P. G. Kevrekidis, and M. K. Oberthaler, Physical Review A **92**, 053614 (2015) (Cited on page 30).

[225] K. Shibata, A. Torii, H. Shibayama, Y. Eto, H. Saito, and T. Hirano, Physical Review A **99**, 013622 (2019) (Cited on page 30).

[226] S. Roy, M. Landini, A. Trenkwalder, G. Semeghini, G. Spagnolli, A. Simoni, M. Fattori, M. Inguscio, and G. Modugno, Physical Review Letters **111**, 053202 (2013) (Cited on pages 30, 36, and 65).

[227] P. Cheiney, C. R. Cabrera, J. Sanz, B. Naylor, L. Tanzi, and L. Tarruell, Physical Review Letters **120**, 135301 (2018) (Cited on pages 31, 124, and 129).

[228] D. S. Petrov, Physical Review Letters **112**, 103201 (2014) (Cited on page 32).

[229] L. Lavoine, A. Hammond, A. Recati, D. S. Petrov, and T. Bourdel, Physical Review Letters **127**, 203402 (2021) (Cited on page 32).

[230] A. Hammond, L. Lavoine, and T. Bourdel, Physical Review Letters **128**, 083401 (2022) (Cited on page 32).

[231] N. Lundblad, P. J. Lee, I. B. Spielman, B. L. Brown, W. D. Phillips, and J. V. Porto, Physical Review Letters **100**, 150401 (2008) (Cited on page 32).

[232] C. Shkedrov, M. Menashes, G. Ness, A. Vainbaum, E. Altman, and Y. Sagi, Physical Review X **12**, 011041 (2022) (Cited on page 32).

[233] K. Jiménez-García. PhD thesis. Joint Quantum Institute. 2012 (Cited on pages 33, 37, and 42).

[234] D. L. Campbell. PhD thesis. University of Maryland. 2015 (Cited on pages 33 and 66).

[235] J. Dalibard. In *Quantum Matter at Ultralow Temperatures: Proceedings of the International School of Physics "Enrico Fermi", Course CXCI*. Ed. by M. Ignuscio, W. Ketterle, and S. Stringari (IOS Press. Amsterdam. 2016) (Cited on page 33).

[236] M. A. Khamehchi, K. Hossain, M. E. Mossman, Y. Zhang, Th. Busch, M. McNeil Forbes, and P. Engels, Physical Review Letters **118**, 155301 (2017) (Cited on pages 33, 35, 40, 71, 72, and 78).

[237] R. A. Williams, L. J. LeBlanc, K. Jiménez-García, M. C. Beeler, A. R. Perry, W. D. Phillips, and I. B. Spielman, Science **335**, 314 (2012) (Cited on pages 33, 35, 36, and 40).

[238] L. Zhang, J.-Y. Zhang, S.-C. Ji, Z.-D. Du, H. Zhai, Y. Deng, S. Chen, P. Zhang, and J.-W. Pan, Physical Review A **87**, 011601 (2013) (Cited on page 35).

[239] J. Cabedo, J. Claramunt, A. Celi, Y. Zhang, V. Ahufinger, and J. Mompart, Physical Review A **100**, 063633 (2019) (Cited on pages 36, 91, 95, and 96).

[240] J. Jiang, L.-Y. Tang, and J. Mitroy, Physical Review A **87**, 032518 (2013) (Cited on page 36).

[241] J. Jiang and J. Mitroy, Physical Review A **88**, 032505 (2013) (Cited on page 36).

[242] G. Roati, M. Zaccanti, C. D'Errico, J. Catani, M. Modugno, A. Simoni, M. Inguscio, and G. Modugno, Physical Review Letters **99**, 010403 (2007) (Cited on page 36).

[243] C. D'Errico, M. Zaccanti, M. Fattori, G. Roati, M. Inguscio, G. Modugno, and A. Simoni, New Journal of Physics **9**, 223 (2007) (Cited on page 36).

[244] L. Tanzi, C. R. Cabrera, J. Sanz, P. Cheiney, M. Tomza, and L. Tarruell, Physical Review A **98**, 062712 (2018) (Cited on pages 36, 97, and 120).

[245] J. Etrych, G. Martirosyan, A. Cao, J. A. P. Glidden, L. H. Dogra, J. M. Hutson, Z. Hadzibabic, and C. Eigen, Physical Review Research **5**, 013174 (2023) (Cited on page 36).

[246] M. Ballu, *Développement d'un système laser Raman pour le couplage cohérent de deux condensats de Bose-Einstein de potassium*. Stage de Recherche - Phytem master première année, Ecole Normale Supérieure Paris-Saclay. 2018 (Cited on page 37).

[247] P. Wang, Z.-Q. Yu, Z. Fu, J. Miao, L. Huang, S. Chai, H. Zhai, and J. Zhang, Physical Review Letters **109**, 095301 (2012) (Cited on pages 39 and 74).

[248] L. W. Cheuk, A. T. Sommer, Z. Hadzibabic, T. Yefsah, W. S. Bakr, and M. W. Zwierlein, Physical Review Letters **109**, 095302 (2012) (Cited on pages 40 and 41).

[249] L. Huang, Z. Meng, P. Wang, P. Peng, S.-L. Zhang, L. Chen, D. Li, Q. Zhou, and J. Zhang, Nature Physics **12**, 540 (2016) (Cited on page 42).

[250] Z. Meng, L. Huang, P. Peng, D. Li, L. Chen, Y. Xu, C. Zhang, P. Wang, and J. Zhang, Physical Review Letters **117**, 235304 (2016) (Cited on page 42).

[251] X.-T. Xu, C.-R. Yi, B.-Z. Wang, W. Sun, Y. Deng, X.-J. Liu, S. Chen, and J.-W. Pan, Science Bulletin **63**, 1464 (2018) (Cited on page 42).

[252] P. L. Gould, G. A. Ruff, and D. E. Pritchard, Physical Review Letters **56**, 827 (1986) (Cited on page 42).

[253] Yu. B. Ovchinnikov, J. H. Müller, M. R. Doery, E. J. D. Vredenbregt, K. Helmerson, S. L. Rolston, and W. D. Phillips, Physical Review Letters **83**, 284 (1999) (Cited on page 42).

[254] B. Gadway, D. Pertot, R. Reimann, M. G. Cohen, and D. Schneble, Optics Express **17**, 19173 (2009) (Cited on page 42).

[255] A. Altland and B. Simons, *Condensed Matter Field Theory* (Cambridge University Press. Cambridge. 2006) (Cited on page 47).

[256] L. Faddeev and R. Jackiw, Physical Review Letters **60**, 1692 (1988) (Cited on pages 48 and 52).

[257] R. Jackiw. In "*Diverse Topics in Theoretical and Mathematical Physics*" (World Scientific. Singapore. 1995). Chap. (Constrained) quantization without tears, 367 (Cited on page 48).

[258] C. Muschik, M. Heyl, E. Martinez, T. Monz, P. Schindler, B. Vogell, M. Dalmonte, P. Hauke, R. Blatt, and P. Zoller, New Journal of Physics **19**, 103020 (2017) (Cited on pages 49, 53, 54, and 56).

[259] R. Jackiw and S.-Y. Pi, Physical Review Letters **64**, 2969 (1990) (Cited on page 50).

[260] R. Jackiw and S.-Y. Pi, Physical Review D **42**, 3500 (1990) (Cited on page 50).

[261] A. Kundu, Physical Review Letters **83**, 1275 (1999) (Cited on pages 51 and 139).

[262] M. Bonkhoff, K. Jägering, S. Eggert, A. Pelster, M. Thorwart, and T. Posske, Physical Review Letters **126**, 163201 (2021) (Cited on pages 51 and 139).

[263] R. Floreanini and R. Jackiw, Physical Review Letters **59**, 1873 (1987) (Cited on page 51).

[264] N. R. Cooper, J. Dalibard, and I. B. Spielman, Reviews of Modern Physics **91**, 015005 (2019) (Cited on page 51).

[265] P. A. M. Dirac, Canadian Journal of Mathematics **2**, 129 (1950) (Cited on page 53).

[266] M. Henneaux and C. Teitelboim, *Quantization of Gauge Systems* (Princeton University Press. Princeton. 2020) (Cited on page 53).

[267] D. B. Kaplan and J. R. Stryker, Physical Review D **102**, 094515 (2020) (Cited on page 54).

[268] J. Bender and E. Zohar, Physical Review D **102**, 114517 (2020) (Cited on page 54).

[269] J. F. Haase, L. Dellantonio, A. Celi, D. Paulson, A. Kan, K. Jansen, and C. A. Muschik, Quantum **5**, 393 (2021) (Cited on page 54).

[270] D. Paulson, L. Dellantonio, J. F. Haase, A. Celi, A. Kan, A. Jena, C. Kokail, R. van Bijnen, K. Jansen, P. Zoller, and C. A. Muschik, PRX Quantum **2**, 030334 (2021) (Cited on page 54).

[271] A. Celi, B. Vermersch, O. Viyuela, H. Pichler, M. D. Lukin, and P. Zoller, Physical Review X **10**, 021057 (2020) (Cited on page 54).

[272] D. Banerjee, S. Caspar, F.-J. Jiang, J.-H. Peng, and U.-J. Wiese, Physical Review Research **4**, 023176 (2022) (Cited on page 54).

[273] L. Griguolo and D. Seminara, Nuclear Physics B **516**, 467 (1998) (Cited on pages 55, 56, 65, 69, and 71).

[274] R. J. Dingwall, M. J. Edmonds, J. L. Helm, B. A. Malomed, and P. Öhberg, New Journal of Physics **20**, 043004 (2018) (Cited on pages 57, 65, 138, and 139).

[275] R. J. Dingwall and P. Öhberg, Physical Review A **99**, 023609 (2019) (Cited on pages 57 and 65).

[276] I. A. Bhat, S. Sivaprakasam, and B. A. Malomed, Physical Review E **103**, 032206 (2021) (Cited on pages 57 and 65).

[277] M. J. Edmonds, M. Valiente, and P. Öhberg, EPL (Europhysics Letters) **110**, 36004 (2015) (Cited on page 57).

[278] J.-h. Zheng, B. Xiong, G. Juzeliūnas, and D.-W. Wang, Physical Review A **92**, 013604 (2015) (Cited on page 57).

[279] L. Chen and Q. Zhu, New Journal of Physics **24**, 053044 (2022) (Cited on page 57).

[280] Y.-J. Lin, R. L. Compton, K. Jiménez-García, W. D. Phillips, J. V. Porto, and I. B. Spielman, Nature Physics **7**, 531 (2011) (Cited on pages 66 and 124).

[281] J.-Y. Zhang, S.-C. Ji, Z. Chen, L. Zhang, Z.-D. Du, B. Yan, G.-S. Pan, B. Zhao, Y.-J. Deng, H. Zhai, S. Chen, and J.-W. Pan, Physical Review Letters **109**, 115301 (2012) (Cited on pages 66, 102, and 124).

[282] P. Thomas. Master's thesis. Universität Hamburg. 2017 (Cited on page 66).

[283] M. Kozuma, L. Deng, E. W. Hagley, J. Wen, R. Lutwak, K. Helmerson, S. L. Rolston, and W. D. Phillips, Physical Review Letters **82**, 871 (1999) (Cited on page 66).

[284] D. A. Steck. PhD thesis. The University of Texas. 2001 (Cited on page 66).

[285] A. L. Marchant, T. P. Billam, T. P. Wiles, M. M. H. Yu, S. A. Gardiner, and S. L. Cornish, Nature Communications **4**, 1865 (2013) (Cited on page 71).

[286] G. R. Dennis, J. J. Hope, and M. T. Johnsson, Computer Physics Communications **184**, 201 (2013) (Cited on pages 72, 77, 138, and 141).

[287] A.-C. Lee, D. Baillie, and P. B. Blakie, Physical Review Research **3**, 013283 (2021) (Cited on page 72).

[288] G. I. Martone. PhD thesis. Università Degli Studi di Trento. 2014 (Cited on pages 83, 86, 88, 93, 102, 114, 133, and 138).

[289] H. Suzuki, Journal of the Physical Society of Japan **35**, 1472 (1973) (Cited on page 84).

[290] D. S. Greywall, Physical Review B **16**, 1291 (1977) (Cited on page 84).

[291] P.-C. Ho, I. P. Bindloss, and J. M. Goodkind, Journal of Low Temperature Physics **109**, 409 (1997) (Cited on page 84).

[292] E. Blackburn, J. M. Goodkind, S. K. Sinha, J. Hudis, C. Broholm, J. van Duijn, C. D. Frost, O. Kirichek, and R. B. E. Down, Physical Review B **76**, 024523 (2007) (Cited on page 84).

[293] A. C. Clark, X. Lin, and M. H. W. Chan, Physical Review Letters **97**, 245301 (2006) (Cited on page 84).

[294] S. Sasaki, R. Ishiguro, F. Caupin, H. J. Maris, and S. Balibar, Science **313**, 1098 (2006) (Cited on page 84).

[295] S. Balibar, Nature **464**, 176 (2010) (Cited on page 84).

[296] N. Prokof'ev and B. Svistunov, Physical Review Letters **94**, 155302 (2005) (Cited on page 84).

[297] M. Boninsegni, A. B. Kuklov, L. Pollet, N. V. Prokof'ev, B. V. Svistunov, and M. Troyer, Physical Review Letters **97**, 080401 (2006) (Cited on page 84).

[298] T. Langen, Physics Today **75**, 36 (2022) (Cited on page 84).

[299] M. Boninsegni and S. Moroni, Results in Physics **44**, 106186 (2023) (Cited on page 84).

[300] A. B. Kuklov, L. Pollet, N. V. Prokof'ev, and B. V. Svistunov, Physical Review B **90**, 184508 (2014) (Cited on page 84).

[301] A. Eyal, X. Mi, A. V. Talanov, and J. D. Reppy, Proceedings of the National Academy of Sciences **113**, E3203 (2016) (Cited on page 84).

[302] S. Giovanazzi, D. O'Dell, and G. Kurizki, Physical Review Letters **88**, 130402 (2002) (Cited on page 84).

[303] K. Góral, L. Santos, and M. Lewenstein, Physical Review Letters **88**, 170406 (2002) (Cited on page 84).

[304] T. Lahaye, C. Menotti, L. Santos, M. Lewenstein, and T. Pfau, Reports on Progress in Physics **72**, 126401 (2009) (Cited on page 84).

[305] M. A. Baranov, M. Dalmonte, G. Pupillo, and P. Zoller, Chemical Reviews **112**, 5012 (2012) (Cited on page 84).

[306] N. Henkel, R. Nath, and T. Pohl, Physical Review Letters **104**, 195302 (2010) (Cited on page 84).

[307] K. T. Geier, G. I. Martone, P. Hauke, and S. Stringari, Physical Review Letters **127**, 115301 (2021) (Cited on pages 85, 100, 101, 102, 104, 106, 107, 108, 115, 116, and 117).

[308] K. T. Geier, G. I. Martone, P. Hauke, W. Ketterle, and S. Stringari, Physical Review Letters **130**, 156001 (2023) (Cited on pages 85, 100, 108, 115, 116, and 134).

[309] Z. Chen and H. Zhai, Physical Review A **86**, 041604 (2012) (Cited on pages 87, 100, 101, 102, and 108).

[310] G. I. Martone, Y. Li, and S. Stringari, Physical Review A **90**, 041604 (2014) (Cited on pages 90 and 96).

[311] Z. Chen and Z. Liang, Physical Review A **93**, 013601 (2016) (Cited on page 90).

[312] G. I. Martone, T. Ozawa, C. Qu, and S. Stringari, Physical Review A **94**, 043629 (2016) (Cited on page 90).

[313] J. Cabedo, J. Claramunt, and A. Celi, Physical Review A **104**, L031305 (2021) (Cited on page 91).

[314] J. Cabedo and A. Celi, Physical Review Research **3**, 043215 (2021) (Cited on page 91).

[315] T. Zibold, E. Nicklas, C. Gross, and M. K. Oberthaler, Physical Review Letters **105**, 204101 (2010) (Cited on page 94).

[316] A. Recati and S. Stringari, Annual Review of Condensed Matter Physics **13**, 407 (2022) (Cited on pages 94 and 100).

[317] M. Abad and A. Recati, The European Physical Journal D **67** (2013) (Cited on pages 94 and 112).

[318] G. I. Martone, The European Physical Journal Special Topics **224**, 553 (2015) (Cited on page 96).

[319] D. Gordon and C. M. Savage, Physical Review A **58**, 1440 (1998) (Cited on page 97).

[320] M. J. Bijlsma and H. T. C. Stoof, Physical Review B **56**, 14631 (1997) (Cited on page 99).

[321] D. Petter, G. Natale, R. M. W. van Bijnen, A. Patscheider, M. J. Mark, L. Chomaz, and F. Ferlaino, Physical Review Letters **122**, 183401 (2019) (Cited on page 100).

[322] G. Natale, R. M. W. van Bijnen, A. Patscheider, D. Petter, M. J. Mark, L. Chomaz, and F. Ferlaino, Physical Review Letters **123**, 050402 (2019) (Cited on pages 100 and 111).

[323] L. Tanzi, J. G. Maloberti, G. Biagioni, A. Fioretti, C. Gabbanini, and G. Modugno, Science **371**, 1162 (2021) (Cited on page 100).

[324] M. A. Norcia, E. Poli, C. Politi, L. Klaus, T. Bland, M. J. Mark, L. Santos, R. N. Bisset, and F. Ferlaino, Physical Review Letters **129**, 040403 (2022) (Cited on page 100).

[325] J. Léonard. PhD thesis. ETH Zurich. 2017 (Cited on pages 100 and 111).

[326] J. Lang, F. Piazza, and W. Zwerger, New Journal of Physics **19**, 123027 (2017) (Cited on page 100).

[327] Y. Li, G. I. Martone, L. P. Pitaevskii, and S. Stringari, Physical Review Letters **110**, 235302 (2013) (Cited on pages 100 and 112).

[328] L. Chen, H. Pu, Z.-Q. Yu, and Y. Zhang, Physical Review A **95**, 033616 (2017) (Cited on pages 100, 101, and 102).

[329] R. Ravisankar, H. Fabrelli, A. Gammal, P. Muruganandam, and P. K. Mishra, Physical Review A **104**, 053315 (2021) (Cited on page 100).

[330] H. Watanabe and T. Brauner, Physical Review D **85**, 085010 (2012) (Cited on page 100).

[331] T. Macrì, F. Maucher, F. Cinti, and T. Pohl, Physical Review A **87**, 061602 (2013) (Cited on page 100).

[332] Y. Guo, R. M. Kroeze, B. P. Marsh, S. Gopalakrishnan, J. Keeling, and B. L. Lev, Nature **599**, 211 (2021) (Cited on page 100).

[333] Y. Li, G. I. Martone, and S. Stringari, EPL (Europhysics Letters) **99**, 56008 (2012) (Cited on page 100).

[334] C. Fort and M. Modugno, Physical Review A **106**, 043311 (2022) (Cited on pages 100 and 102).

[335] L. Cavicchioli, C. Fort, M. Modugno, F. Minardi, and A. Burchianti, Physical Review Research **4**, 043068 (2022) (Cited on pages 100, 102, and 103).

[336] C. Menotti and S. Stringari, Physical Review A **66**, 043610 (2002) (Cited on pages 104, 105, and 106).

[337] T. Kimura, Physical Review A **66**, 013608 (2002) (Cited on page 104).

[338] H. Pu and N. P. Bigelow, Physical Review Letters **80**, 1134 (1998) (Cited on page 107).

[339] J. H. Kim, D. Hong, and Y. Shin, Physical Review A **101**, 061601 (2020) (Cited on page 112).

[340] R. Cominotti, A. Berti, A. Farolfi, A. Zenesini, G. Lamporesi, I. Carusotto, A. Recati, and G. Ferrari, Physical Review Letters **128**, 210401 (2022) (Cited on page 112).

[341] R. Meppelink, S. B. Koller, and P. van der Straten, Physical Review A **80**, 043605 (2009) (Cited on page 112).

[342] I. Shvarchuck, C. Buggle, D. S. Petrov, K. Dieckmann, M. Zielonkowski, M. Kemmann, T. G. Tiecke, W. von Klitzing, G. V. Shlyapnikov, and J. T. M. Walraven, Physical Review Letters **89**, 270404 (2002) (Cited on pages 119, 125, and 138).

[343] L. Asteria, H. P. Zahn, M. N. Kosch, K. Sengstock, and C. Weitenberg, Nature **599**, 571 (2021) (Cited on pages 119, 125, 126, 127, and 138).

[344] P. A. Murthy, D. Kedar, T. Lompe, M. Neidig, M. G. Ries, A. N. Wenz, G. Zürn, and S. Jochim, Physical Review A **90**, 043611 (2014) (Cited on page 125).

[345] M. E. Mossman, E. S. Delikatny, M. McNeil Forbes, and P. Engels, Physical Review A **102**, 053310 (2020) (Cited on page 125).

[346] M. R. Andrews, C. G. Townsend, H.-J. Miesner, D. S. Durfee, D. M. Kurn, and W. Ketterle, Science **275**, 637 (1997) (Cited on page 126).

[347] B. Xiong, T. Yang, and K. A. Benedict, Physical Review A **88**, 043602 (2013) (Cited on pages 126, 127, 128, and 129).

[348] H. F. Talbot, The London, Edinburgh, and Dublin Philosophical Magazine and Journal of Science **9**, 401 (1836) (Cited on page 127).

[349] F. R. S. Lord Rayleigh, The London, Edinburgh, and Dublin Philosophical Magazine and Journal of Science **11**, 196 (1881) (Cited on page 127).

[350] Y. Zhai, C. H. Carson, V. A. Henderson, P. F. Griffin, E. Riis, and A. S. Arnold, Optica **5**, 80 (2018) (Cited on page 128).

[351] J. H. V. Nguyen, P. Dyke, D. Luo, B. A. Malomed, and R. G. Hulet, Nature Physics **10**, 918 (2014) (Cited on page 138).

[352] Q. Jia, H. Qiu, and A. Muñoz Mateo, Physical Review A **106**, 063314 (2022) (Cited on page 138).

[353] R. Thomas, M. Chilcott, C. Chisholm, A. B. Deb, M. Horvath, B. J. Sawyer, and N. Kjærgaard, Journal of Physics: Conference Series **875**, 012007 (2017) (Cited on page 139).

[354] M. T. Batchelor, X.-W. Guan, and A. Kundu, Journal of Physics A: Mathematical and Theoretical **41**, 352002 (2008) (Cited on page 139).

[355] G. Valentí-Rojas, A. J. Baker, A. Celi, and P. Öhberg, *Topological Gauge Fields and the Composite Particle Duality*. arXiv 2211.06668. (2022) (Cited on page 139).

[356] G. Valentí-Rojas, N. Westerberg, and P. Öhberg, Physical Review Research **2**, 033453 (2020) (Cited on page 139).

[357] M. Correggi, R. Duboscq, D. Lundholm, and N. Rougerie, EPL (Europhysics Letters) **126**, 20005 (2019) (Cited on page 139).

[358] S. Butera, P. Öhberg, and I. Carusotto, Physical Review A **96**, 013611 (2017) (Cited on page 139).

[359] S. Butera, N. Westerberg, D. Faccio, and P. Öhberg, Classical and Quantum Gravity **36**, 034002 (2019) (Cited on page 139).

[360] J. Sánchez-Baena, J. Boronat, and F. Mazzanti, Physical Review A **101**, 043602 (2020) (Cited on page 139).

[361] J. Sánchez-Baena, J. Boronat, and F. Mazzanti, Physical Review A **102**, 053308 (2020) (Cited on page 139).

[362] R. Sachdeva, M. Nilsson Tengstrand, and S. M. Reimann, Physical Review A **102**, 043304 (2020) (Cited on page 139).

[363] J. Sánchez Baena. PhD thesis. Universitat Politècnica de Catalunya. 2020 (Cited on page 139).

[364] B. Santra, C. Baals, R. Labouvie, A. B. Bhattacherjee, A. Pelster, and H. Ott, Nature Communications **8**, 15601 (2017) (Cited on page 140).

[365] Y. Takahashi, K. Honda, N. Tanaka, K. Toyoda, K. Ishikawa, and T. Yabuzaki, Physical Review A **60**, 4974 (1999) (Cited on page 140).

[366] J. Tao, M. Zhao, and I. Spielman, *Observation of anisotropic superfluid density in an artificial crystal*. arXiv 2301.01258. (2023) (Cited on page 140).

[367] G. Chauveau, C. Maury, F. Rabec, C. Heintze, G. Brochier, S. Nascimbene, J. Dalibard, J. Beugnon, S. M. Roccuzzo, and S. Stringari, *Superfluid fraction in an interacting spatially modulated Bose-Einstein condensate*. arxiv 2302.01776. (2023) (Cited on page 140).

[368] L. Balents, Europhysics Letters (EPL) **33**, 291 (1996) (Cited on page 140).